博士論文

論文題目　Visualization of multiple constituents in food by fluorescence fingerprint imaging

（蛍光指紋イメージングによる食品中成分の可視化）

氏名　粉川　美踏

Table of Contents

Preface

This thesis is the summary of my research through master and doctoral courses. Fortunately, my research topic, fluorescence fingerprint (FF) imaging, had so much potential to study into and to develop that it kept me busy for a full five years. Although it is not possible to record the full length of work, I hope I have been able to put down the most important points in this thesis.

The theme of bread has fascinated me for a long time. I like eating it and making it, and it makes my excited to study it. However, experimenting on different ingredients and manufacturing methods to make bread was not my idea of research. I wanted to do something more fundamental and something that was connected to other research areas. This difficult desire was fully met with my research topic, which was connected to bread but also was a topic that could apply studies in other research areas such as optical engineering, image analysis and remote sensing.

The goal of this study was simple, to create an image that shows the distributions of constituents in the food sample. In order to achieve this goal, methods of sample preparation, data acquisition, and analysis methods were improved and developed. Although most of the work was done by myself (while receiving advice from many people), I learnt from the three years in doctoral course that there was a limit to what I can do by myself, or what our laboratory team could do by ourselves. I learnt that working with people of different areas of expertise can achieve results that are much better than what was imagined for. As a researcher, I would like to keep this in mind, and develop good relationships with a broad range of experts.

要旨

食品中の成分は、その分布の仕方によって食品の食感、見た目、安定性など様々な品質に大きな影響を及ぼす。したがって、食品中の成分分布を可視化する技術は食品研究において不可欠であり、その適用範囲は「おいしさ」の性質を探求する基礎的研究から食品製造工程などの応用的場面にまでおよぶ。

しかし、従来の成分可視化技術は試料を染色したり、凍結乾燥させたりするなどの前処理を必要とするものが多く、これらの前処理による試料の変質が避けられない。また、成分毎に染色剤を用いる必要があるため、複数成分の可視化に適さない。そこで本研究では、蛍光指紋計測および分光イメージングという二つの技術に着目し、染色等の前処理を必要としない可視化手法を開発した。

蛍光指紋は励起蛍光マトリクス（Excitation-Emission Matrix: EEM）ともよばれ、試料に照射する励起光の波長を連続的に変化させながら測定した複数の蛍光スペクトルを三次元的に重ね合わせたデータである。一方、分光イメージングでは吸光スペクトルなどの光学的情報に加えて、X・Y 方向の位置情報を同時に取得することによって、試料中の成分分布を可視化する。本研究では、蛍光指紋による成分情報と分光イメージングの位置情報を合わせた、「蛍光イメージング手法」を新たに開発し、この手法を用いて食品中の複数の成分の分布を可視化した。

本論文では、まず２章において、開発した可視化装置の構造や制御方法を説明している。本研究で用いた可視化装置は、研究を進めるにあたって組み立て、改良を重ねたものであり、本研究の大きな成果ということができる。

本研究では以下に示すように大きく三段階に分けて、可視化手法を開発した。

1. グルテン・澱粉・純水を混合したモデル試料におけるグルテン分布可視化（二成分の可視化）[1]：３章

   可視化手法の開発を第一目的に、試薬として販売されているグルテン、及び澱粉を用い、それぞれの割合を変えながら試料を作製し、成分の可視化を試みた。また、試料を薄片化せず、塊のまま可視化できるかどうかを調べた。

   蛍光指紋からグルテン・澱粉割合を推定するために、蛍光指紋とグルテン割合を PLS (Partial least squares) 回帰分析で結びつけるモデルを作成した。この PLS モデルを元に、推定に有用な波長条件を新たに選定し、各試料の蛍光画像を取得した。選定された波長条件で取得したデータを基に改めて PLS モデルを構築し、各画素のグルテン割合を推定した。そして、推定したグルテン割合に応じた色を各画素に当てはめることによって、グルテン・澱粉分布の画像を作成した。

   この画像では、平均的な成分割合を反映することができたが、澱粉粒やグ

ルテン等、細かい構造を可視化するには、薄片化が必要であることがわかった。

2. パン生地モデルにおけるグルテン・澱粉・気泡の可視化と定量化（二成分の可視化）[2, 3, 4, 5]：４章
実際の食品への応用を考え、定性的な可視化手法を目指した。試料には小麦粉に水を混ぜたパン生地モデルを用い、グルテン・澱粉・気泡分布の可視化を試みた。
パン生地モデルは、ミキシング不足・最適ミキシング・ミキシング過剰の３段階で捏ねた生地を用意し、クライオトームを用いて薄片を作成した。この試料を 63 波長条件（励起波長・蛍光波長の組み合わせ）で撮像し、各画素の蛍光指紋を調べた。別に計測した、純粋なグルテンおよび澱粉の蛍光指紋に対し、各画素のコサイン類似度を求め、例えばグルテンとの類似度が高ければグルテンを多く含む、というように各画素のグルテン・澱粉量を推定した。そして、グルテン量は赤の色軸、澱粉量は緑の色軸に合わせて各画素の色を決め、グルテン・澱粉分布を可視化した。さらに、本手法の妥当性を検証するため、蛍光指紋での可視化結果と染色画像を比較した。
次に、ミキシングの３つの段階におけるグルテン・澱粉・気泡の分布を可視化し、ミキシングに伴う変化を定量化した。その結果、ミキシング不足から最適ミキシング段階にかけては、グルテンと澱粉の分布が均一になり、最適ミキシングからミキシング過剰にかけては気泡量が増えることが確認された。

3. パイ生地モデルにおけるグルテン・澱粉・バターの可視化（三成分以上の可視化）：５章
試料には小麦粉・水・バターからなるパイ生地を用い、グルテン・澱粉・バターの三成分の可視化を試みた。これらの三成分を可視化することができれば、タンパク質・多糖類・油脂という食品や生体の構造を作る高分子の可視化ができることになり、応用範囲は広いと思われる。
試料には折パイ生地および練りパイ生地を用いた。試料を厚さ 10 μm に切片化し、スライドガラスの上に乗せて蛍光画像を取得した。蛍光画像は、励起波長 270-330 nm、蛍光波長 350-420 nm の範囲を 10 nm 間隔で網羅し、全部で 53 波長条件で画像を取得した。
各画素の解析にはリモートセンシングの分野で多く用いられている、拘束条件付のスペクトル分解手法を用いた。スペクトルおよび含有率が非負値、一画素の成分和は 1、スライドガラスの含有率は 1 または 0 という拘束条件のもと、各画素の蛍光指紋をグルテン・澱粉・バター・種皮成分（ポリフェノール類）・スライドガラスの五つの蛍光指紋に分解した。それぞれの成分の含有率を色に変換することにより、可視化画像を得た。

蛍光指紋イメージングは、近赤外イメージングなど他の非破壊イメージング

手法と比べても、空間解像度が比較的高く、装置の価格も低い。データ計測時間が長いという欠点があるものの、装置や解析方法を確立させれば、多くの分野で用いられることが期待される。

【参考文献】

1. Kokawa, M., Sugiyama, J., Tsuta, M., Yoshimura, M., Fujita, K., Shibata, M., Araki, T., Nabetani, H., Development of a quantitative visualization technique for gluten in dough using fluorescence fingerprint imaging. Food and Bioprocess Technology, (2013). **6**(11): p. 3113-3123.

2. Kokawa, M., Fujita, K., Sugiyama, J., Tsuta, M., Shibata, M., Araki, T., Nabetani, H., Quantification of the distributions of gluten, starch and air bubbles in dough at different mixing stages by fluorescence fingerprint imaging. Journal of Cereal Science, (2012). **55**(1): p. 15-21.

3. Kokawa, M., Fujita, K., Sugiyama, J., Tsuta, M., Shibata, M., Araki, T., Nabetani, H., Visualization of gluten and starch distributions in dough by fluorescence fingerprint imaging. Bioscience Biotechnology and Biochemistry, (2011). **75**(11): p. 2112-2118.

4. Kokawa, M., Fujita, K., Sugiyama, J., Tsuta, M., Shibata, M., Araki, T., Nabetani, H., Visualization of the distribution of multiple constituents in bread dough by use of fluorescence fingerprint imaging. Procedia Food Science, (2011). **1**(0): p. 927-934.

5. Kokawa, M., Sugiyama, J., Tsuta, M., Yoshimura, M., Fujita, K., Shibata, M., Araki, T., Nabetani, H., Fluorescence fingerprint imaging of gluten and starch in wheat flour dough with consideration of total constituent ratio. Food Science and Technology Research, (2013). **19**(6): p. 933-938.

1. Introduction

1. 1 Objective of this study

One of the most important missions of the modern food scientist is to study the causal relationship between the input and output of food production, i.e., how different manufacture processes affect the quality of the end product. An important link between manufacturing processes and the end product is the food microstructure. Different processes create different microstructures, and the microstructure affects the texture, appearance, taste perception, stability, and many other qualitative characters of food. Therefore, observing this microstructure and understanding its effect on the quality of the end product is very important in food science and technology.

There are multiple requirements for a good observation technique: least sample preparation, good contrast between constituents of interest, and short measurement times are just a few of them [1]. No existing technique fully meets these requirements, and new techniques need to be developed. The objective of this study is to develop a novel imaging technique by combining the fluorescence fingerprint (FF) and hyperspectral imaging to visualize multiple constituents in food without any staining.

1. 2 Structure of this thesis

The thesis is structured as shown in Figure 1-1:

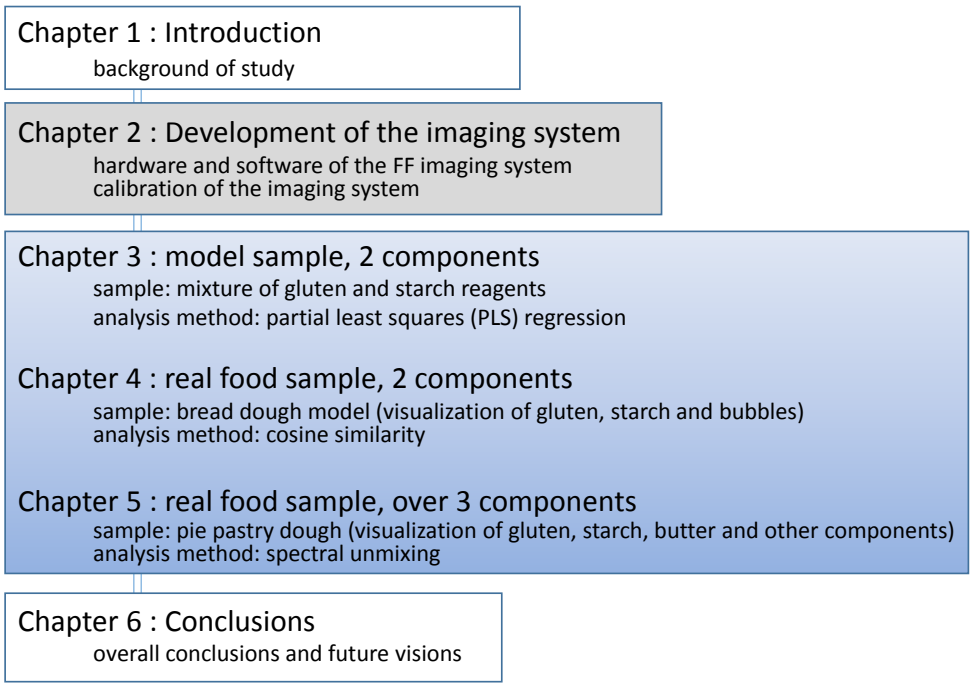

Figure 1-1 Structure of thesis

The introduction will explain basic studies regarding the topics of fluorescence and imaging. The second chapter shows the setup of the imaging system which was used throughout the research. The imaging system could be cited as the most important achievement of this research, since it can be applied to many other samples in the future. The main chapters explain the applications of FF imaging in three steps, going from model samples to real foods, and increasing the number of components visualized. These chapters are based on five original papers. The last chapter summarizes the conclusions and draws future visions.

1. 3 Fluorescence

Fluorescence is the light (luminescence) emitted by molecules when they are excited by photons [2]. Energy levels of an organic molecule are determined by the electronic, vibrational and spin state of the molecule, and take discrete values called quanta. The most stable form of the molecule is the ground level, S_0, when the energy level is at its lowest value. When the molecule absorbs a discrete quantum of energy from an outside source, the energy of the molecule rises to a higher level. The energy absorbed equals the difference between the two molecular energy states. As the molecule returns to its ground electronic state, the absorbed energy is released in some way. If this absorbed energy is emitted as light, it is called fluorescence.

In this study, "fluorescence" refers to observable light in the near UV to VIS (approximately 200-700 nm). Therefore, for a molecule to emit fluorescence, two conditions need to be met:

1. The molecule absorbs UV to VIS light.
2. The absorbed light is released as light emission.

1. 3. 1 Absorbance

In order for light to be absorbed by a molecule, the photon of the light needs to have the proper energy to reach a discrete excited state of the molecule. The energy of light absorbed (mole basis) is given by the Planck frequency relation:

$$E = Nh\nu = \frac{Nhc}{\lambda} \qquad \dots (1)$$

E is the energy associated with frequency ν and wavelength λ, c is the velocity of light, and N is Avogadro's number. Absorption only occurs if E equals the difference in energy between the ground electronic state and an excited state of the absorber.

In this study, we are focusing on light in the near UV to VIS region, i.e. approximately 200-700 nm. According to the Planck frequency relation, this corresponds to an energy value of 170-598 kJ/mol ($N = 6.022 \times 10^{23}$, $h = 6.626 \times 10^{-34}, c = 2.998 \times 10^{8}$).

This energy difference of approximately 200-600 kJ/mol is only achieved in molecules with π molecular orbitals. The π orbital exists in molecules with double or triple bonds. Molecules with only σ orbitals, consisting only of singular bonds, have a much higher energy gap between the ground and excited states. These molecules only absorb light in the far UV.

Furthermore, molecules with multiple double bonds connected alternately with singular bonds are called conjugated molecules, and require smaller energy for electron transition. As shown in Table 1-1, the more conjugated a molecule is, the smaller energy it needs for electron transition to occur [3].

Table 1-1 Absorbance wavelengths of conjugated polyenes

n	molecule	structure	wavelength [nm]
1	ethylene	CH2=CH2	165
2	butadiene	CH2=CH-CH=CH2	217
3	hexatriene	CH2=CH-CH=CH-CH=CH2	268
4	octatetraene	CH2=CH-CH=CH-CH=CH-CH=CH2	304
5	decapentaene	CH2=CH-CH=CH-CH=CH-CH=CH-CH=CH2	334
6	dodecahexaene	CH2=CH-CH=CH-CH=CH-CH=CH-CH=CH-CH=CH2	364
7	tetradecaheptaene	CH2=CH-CH=CH-CH=CH-CH=CH-CH=CH-CH=CH-CH=CH2	390
8	hexadecaoctaene	CH2=CH-CH=CH-CH=CH-CH=CH-CH=CH-CH=CH-CH=CH-CH=CH2	410
10	eicosadecaene	CH2=CH-CH=CH-CH=CH-CH=CH-CH=CH-CH=CH-CH=CH-CH=CH-CH=CH-CH=CH2	450

Conjugated systems also show π to π^* transition (π^* is the excited state) when they are cyclized (turned into rings), but some of these molecules show characteristics that cannot be explained by the conjugated systems alone. One of these molecules is benzene (C_6H_6).

Benzene has three single bonds and three double bonds. However, the actual bond lengths between the carbon atoms are all the same. This is explained by the delocalization of electrons in the ring. The delocalization of electrons makes the benzene molecule a very stable one. This is why benzene absorbs at a shorter wavelength (255 nm) than hexatriene, a linear conjugated hydrocarbon with the same number of carbon atoms and double bonds. Cyclized conjugated molecules that show the typical characteristics of benzene are called aromatic compounds.

Molecules formed from fused benzenes such as naphthalene (two benzenes combined) and anthracene (three benzenes combined) show absorbance at longer wavelengths than benzene [4]. Furthermore, the combination of functional groups such as –OH and $–NO_2$ to benzene also shifts the absorbance to longer wavelengths.

Aromatic amino acids such as phenylalanine, tyrosine, histidine, and tryptophan have a benzene ring in their molecular structures and show near UV to VIS absorbance. Table 1-2 shows some typical aromatic compounds and their absorbing wavelengths [5].

Table 1-2 Typical aromatic compounds and absorbing wavelengths

molecule	structure	wavelength [nm]
benzene	C_6H_6	255
naphthalene	(two benzenes fuzed) $C_{10}H_8$	286
anthracene	(three benzenes fuzed)$C_{14}H_{10}$	375
phenole	benzene + OH	290

As a conclusion, an important condition for a molecule to absorb light in the near UV to VIS is to contain conjugated double bonds or aromatic structures. Details concerning atomic and molecular orbitals are shown in Appendix I.

1. 3. 2 Fluorescence

The absorption of light causes the molecule to transfer to an “excited” state. This is a very unstable state, so the energy is released again and the molecule goes back to its most stable state. This release of energy is called deexcitation. There are many deexcitation processes, and for a molecule to show fluorescence, the release of energy as light needs to dominate over the other deexcitation processes. Below are the main deexcitation processes:

1. Fluorescence (includes phosphorescence)
2. Radiationless transition (molecule loses energy as heat)
3. Excitation energy is transformed to another molecule
4. Excited electron leaves the molecule that absorbed the photon

All these processes progress at a certain rate, expressed with a constant *k*. If a particular process has a large rate constant (the reaction proceeds quickly), the majority of energy will be released through that process. Therefore, for fluorescence to be observed strongly, the rate constant *k* for fluorescence needs to be relatively large compared to the other reactions.

Two common reasons for the weakening of fluorescence is high temperature and the existence of substances referred to as “quenchers”. At high temperature, radiationless transitions are more likely to happen due to the increase in vibrational energy. The rate constant *k* for fluorescence becomes small compared to the rate constant for radiationless transition, leading to weaker fluorescence.

Quenchers are substances that are easily excited. The presence of these substances activates energy transfer between molecules, and the energies of the excited molecules are transformed to the quencher. This decreases the energy released as fluorescence and lowers fluorescence intensity.

Details on the deexcitation processes, their rate constants and the effect on fluorescence intensity are explained in Appendix II.

1. 3. 3 Fluorophors and applications of fluorescence

Intrinsic fluorophors

Fluorophors are chemical and physical substances that show fluorescence. Natural or intrinsic fluorophors exist in the sample itself, while extrinsic fluorophors are added to the sample to enable analysis or imaging by fluorescence.

Typical intrinsic fluorophors observed in foods are aromatic amino acids, enzyme cofactors such as nicotinamide adenine dinucleotide (NADH) and vitamins, flavins, and chlorophyll. Tryptophan is the dominant source of emission in proteins [6]. Tryptophan is typically excited at 295 nm and emits fluorescence at 353 nm (in water, neutral pH) but the emission is highly sensitive to the local environment. This sensitivity allows it to be used as a reporter group for protein conformational changes. Tyrosine has a higher quantum yield than tryptophan but is often quenched when it exists with tryptophan. Fluorescence of phenylalanine can only be observed when the protein lacks both tryptophan and tyrosine.

NADH is universally present in living cells and has an excitation and emission maxima at 340 and 460 nm [6]. NADH has been observed on the surface of meat, assumedly emitted by bacteria [7]. Figure 1-2 shows the fluorescence spectra of the three aromatic amino acids and NADH, measured in three-dimensional mode (data acquired by spectrophotometer in laboratory).

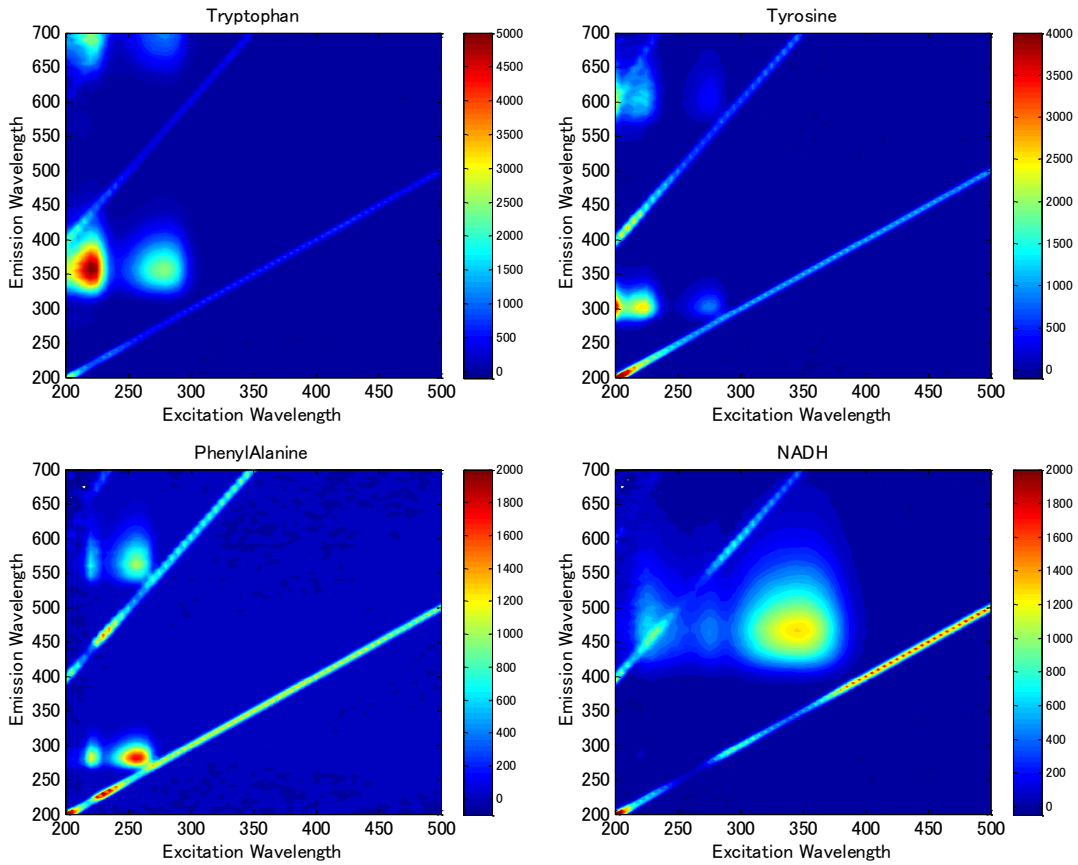

Figure 1-2 Fluorescence spectra of Tryptophan, Tyrosine, Phenylalanine, and NADH. The spectra were measured in the laboratory with F7000 (Hitachi high technologies). [7]

Tryptophan: 5 mol/l, photomultiplier 550V

Tyrosine: 5 mol/l, 580V

Phenylalanine: 3 mol/l, 700V

NADH: 4 mol/l, 580V

Slit: 5 nm, scanning speed: 60000 nm/min

Vitamin A (retinol), B_2 (riboflavin), B_6 (pyridoxine) and E (tocopherols) all show fluorescence [8]. Retinol is known to be excited around 325 nm and its emission maxima to range from 475 to 510 nm. Riboflavin has a high quantum yield around 0.25 and a fluorescence maxima around 515 nm in neutral aqueous solutions. Tocopherols dissolved in ethanol fluoresce at 340 nm (excitation 295 nm). Figure 1-3 shows the fluorescence spectra of these molecules [9].

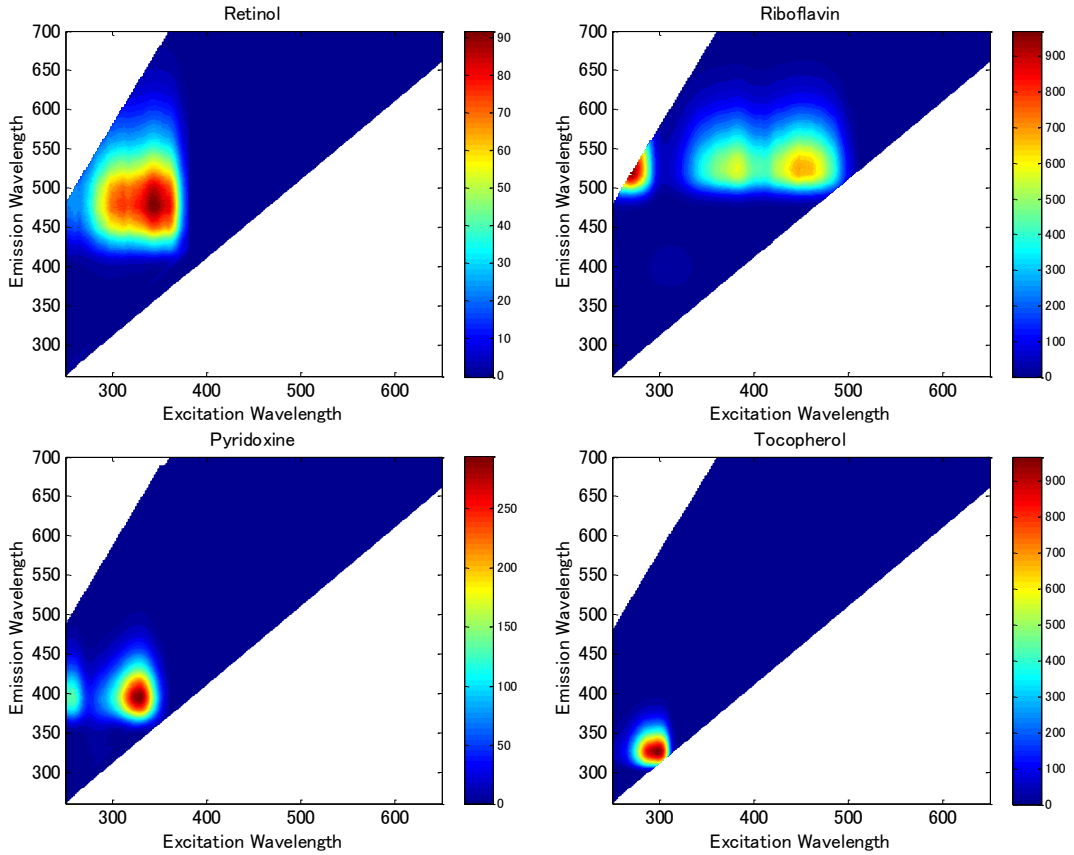

Figure 1-3 Fluorescence spectra of Retinol, Riboflavin, Pyridoxine, and Tocopherol. The spectra were measure with LS50B (PerkinElmer).[9]

Chlorophyll is a complex of porphyrin and metal ions and exists in all photosynthetic organisms. There many types of chlorophyll, and the two mail types are chlorophyll a and b. The porphyrin ring is highly conjugated and provides many delocalized π electrons that allow light absorption in the VIS range. Chlorophyll absorbs in both the red and blue wavelengths but its fluorescence is mainly in the red region [2].

Extrinsic fluorophors

Extrinsic fluorophors or probes are used when the molecules of interest are non-fluorescent. Many types of fluorophors have been developed, not just for identifying certain molecules but for measuring temperature [10], pH [11], concentrations of substances such as Cl- [12], Na+ [13] and Ca2+, and enzymatic cleavage [14]. There probes make use of a characteristic of fluorescence that the emission wavelength and intensity are affected by many factors such as the

configuration of protein and vibration of molecules

The green fluorescent protein (GFP) is a notable probe. Since the GFP chromophore forms without enzymatic synthesis, it is possible to express the gene for GFP into cells [15]. When GFP is fused to proteins, the protein becomes fluorescent without any change to its normal functions. Practically every major organelle of the cell has been successfully visualized with GFP.

Most fluorescence probes are organic molecules, but quantum dots are nano-crystals of semiconducting inorganic materials containing 130-150 atoms [16]. The light characteristics of quantum dots can be tuned by changing the radius of the quantum dot (the smaller the radius the longer the wavelength).

Most probes are synthesized for a certain purpose but there is also a new approach called diversity oriented fluorescence library approach [17] that first creates a library of over 10,000 intrinsically fluorescent small molecules without any specific target. For each new application, the whole library is scanned and the best fluorescent molecule is chosen.

Almost all applications of fluorescence are based on the use of extrinsic fluorophors. Some recent applications of fluorescence are explained in Appendix III.

1. 3. 4 The Fluorescence Fingerprint

In conventional fluorescence spectroscopy, light of one specific wavelength is irradiated on the sample and the emission spectrum is measured. The wavelength of the emission peak is used for qualitative analysis (determination of the constituents which compose the sample) and the height of the peak for quantitative analysis (determination of the amount of the constituent). Instead of one emission spectrum from one excitation wavelength, multiple emission spectra can be acquired by irradiating the sample with a set of consecutive excitation wavelengths. The fluorescence fingerprint (FF), also known as the excitation-emission matrix (EEM), is a set of these fluorescence spectra, aligned in order of the excitation wavelength so as to create a three-dimensional diagram [18] (Figure 1-4). The pattern of this diagram, rather like a fingerprint, is unique for each constituent.

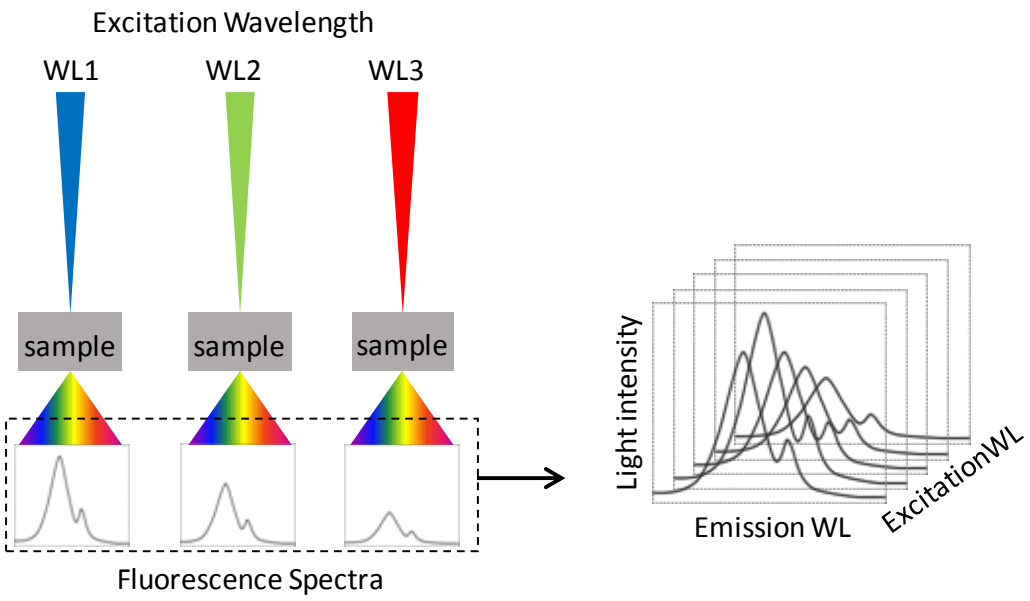

Figure 1-4 Multiple emission spectra constructing the fluorescence fingerprint [18]

Unlike the conventional fluorescence spectrum which focuses mainly on the spectrum peak, the FF makes use of the whole pattern, taking in consideration the fluorescence intensity of wavelengths other than the peak point. This means that FF can discriminate between samples which have a similar dominating component but have differences in minor components, for example, fruits of the same variety cultivated in a different region [19].

The advantages of FF measurement can be brought out by the combination with multivariate analysis methods. Fluorescence spectra tend to be broad, have bad resolution and overlap when there are multiple sources of fluorescence. Furthermore, the peaks may also contain physical and structural information of the sample, not only the chemical information, making it even more difficult to identify the specific fluorescent substance connected to the peak [20]. This problem can be resolved by analyzing the entire FF pattern with multivariate analysis methods. Some multivariate analysis methods are capable of decomposing the data into information about the sample on one hand and information about the fluorescence spectra on the other. Information about the fluorescence spectra may allow the specific fluorescence substance to be defined.

Many qualitative and quantitative studies using the FF and multivariate analysis methods have been reported for various target foods. Some cases are reviewed below.

Guimet et al. [21] combined FF measurement with unfold principal component analysis (U-PCA) and parallel factor analysis (PARAFAC) to discriminate between

virgin olive oil and pure olive oil. Both analyses showed that it was not the dominating fluorophor, chlorophyll that discriminated between the two types of oils, but vitamin E whose fluorescence was found in a different wavelength. This showed that the simple measurement of the dominating fluorophor was not enough to achieve the desired result.

Sikorska et al. [22] analyzed the amount of riboflavin and aromatic amino acids in beer by applying partial least squares (PLS) regression to the FF data. Compared to the conventional methods based on chromatographic techniques to measure the amount of these amino acids, the measurement and analysis of FF data proved to be rapid and less expensive, requiring no pre-treatment.

Yin et al. [23] investigated the variety, brewery and vintage of wines using principal component analysis (PCA) with FF spectroscopy. In the score plot of the first two principal components, wines with the same properties grouped together. Although the study was preliminary and needed a larger set of samples for the method to be confirmed, if showed the potential of FF spectroscopy to measure wine quickly, easily and non-destructively.

Discrimination of agricultural products based on their geographic origin has been achieved by combining FF measurement and discrimination analysis [19, 24] and applied to mangoes and taros (*Colocasia esculenta*). The discrimination accuracy was equivalent to that of inorganic elements composition, which requires complicated sample treatment.

1. 4 Non-destructive imaging methods

Many non-destructive imaging methods have been developed through the 20-21st century. The imaging methods differ in their applications, cost, acquisition times, spatial resolution etc. Characterizing these imaging methods would, in turn, enable us to understand the standing position of fluorescence fingerprint imaging.

Figure 1-5 shows the spatial resolution × acquisition time × cost matrix for typical non-destructive imaging methods. The spatial resolution for imaging methods that use light as the imaging medium are limited by the diffraction resolution of light. i.e., the shorter the wavelength, the higher the resolution. However, near-infrared imaging has a lower resolution than the diffraction limit, owing to the limitations of sample thickness. Although each imaging method will be explained in the following sections, a notable point is that FF imaging can achieve relatively high spatial resolution with affordable machinery. This point will be explained again at the end of this chapter.

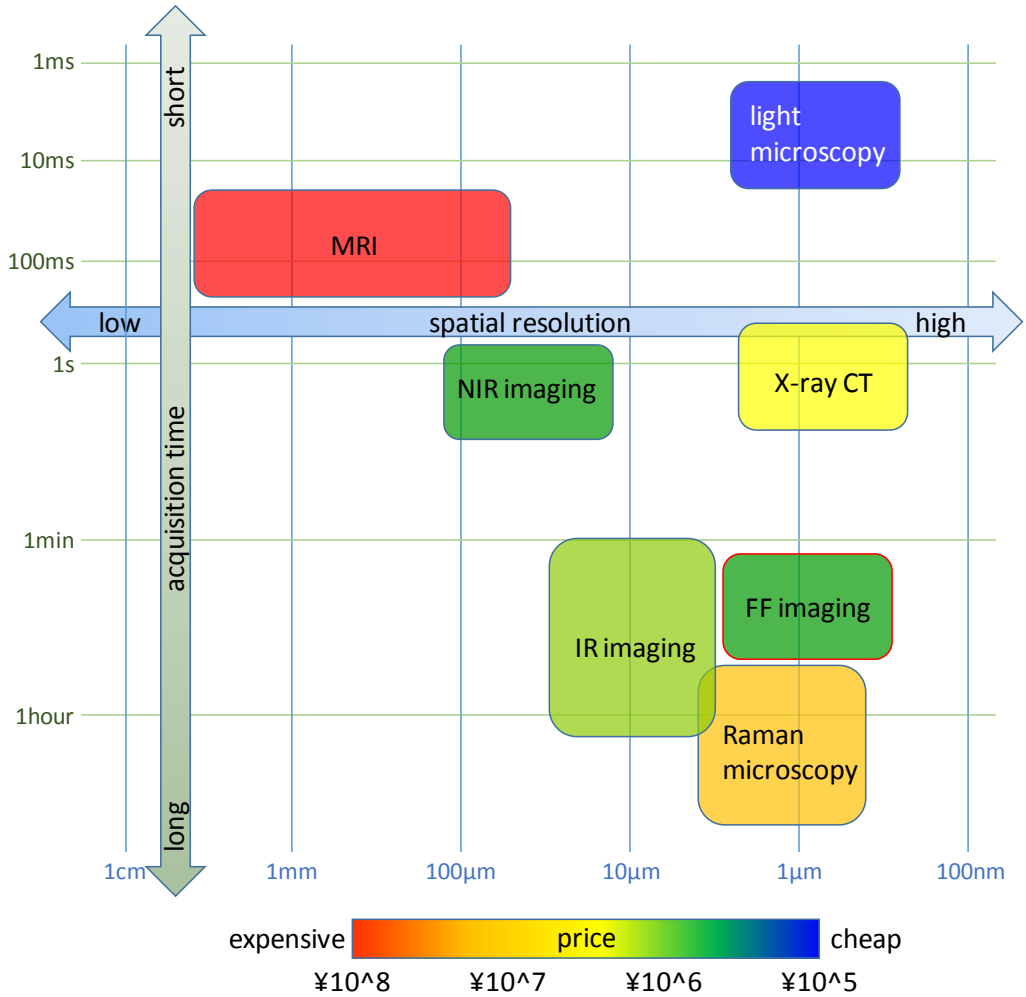

Figure 1-5 Spatial resolutions, acquisition times, and price for typical non-destructive imaging methods. ¥=Japanese yen. References: [25, 26, 27, 28, 29]

1. 4. 1 Light microscopy

Light microscopy is the basic form of optical microscopy with the simplest form consisting of an objective lens and an eyepiece [30]. By adding a light source and condenser underneath the sample (on the opposite side of the objective lens), the simplest form of bright field microscopy can be achieved. In order to achieve contrast between different constituents and features, the sample is stained.

Non-destructive observation without any staining is possible using methods such as phase contrast and polarization. Phase contrast is a method to visualize semi-transparent, unstained samples [31]. When light passes through these samples, the light phase is retarded, typically by a ¼ of a wavelength. On the contrary, background light is shifted positively by ¼ of a wavelength by an annular aperture and a matching phase ring [32]. As a result, light passing through the sample and background light cancel out, and the sample can be observed as a dark figure.

Polarization light microscopy can be used to observe crystalline structures. A typical application in food, is to observe the disappearance of the birefringence of starch, due to gelatinization [33]. In polarization light microscopy, light that oscillates in one orientation (polarized light) is radiated onto the sample. Some crystals have a property of double refraction, i.e., the radiated light is split into an ordinary and extra-ordinary ray at the refractive index interface [34]. These ordinary and extra-ordinary rays are mutually perpendicular and when they pass through another polarizer before the observation tube, they are combined with constructive and destructive interference [35]. As a result, some orientations shine brighter than others.

Phase contrast and polarization microscopy systems are relatively easy to mount on a normal light microscope. Since the FF imaging system, explained in chapter 2 is based on a light microscope, mounting these systems to acquire further information from the sample could be a realistic development in the future.

1. 4. 2 Hyperspectral imaging

Hyperspectral imaging, a technique that integrates conventional spectroscopy with imaging methods, is currently used in diverse fields such as astronomy, agriculture and medicine as well as food technology [36]. Its main idea is to acquire the spectroscopic information for each spatial position of the sample, which can be analyzed to give the contemplated information (Figure 1-6).

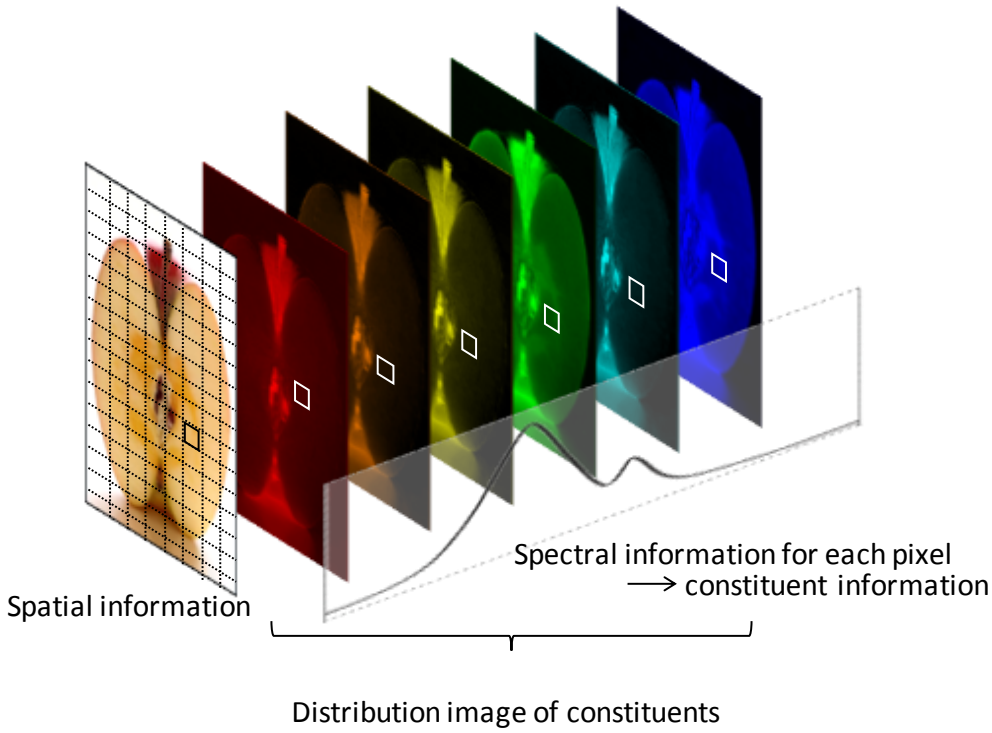

Figure 1-6 Hyperspectral imaging. Both spatial and spectral information are acquired concurrently. Spectral data gives information on the chemical and physical properties of the constituent measured. Therefore, by measuring these two information together, we can acquire the distribution image of constituents and properties.

Hyperspectral imaging methods can be divided into several groups. One way to categorize different hyperspectral imaging methods would be to divide them based on the method to acquire data: area scanning, point scanning, or line scanning [37]. Area scanning is also called staring imaging or focal plane scanning, and images of a fixed field of view is acquired in one wavelength after another. Point scanning involves measuring the spectrum of a single point, moving the sample and measuring the spectrum at the next point. Line scanning is also called pushbroom, where spectral measurements from a line of sample are acquired with an array detector while the sample is moved in a perpendicular direction.

Another way of distinguishing groups would be to divide them based on the spectroscopic data. This can be expressed in several modes: reflectance, fluorescence or transmission. Most studies using hyperspectral imaging in food have used the reflectance mode, usually measured in the Vis-NIR or NIR range, and some in the IR region. Raman scattering has also been used, although it is not as wide spread as NIR.

These imaging methods are discussed below.

Near-infrared imaging

The NIR region of the electromagnetic spectrum is roughly in the range of 780-2526 nm, according to the American Society of Testing and Materials (ASTM) [38]. The absorption bands occurring in this region correspond to the overtones and combinations of vibrations of –CH, -NH, -OH and –SH functional groups. The fundamental vibrations of these functional groups occur in the mid IR region.

The change in vibrational state that is explained with a harmonic oscillation model (two masses connected with a spring) follows the selection rule of $\Delta v = \pm 1$ where v is the vibrational quantum number. The absorption of NIR light corresponds to transitions of $\Delta v > 1$, which is basically forbidden in a harmonic vibration model. Absorption of overtones ($\Delta v > 1$) can only be explained in an anharmonic oscilliation model where the Morse potential energy gives more realistic values. Even though overtones are not rigorously excluded in anharmonic oscillation models, they are still forbidden transitions, and therefore, absorption of NIR is much weaker than the fundamental absorption in the mid IR region.

NIR spectroscopy also measures combination bands, which are results of vibrational interactions [38]. Two NIR absorption bands of a molecule with the same frequency are known to not simply sum up, but split into two peaks of higher and lower frequencies. This type of configuration interaction is called Fermi resonance.

These two types of bands, i.e., overtones and combination bands, are broad, overlapping and 10-100 times weaker than the fundamental absorptions. Therefore, in order to make use of this data, chemometrical data processing is needed. This also applies to imaging with NIR, the spectroscopic data always needs to be analyzed before meaningful images can be acquired.

NIR imaging has been applied to many foods, with several objectives. One of these objectives is to visualize the distributions of constituents of interest, for example, fat distribution in fish [39, 40, 41, 42] and beef [43] and sugar distribution in fruit [44]. These methods involve creating a calibration curve that links NIR spectra with the quantity of constituent. Since measurement is performed on the whole sample (fish or chunks of meat), the measurement is macroscopic with one pixel of the camera corresponding to around 0.4 mm/pixel [40].

Another popular objective is the detection of unwanted substances such as foreign materials in batches of fruit [45, 46] and carcasses on poultry [47]. In this case,

discrimination functions are created from pixels whose category (ex. foreign materials or fruit) is known, and the remaining pixels are classified by the discrimination function. The spatial resolution is normally lower than that of constituent visualization, since large areas need to be scanned for practical use.

The use of NIR imaging is also much studied for chemical imaging in pharmaceutical analysis [48, 49]. Medicine tablets need to have a certain amount of active substances which need to be homogeneously distributed throughout the whole tablet or package of powder. This requires higher spatial resolution compared to the two former applications, and resolutions such as $200\ \mu m \times 200\ \mu m$/pixel are used [49].

These applications use a relatively low spatial resolution compared to the diffraction limit (resolution limit due to the wavelength of light) because there is more emphasis in measuring many samples in a short time. However, NIR is not suited to observe samples in high resolution for the following reasons [25]: since NIR spectra are combinations and overtones of the fundamental vibrational spectra, the sample needs to be thick for measureable signals to be acquired (over 100 μm for spectra in the range of 1200-2450 nm and over 500 mm that of 950-1720 nm). On the other hand, to achieve maximum spatial resolution, the numerical aperture (NA) value of the objective lens needs to be small. Since focal depth is inversely proportional to the square of NA value, a small NA value means that the whole thickness of the sample will be in focus. For this reason, the standard objective of the NIR imaging system is a refractive lens with $1\times$ magnification, in which case the resolution would be in the order of 10-100 μm.

The image acquisition speed for NIR imaging is at trade off with the spatial and spectral resolution, but is relatively fast compared to other imaging methods. For example, Segtnan et al. [40] have used scanners that collect 10000 spectra per second (15 wavelengths per spectrum) when the field of view was 60 pixels across and 500 to 670 pixels lengthwise.

Infrared imaging

Spectral imaging in the infrared is typically conducted with a Fourier transform infrared (FT-IR) imaging system, which uses an interferometer to acquire the IR spectrum. With a point scanning type, where the spectrum of each pixel is measured at a time, measurement could take tens of hours if the spatial resolution is to be high [25]. This is because as the spatial resolution is made higher, the intensity of the light entering the spectrometer is lowered, and therefore, a large number of scans (typically hundreds) need to be averaged to achieve desired S/N ratio.

The area scanning type of FT-IR imaging system acquires images of the sample at different combination of lights produced by the interferogram. These types of imaging systems take much less time to acquire images with high spatial resolution, in the orders of minutes [25]. Spatial resolution can be enhanced by using an attenuated total reflection (ATR) accessory, where the sample is immersed in a medium of high refractive index, such as germanium (n = 4.0). However, with ATR imaging, the sample plane needs to be completely flat, and this limits the form of sample that could be observed.

Raman imaging

The advantage of Raman imaging is that the diffraction limit is in the order of the VIS light range and is much higher than IR imaging, while the acquired information is of molecular vibration. The point scanning type of Raman imaging systems have a confocal design where the laser light source is focused on a small focal volume within the sample. The Raman- and Rayleigh-scattered light is collected by the objective lens, Rayleigh-light is filtered with a dichroic beamsplitter, and the spectrum of the Raman-light is measured with a spectrophotometer. However, similarly to the point scanning type IR imaging system, image acquisition times can be very long. For example, Qin et al. [28] has reported an imaging system that acquires images of 370×50 pixels, corresponding to an area of $74 \times 10\ \mathrm{mm}^2$, which takes approximately 3 hours. This system was used to detect melamine concentrations in dry milk [28] and lycopene in tomatoes [50].

1. 4. 3 Magnetic resonance imaging (MRI)

Magnetic resonance imaging (MRI) is an imaging method based on nuclear magnetic resonance (NMR) which measures the resonance absorption of radiation by nuclei or unpaired electrons in a magnetic field [16] and reveals information on the electronic structure (chemical groups). In MRI, information such as the distributions of protons (or hydrogen nuclei) in a solid object are measured by applying an inhomogeneous magnetic field (a magnetic field that is linearly varied with a certain gradient) to the object.

The biggest advantage of MRI is that it can nondestructively visualize opaque samples in two-dimensional and three-dimensional form. In the field of food science, MRI has been used to visualize the internal structure and physical state of water in fruit [29], fat and water in meat [51] and live pigs [52], and to investigate structures of

cheese [53].

The spatial resolution of MRI depends on the magnetic field gradient, i.e., the intensity of the magnetic field needs to be different at each pixel [29]. By applying a strong magnetic field gradient, the spatial resolution can be enhanced, but the S/N ratio could be sacrificed. Van As et al. [29] have shown that a resolution of 39×39 μm shows clearer images than 31×31 μm resolution in terms of S/N ratio. In most cases MRI measurements are performed on macro-scale samples with one pixel corresponding to orders of millimeters.

Although MRI is a promising method to visualize the internal structure and constituent distribution in food, the measurement system is too expensive to be applied to food in practice.

1. 4. 4 X-ray computed tomography

X-ray computed tomography (CT) is another method where images of an opaque sample can be acquired non-destructively. In the field of medical imaging, X-ray CT and MRI are two methods that are used complementarily to acquire images of the insides of the body.

CT images are acquired by transmitting X-rays through the sample. X-rays are electromagnetic waves that have wavelengths from 1 pm to 10 nm, and consequently have very high energies, which allow them to transmit through samples. The transmitted intensity of the X ray I_t follows the Lambert-Beer law as in

$$I_t = I_0 \exp(-\mu l) \qquad \dots (2)$$

where I_0 is the initial intensity, l is the length of the beam path and μ is the linear attenuation coefficient which varies according to a material's density and atomic composition [54]. μ is usually converted to CT numbers using the linear attenuation coefficient of water, μ_w.

$$\text{CT number} = \frac{1000(\mu - \mu_w)}{\mu_w} \qquad \dots (3)$$

CT numbers of air, fat and bone are -1006, -90, and +1005, respectively [54].

In food science, CT has been used to measure aerated foods to visualize the distribution of bubbles [55, 56], assess the fat in beef [57] and visualize the distribution of salt and fat in salmon [40]. With an X-ray micro-CT system, spatial resolutions up to 5 μm can

be obtained. One scan takes less than a second, and many studies take multiple scans to obtain three-dimensional images of the sample.

1. 5 Microstructure of bread and pastry

1. 5. 1 Bread and observation of its microstructure

Bread is the staple food in Europe, most countries in the North and South American continent and the Middle East / North Africa but is eaten all over the world and could be said as the world's most important food. It is said to be first invented in Egypt where the yeast existing on the surface of the wheat grain caused the bread to leaven, creating the original form of the aerated bread today.

One of the important factors determining the palatability of bread is the texture [58]. The various advertising copies of bread, claiming that the bread is "soft and smooth" or "crispy", are examples of the consciousness of consumers toward the texture of bread. The texture of the final product is affected by multiple processes in bread making, but it can be said that the first step, the mixing process is a key step in the production of dough [59]. As flour, water and other ingredients are mixed, the dough goes through many stages of mixing. The optimal mixing state may slightly differ depending on the type of texture required for the end product, but generally, three things are known to be accomplished: a homogenous mass of flour and water is formed, a three-dimensional protein network with the capacity to hold gas is developed, and air cells are incorporated into the dough [60]. The protein which forms the three-dimensional network, gluten, dominates the rheological behavior of dough during extensive deformation [61] and along with the starch which acts as a filler, determines the texture of the bread. The bubbles incorporated in the dough through the mixing process also affect the end product because these small bubbles act as the nuclei of bigger bubbles created through the fermentation and baking process and no further occlusion of gas occurs after the mixing process [62].

While mixing is the key process in creating bread, it is one of the most difficult processes since the point of optimal mixing is hard to determine. The total amount of energy required to fully develop the dough to the optimal point depends on many factors and therefore it has been the job of experienced artisans to determine the optimal mixing speed and time for each batch of dough. Consequently, many studies have tried to capture this state of "optimal mixing" objectively with the application of many new technologies. The most straightforward approach is to examine the structure of dough and distribution of gluten and starch in it with a microscope. Many microscopic imaging

techniques have been developed for this purpose.

The optical microscopic approach and the electron microscopic approach are the main method used to visualize the structure of dough, with a few studies using X-ray tomography [58] and magnetic resonance microscopy [63]. The optical microscopic approach includes bright field [64, 65, 66], confocal scanning laser [67, 68, 69, 70, 71] and epifluorescence light [72] microscopies. While optical microscopy can visualize specific chemical compounds in the complex mixture and is therefore suitable for foods which are complicated multi-component materials [73], it always involves pretreatment with staining. The problem with staining is that the results could greatly vary by the selection of stains and staining conditions such as the concentration, solvent and staining time. The researcher's technique to stain the sample evenly or prevent color degradation may also affect the result. The risk of sample alteration is hard to eliminate.

Much research has been done with the electron microscopic approach such as scanning electron microscopy (SEM) [74, 75] and transmission electron microscopy (TEM) [76]. SEM is heavily used in the visualization of dough development for its high magnifications and clear images [77] but the risk of sample alteration is difficult to eliminate since the sample needs to be either dried or frozen below -80 ºC and covered in a 5-20-nm-thick metal layer [78]. Environmental scanning electron microscopy (ESEM) is a variable-pressure SEM, allowing the sample to be observed without dehydration or surface coating [79, 80, 81] but differences between chemical compounds cannot be visualized.

1. 5. 2 Pastry dough and laminated products

In the western food culture, baked products can be categorized into several groups, namely, bread and fermented goods, sponges and cakes, biscuits and cookies, and pastry [82]. Pastry doughs are made of wheat flour mixed with a large ratio of fat, and can be further categorized into short pastry and laminated doughs.

Laminate doughs are made by folding a piece of dough to encase a block of fat (usually butter), creating hundreds of layers of pastry [83]. The pockets of air trapped between the layers expands when the pastry is baked, and along with the steam from the dough and butter, forces the layers to separate and rise. In the initial step of making the laminated dough, flour, water and salt are mixed together, and gluten is formed. Conversely, short pastry is made by mixing flour, fat and water together. The fat inhibits the formation of a gluten matrix, and this results in a "short" texture.

There are few studies visualizing the structure of pastry and only a few studies on the structure of cookies [1, 84] . Therefore, visualizing the structure of these doughs

would have a great impact on cereal science.

1. 6 Summary

Fluorescence has been used in many areas of science as a tool for imaging. However, most of its applications use extrinsic fluorophors, fluorescent substances that are added to the sample so that constituents or features of interest show up with high contrast. Studies on the structure and constituent distribution of bread and other wheat flour-based products follow this trend, and most of the past research have stained the dough with fluorescence stains.

However, wheat contains proteins which are constructed from amino-acids, and some amino-acids that have a benzene ring in their structure, namely, aromatic amino-acids, show strong intrinsic fluorescence. Many other substances existing in food show fluorescence, such as vitamins and chlorophyll.

Measuring these intrinsic fluorophors with multiple combinations of excitation and emission wavelengths, gives their fluorescence fingerprints (FFs). By combining the FF with hyperspectral imaging techniques, this study aims to visualize multiple constituents in food without preprocesses such as staining.

References

1. Maeda, T., Kokawa, M., Miura, M., Araki, T., Yamada, M., Takeya, K., Sagara, Y., Development of a novel staining procedure for visualizing the gluten–starch matrix in bread dough and cereal products. Cereal Chemistry Journal, (2013). **90**(3): p. 175-180.

2. Nobel, P.S., Physicochemical and environmental plant physiology. 4th ed. (2009): Academic Press. 582.

3. 第３章　光と分子. http://bunshi.c.u-tokyo.ac.jp/~endolab/Jpn/lab/kisogendai/no6_web.pdf.

4. Shimadzu. Uv talk letter vol.2(2008) 紫外可視吸収と有機化合物の構造との関係. http://www.an.shimadzu.co.jp/uv/support/lib/uvtalk/uvtalk2/apl.htm.

5. 山本勝博. 紫外スペクトル法による天然水中の有機成分の測定. http://www.osaka-c.ed.jp/kak/rika1/osaka-ch/chem11-4.htm.

6. Lakowicz, J.R., Principles of fluorescence spectroscopy. 3rd Edition ed. (2006), NewYork: Springer Science+Business Media, LLC.

7. Yoshimura, M., Sugiyama, J., Tsuta, M., Fujita, K., Shibata, M., Kokawa, M., Oshita, S., Oto, N., Prediction of aerobic plate count on beef surface using fluorescence fingerprint. Food and Bioprocess Technology, (2013).

8. Schulman, S.G., Molecular luminescence spectroscopy methods and applications: Part 1. (1985), USA: John Wiley & Sons, Inc.

9. Christensen, J. Foodfluor - food fluorescence libary. 2005; http://www.models.kvl.dk/foodfluor.

10. Feng, J., Xiong, L., Wang, S., Li, S., Li, Y., Yang, G., Fluorescent temperature sensing using triarylboron compounds and microcapsules for detection of a wide temperature range on the micro- and macroscale. Advanced Functional Materials, (2013). **23**(3): p. 340-345.

11. Wang, R., Yu, C., Yu, F., Chen, L., Molecular fluorescent probes for

monitoring ph changes in living cells. TrAC Trends in Analytical Chemistry, (2010). **29**(9): p. 1004-1013.

12. Biwersi, J., Tulk, B., Verkman, A.S., Long-wavelength chloride-sensitive fluorescent indicators. Analytical Biochemistry, (1994). **219**(1): p. 139-143.

13. Lakowicz, J.R., Probe design and chemical sensing, in *Topics in fluorescence spectroscopy*, Lakowicz, J.R., Editor (2002), Kluwer academic publishers.

14. Haugland, R., Johnson, I., Detecting enzymes in living cells using fluorogenic substrates. Journal of Fluorescence, (1993). **3**(3): p. 119-127.

15. Tsien, R.Y., The green fluorescent protein. Annual Review of Biochemistry, (1998). **67**: p. 509-544.

16. Peter, A., Julio, d.P., Atkins' physical chemistry. 8th ed. (2006).

17. Kang, N.-Y., Ha, H.-H., Yun, S.-W., Yu, Y.H., Chang, Y.-T., Diversity-driven chemical probe development for biomolecules: Beyond hypothesis-driven approach. Chemical Society Reviews, (2011). **40**(7): p. 3613-3626.

18. Jiang, J.K., Wu, J., Liu, X.H., Fluorescence properties of lake water. Spectroscopy and Spectral Analysis, (2010). **30**(6): p. 1525-1529.

19. 中村結花子，藤田かおり，蔦瑞樹，柴田真理朗，吉村正俊，粉川美踏，杉山純一，鍋谷浩志，荒木徹也，蛍光指紋計測によるマンゴーの産地判別．日本食品科学工学会誌, (2012). **59**(8): p. 387-393.

20. Sadecka, J., Tothova, J., Fluorescence spectroscopy and chemometrics in the food classification - a review. Czech Journal of Food Sciences, (2007). **25**(4): p. 159-173.

21. Guimet, F., Ferre, J., Boque, R., Rius, F.X., Application of unfold principal component analysis and parallel factor analysis to the exploratory analysis of olive oils by means of excitation-emission matrix fluorescence spectroscopy. Analytica Chimica Acta, (2004). **515**(1): p. 75-85.

22. Sikorska, E., Glisuzynska-Swiglo, A., Insinska-Rak, M., Khmelinskii, I., De Keukeleire, D., Sikorski, M., Simultaneous analysis of riboflavin and aromatic amino acids in beer using fluorescence and multivariate calibration methods. Analytica

Chimica Acta, (2008). **613**(2): p. 207-217.

23. Yin, C.L., Li, H., Ding, C.H., Wang, H., Preliminary investigation on variety, brewery and vintage of wines using three-dimensional fluorescence spectroscopy. Food Science and Technology Research, (2009). **15**(1): p. 27-38.

24. 中村結花子，藤田かおり，蔦瑞樹，杉山純一，粉川美踏，吉村正俊，柴田真理朗，鍋谷浩志，荒木徹也，中村哲，蛍光指紋によるサトイモの産地判別法開発．日本食品工学会誌, (2013). **14**(3): p. 125-129.

25. Salzer, R., Siesler, H.W., eds. Infrared and raman spectroscopic imaging. (2009), Wiley-VCH Verlag GmbH & Co.

26. Arnone, D., Ciesla, C., Pepper, M., Terahertz imaging comes into view. Physics World, (2000): p. 35-40.

27. Crawford, P. How much does a ct scanner cost? Referbished Medical Imaging Industry Blog 2013 2014.1.22]; http://info.blockimaging.com/bid/67932/How-Much-Does-a-CT-Scanner-Cost.

28. Qin, J., Chao, K., Kim, M.S., Raman chemical imaging system for food safety and quality inspection. Transactions of the ASABE, (2010). **53**(6): p. 1873-1882.

29. Van As, H., Scheenen, T., Vergeldt, F.J., Mri of intact plants. Photosynthesis Research, (2009). **102**(2-3): p. 213-222.

30. Diaspro, A., ed. Optical fluorescence microscopy, from the spectral to the nano dimension. (2011), Springer.

31. Spring, K.R., Keller, H.E., Davidson, M.W. Objectives for specialized applications. Olympus Microscopy Resource Center; http://www.olympusmicro.com/primer/anatomy/specialobjectives.html.

32. Kas, J.A. Phase contrast microscopy. 2009; http://www.uni-leipzig.de/~pwm/web/?section=introduction&page=phasecontrast.

33. Marchant, J.L., Blanshard, J.M.V., Studies of the dynamics of the gelatinization of starch granules employing a small angle light scattering system. Starch - Stärke, (1978). **30**(8): p. 257-264.

34. Carlton, R., Pharmaceutical microscopy. (2011): Springer New York. 321.

35. Robinson, P.C., Davidson, M.W. Introduction to polarized light microscopy. Nikon Microscopy - the source for microscopy education -; http://www.microscopyu.com/articles/polarized/polarizedintro.html.

36. Gowen, A.A., O'Donnell, C.P., Cullen, P.J., Downey, G., Frias, J.M., Hyperspectral imaging - an emerging process analytical tool for food quality and safety control. Trends in Food Science & Technology, (2007). **18**(12): p. 590-598.

37. Sun, D.W., ed. Hyperspectral imaging for food quality analysis and control. (2010), Academic Press.

38. Reich, G., Near-infrared spectroscopy and imaging: Basic principles and pharmaceutical applications. Advanced Drug Delivery Reviews, (2005). **57**(8): p. 1109-1143.

39. Segtnan, V.H., Hoy, M., Lundby, F., Narurn, B., Wold, J.P., Fat distribution analysis in salmon fillets using non-contact near infrared interactance imaging: A sampling and calibration strategy. Journal of near Infrared Spectroscopy, (2009). **17**(5): p. 247-253.

40. Segtnan, V.H., Hoy, M., Sorheim, O., Kohler, A., Lundby, F., Wold, J.P., Ofstad, R., Noncontact salt and fat distributional analysis in salted and smoked salmon fillets using x-ray computed tomography and nir interactance imaging. Journal of Agricultural and Food Chemistry, (2009). **57**(5): p. 1705-1710.

41. Liu, D., Zeng, X.A., Sun, D.W., Nir spectroscopy and imaging techniques for evaluation of fish quality-a review. Applied Spectroscopy Reviews, (2013). **48**(8): p. 609-628.

42. ElMasry, G., Wold, J.P., High-speed assessment of fat and water content distribution in fish fillets using online imaging spectroscopy. Journal of Agricultural and Food Chemistry, (2008). **56**(17): p. 7672-7677.

43. ElMasry, G., Sun, D.W., Allen, P., Chemical-free assessment and mapping of major constituents in beef using hyperspectral imaging. Journal of Food Engineering, (2013). **117**(2): p. 235-246.

44. Tsuta, M., Sugiyama, J., Sagara, Y., Near-infrared imaging spectroscopy based on sugar absorption band for melons. Journal of Agricultural and Food Chemistry, (2002). **50**(1): p. 48-52.

45. Sugiyama, T., Sugiyama, J., Tsuta, M., Fujita, K., Shibata, M., Kokawa, M., Araki, T., Nabetani, H., Sagara, Y., Nir spectral imaging with discriminant analysis for detecting foreign materials among blueberries. Journal of Food Engineering, (2010). **101**(3): p. 244-252.

46. Kim, M.S., Lefcourt, A.M., Chao, K., Chen, Y.R., Kim, I., Chan, D.E., Multispectral detection of fecal contamination on apples based on hyperspectral imagery: Part i. Application of visible and near-infrared refrectance imaging. Transactions of the ASAE, (2002). **45**(6): p. 2027-2037.

47. Chen, Y.R., Park, B., Huffman, R.W., Nguyen, M., Classification of on-line poultry carcasses with backpropagation neural networks. Journal of Food Process Engineering, (1998). **21**(1): p. 33-48.

48. Cruz, J., Bautista, M., Amigo, J.M., Blanco, M., Nir-chemical imaging study of acetylsalicylic acid in commercial tablets. Talanta, (2009). **80**(2): p. 473-478.

49. Cruz, J., Blanco, M., Content uniformity studies in tablets by nir-ci. Journal of Pharmaceutical and Biomedical Analysis, (2011). **56**(2): p. 408-412.

50. Qin, J.W., Chao, K.L., Kim, M.S., Investigation of raman chemical imaging for detection of lycopene changes in tomatoes during postharvest ripening. Journal of Food Engineering, (2011). **107**(3-4): p. 277-288.

51. Monziols, M., Collewet, G., Bonneau, M., Mariette, F., Davenel, A., Kouba, M., Quantification of muscle, subcutaneous fat and intermuscular fat in pig carcasses and cuts by magnetic resonance imaging. Meat Science, (2006). **72**(1): p. 146-154.

52. Baulain, U., Magnetic resonance imaging for the in vivo determination of body composition in animal science. Computers and Electronics in Agriculture, (1997). **17**(2): p. 189-203.

53. Rosenberg, M., McCarthy, M., Kauten, R., Evaluation of eye formation and structural quality of swiss-type cheese by magnetic-resonance-imaging. Journal of Dairy Science, (1992). **75**(8): p. 2083-2091.

54. Banik, S., Rangayyan, R.M., Boag, G.S., Landmarking and segmentation of 3d ct images. (2009): Morgan & Claypool.

55. Lim, K.S., Barigou, M., X-ray micro-computed tomography of cellular food products. Food Research International, (2004). **37**(10): p. 1001-1012.

56. Babin, P., Della Valle, G., Chiron, H., Cloetens, P., Hoszowska, J., Pernot, P., Reguerre, A.L., Salvo, L., Dendievel, R., Fast x-ray tomography analysis of bubble growth and foam setting during breadmaking. Journal of Cereal Science, (2006). **43**(3): p. 393-397.

57. Frisullo, P., Marino, R., Laverse, J., Albenzio, M., Del Nobile, M.A., Assessment of intramuscular fat level and distribution in beef muscles using x-ray microcomputed tomography. Meat Science, (2010). **85**(2): p. 250-255.

58. Babin, P., Della Valle, G., Dendievel, R., Lassoued, N., Salvo, L., Mechanical properties of bread crumbs from tomography-based finite element simulations. Journal of Materials Science, (2005). **40**(22): p. 5867-5873.

59. Ross, K.A., Pyrak-Nolte, L.J., Campanella, O.H., The use of ultrasound and shear oscillatory tests to characterize the effect of mixing time on the rheological properties of dough. Food Research International, (2004). **37**(6): p. 567-577.

60. Seabourn, B.W., Xie, F., Chung, O.K., Rapid determination of dough optimum mixing time for early generation wheat breeding lines using ft-hatr infrared spectroscopy. Crop Science, (2008). **48**(4): p. 1575-1578.

61. Peighambardoust, S.H., van der Goot, A.J., van Vliet, T., Hamer, R.J., Boom, R.M., Microstructure formation and rheological behaviour of dough under simple shear flow. Journal of Cereal Science, (2006). **43**(2): p. 183-197.

62. Sroan, B.S., Bean, S.R., MacRitchie, F., Mechanism of gas cell stabilization in bread making. I. The primary gluten-starch matrix. Journal of Cereal Science, (2009). **49**(1): p. 32-40.

63. Bonny, J.M., Rouille, J., Della Valle, G., Devaux, M.F., Douliez, J.P., Renou, J.P., Dynamic magnetic resonance microscopy of flour dough fermentation. Magnetic Resonance Imaging, (2004). **22**(3): p. 395-401.

64. Salmenkallio-Marttila, M., Roininen, K., Autio, K., Lahteenmaki, L., Effects of gluten and transglutaminase on microstructure, sensory characteristics and instrumental texture of oat bread. Agricultural and Food Science, (2004). **13**(1-2): p. 138-150.

65. Auger, F., Morel, M.H., Lefebvre, J., Dewilde, M., Redl, A., A parametric and microstructural study of the formation of gluten network in mixed flour-water batter. Journal of Cereal Science, (2008). **48**(2): p. 349-358.

66. Kuktaite, R., Larsson, H., Marttila, S., Johansson, E., Effect of mixing time on gluten recovered by ultracentrifugation studied by microscopy and rheological measurements. Cereal Chemistry, (2005). **82**(4): p. 375-384.

67. Peressini, D., Peighambardoust, S.H., Hamer, R.J., Sensidoni, A., van der Goot, A.J., Effect of shear rate on microstructure and rheological properties of sheared wheat doughs. Journal of Cereal Science, (2008). **48**(2): p. 426-438.

68. Durrenberger, M.B., Handschin, S., Conde-Petit, B., Escher, F., Visualization of food structure by confocal laser scanning microscopy (clsm). Lebensmittel-Wissenschaft Und-Technologie-Food Science and Technology, (2001). **34**(1): p. 11-17.

69. Li, W., Dobraszczyk, B.J., Wilde, P.J., Surface properties and locations of gluten proteins and lipids revealed using confocal scanning laser microscopy in bread dough. Journal of Cereal Science, (2004). **39**(3): p. 403-411.

70. Renzetti, S., Arendt, E.K., Effect of protease treatment on the baking quality of brown rice bread: From textural and rheological properties to biochemistry and microstructure. Journal of Cereal Science, (2009). **50**(1): p. 22-28.

71. Primo-Martin, C., de Pijpekamp, A.V., van Vliet, T., de Jongh, H.H.J., Plijter, J.J., Hamer, R.J., The role of the gluten network in the crispness of bread crust. Journal of Cereal Science, (2006). **43**(3): p. 342-352.

72. Peighambardoust, S.H., Dadpour, M.R., Dokouhaki, M., Application of epifluorescence light microscopy (eflm) to study the microstructure of wheat dough: A comparison with confocal scanning laser microscopy (cslm) technique. Journal of Cereal Science, (2010). **51**(1): p. 21-27.

73. Autio, K., Salmenkallio-Marttila, M., Light microscopic investigations of cereal grains, doughs and breads. Lebensmittel-Wissenschaft Und-Technologie-Food Science and Technology, (2001). **34**(1): p. 18-22.

74. Indrani, D., Prabhasankar, P., Rajiv, J., Rao, G.V., Scanning electron microscopy, rheological characteristics, and bread-baking performance of wheat-flour dough as affected by enzymes. Journal of Food Science, (2003). **68**(9): p. 2804-2809.

75. Unbehend, L., Lindhauer, M.G., Meuser, F., Physical and microscopic studies of flour-water systems. European Food Research and Technology, (2004). **219**(5): p. 514-521.

76. Lindsay, M.P., Skerritt, J.H., The glutenin macropolymer of wheat flour doughs: Structure-function perspectives. Trends in Food Science & Technology, (1999). **10**(8): p. 247-253.

77. Paredeslopez, O., Bushuk, W., Development and undevelopment of wheat dough by mixing - microscopic structure and its relations to bread-making quality. Cereal Chemistry, (1983). **60**(1): p. 24-27.

78. Kalab, M., Allanwojtas, P., Miller, S.S., Microscopy and other imaging techniques in food structure-analysis. Trends in Food Science & Technology, (1995). **6**(6): p. 177-186.

79. Bache, I.C., Donald, A.M., The structure of the gluten network in dough: A study using environmental scanning electron microscopy. Journal of Cereal Science, (1998). **28**(2): p. 127-133.

80. Letang, C., Piau, M., Verdier, C., Characterization of wheat flour-water doughs. Part i: Rheometry and microstructure. Journal of Food Engineering, (1999). **41**(2): p. 121-132.

81. Roman-Gutierrez, A.D., Guilbert, S., Cuq, B., Description of microstructural changes in wheat flour and flour components during hydration by using environmental scanning electron microscopy. Lebensmittel-Wissenschaft Und-Technologie-Food Science and Technology, (2002). **35**(8): p. 730-740.

82. Cauvain, S.P., Young, L.S., Baked products: Science, technology and practice. (2006), Oxford: Blackwell Publishing Ltd. 228.

83. Amendola, J., Rees, N., Understanding baking: The art and science of baking. 3 ed. (2003), New Jersey: John Wiley & Sons, Inc. 279.

84. Pareyt, B., Wilderjans, E., Goesaert, H., Brijs, K., Delcour, J.A., The role of gluten in a sugar-snap cookie system: A model approach based on gluten-starch blends. Journal of Cereal Science, (2008). **48**(3): p. 863-869.

2. Development of a fluorescence fingerprint imaging system

The FF imaging system that has been used in this study has been developed along with the research. In this chapter, the current system which has been improved considerably from the former system made three years ago, is explained.

2. 1 Basic structure of the FF imaging system

Figure 2-1 shows the overall structure of the FF imaging system. The FF imaging system mainly consists of a light source, CCD camera, two sets of band-pass filters and an objective lens.

The light from the xenon light sources passes through a bandpass filter and light of a particular wavelength is shone onto the sample. The sample is excited and emits fluorescence. The fluorescence emitted from the sample contains light in many wavelengths but only light of a particular wavelength passes through the second band-pass filter and reaches the CCD camera. By changing the band-pass filter at the excitation and emission sides, fluorescence images in many combinations of excitation and emission wavelengths can be acquired.

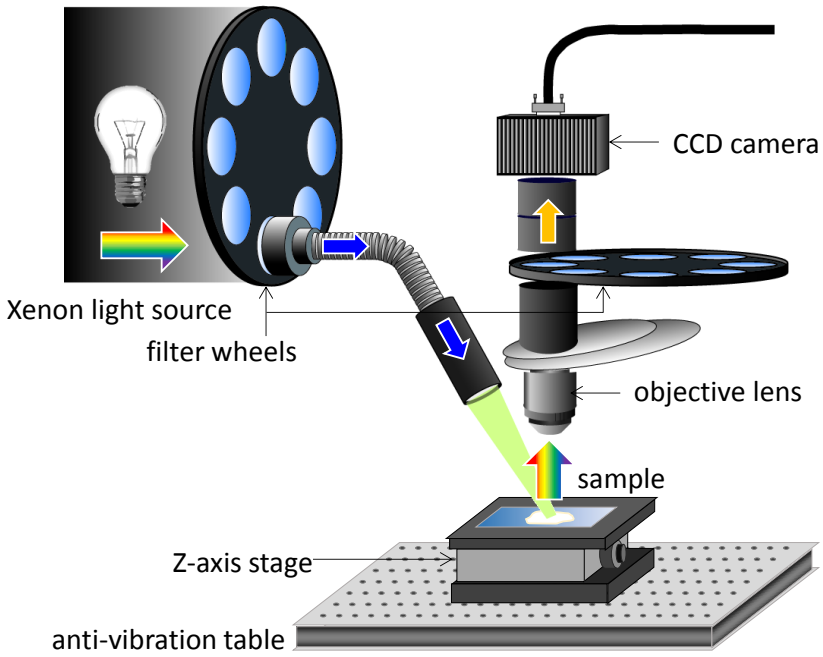

Figure 2-1 Structure of FF imaging system

As explained in chapter 3, the filter wheels can be replaced by other light filters such as a liquid crystal tunable filter (LCTF). Furthermore, the optical devices can be adjusted according to the size order of the sample, i.e., macroscopic or microscopic. The imaging system used in this study was made to measure the microscopic structure of food, which is in the order of 10 to 100 μm.

2. 2 System development

The original FF imaging system was built on top of a rotating slicer (Figure 2-2) [1]. The illuminator hung from a big frame which was set upon two I-shaped blocks. This configuration caused a problem when samples in the micro-scale were observed, at magnifications above ×10. The field of view wavered continuously because the frame picked up vibrations from the surrounding environment. The following steps were taken to create an imaging system that enabled FF imaging at high magnification.

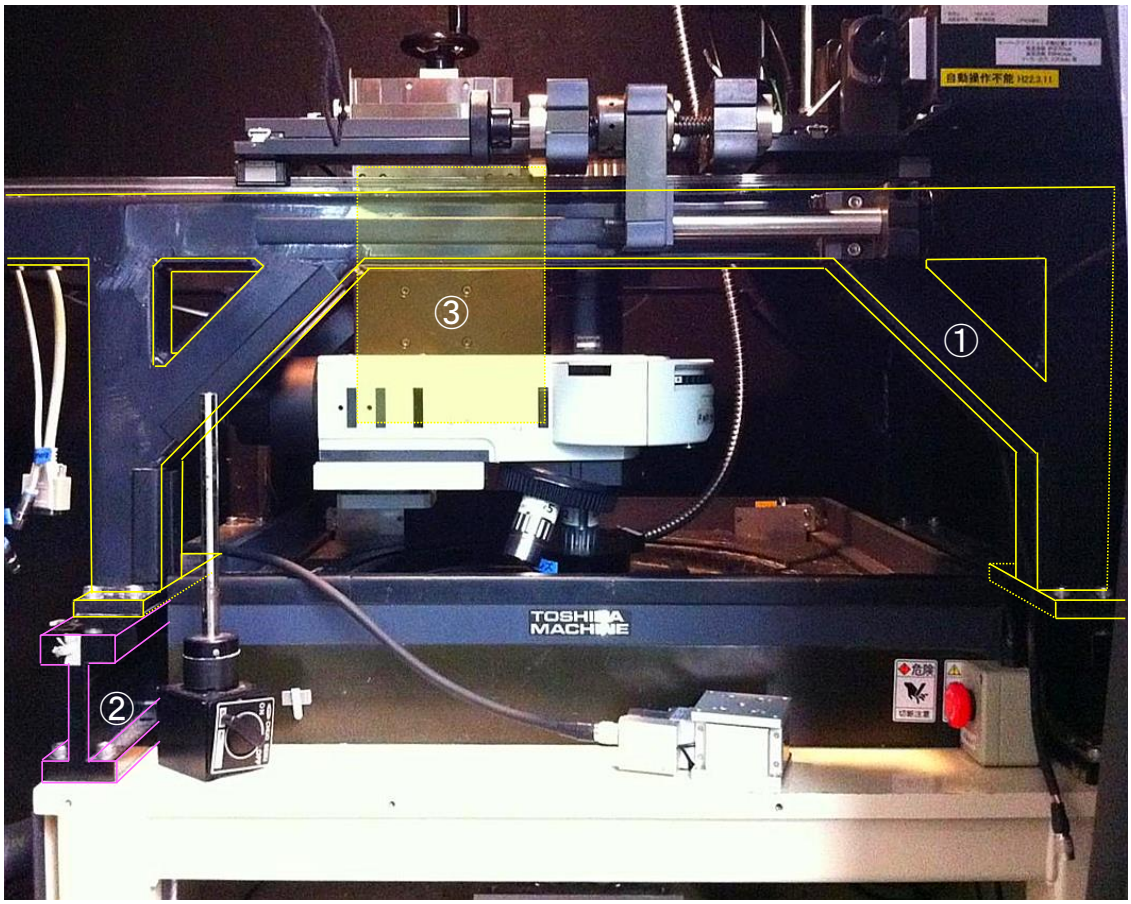

Figure 2-2 The original FF imaging system

First, the base was made by covering the original base of the slicer with a wooden frame and mounting an anti-vibration table (HMX-0605, Nippon Boushin Industry co., ltd., Shizuoka, Japan) on top of the wooden frame. The I-shaped blocks and steel frame were removed (Figure 2-3).

Figure 2-3 Base of the imaging system

The anti-vibration table removes two types of vibration [2]. The first type of vibration reaches the top of the anti-vibration table directly, such as vibration of motors set on the table or vibration of air caused by noise. This type of vibration causes the table-top to resonate, causing stronger vibration. In order to avoid resonation, the natural frequency of the table-top needs to be different from other possible vibrations. Therefore, the table-top is made from a rigid substance which has a high natural frequency.

The second type reaches the table-top indirectly, such as vibration of the floor. This type of vibration has a similar frequency as the natural frequency of the table-top and needs to be absorbed before reaching the table-top. This is achieved by an absorber such as an air or oil dumper. The anti-vibration table used in this study (HMX-0605) (Figure 2-4) has an air suspension that absorbs vibration from below.

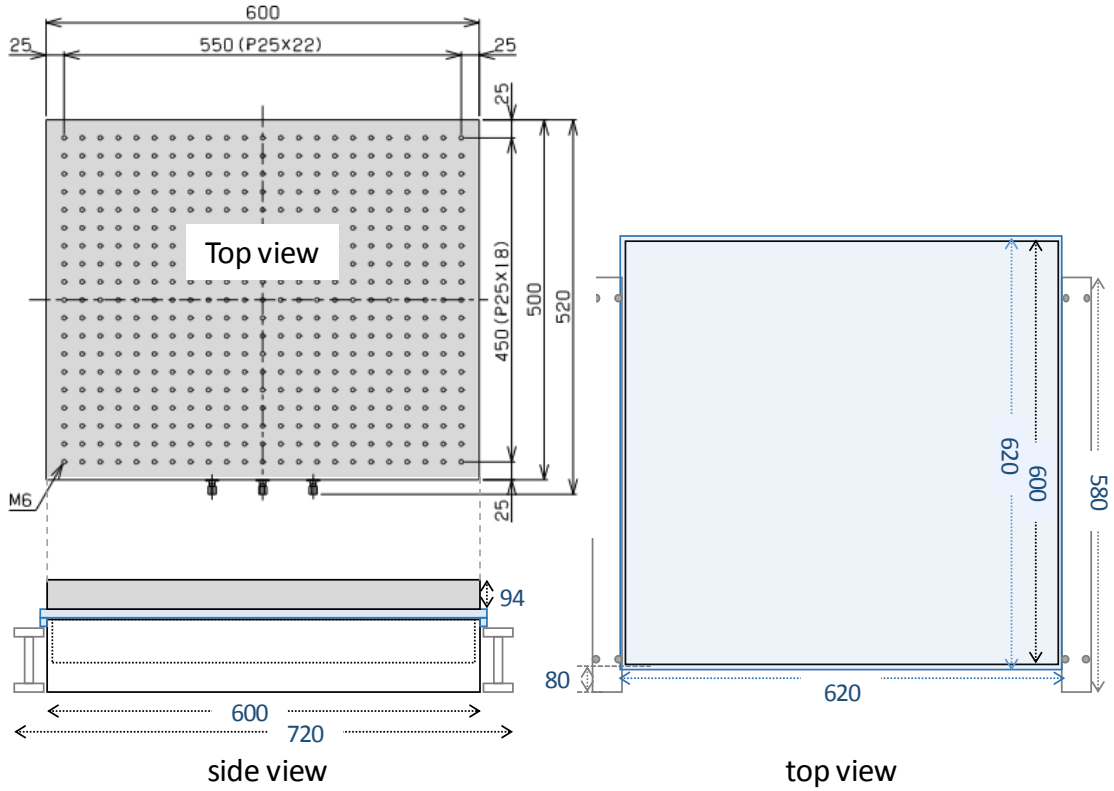

Figure 2-4 Anti-vibration table, top and side view

The microscopic system that was originally hung by a large iron plate was fixed to the table-top with an illuminator holder and a shaft and shaft holder made from stainless steel. The shaft and shaft holder was designed to hold the whole weight of the imaging system (Figure 2-5).

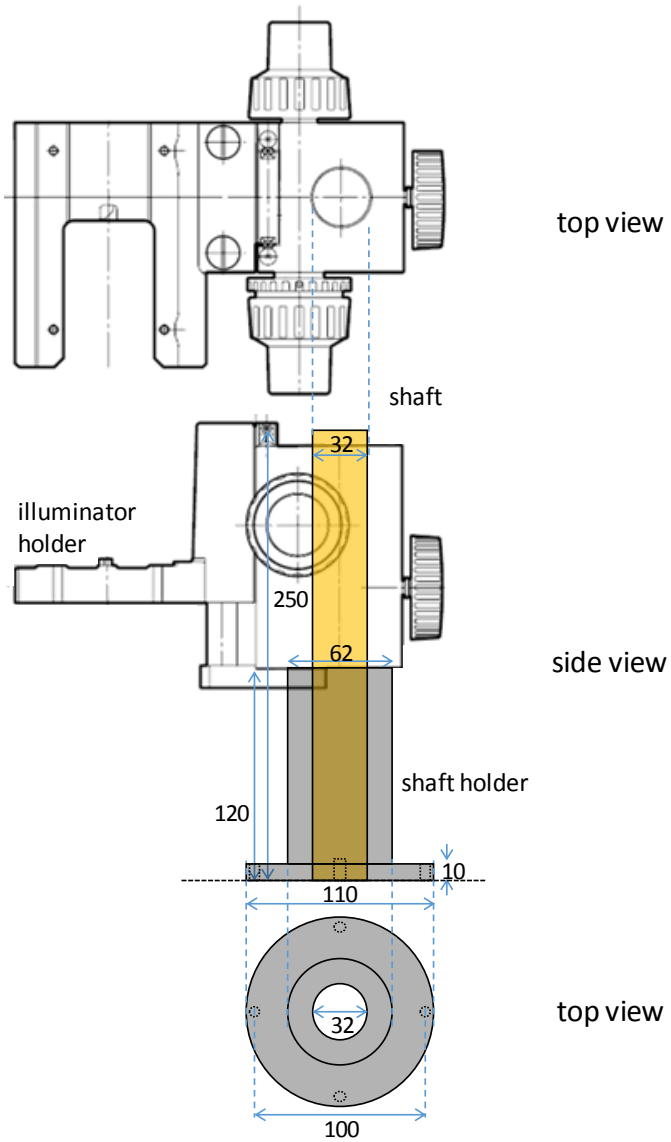

Figure 2-5 Illuminator, shaft and shaft holder

Figure 2-6 shows the composition of the microscopic imaging system. The main microscope system is based on a fluorescence microscope. The illuminator (BX-RFA, Olympus Optical co., ltd, Tokyo, Japan) is normally used in an epi-illumination system, but epi-illumination was not used in this FF imaging system because it was non-compliant with UV light.

The samples were mounted on a XYZ stage composed of a Z-axis motorized stage (MMU-60V, Chuo Precision Industrial co., ltd, Tokyo, Japan) and a manual X-Y axis stage (Sigma Koki co., ltd, Tokyo, Japan). The Z-axis stage was essential to adjust the sample height to match the focal plane which changed slightly for each emission

wavelength.

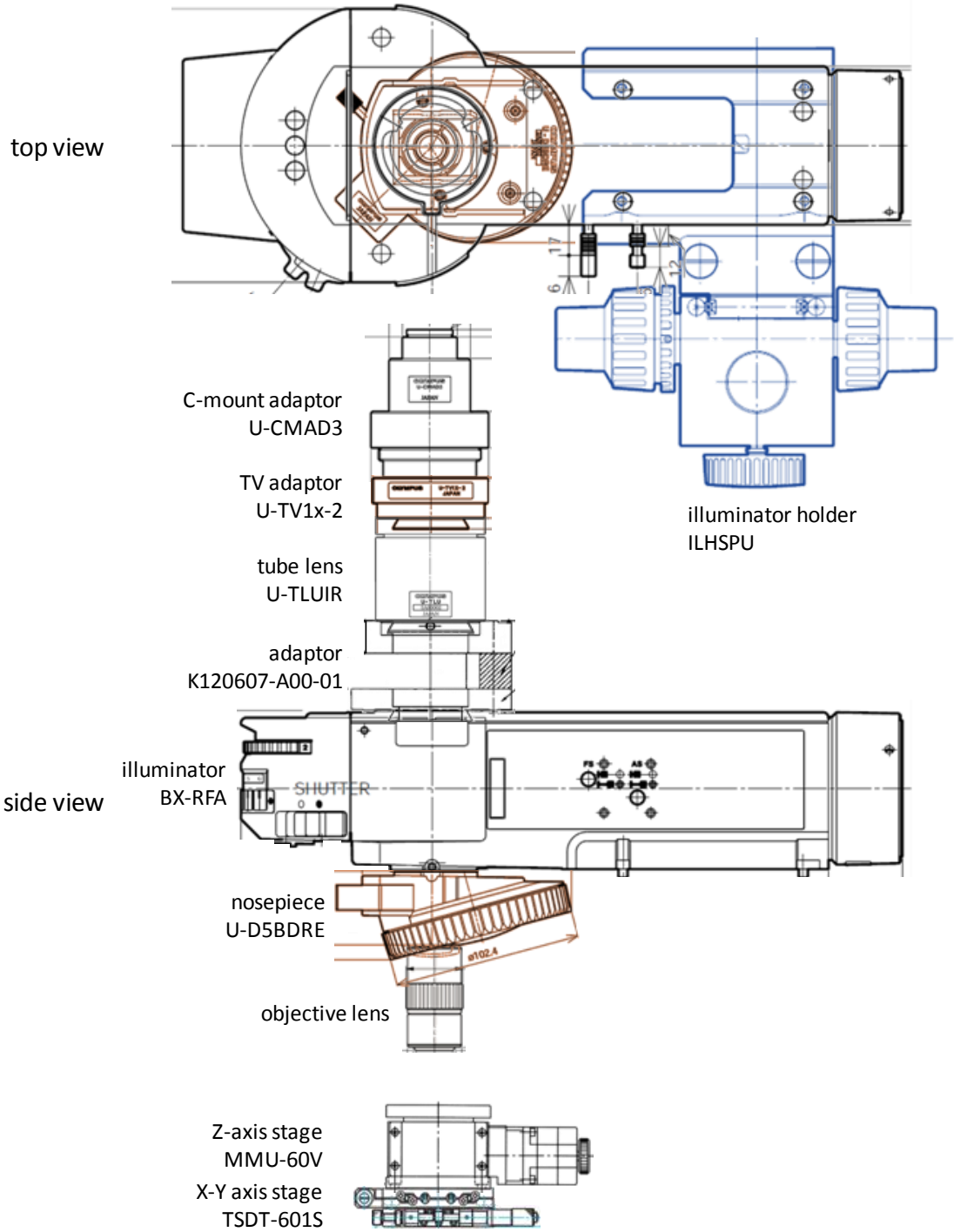

Figure 2-6 Microscopic imaging system

The tube lens (U-TLUIR, Olympus Optical), TV adaptor (U-TV1x-2, Olympus Optical) and C-mount adaptor (U-CMAD3, Olympus Optical) were set above the illuminator with a custom-built adaptor (K120607-A00-01, Asahi Spectra, Tokyo, Japan) set in between. This adaptor was made to fit the filter wheel holding the band-pass filters that determine the emission wavelength. The filter wheel was fit from the left side of the illuminator (opposite side of the illuminator holder) and set so that one filter fitted into the optical path of the microscope (Figure 2-7).

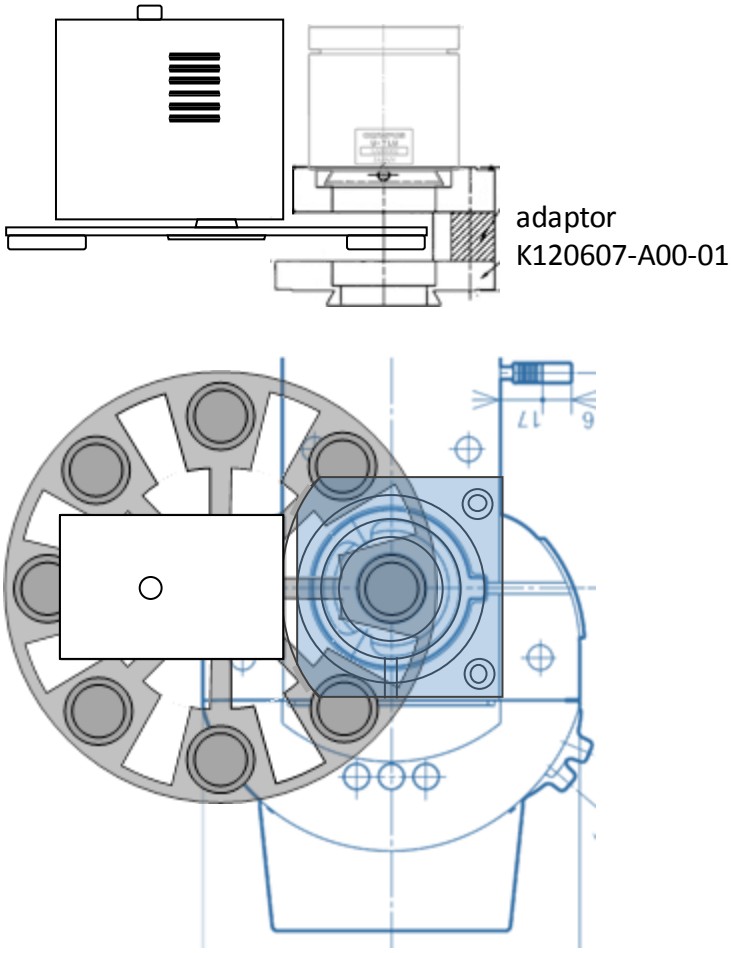

Figure 2-7 Filter wheel

This system is an infinity-corrected optical system, where there is a parallel optical path between the objective and tube lenses. Fitting the emission band-pass filters into the parallel optical path minimizes the effect on focus and aberration corrections.

Two xenon lamps (MAX 302, 303, Asahi Spectra) were used for the excitation light. MAX 302 and 303 were equipped with a UV and VIS mirror module, which restricted the light going out of the xenon lamp to a range of 250-385 nm and 300-600 nm,

respectively. By coupling band-pass filters with these modules, the cutoff range of band-pass filters would only need to cover the wavelength range of the modules. Band-pass filters are designed to cut off light except for a specific wavelength band, and an ideal band-pass filter would have 100% transmittance at the designed wavelength and 0% transmittance at other wavelengths. However, in reality, it is only possible to cut of light within a certain range of wavelengths, and the larger the range becomes, the higher the transmittance of light at unwanted wavelengths or the lower the transmittance at the designed wavelength. Therefore, by limiting the range of cutoff wavelengths, it is possible to ensure a high ratio of transmittance between wanted and unwanted wavelengths.

The lamps have a built-in filter wheel which holds 8 filters each. Light from the xenon light source passes through the filter held in the filter wheel, is guided through a light fiber and is shone onto the sample with a rod lens. The optical system of the rod lens mixes the light coming out from individual fibers and creates a uniform band of light.

Figure 2-8 shows the overall view of the FF imaging system, except for the xenon lamp house which is set outside the dark room. An important point is that the spatial relationship between the objective lens and beam of excitation light is constant even if the height of the sample changes. The distance between the sample and objective lens is adjusted with the Z-axis stage below the sample, so if the sample surface is in focus, the excitation light intensity should be constant.

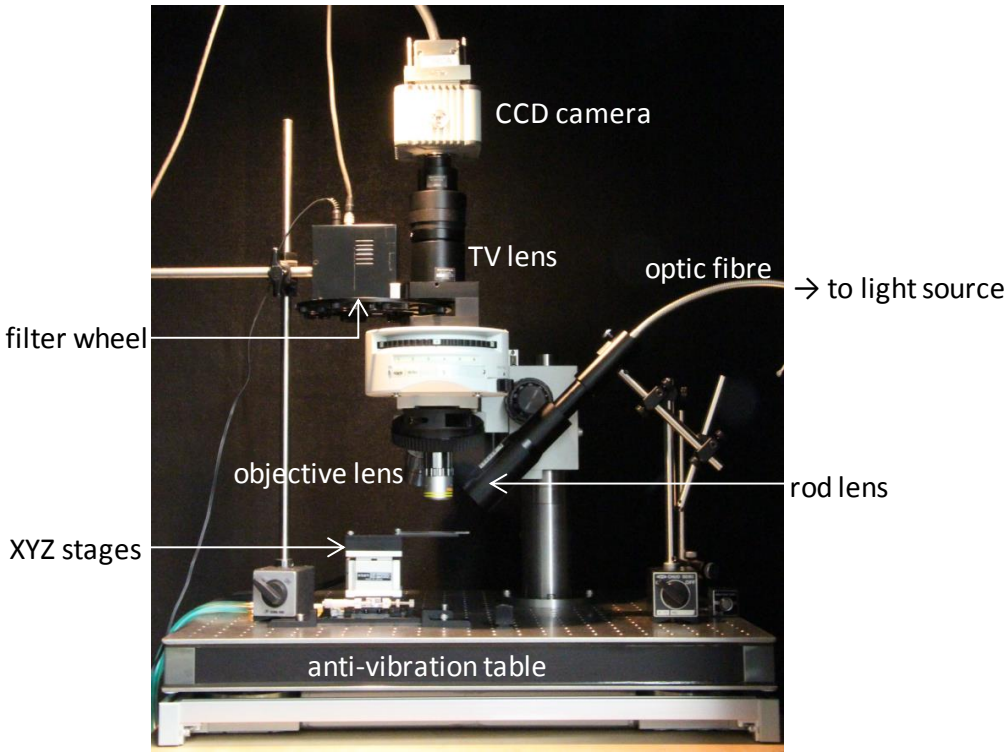

Figure 2-8 Overall view of the new imaging system

2. 3 Software

2. 3. 1 Control of FF imaging system by LabVIEW

Acquisition of fluorescence images in multiple wavelength conditions is a cumbersome task if done manually. Long measurement times due to manual operation would have detrimental effects on the sample, since the sample would be exposed to UV light or moderate temperatures during that time. Therefore, the system was made to be automatically controlled from a personal computer (PC) by using LabVIEW (Laboratory Virtual Instrumentation Engineering Workbench, National Instruments, USA).

A set of FF imaging data consists of fluorescence images in all the wavelength conditions that make up the FF. For each fluorescence image, the parameters shown in Table 2-1 needed to be set before acquisition.

Table 2-1 Image acquisition parameters

Parameters	Corresponding machinery
Excitation wavelength	xenon lamphouse
Emission wavelength	filter wheel controller
Exposure time	CCD camera
Binning	CCD camera
Gain	CCD camera
Offset	CCD camera
Light intensity	xenon lamphouse
Z-position	Z-axis controller

Figure 2-9 shows the flow chart for FF data acquisition. All the parameters are read from a csv file and outputted to the corresponding instruments through serial ports. The acquired fluorescence image is saved with a file name that contains the main parameters.

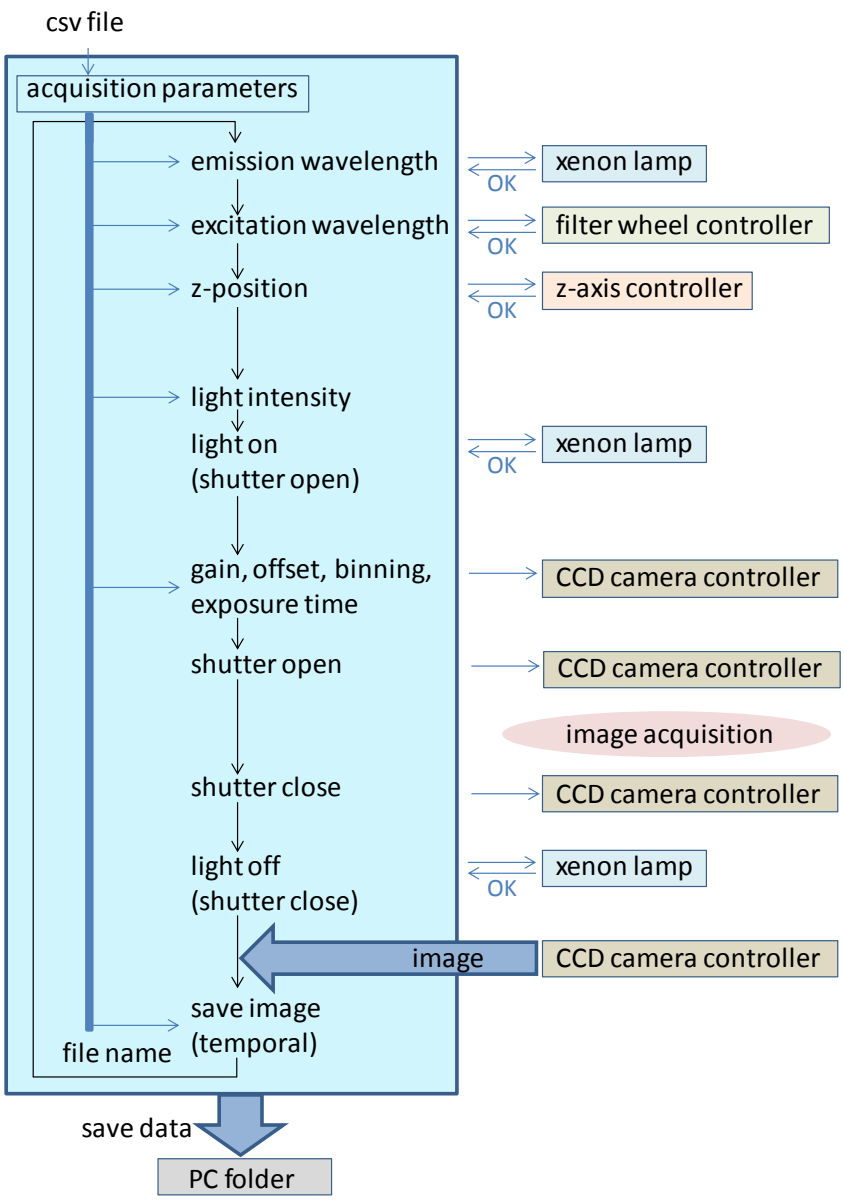

Figure 2-9 Flow chart of image acquisition

2. 3. 2 Analysis of data by MATLAB

The set of fluorescence images were analyzed using MATLAB (MATrix LABoratory, MathWorks, USA), a numerical analysis software. Since details on the method of analysis are explained in each chapter, this section will describe the overall flow of analysis.

In the first step, the fluorescence images saved in tif (tagged image file) format are read into the MATLAB space as two-dimensional matrices (number of pixels in height × number of pixels in width).

Next, the fluorescence images are stacked three dimensionally, so that the whole

dataset is a three-dimensional matrix of (height) × (width) × (number of images). The number of images equals all the combinations of excitation and emission wavelengths. Therefore, the two-dimensionality of the FF (excitation × emission wavelength) is lost at this point. The images are carefully aligned to each other, so that every fluorescence image represents the exact same area of the sample.

This three-dimensional data is degraded into two-dimensional data by unfolding the (height) × (width) data of an image to a single-dimensional vector of (number of pixels) × 1 (Figure 2-10). The whole data becomes a two-dimensional matrix of (number of pixels)× (wavelength conditions). In this matrix, each pixel can be treated as samples, and the wavelength conditions as measurement variables. From this point, analysis methods such as cosine similarity, principal component analysis (PCA), partial least squares (PLS) are applied to the data.

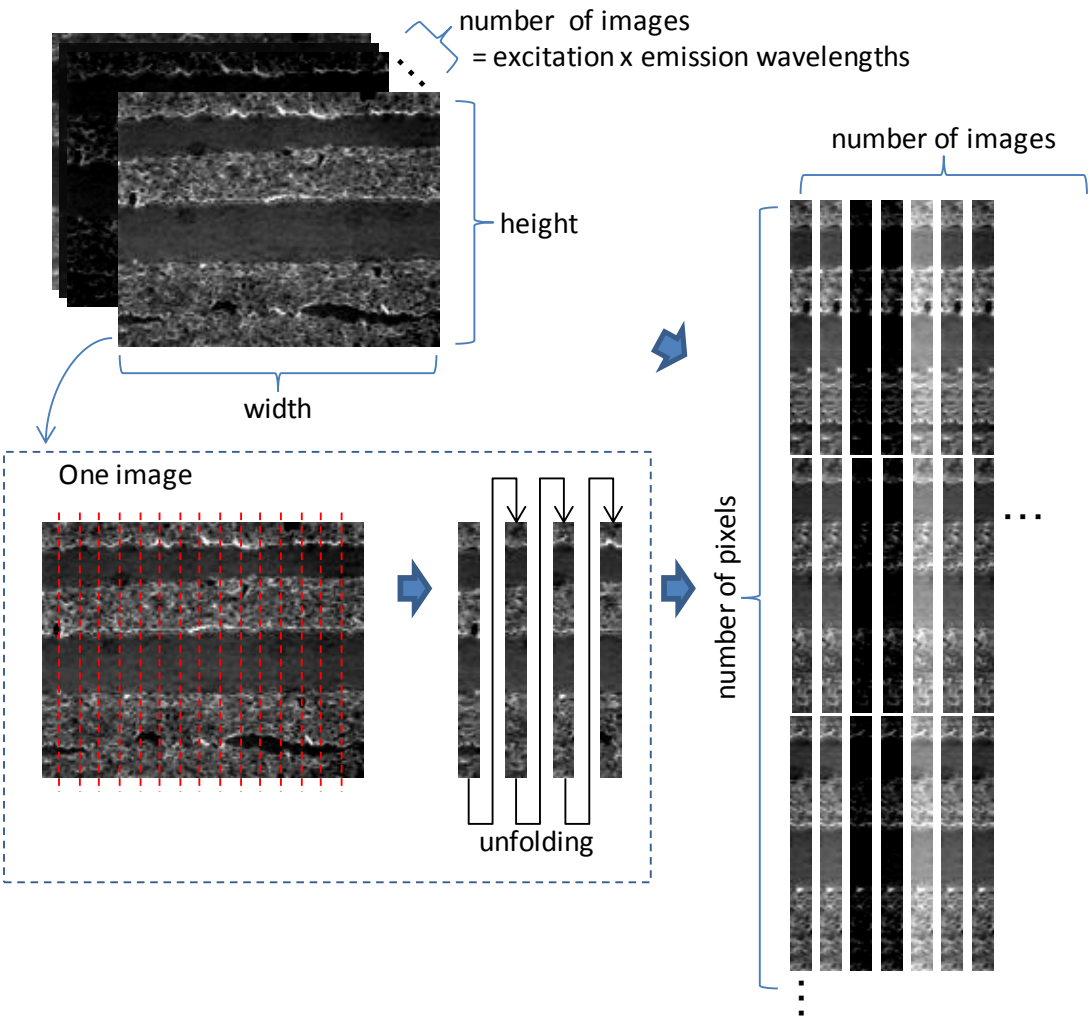

Figure 2-10 Degradation of imaging data

2. 4 Properties and calibration of hardware

2. 4. 1 Theory

The FF imaging system is constructed from several optical hardware, which has specific properties that are dependent on the wavelength of light. The ideal light source would give out light of uniform intensity throughout the whole spectrum and the ideal camera would have the same photographic sensitivity for any wavelength of light. However, in reality this is impossible, and the light intensity or sensitivity is dependent on the wavelength of light. Similarly, the ideal band-pass filter would have 100% transmission at a specific wavelength and 0% transmission at other wavelengths, but in reality, there is transmission of light at wavelengths other than the intended wavelength.

The light intensity of the light source is dependent on the excitation wavelength λ_{ex} and is denoted $I_{\mathrm{s}}(\lambda_{\mathrm{ex}})$. The transmittance function of the excitation band-pass filter whose designed wavelength is $\lambda\mathrm{EX}$ is denoted $T_{\mathrm{B}\lambda\mathrm{EX}}(\lambda_{\mathrm{ex}})$. Similarly, the transmittance function of the emission band-pass filter whose designed wavelength is $\lambda\mathrm{EM}$ is denoted $T_{\mathrm{B}\lambda\mathrm{EM}}(\lambda_{\mathrm{em}})$. The photographic sensitivity of the camera is denoted $S_{\mathrm{C}}(\lambda_{\mathrm{em}})$. Finally, the fluorescence efficiency of the sample, is denoted $FF(\lambda_{\mathrm{ex}}, \lambda_{\mathrm{em}})$. Naturally, the aim of measurement would be to acquire $FF(\lambda_{\mathrm{ex}}, \lambda_{\mathrm{em}})$, in other words, the FF.

The excitation light that is shone onto the sample through a band-pass filter whose designed wavelength is $\lambda\mathrm{EX}$, $\mathrm{I}_{\lambda\mathrm{EX}}(\lambda_{\mathrm{ex}})$, is the product between the light intensity function of the light source and the transmittance function of the excitation band-pass filter:

$$I_{\lambda\mathrm{EX}}(\lambda_{\mathrm{ex}}) = I_{\mathrm{s}}(\lambda_{\mathrm{ex}}) \times T_{\mathrm{B}\lambda\mathrm{EX}}(\lambda_{\mathrm{ex}}) \qquad \dots (1)$$

The sample absorbs this light and gives out fluorescence according to its fluorescence characteristics. The fluorescence that the sample gives out, $F(\lambda_{\mathrm{em}})$ is

$$F(\lambda_{\mathrm{em}}) = \sum_{\lambda_{\mathrm{ex}}} FF(\lambda_{\mathrm{ex}}, \lambda_{\mathrm{em}}) \times I_{\lambda\mathrm{EX}}(\lambda_{\mathrm{ex}}) \qquad \dots (2)$$

This passes through the emission filter whose designed wavelength is $\lambda\mathrm{EM}$ and is received by the camera. The intensity of the signal that the CCD camera receives, $I_{\mathrm{Cin}}(\lambda_{\mathrm{em}})$ is:

$$I_{\mathrm{Cin}}(\lambda_{\mathrm{em}}) = S_{\mathrm{c}}(\lambda_{\mathrm{em}}) \times T_{\mathrm{B}\lambda\mathrm{EM}}(\lambda_{\mathrm{em}}) \times F(\lambda_{\mathrm{em}}) \qquad \dots (3)$$

The CCD camera has no system to differentiate between different wavelengths, and the actual "intensity" value of each pixel, I_{sum}, is the sum of all the signals that the camera receives:

$$I_{\mathrm{sum}} = \sum_{\lambda_{\mathrm{em}}} I_{\mathrm{Cin}}(\lambda_{\mathrm{em}}) \qquad \dots (4)$$

From the equations above,

$$I_{\mathrm{sum}} = \sum_{\lambda_{\mathrm{em}}} S_{\mathrm{c}}(\lambda_{\mathrm{em}}) \times T_{\mathrm{B}\lambda\mathrm{EM}}(\lambda_{\mathrm{em}}) \times \left[\sum_{\lambda_{\mathrm{ex}}} FF(\lambda_{\mathrm{ex}}, \lambda_{\mathrm{em}}) \times I_{\mathrm{s}}(\lambda_{\mathrm{ex}}) \times T_{\mathrm{B}\lambda\mathrm{EX}}(\lambda_{\mathrm{ex}}) \right] \qquad \dots (5)$$

An ideal band-pass filter would have the characteristics below:

$$T_{\mathrm{B}\lambda\mathrm{EX}}(\lambda_{\mathrm{ex}}) = \begin{cases} T_{\mathrm{B}\lambda\mathrm{EX}}\ (\lambda_{\mathrm{ex}} = \lambda\mathrm{EX}) \\ 0\ (\lambda_{\mathrm{ex}} \neq \lambda\mathrm{EX}) \end{cases} \qquad \dots (6)$$

$$T_{\mathrm{B}\lambda\mathrm{EM}}(\lambda_{\mathrm{em}}) = \begin{cases} B_{\mathrm{T}\lambda\mathrm{EM}}\ (\lambda_{\mathrm{em}} = \lambda\mathrm{EM}) \\ 0\ (\lambda_{\mathrm{em}} \neq \lambda\mathrm{EM}) \end{cases} \qquad \dots (7)$$

Therefore, the equation (5) would be:

$$I_{\mathrm{sum}} = S_{\mathrm{c}}(\lambda\mathrm{EM}) \times T_{\mathrm{B}\lambda\mathrm{EM}} \times FF(\lambda\mathrm{EX}, \lambda\mathrm{EM}) \times I_{\mathrm{s}}(\lambda\mathrm{EX}) \times T_{\mathrm{B}\lambda\mathrm{EX}} \qquad \dots (8)$$

To compare the actual imaging system with an ideal system, we simulate the measurement of a white reflection standard. A white reflection standard is an optically white plate which has the characteristics below:

$$FF_{\mathrm{white}} = \begin{cases} 1\ (\lambda_{\mathrm{em}} = \lambda_{\mathrm{ex}}) \\ 0\ (\lambda_{\mathrm{em}} \neq \lambda_{\mathrm{ex}}) \end{cases} \qquad \dots (9)$$

When a white reflection standard is measured with an ideal imaging system,

$$\mathrm{I_{sum}} = \begin{cases} S_{\mathrm{c}}(\lambda\mathrm{EM}) \times T_{\mathrm{B}\lambda\mathrm{EM}} \times I_{\mathrm{s}}(\lambda\mathrm{EX}) \times T_{\mathrm{B}\lambda\mathrm{EX}} \ (\lambda\mathrm{EM} = \lambda\mathrm{EX}) \\ 0 \ (\lambda\mathrm{EM} \neq \lambda\mathrm{EX}) \end{cases} \quad \ldots (10)$$

This means that in an ideal imaging system, a white reflection standard would show no signal if the excitation and emission filters are different. In actual band-pass filters, equation (10) does not strictly apply, but it is important to check that there is no apparent signal when measuring a white reflection standard with excitation and emission filters of different wavelengths.

If the band-pass filter can be treated as an ideal band-pass filter, the FF of the sample, $FF(\lambda_{\mathrm{ex}}, \lambda_{\mathrm{em}})$ is calculated as:

$$FF(\lambda_{\mathrm{ex}}, \lambda_{\mathrm{em}}) = \frac{I_{\lambda\mathrm{ex},\lambda\mathrm{em}}}{S_{\mathrm{c}}(\lambda_{\mathrm{em}}) \times T_{\mathrm{B}\lambda\mathrm{em}} \times I_{\mathrm{s}}(\lambda_{\mathrm{ex}}) \times T_{\mathrm{B}\lambda\mathrm{ex}}} \quad \ldots (11)$$

$T_{\mathrm{B}\lambda\mathrm{ex}}$ and $T_{\mathrm{B}\lambda\mathrm{em}}$ are the transmittances of the excitation and emission band-pass filters at their designed wavelengths, $I_{\lambda\mathrm{ex},\lambda\mathrm{em}}$ is the light intensity measured by the CCD camera when using these band-pass filters. The first and last two terms can be coupled as the excitation and emission machine functions, denoted as $F_{\mathrm{EM}}(\lambda_{\mathrm{em}})$ and $F_{\mathrm{EX}}(\lambda_{\mathrm{ex}})$, respectively. This gives,

$$FF(\lambda_{\mathrm{ex}}, \lambda_{\mathrm{em}}) = \frac{I_{\lambda\mathrm{ex},\lambda\mathrm{em}}}{F_{\mathrm{EM}}(\lambda_{\mathrm{em}}) \times F_{\mathrm{EX}}(\lambda_{\mathrm{ex}})} \quad \ldots (12)$$

Therefore, in order to obtain the FF, functions F_{EM} and F_{EX} need to be known. The light intensity of excitation light, $F_{\mathrm{EX}}(\lambda_{\mathrm{ex}})$, can be measured with a power meter. Once $F_{\mathrm{EX}}(\lambda_{\mathrm{ex}})$ is obtained, $F_{\mathrm{EM}}(\lambda_{\mathrm{em}})$ can be obtained by measuring a white reflection standard where equation (9) applies. Hence, when $\lambda_{\mathrm{ex}} = \lambda_{\mathrm{em}}$

$$\begin{aligned} FF_{\mathrm{white}}(\lambda_{\mathrm{ex}}, \lambda_{\mathrm{em}}) &= \frac{I_{\lambda\mathrm{ex},\lambda\mathrm{em}}}{F_{\mathrm{EM}}(\lambda_{\mathrm{em}}) \times F_{\mathrm{EX}}(\lambda_{\mathrm{ex}})} = 1 \\ F_{\mathrm{EM}}(\lambda) &= \frac{I_{\lambda}}{F_{\mathrm{EX}}(\lambda)} \end{aligned} \quad \ldots (13)$$

2. 4. 2 Band-pass filter

To check that the band-pass filters satisfy equation (10), the FF of a white reflection standard was measured. Light from xenon light sources (MAX 302, MAX303, Asahi Spectra) transmitted the band-pass filters (HQBP filter and M.C. filter, Asahi Spectra) and was shone onto the white reflection standard. The emitted light passed through a liquid crystal tunable filter (LCTF) (VariSpec, Cambridge Research & Instrumentation, Inc., Hopkinton, USA), and a CCD camera (ORCA-ER-1394, Hamamatsu Photonics, Shizuoka, Japan) was used to measure the intensity of transmitted light.

Figure 2-11A shows the measured FF of the white reflection standard. According to equation (10), the white reflection standard should show no emission since all the wavelength conditions satisfy $\lambda_{\mathrm{ex}} \neq \lambda_{\mathrm{em}}$. However, relatively strong light is observed in the longer wavelengths with excitation filters of 260-370 nm. This shows that these filters transmit light in the longer wavelengths.

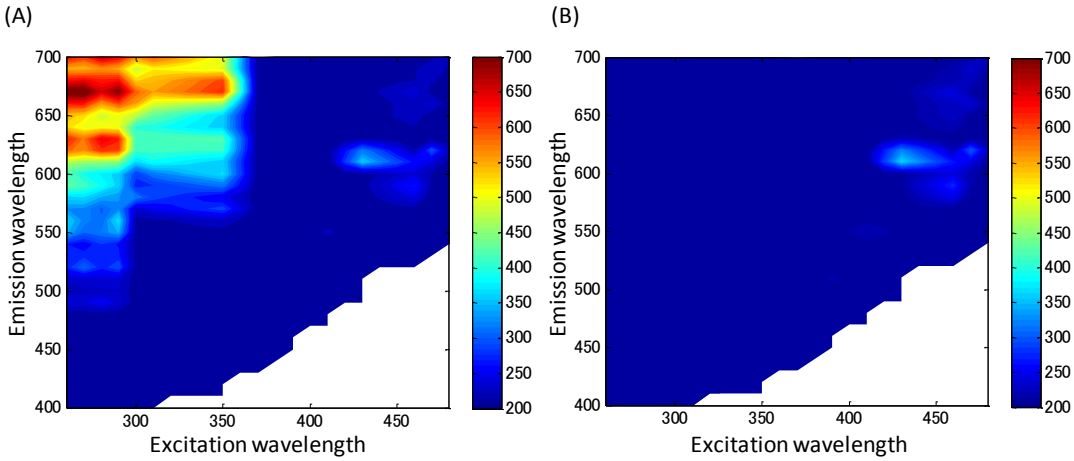

Figure 2-11 Measured FF of white reflection standard without (A) and with the short-pass filter. Without the short pass filter, excitation light in the longer wavelengths pass through.

In order to cut the transmitted light, a short-pass filter was set between the band-pass filters and the xenon light source. Figure 2-11B shows the FF of the white reflection standard measured with the low-pass filter. The light that had transmitted the light at longer wavelengths has been cut.

Furthermore, when measuring the white reflection standard with emission wavelengths lower than 400 nm, relatively strong light was observed with the combination of 290 nm and 390 nm for excitation and emission band-pass filters, respectively. This transmitted light could also be measured with a spectrometer. Therefore, another short-pass filter which cut light over 350 nm was set between the xenon light

source and short-pass filter described above.

2. 4. 3 Excitation machine functions

The xenon lamp shows different intensities at different wavelengths, and each band-pass filter shows different transmittance. Therefore, the light intensity of each excitation wavelength is different. This needed correcting if the FFs acquired by the imaging system were to be compared to fluorescence patterns of specific fluorophors in literature.

Uniformization of light intensity at each excitation wavelength was achieved by using a continuously variable ND filter fixed in front of the light source. The ND filter enabled adjustment of the output light intensity in respect to the original light intensity of the light source and was controlled through a parameter named “LI” (light intensity) which could be set between 5% and 100% at increments of 1%.

As noted above, the light intensity of the excitation light is affected by several factors, such as the light intensity of the light source, the transmission rate of the band-pass filter, and any other filters that may be used such as low-pass and high-pass filters. However, each factor does not need to be separated, as long as the intensity of the light irradiated on the sample is uniform. Therefore, the light intensity of each excitation wavelength was measured with a power meter (NOVA2, Ophir Photonics Ltd., Jerusalem, Israel) using the same setup as that used for imaging.

The relationship between actual light intensity and the value of LI was measured beforehand and was known to be linear between 20 and 90% (Figure 2-12). Therefore, after measuring the light intensity at 100% LI, the LI at each wavelength was calculated so that the actual light intensity would be equal to that of the weakest wavelength. Finally, the light intensity at each excitation wavelength with the LI set to the calculated value was measured, and the LI was adjusted so that the readings of the power meter were uniform. Table 2-2 shows the final LI values for each wavelength.

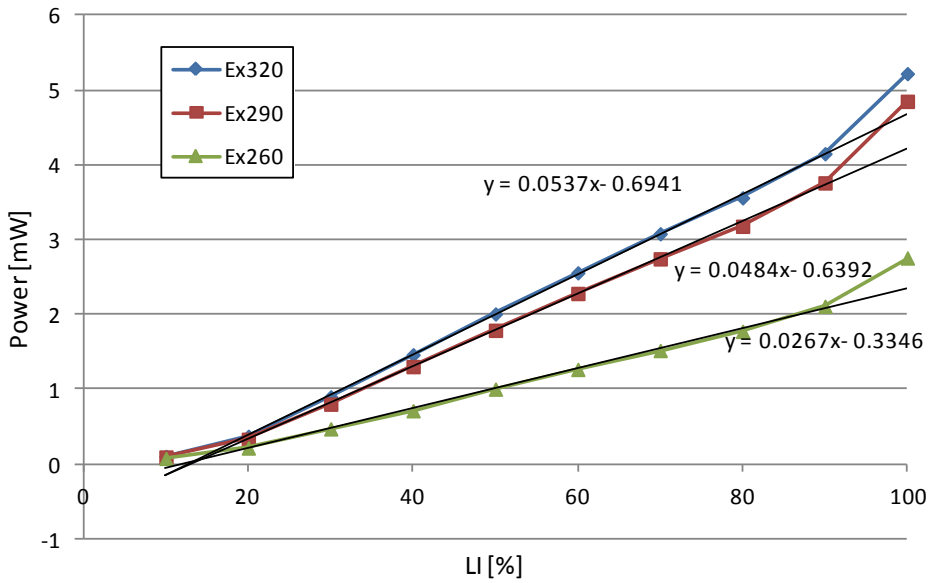

Figure 2-12 Relation between LI and measured power for wavelengths 260, 290, and 320 nm. The range between 20% and 90% shows linear correlation. The LI is adjusted by the angle of the ND filter.

Table 2-2 LI of each wavelength

Wavelength [nm]	LI [%]
270	100
280	93
290	97
300	70
310	62
320	57
330	64

2. 4. 4 Emission machine functions

Similar to the excitation intensity, the emission filters and camera have different transmission ratios and sensitivity towards light in different wavelengths. This was corrected by adjusting the exposure time for each emission wavelength. As in the correction for excitation light, there is no need to separate the effects of the camera and emission filters. Together, they will be referred to as the emission sensitivity.

Since it was possible to obtain uniform intensities of light at every wavelength as explained above, this uniform light and a reflection standard was used to correct for the emission light sensitivity. Assuming that the reflection standard shows uniform reflectance at all wavelengths, images of the refection standard was acquired using the

same wavelengths for excitation and emission. Since the excitation light intensities were uniform, the difference in the intensity of the acquired image showed the difference in emission sensitivity. Therefore, the exposure time of the least sensitive emission wavelength was set to the maximum of 10 s, and those of the other wavelengths were adjusted depending on the intensity of the reflection standard image.

Table 2-3 Exposure times (in milliseconds) for each emission wavelength

Wavelength [nm]	Exposure time [ms]
350	10000
360	4385
370	2666
380	2389
390	1645
400	1578
410	1304
420	955

2. 4. 5 Autofocus

In the FF imaging system, the emission wavelength is controlled by band-pass filters that are fitted between the objective lens and the CCD camera. Each band-pass filter has a different refractive index, which results in different focus lengths for each emission wavelength. Therefore, the position of the z-axis stage for each emission wavelength was determined prior to FF measurement.

The point of focus was determined by an autofocus program made using LabVIEW. There are two methods of autofocusing: active focusing, which utilizes some kind of energy, such as laser beam, to measure the distance to the object, and passive focusing which analyses images captured at different planes to obtain the optimum point [3]. This study used passive focusing.

Microscope autofocusing systems determine the in-focus position by searching for the maximum of an autofocus function over a range of z-axis positions. An autofocus function provides a quantitative measure of focal sharpness for a given image. By applying the autofocus function to images acquired at different z-axis positions, and comparing them, the in-focus position can be obtained as shown in Figure 2-13.

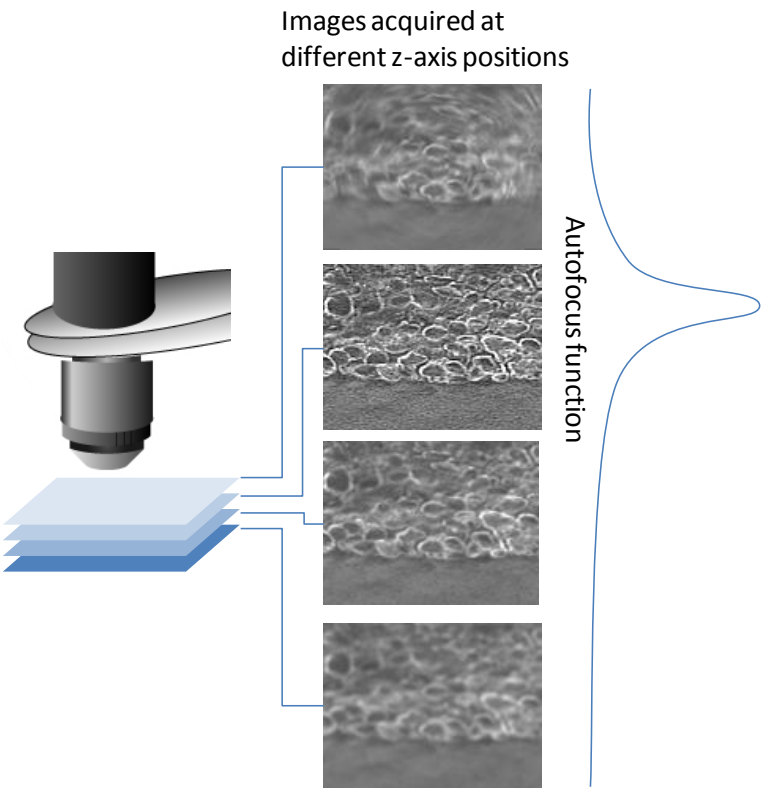

Figure 2-13 Scheme of autofocusing. Images are acquired at different z-axis positions and focal sharpness is calculated by applying an autofocus function to the image.

Many autofocus functions are known, such as those based on Fourier convolution, differentiation, and depths of peaks and valleys [4]. In this study we convoluted the image and the following kernel, C:

$$C = \begin{pmatrix} 0 & -1 & 0 \\ -1 & 0 & 1 \\ 0 & 1 & 0 \end{pmatrix} \qquad \ldots (14)$$

for edge detection, and calculated the standard deviation of the edge detected image. A large standard deviation means that the detected edges are sharp (high intensity), which indicates that the sample is in focus.

This autofocus function needs to be applied to images in many z-axis positions. In order to speed up the process, we used the method of steepest descent [5] and golden section search [6] to find the maximum point of the autofocus function.

Two initial points, x_1 and x_2 were set at 100 increments apart. The method of steepest descent determines the direction of the third point by comparing $f(x_1)$ and $f(x_2)$

when $f(x)$ is the autofocus function. If $f(x_1) > f(x_2)$, x_3 is in the direction of x_1 (Figure 2-14A) and if $f(x_1) < f(x_2)$, x_3 is in the direction of x_2 (Figure 2-14B). This was performed until x passed through the maximum point, i.e., when $f(x_{n+1}) < f(x_n)$ if $x_{n+1} > x_n > x_{n-1}$ or $x_{n+1} < x_n < x_{n-1}$ (Figure 2-14C). At this point, x_{n-1} was set as x_1 and x_{n+1} as x_2, and the golden section method was applied.

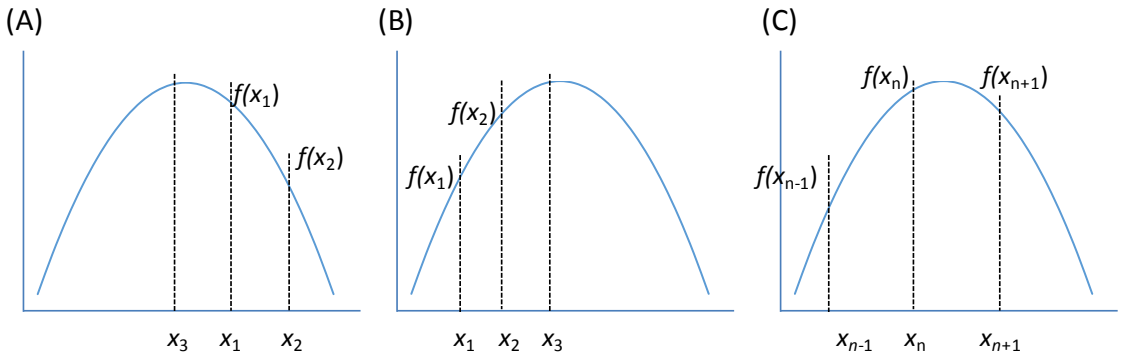

Figure 2-14 Method of steepest descent

With the golden section method, the positions of x_3 and x_4 were determined as

$$x_3 = x_1 + \frac{\tau - 1}{\tau} d, \qquad x_4 = x_1 + \frac{1}{\tau} d \qquad \ldots (15)$$

where $\tau = \frac{1+\sqrt{5}}{2}$ (golden ratio) and d is the distance between x_1 and x_2. For the next step, if $f(x_3) < f(x_4)$, $x_1 = x_3$ and if $f(x_3) > f(x_4)$, $x_2 = x_4$ (Figure 2-15). This is repeated until is d became smaller than a certain number ($d < 5$ increments on the z − axis in this study).

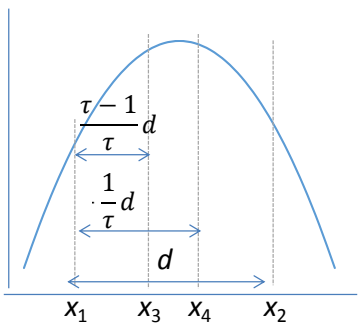

Figure 2-15 Golden section method

With these methods, it was possible to arrive at the optimum z-position with approximately 10 images. Figure 2-16 shows the focus positions for emission filters from 370 nm to 650 nm. Values vary greatly between wavelengths.

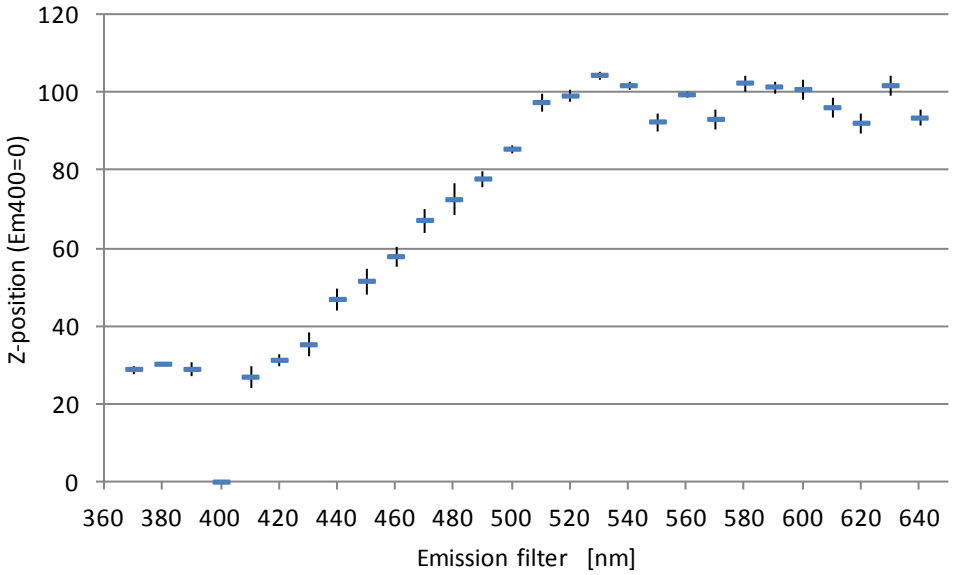

Figure 2-16 The focus position for emission filters from 370 nm to 650 nm. Values of three measurements are averaged. For each measurement, the z-position of emission filter 400 nm is set at 0.

2. 5 The imaging system used in chapters three to five

The imaging system has been developed through the whole study, and the final form explained in this chapter was used to measure the pie pastry explained in chapter 5. The systems used in chapter 3 and 4 lack some of the features that are included in the final system. Table 2-4 shows the features of the imaging system used to acquire the data explained in chapters 3 to 5.

Table 2-4 Features of the imaging system used in chapters 3 to 5

	Chapter 3	Chapter 4	Chapter 5
anti-vibration table	×	×	○
X-Y stage	×	×	○
light source	MAX302,303	MAX302	MAX302
dispersion of excitation WL	bandpass filter	bandpass filter	bandpass filter
low-pass filter	○	×	○
excitation WL	260-600	260-320	270-320
calibration of excitation WL	×	×	○
objective lens	x5	x5	x10
dispersion of emission WL	LCTF	bandpass filter	bandpass filter
emission WL	400-700	370-450	350-430
calibration of emission WL	×	×	○
automation	○	×	○
Z-axis adjustment	○	×	○

Apart from the features described in the former sections, a significant improvement of the imaging system can be seen in the lower limit of the emission wavelength. Tryptophan, an important fluorophor in food, emits strong fluorescence at 350 nm. However, the objective lens used in chapters 3 and 4 transmitted UV light poorly and was only usable at wavelengths above 370 nm. Furthermore, the LCTF used in chapter 3 did not transmit light at wavelengths below 400 nm. Using UV-compliant optical apparatus allowed clear visualization of proteins which contain aromatic amino acids such as Tryptophan.

The magnification of the objective lens is also significant. An important feature in wheat flour doughs is the starch granule. Wheat starch is a mixture of two types of granules, large and small, and their sizes are 15-40 μm and 2-10 μm, respectively. Using an objective lens with a magnification of $\times 10$ enables the observation of single granules of the larger type. Since individual starch granules could not be observed under a magnification of $\times 5$, this was a large improvement.

2. 6 Conclusions

The goal of the FF imaging system is to acquire sharp and clear fluorescence images at multiple excitation and emission wavelengths, quickly and accurately. Observation in the near UV is important for organic materials, but not many devices are UV-compliant and there is scope for development. The intensity of the xenon light sources used in this study is low in the UV wavelengths, and so is the transmittance of the band-pass filters. If these devices could be developed, the exposure times of the camera could be shortened,

leading to shorter data acquisition time.

In this study, the observation target was the microstructure of dough, and therefore, the optical systems were chosen to enable microscopic observation. Greater precision of the measurement system was required as the magnification of observation increased, and although it was possible to attach objective lenses with higher magnification, this did not yield good results. If observation at higher magnification is needed in the future, further improvement of the system may be needed.

References

1. Ueno, S., Do, G.-S., Sagara, Y., Kudoh, K., Higuchi, T., Three-dimensional measurement of ice crystals in frozen dilute solution. International Journal of Refrigeration, (2004). **27**: p. 302-308.

2. CVI_Melles_Griot, 除振システムについて. 2011; http://www.cvimgkk.com/products/pdf/03_Chapter18/w18-all.pdf. Last accessed: 2014.1.23

3. Wu, Q., Merchant, F.A., Castleman, K.R., Microscope image processing. (2008): Elsevier.

4. Groen, F.C., Young, I.T., Ligthart, G., A comparison of different focus functions for use in autofocus algorithms. Cytometry, (1985). **6**(2): p. 81-91.

5. Weisstein, E.W., Method of steepest descent. MathWorld - A Wolfram Web Resource; http://mathworld.wolfram.com/MethodofSteepestDescent.html. Last accessed: 2014.1.23

6. The golden section search method. 2005; http://homepages.math.uic.edu/~jan/mcs471/Lec9/gss.pdf. Last accessed: 2014.1.23

3. Development of a quantitative visualization technique for gluten and starch in model dough

3. 1 Abstract

The distribution of constituents in food affects its end qualities such as texture, and there is a growing demand to develop a method for studying this distribution easily, accurately and nondestructively. The objective of this study was to develop an imaging method that visualizes the precise quantity of constituents, using FF. In this study, the target for visualization was the distribution of gluten and starch in dough samples. Dough samples were prepared with different ratios of gluten, starch, and water, and fluorescence images were acquired at multiple combinations of excitation and emission wavelengths. This data can be interpreted as the FFs of all the pixels in the image, and the FF data of each pixel reflects the constituents of the corresponding point in the sample. A partial least-squares regression (PLSR) model was built using the average FFs of the samples and the corresponding gluten ratios as the explanatory and objective variables, respectively. The importance of each wavelength in the PLSR model was assessed using the selectivity ratio, and optimum wavelengths for accurate prediction of gluten ratio were selected. Finally, the gluten ratio of each pixel was predicted with the PLSR model using the selected wavelengths, and each pixel was colored according to the predicted gluten ratio. The imaging method developed enables the distribution of constituents to be visualized with colors corresponding to their actual quantities or ratios.

3. 2 Introduction

This chapter explains the first stage of FF imaging, to visualize the distribution of two constituents, gluten and starch, in a model system made by mixing the two substances in known quantities. The sample used here is a model of wheat flour dough, since wheat flour dough will be used in chapters 4 and 5.

The work in this chapter is challenging in several ways:

1. Since we aimed to visualize constituents in the sample with as little sample preparation as possible, we did not freeze or slice the sample into thin sections, and observed the sample by just inserting it in a cell with a quartz glass window.

2. We aimed to create a quantitative image, which means that the color of each pixel corresponds to a certain ratio of gluten / starch.
3. In order to select the optimum set of excitation and emission wavelengths, we applied methods developed in the field of chemometrics, so that the accuracy of the image would not decrease, but would increase through the elimination of unnecessary data.

The second point was inspired by previous studies in NIR imaging such as the visualization of sugar in fruit [1] and oil and water in fish [2], and meant that a calibration model would have to be made to link the spectral data to the quantity of each constituent.

As a conclusion, the first point did not work out, i.e., we found out the making thin sections were essential for this method of imaging. However, this negative discovery is very important when we think of the physical model of FF imaging. This will be discussed in detail at the end of this chapter.

3. 3 Materials and methods

3. 3. 1 Sample preparation

Pure wheat gluten (Wako Pure Chemical Industries Ltd., Osaka, Japan) and pure wheat starch (Wako Pure Chemical Industries Ltd.) were mixed at gluten ratios ranging from 0 to 100%, in 20% increments. For each mixture of gluten and starch, distilled water was added at three levels to create a dough-like texture, ranging from relatively soft dough to hard dough. The ratios of gluten and starch, and the water levels for each sample are shown in Table 3-1. The samples were set in a cell with a quartz glass window and the samples were pressed against the glass to obtain a flat surface. The cell was sealed so that the sample would not dry during measurement.

Table 3-1 Ratios of gluten and starch, and water levels

gluten (% d.b.)	starch (% d.b.)	water level (% d.b.)		
		low	medium	high
0	100	50	55	60
20	80	50	60	70
40	60	60	70	80
60	40	70	80	90
80	20	80	90	100
100	0	80	90	100

The ratios of gluten and starch were set in the range of 0 to 100% in order to visualize features such as starch granules and gluten strands on the surface of the dough. A starch granule on the surface was expected to show similar FFs to that of the starch 100% sample, and conversely, a gluten strand should show similar FFs to that of the gluten 100% sample. The water content was set at three levels because the distribution of water in micro-scale was unknown, for example it was unknown whether a starch granule at the surface of dough would contain 50, 55 or 60% of water.

Three sets of samples were made, corresponding to the three experiments shown in Figure 3-1. Details regarding each experiment are discussed later.

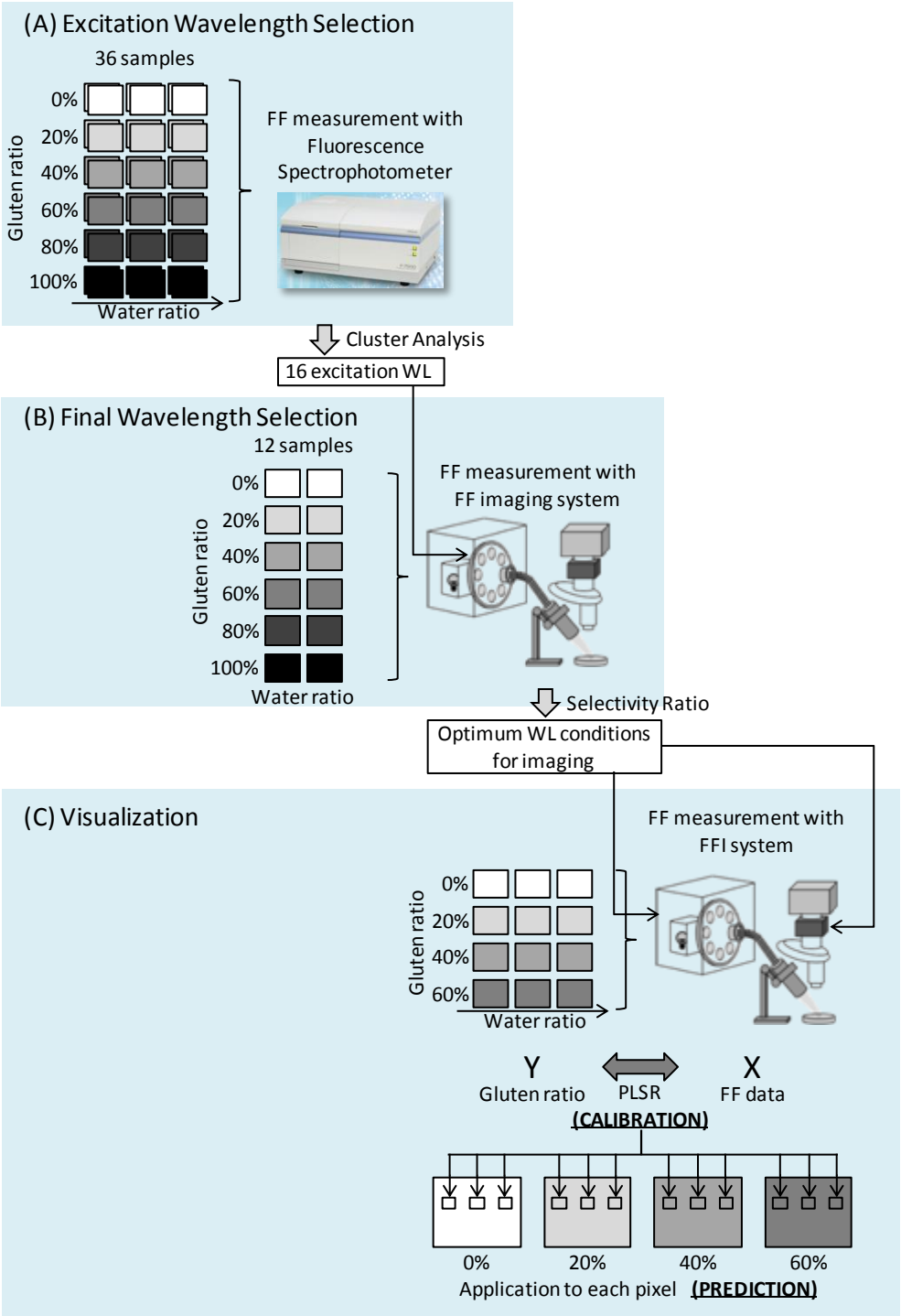

Figure 3-1 Flowchart of wavelength selection and visualization. (A) The FFs of 36 samples are measured using a fluorescence spectrophotometer, and 16 excitation wavelengths are selected by cluster analysis. The selected excitation wavelengths are used in the FF imaging system. (B) Fluorescence images of 12 samples are acquired with the FF imaging system and the optimum wavelength conditions for predicting the

gluten ratio are selected using selectivity ratio. These wavelength conditions are used acquire the image data. (C) Fluorescence images of 12 samples are acquired for visualization, using the optimum wavelength conditions. A calibration model between the FF data and gluten ratio is calculated using PLSR. The calibration model is applied to each pixel of the images, thereby predicting the gluten ratio of each pixel.

3. 3. 2 FF imaging system

The FF imaging system was constructed as explained in Chapter 2 with the features shown in Table 2-4. A liquid crystal tunable filter (LCTF) (VariSpec, Cambridge Research & Instrumentation, Inc., Hopkinton, USA) was used in place of the emission band-pass filters because the filter wheel held only eight band-pass filters and more emission wavelengths were needed in this experiment.

3. 3. 3 Selection of excitation wavelengths

The imaging procedure was conducted according to the flowchart in Figure 3-1. First, preliminary measurement was conducted to determine the optimal wavelength conditions, i.e., combinations of excitation and emission wavelengths, for estimating the gluten ratio of the sample. This was carried out in two steps: first, selecting a limited number of excitation wavelengths with data from a fluorescence spectrometer (Figure 3-1A), and second, selecting the final wavelength conditions with data from the FF imaging system (Figure 3-1B).

A critical constraint condition of the FF imaging system was that the two light sources could only hold eight band-pass filters each, meaning the maximum number of wavelengths that could be used for the excitation light was 16. Therefore, as the first experiment, the selection of these 16 excitation wavelengths was carried out with FF data acquired with a fluorescence spectrophotometer (F-7000, Hitachi High-Technologies Corporation, Tokyo, Japan).

For this first experiment (Figure 3-1A), 36 samples were prepared: two samples for all combinations of gluten (six levels) and water (three levels) ratio. The samples were set in the fluorescence spectrophotometer and the FF of each sample was measured using the attached software (FL Solutions 2.1, Hitachi High-Technologies). The excitation and emission wavelengths measured were both in the range of 200-700 nm at 10 nm intervals. The slit width was set at 10 nm for both excitation and emission lights. The scanning speed was 30000 nm/min, the response time was 0.002 s, and the power voltage of the photomultiplier was 400 V.

The FFs measured included the first-, second- and third-order scattered lights,

which occurred at wavelengths where the emission wavelength was equal to, twice, and three times the excitation wavelength, respectively [3]. Since these signals were stronger in intensity than the fluorescence, they were removed and replaced with first-order interpolation [4, 5]. Next, the wavelength conditions that could not be achieved with the FF imaging system were removed, leaving FF data with excitation and emission wavelengths in the ranges of 260-630 nm and 400-700 nm, respectively. Finally, the wavelength conditions where the emission wavelengths were shorter than or within 50 nm of the excitation wavelengths were removed because they corresponded to the non-fluorescent and scattered lights in the FF imaging system, respectively.

Data analysis was carried out using MATLAB R2011b (The MathWorks, Inc., Massachusetts, USA) and PLS_Toolbox 6 (Eigenvector research, Inc., Washington, USA). The acquired fluorescence data was a three-way data, with modes “excitation wavelength”, “emission wavelength” and “sample”. This was unfolded [6] into a two-way data with mode “excitation wavelength” and a combined mode “emission wavelength × sample”. Cluster analysis using Ward’s method was applied to this FF data to group the excitation wavelengths into 16 clusters. The shortest wavelengths in each cluster were selected as the excitation wavelengths in the FF imaging system. Since the emission wavelengths are always longer than the excitation wavelengths, selecting the shortest excitation wavelength in the cluster would maximize the number of wavelength conditions used in the FF imaging system.

3. 3. 4 Selection of wavelength conditions for imaging

In the second experiment, the final wavelength conditions were selected using an actual FF imaging system (Figure 3-1B). Dough samples were made at the same 6 levels of gluten ratio, and 2 levels of water were set for each gluten ratio, resulting in 12 samples. The dough samples were set in the sample cell for measurement.

The excitation wavelengths used for imaging were the 16 wavelengths selected from the fluorescence spectrometer data. The emission wavelengths used were in the range of 400-700 nm in 10 nm increments, and set to be 60 nm longer than the excitation wavelengths or more. This resulted in 360 wavelength conditions.

Fluorescence images of the samples were acquired with the FF imaging system with an exposure time of 0.625 s and binning of 8 × 8 [7]. A binning of 8 × 8 means that the signals of 64 pixels would be integrated for one virtual pixel. This resulted in a dataset of 360 grayscale images, corresponding to the 360 wavelength conditions, each with a size of 168 × 128 pixels. These were saved as tagged image file format (tiff) images.

A partial least squares regression (PLSR) model [8] was constructed from these data as shown in Figure 3-2. The fluorescence images were divided into four areas with half-lengths and half-widths of the original images and the light intensities of all the pixels in each area were averaged. In this way, four sets of FF data could be acquired for each sample, with each data reflecting the gluten ratio of the sample as a whole. The PLSR model was constructed using the actual gluten ratio of the sample as the objective variable (Y) and the FF data as the explanatory variable (X). The FF data were mean-centered [9] prior to the calculation of the PLSR model, and the number of latent variables was determined by a cross-validation method [10]. Two PLSR models were constructed: one using all the data as calibration data, and the other using half of the data (two FF data from each sample) as calibration data and the other half as validation data. Data for calibration and validation were divided randomly.

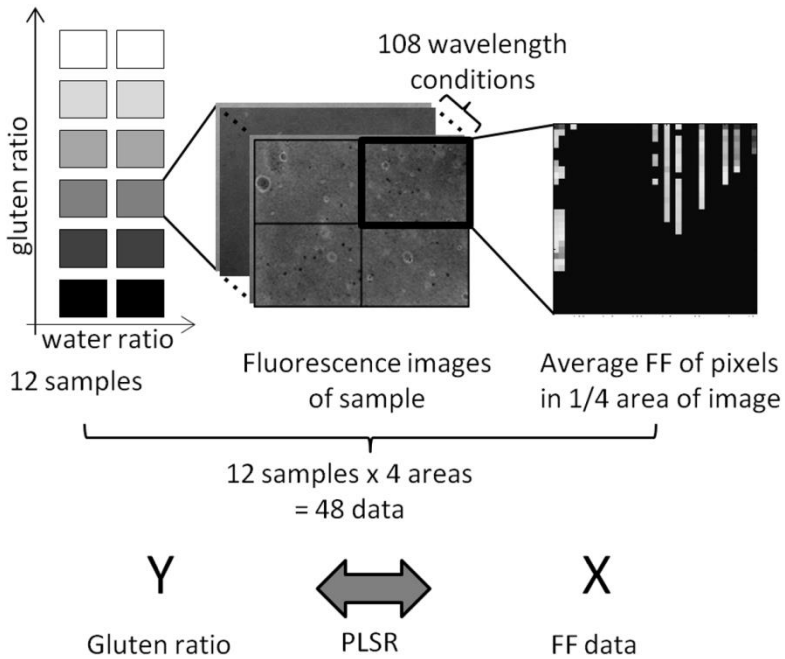

Figure 3-2 Flowchart of PLSR model construction. Fluorescence images of 12 samples with different gluten ratios and water contents are acquired. Each image is split into four equal areas and the average FFs of all the pixels in each area are calculated, resulting in 48 FF data. A PLSR model is constructed using the actual gluten ratio of each sample as the objective variable Y and the FF data as the explanatory variable X.

To select the wavelength conditions most relevant in predicting the gluten ratio of the sample, the concept of selectivity ratio was used. Selectivity ratio provides a simple numerical assessment of the importance of each variable in the PLSR model [11, 12],

i.e., the higher the selectivity ratio, the more useful the variables are for prediction. The selectivity ratio of variable i (SR_i) is defined as the ratio of explained variance ($V_{expl,\,i}$) to residual variance ($V_{res,\,i}$) for variable i as shown in (1).

$$SR_i = V_{expl,i}/V_{res,i} \qquad \dots (1)$$

The explained variance is the y-relevant variation in the x-variables, calculated from the target projected scores and loadings. Conversely, the residual variance is the variation that non-relevant to y [12]. Wavelength conditions were selected by order of selectivity ratio, and the coefficient of determination, R^2, was calculated while the number of wavelength conditions was increased from 10% to 100% of the original number of wavelength conditions in 10% increments. The optimum number of wavelength conditions was determined as the data giving the highest R^2 for both calibration and validation.

3. 3. 5 Visualization of gluten ratio

For the third experiment (Figure 3-1C), a new set of fluorescence images were acquired using the wavelength conditions selected as shown above to visualize the spatial distribution of gluten in the dough.

Dough samples were made with gluten ratios of 0, 20, 40, and 60%, and 3 levels of water were set for each gluten ratio, resulting in 12 samples. The dough samples were set in a sample cell.

Exposure time and binning were set at 10 s and 2 × 2, respectively. A smaller binning was selected to enhance the resolution of the image, and exposure time was lengthened to make up for the reduction in the amount of light focused on each pixel. The fluorescence images of the 12 samples were acquired under these conditions. The size of the images was 672 × 512 pixels.

A PLSR model that predicts the gluten ratio from FF data was constructed from the newly acquired data following the method shown in Figure 3-2. Each fluorescence image was divided into 9 areas (3 × 3) instead of 4, resulting in 108 sets of data. All the data were used as the calibration set.

Next, the gluten ratio of each pixel in the image was predicted by applying the FF of the pixel to the PLSR model calculated above. The predicted gluten ratio was converted to a color through a color axis ranging from blue (0%) to green (30%) to red (60%), and the pixel was colored accordingly. In these pseudo-color images, the color of each pixel shows the gluten ratio at that spot. Pseudo-color images of the dough samples

with total gluten ratios of 0%, 20%, 40%, and 60% were created.

3. 4 Results and discussion

3. 4. 1 Selection of excitation wavelengths

The time required for acquiring fluorescence images is proportional to the number of wavelength conditions. Therefore, measuring the sample under wavelength conditions other than the optimal wavelengths would unnecessarily lengthen measurement time. The sample is exposed to light in the UV-VIS range during measurement, but longer measurement times could possibly denature the sample. Therefore, selecting the minimum yet sufficient number of wavelength conditions for predicting the gluten ratio is a very important step in imaging operation.

The selection of wavelengths should be performed using data acquired under similar conditions as the final data for imaging. Although it would be easy to use the data acquired with the fluorescence spectrometer to select the optimum wavelength conditions for the FF imaging system, measurement conditions such as wavelength resolution and sensitivity of the detectors were considered too different to expect compatibility between the two data sets. Measurement conditions affect the signal-to-noise (S/N) ratio of the data. The difference becomes significant at shorter wavelengths where the intensity of the excitation light and the sensitivity of the CCD camera in the FF imaging system decrease. Since many steps are needed to transform the results acquired from one system to another [13], the data from the fluorescence spectrometer was only used to select the 16 excitation wavelengths for the FF imaging system and the rest of the wavelength selection was performed with data from the FF imaging system.

Figure 3-3 shows the cluster analysis results for the first experiment using the fluorescence spectrometer. The excitation wavelengths are clustered according to the squared distance between them. The higher limit of the x-axis is selected to create 16 clusters. The shortest wavelength in each cluster was chosen for the excitation wavelengths in the FF imaging system. These wavelengths were 260, 270, 290, 300, 310, 350, 370, 390, 410, 430, 450, 470, 510, 550, 570, and 600 nm. The main fluorophor in gluten is tryptophan [14], which has a fluorescence peak at excitation and emission wavelengths of approximately 280 nm and 350 nm, respectively [15]. Although the wavelength range of the FF data used in analysis did not include this fluorescence peak, the data are thought to have been affected by it since the wavelengths selected are narrowly spaced around 280 nm.

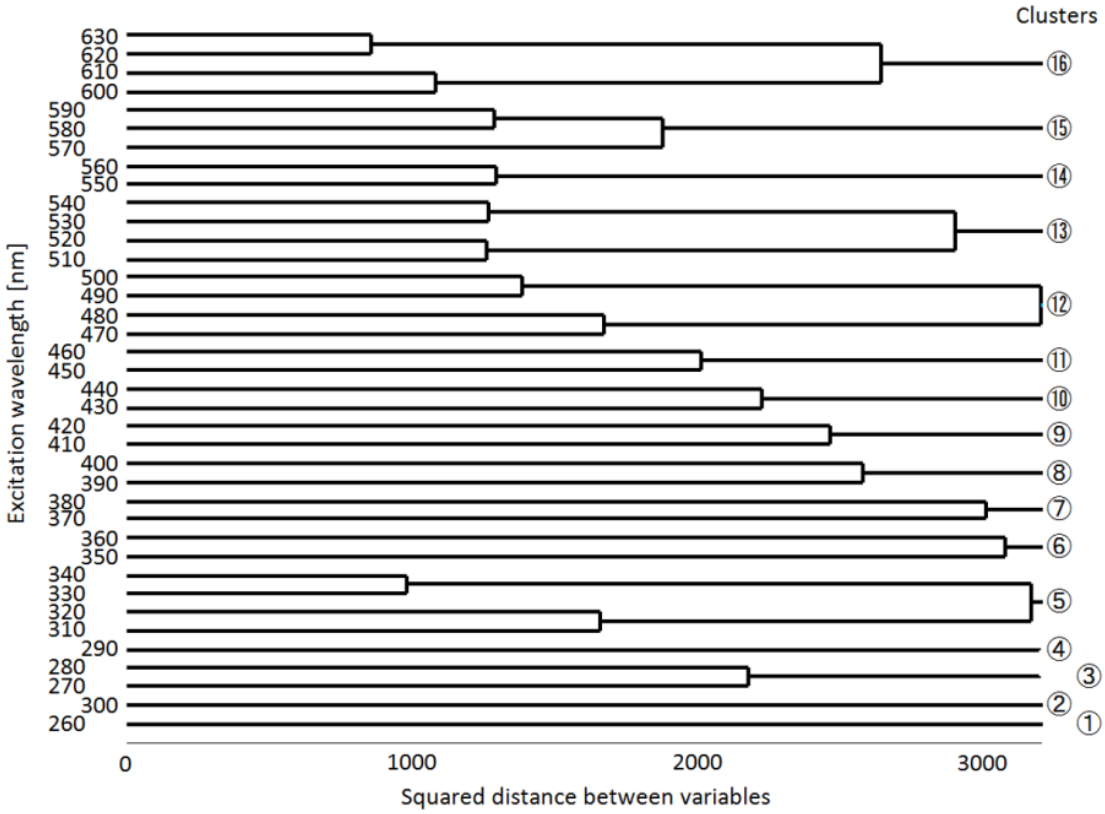

Figure 3-3 Results of the cluster analysis. The excitation wavelengths shown on the left are clustered according to squared distance. The resulting clusters are shown on the right.

3. 4. 2 Selection of wavelength conditions for imaging

Fluorescence images to determine the wavelength conditions were acquired with the FF imaging system using the 16 excitation wavelengths shown above and emission wavelengths in the range of 400-700 nm (experiment 2). To minimize measurement time, binning was set at its maximum, 8 × 8. The final data acquisition for visualized imaging (experiment 3) was planned to be performed with 2 × 2 binning (4 pixels integrated for one virtual pixel), meaning that the number of pixels integrated for one virtual pixel would be 1/16 of that in this acquisition. Therefore, the exposure time for this preliminary data acquisition was also set to be 1/16 of that for the final data acquisition. Since the exposure time of the final data acquisition was planned to be 10 s, the exposure time for this preliminary data acquisition was set to be 0.625 s, or 10 s divided by 16.

A PLSR model was constructed to predict the gluten ratio of each sample. Figure 3-4A shows the gluten ratio of each sample predicted by the PLSR model plotted against

actual gluten ratio. The coefficient of determination, R^2, was 0.918. It can be seen that the predicted gluten ratio value increases constantly from 0 to 60%, but does not change much from 60 to 100%. It seems that the increase in gluten ratio from 60 to 80% could not be modeled from the FF data using PLS which is a linear model. This may be due to the quenching of fluorescence, which occurs when the concentration of fluorophors becomes too high [16]. It could be that the fluorescence signal of tryptophan increases linearly with gluten ratio when the ratio is low, but not when the ratio exceeds 60%.

To obtain a more accurate prediction model, the data of the samples with gluten ratios of 80% or over were excluded, leaving a dataset with 16 samples, i.e., four levels of gluten ratio with four sets of FF data each. As can be seen from Figure 3-4B, the PLSR model calculated from this data proved to be much more accurate, with R^2 being 0.985. On the other hand, the PLSR model calculated from the samples with gluten ratios of 60, 80, and 100% was unstable and inaccurate (Figure 3-4C), with R^2 being 0.775. In this model, the predicted gluten ratio for samples with actual ratios of 60% and 80% were in the same range. This is thought to be because the original fluorescence fingerprints of these samples do not differ much or change in a nonlinear way which cannot be modeled with PLSR Regarding these results, data from the samples with gluten ratios in the range of 0 to 60% were used for further analysis. Therefore, it is important to note that the prediction model calculated from this data can only be applied to gluten ratios in the same range.

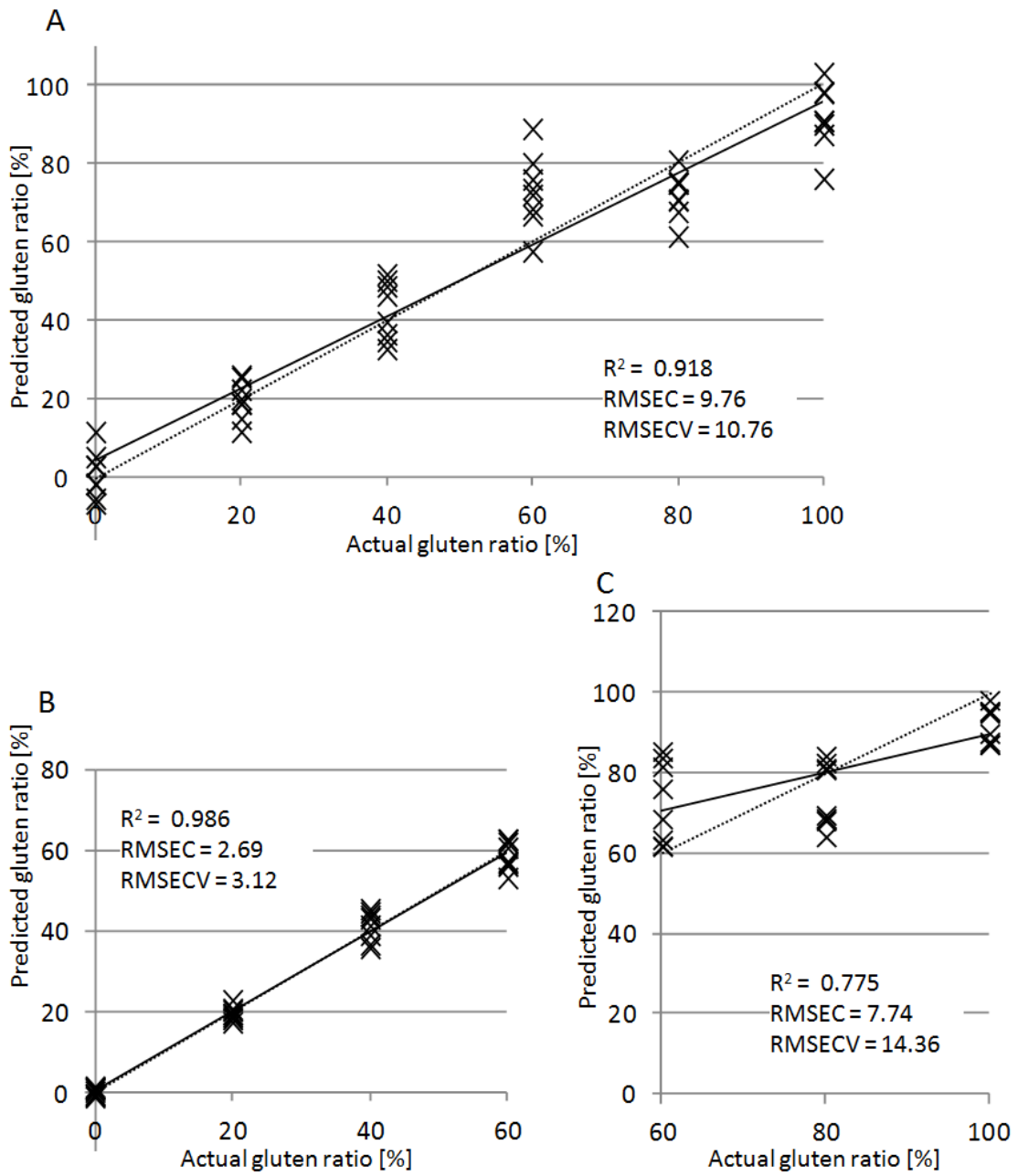

Figure 3-4 Score plots of PLSR models, calculated from different sets of data. The bold line shows the calibration curve calculated from the PLSR model. The dotted line shows the ideal line (predicted value = actual value). (A) PLSR model calculated from all samples. (B) PLSR model calculated from the samples with gluten ratios up to 60%. (C) PLSR model calculated from samples with gluten ratios from 60 to 100%.

Next, the optimum wavelength conditions for predicting the gluten ratio from the FF data were selected on the basis of selectivity ratio. Figure 3-5A shows the selectivity

ratio of the 360 wavelength conditions under which FF imaging was performed. It is interesting to note that the wavelengths shorter than 450 nm show a relatively small selectivity ratio. The reason for this is thought to be the low S/N ratio of these wavelength conditions, owing to the low transmission of the LCTF at wavelengths shorter than 450 nm. By using selectivity ratio to select the wavelength conditions, not only the intrinsic fluorescence of the sample but also the conditions of the measuring instruments can be considered.

Figure 3-5B shows R^2 when the wavelength conditions are selected by order of selectivity ratio. Irrespective of the number of wavelength conditions, R^2 is large when all the samples are used for calibration. However, when all the samples are used for calibration, there is also the danger of overfitting, when the model optimizes itself for the given data but cannot be used for other data [17]. This is likely to happen when the number of variables (in this experiment, 36 to 360) exceeds that of samples (in this experiment, 16). Therefore, we focused on the results where half the data was used as calibration data and the other half as validation data. Excluding the case in which all the wavelength conditions are used (no wavelength reduction), R^2 was largest when the number of wavelength conditions was 30% of the original number, which means 108 wavelength conditions. Since the number of wavelength conditions that could be used for imaging was limited, these 108 wavelength conditions were used to acquire the final imaging data. The selected wavelength conditions are shown in Figure 3-5C.

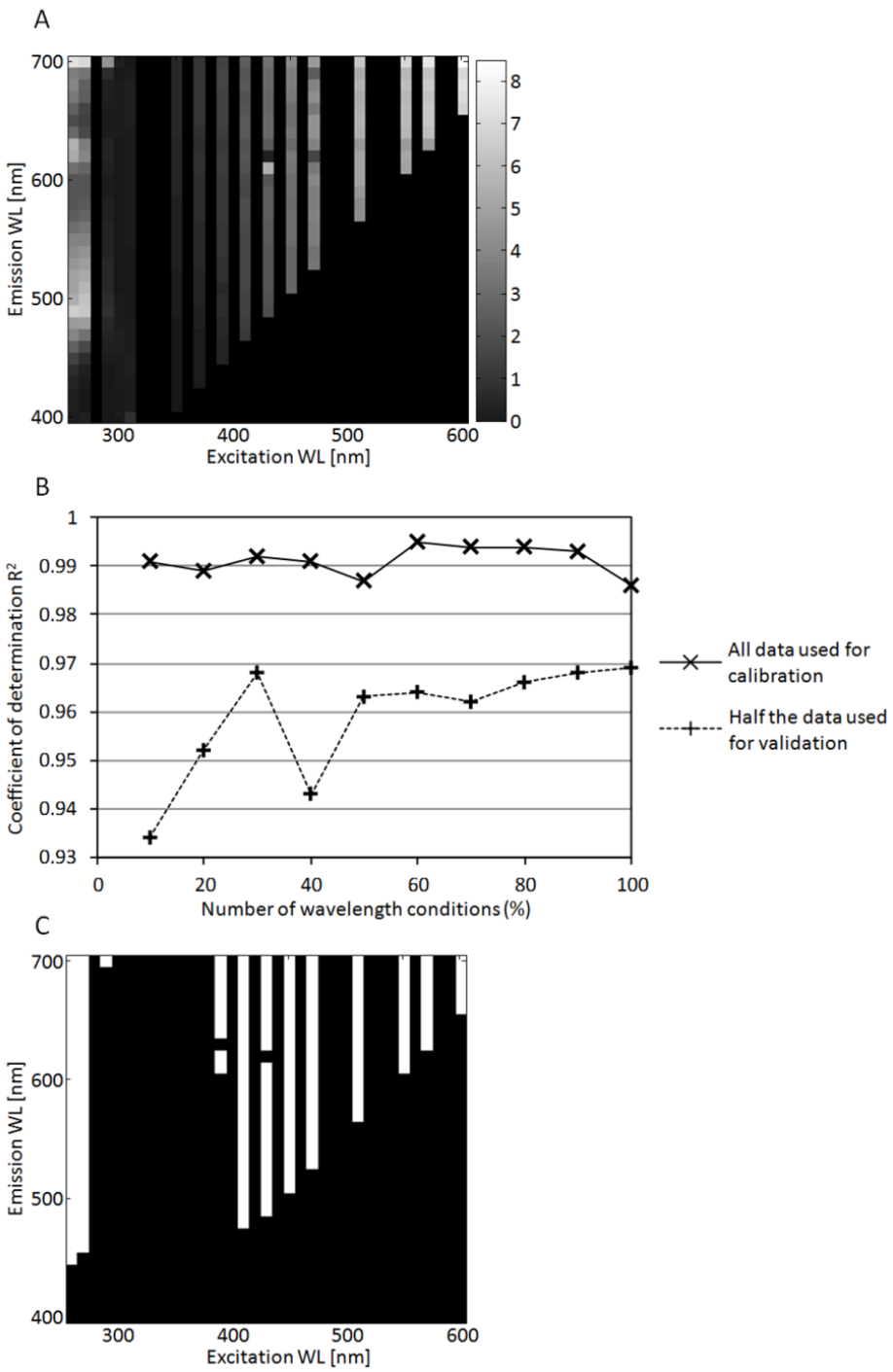

Figure 3-5 (A) Selectivity ratios of all wavelength conditions. The lighter the color, the larger the selectivity ratio. (B) Change in R^2 with number of wavelength conditions. The number of wavelength conditions where R^2 is high for both calibration and validation was used. (C) Selected wavelength conditions used for FF imaging. The white and black areas show the wavelength conditions which were used and not used for visualization, respectively.

3. 4. 3 Pseudo-color image of gluten distribution and ratio

The 108 wavelength conditions were used to acquire the final FF data for visualization imaging (experiment 3). Reflecting the results from experiment 2, only samples with gluten ratios from 0% to 60% were measured and a PLSR model that predicts the gluten ratio from FF data was constructed. Figure 3-6 shows the predicted gluten ratio calculated from the FF data, plotted against the actual gluten ratio of the sample. The R^2 of this PLSR model was 0.964. All data were used as the calibration data. This prediction model was used to predict the gluten ratio of each pixel.

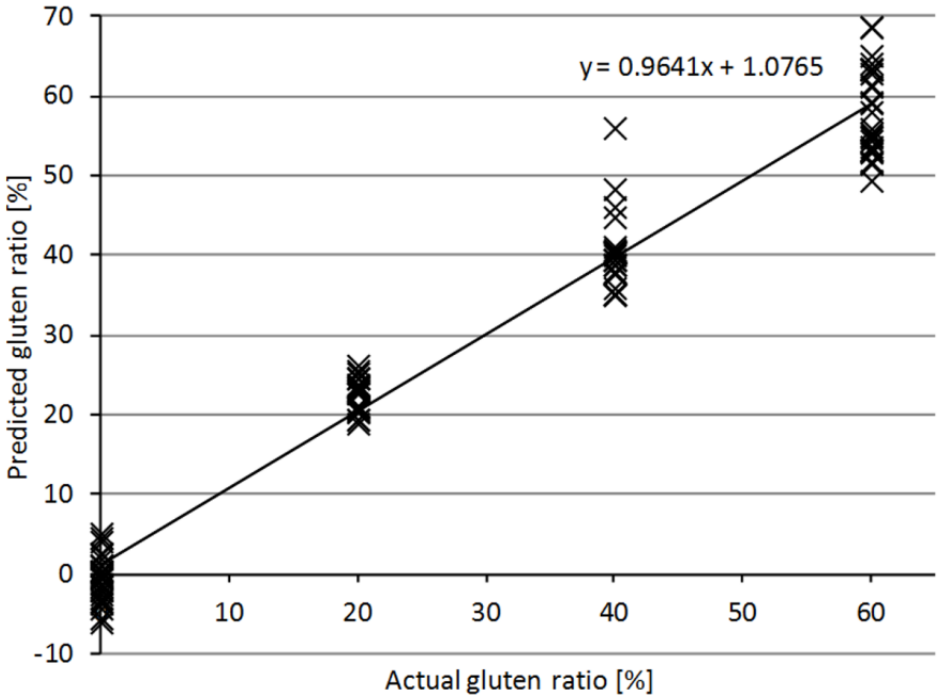

Figure 3-6 Calibration curve between actual gluten ratio and predicted gluten ratio. The actual gluten ratio is derived from the gluten ratio of the whole sample and the predicted gluten ratio is calculated from the PLSR model.

Figure 3-7 shows pseudo-color images of the samples with gluten ratios of 0% for (A) and (B), 20% for (C) and (D), 40% for (E) and (F), and 60% for (G) and (H). Since 60% is the upper limit of the prediction model, pixels whose predicted gluten ratio was higher than 60% were colored the same.

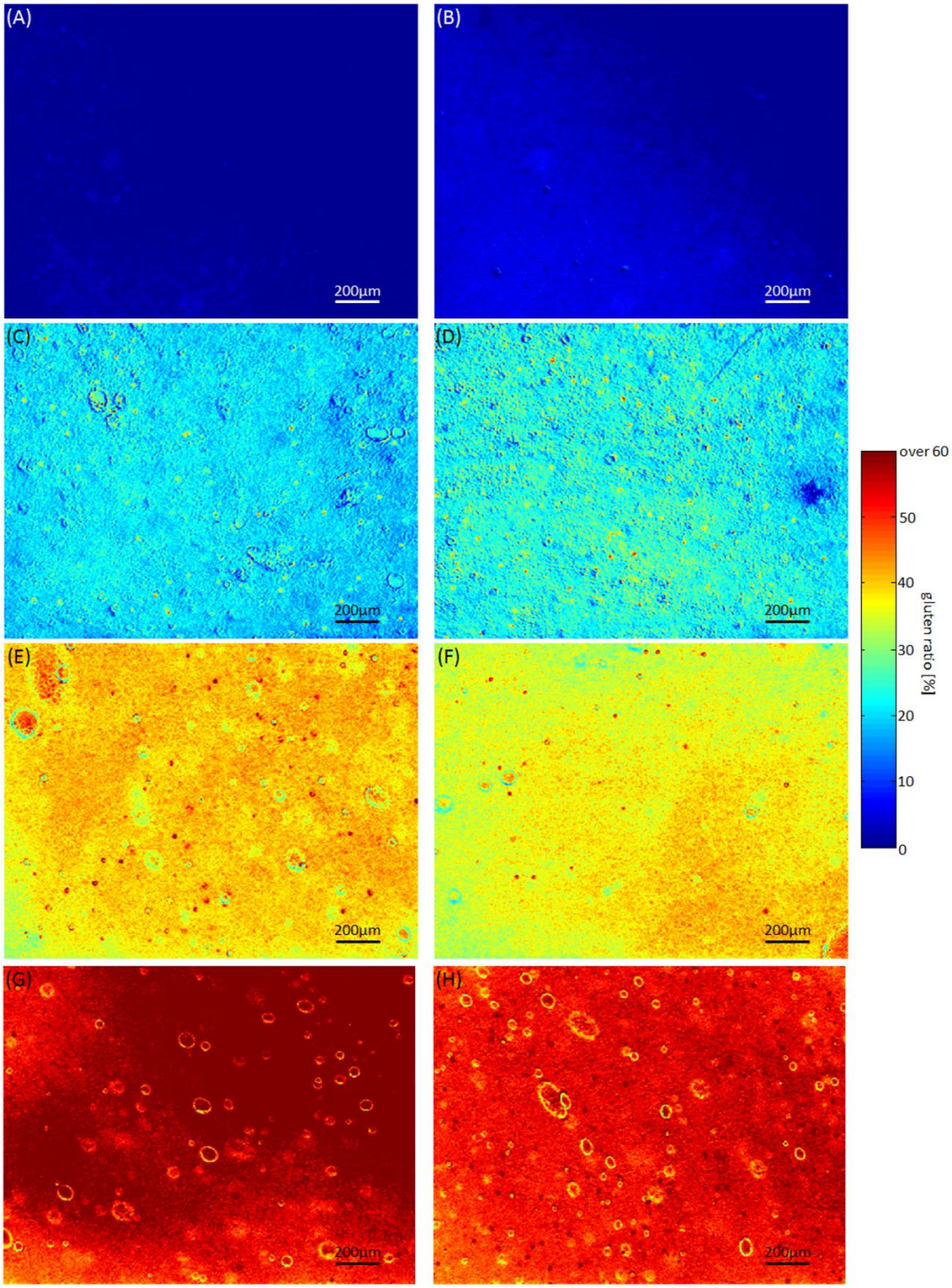

Figure 3-7 Pseudo-color images of the samples colored according to the gluten ratio of each pixel. (A) and (B) , (C) and (D), (E) and (F), (G) and (H) are samples with gluten ratios of 0 %, 20 %, 40 %, and 60% respectively. The samples in the left row contain lower water contents than their counterparts in the right row.

One noticeable feature of the samples with gluten ratios of 20% and 40% is small spots with a high gluten ratio. These are presumed to be remnants of freeze-dried gluten powder that were not hydrolyzed thoroughly. These spots cannot be seen in the samples with a gluten ratio of 0%, supporting our presumption.

For the samples that are mixtures of gluten and starch, it was expected that the pseudo-color images would show starch granules and gluten strands on the surface of the samples such as the features seen in other studies [18, 19, 20, 21]. It was expected that areas where starch granules existed at the top surface of the sample would show a predicted gluten ratio close to 0 % and that these areas would decrease as the gluten ratio of the whole sample increased. However, specific features such as starch granules could not be seen in the results, even though the spatial resolution of the camera was high enough for their visualization. This is thought to be due to the excitation light penetrating into the sample, which in this case is about 2 mm thick, at a depth larger than the thickness of a single starch granule, and the corresponding emission light resulting from all the constituents which the excitation light reaches. Therefore, the fluorescence signal that can be detected by the CCD camera was the summated signal of many overlapping constituents, thereby canceling out fluorescence signals from micro-scale features at the top-most surface of the sample (Figure 3-8). With the current FF imaging system and the micro- to millimeter-scale of the sample, some kind of slicing process with a cryostat may be needed to observe specific features.

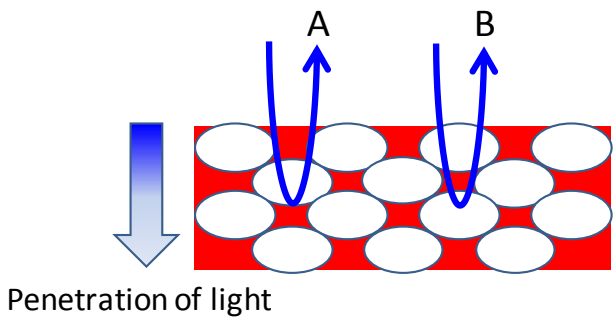

Figure 3-8 Schematic diagram of the physical model of FF imaging. The white ovals and red background are starch granules and gluten, respectively. The excitation light penetrates into the sample, and the emissions of all the overlapping constituents are detected. Although there is gluten and starch on the surface for A and B, respectively, the summated signal observed is almost equal. Theoretical explanations of fluorescence and transmittance in turbid media are found in Oelkrug [22].

3. 4. 4 Water content

One point that should be considered in preparing the dough samples is the water content of gluten and starch in the dough. Gluten and starch absorb different amounts of water [23] but the way water is distributed between these different constituents in dough remains unknown. This is a problem when predicting the ratio of constituents present in a pixel because the FF can be affected by water content. Pure water shows no fluorescence, but mixing water with a fluorescent substance such as gluten would lower the fluorescence intensity by “diluting” it.

The above problem can be solved if the gluten ratio could be predicted irrespective of water content, by selecting a suitable method of preprocessing the FF data or by selecting wavelength conditions that are unaffected by water content. This was made possible by preparing 2 or 3 samples with different water contents for each gluten ratio and by constructing a prediction model so that gluten ratio could be predicted accurately despite fluctuations in water content. Water content was adjusted so that the samples would show a dough-like texture; it ranged from 50% (d.b.) to 100% (d.b.) for the samples with gluten ratios of 0% and 100%, respectively.

For the four pairs of pseudo-color images shown in Figure 3-7, the samples on the right have higher water contents than the corresponding samples on the left. However, this has little influence on the predicted gluten ratio. By combining FF data with PLSR, it was possible to create a model that could predict gluten ratio without being affected by the water content.

3. 5 Conclusions

In this chapter, an imaging method using the FF was developed to visualize the distribution of gluten in dough, quantitatively. To predict gluten ratio in each pixel, a calibration model relating the FF to gluten ratio was created from the average FF of samples of which the total gluten ratio was known. The calibration model was developed so that gluten ratio could be predicted regardless of water content and the optimum wavelength conditions for this purpose were selected on the basis of selectivity ratio.

In this study, the dough samples were measured without creating thin sections or drying. This is a great advantage in visualizing delicate samples such as dough where the structure could easily change through preprocessing. However, it was shown that with thick samples, the fluorescent data contains information from all the constituents that the excitation light reaches, making it difficult to discern individual constituents. It

may be said that preprocesses should be selected depending on the objective of visualization and the scale of the sample. With this done, the proposed method would enable the distribution of constituents to be visualized using colors corresponding to their actual quantities or ratios.

Furthermore, the method could be developed further for the application on real samples such as wheat flour-based dough or more complex foods. This would need the construction of a more flexible model that could incorporate unknown substances. Studies in the area of chemometrics are expected to be applied here.

References

1. Tsuta, M., Sugiyama, J., Sagara, Y., Near-infrared imaging spectroscopy based on sugar absorption band for melons. Journal of Agricultural and Food Chemistry, (2001). **50**(1): p. 48-52.

2. ElMasry, G., Wold, J.P., High-speed assessment of fat and water content distribution in fish fillets using online imaging spectroscopy. Journal of Agricultural and Food Chemistry, (2008). **56**(17): p. 7672-7677.

3. Fujita, K., Tsuta, M., Kokawa, M., Sugiyama, J., Detection of deoxynivalenol using fluorescence excitation-emission matrix Food and Bioprocess Technology, (2010). **3**(6): p. 922-927.

4. Bahram, M., Bro, R., Stedmon, C., Afkhami, A., Eem scatter removal and interpolation, in *http://www.models.kvl.dk/EEM_correction*.

5. Bahram, M., Bro, R., Stedmon, C., Afkhami, A., Handling of rayleigh and raman scatter for parafac modeling of fluorescence data using interpolation. Journal of Chemometrics, (2006). **20**(3-4): p. 99-105.

6. Louwerse, D.J., Smilde, A.K., Multivariate statistical process control of batch processes based on three-way models. Chemical Engineering Science, (2000). **55**(7): p. 1225-1235.

7. Nasibov, H., Kholmatov, A., Akselli, B., Nasibov, A., Baytaroglu, S., Performance analysis of the ccd pixel binning option in particle-image velocimetry measurements. Ieee-Asme Transactions on Mechatronics, (2010). **15**(4): p. 527-540.

8. Wold, S., Hoy, M., Martens, H., Trygg, J., Westad, F., MacGregor, J., Wise, B.M., The pls model space revisited. Journal of Chemometrics, (2009). **23**(1-2): p. 67-68.

9. Seasholtz, M.B., Kowalski, B.R., The effect of mean centering on prediction in multivariate calibration. Journal of Chemometrics, (1992). **6**(2): p. 103-111.

10. Wold, S., Sjostrom, M., Eriksson, L., Pls-regression: A basic tool of chemometrics. Chemometrics and Intelligent Laboratory Systems, (2001). **58**(2): p.

109-130.

11. Rajalahti, T., Arneberg, R., Kroksveen, A.C., Berle, M., Myhr, K.M., Kvalheim, O.M., Discriminating variable test and selectivity ratio plot: Quantitative tools for interpretation and variable (biomarker) selection in complex spectral or chromatographic profiles. Analytical Chemistry, (2009). **81**(7): p. 2581-2590.

12. Kvalheim, O.M., Interpretation of partial least squares regression models by means of target projection and selectivity ratio plots. Journal of Chemometrics, (2010). **24**(7-8): p. 496-504.

13. Fernandez-Ahumada, E., Garrido-Varo, A., Guerrero, J.E., Perez-Marin, D., Fearn, T., Taking nir calibrations of feed compounds from the laboratory to the process: Calibration transfer between predispersive and postdispersive instruments. Journal of Agricultural and Food Chemistry, (2008). **56**(21): p. 10135-10141.

14. Stevenson, S.G., Preston, K.R., Intrinsic fluorescence and quenching studies of gluten proteins. Cereal Chemistry, (1994). **71**(2): p. 155-159.

15. Christensen, J., Norgaard, L., Bro, R., Engelsen, S.B., Multivariate autofluorescence of intact food systems. Chemical Reviews, (2006). **106**(6): p. 1979-1994.

16. Nobel, P.S., Physicochemical and environmental plant physiology. 4th ed. (2009): Academic Press. 582.

17. Defernez, M., Kemsley, E.K., The use and misuse of chemometrics for treating classification problems. TrAC Trends in Analytical Chemistry, (1997). **16**(4): p. 216-221.

18. Peighambardoust, S.H., Dadpour, M.R., Dokouhaki, M., Application of epifluorescence light microscopy (eflm) to study the microstructure of wheat dough: A comparison with confocal scanning laser microscopy (cslm) technique. Journal of Cereal Science, (2010). **51**(1): p. 21-27.

19. Kokawa, M., Fujita, K., Sugiyama, J., Tsuta, M., Shibata, M., Araki, T., Nabetani, H., Visualization of gluten and starch distributions in dough by fluorescence fingerprint imaging. Bioscience Biotechnology and Biochemistry, (2011). **75**(11): p. 2112-2118.

20. Kokawa, M., Fujita, K., Sugiyama, J., Tsuta, M., Shibata, M., Araki, T., Nabetani, H., Quantification of the distributions of gluten, starch and air bubbles in dough at different mixing stages by fluorescence fingerprint imaging. Journal of Cereal Science, (2012). **55**(1): p. 15-21.

21. Peressini, D., Peighambardoust, S.H., Hamer, R.J., Sensidoni, A., van der Goot, A.J., Effect of shear rate on microstructure and rheological properties of sheared wheat doughs. Journal of Cereal Science, (2008). **48**(2): p. 426-438.

22. Oelkrug, D., Fluorescence spectroscopy in turbid media and tissues, in *Topics in fluorescence spectroscopy, probe design and shemical sensing*, Lakowicz, J.R., Editor (1994), Springer.

23. Baker, J.C., Parker, H.K., Mize, M.D., The distribution of water in dough. Cereal Chemistry, (1946). **23**(1): p. 30-38.

4. Visualization and quantification of gluten, starch and air bubble distributions in wheat flour dough

4. 1 Abstract

FF imaging was used to visualize the distributions of gluten, starch and air bubbles and their changes through mixing. Wheat flour dough was mixed up to three stages, i.e., under-mixing, optimum-mixing, and over-mixing, and thin sections of the dough were prepared with a cryotome. Fluorescence images of the sections were acquired in 63 combinations of excitation and emission wavelengths, thereby constructing the FFs of the constituents at each pixel. Similarity values between the FF of each pixel in the dough and those of gluten and starch were calculated. A pseudo-color image of gluten and starch distribution was created in two ways. For the first method, each pixel was colored by fitting a continuous color scale to the cosine similarity value to gluten and starch. After acquisition of FF data, the dough sample was then fluorescently stained for gluten and starch. The stained image showed patterns similar to the pseudo-color FF image, validating the effectiveness of the FF imaging method. In the second method, the pixels were arranged in order of cosine similarity to gluten and pixels with higher values of cosine similarity were categorized as “gluten” and the rest as “non-gluten”. The number of pixels categorized as “gluten” was based on the overall ratio of gluten in the dough. The same process was performed with the FF of starch, and all pixels were divided into “starch” and “non-starch”. Colors were assigned to each division, and the distributions of gluten and starch were visualized.

Furthermore, quantitative parameters concerning gluten and starch distributions and bubble area were extracted from the dough images at each mixing stage, showing the homogenization of gluten and starch and the incorporation of bubbles with mixing. This imaging method is suggested to have an advantage over conventional imaging methods since there is no need to preprocess the sample, and any constituent in the sample can be visualized as long as there is information about the FF of the pure target constituent.

4. 2 Introduction

In this chapter, FF imaging is applied to a real food sample, wheat flour dough,

and the gluten and starch distributions are visualized. In real foods, it is difficult to create an accurate calibration model to quantify each constituent. There are two reasons for this: (1) it is difficult to make samples that vary largely in quantity of each constituent, and (2) other constituents that affect the model may exist. Therefore, a less accurate but more practical method was selected to analyze the FFs of each pixel, cosine similarity. In order to prove the validity of the imaging method, the results were compared to that of the conventional method, i.e., using fluorescence stains to color the different constituents and observing the result with optical microscopy.

As explained in chapter 1, the structure of bread dough as it changes through the mixing process is one of the most intensively studied targets of optical microscopy. However, the two most popular methods, light microscopy and electron microscopy, require the sample to go through harsh preparations such as fluorescence staining, drying, and covering with metal coating. This takes time and requires skill to be performed accurately. Therefore, if visualization of these constituents could be achieved without staining, it would be of great impact in cereal science.

4. 3 Structure of this chapter

This chapter explains the methods and results of two experiments. As shown in Figure 4-1, the flows of the two experiments are roughly the same. In the first experiment, the data was expressed as color images by two methods. In the second experiment, the distributions of gluten, starch and bubbles in dough at different mixing stages were quantified after imaging.

The bread dough samples and imaging methods used in both experiments differ slightly in terms of mixing times and similarity calculation methods, respectively. Therefore, the sample number (samples 1 and 2 for experiment 1 and 2, respectively) will be stated in the text.

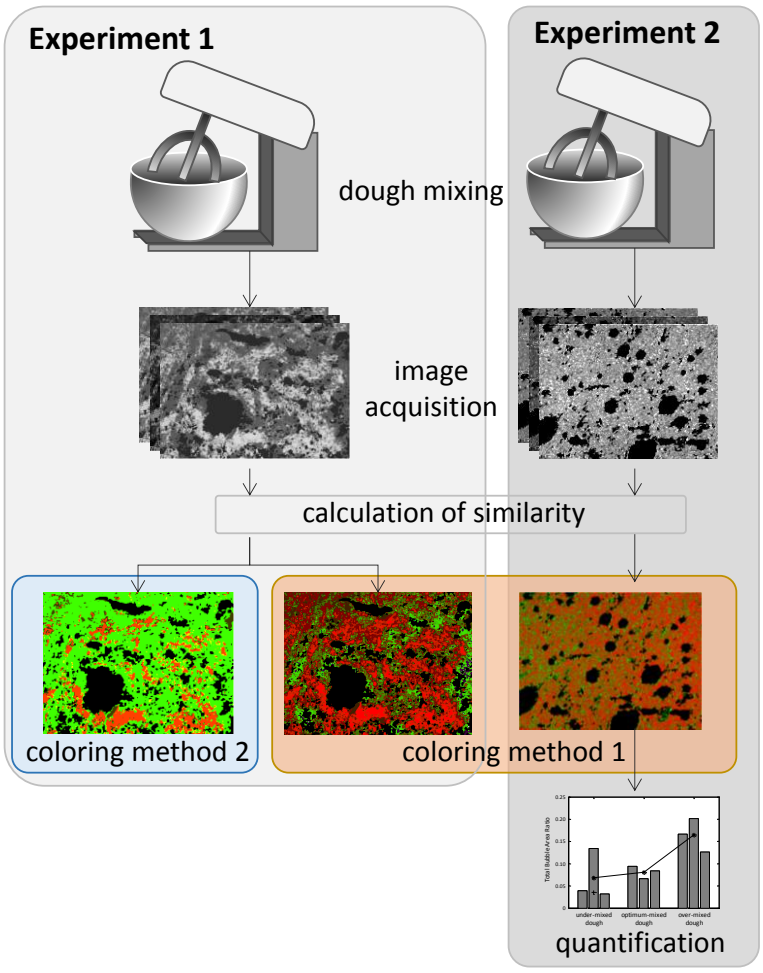

Figure 4-1 Structure of this chapter

4. 4 Materials and methods

4. 4. 1 Sample preparation

For both experiments, two types of samples were prepared: model bread dough of which the distribution of gluten and starch were studied and pure gluten and starch which were extracted from the dough to serve as the reference. Although the standard bread dough contains auxiliary material such as salt, yeast and fat, they were omitted in this model dough for simplification.

To prepare the gluten and starch references in experiment 1, 1400 g of tap water was mixed into 2000 g of flour (Camellia, Nisshin Flour Milling Inc., Tokyo, Japan) and was mixed with a mixer (DTM-30, SK mixer Co., Ltd., Fujimino, Japan) for 2 min at 110 rpm and 6 min at 225 rpm to produce dough. After a 30 min rest in water, the dough was carefully kneaded in water to separate gluten from starch granules and other soluble

substances. When the starch granules were washed away, the remaining gluten aggregated into a highly elastic mass which was then cut into pieces approximately 2 cm square and of 1 cm thickness, frozen and kept at -80 ºC. The aqueous mixture containing starch and other soluble substances was separated into the liquid and sediment parts by centrifugation. The sediment divided into two layers, the upper layer, commonly referred to as the tailing starch, which was a mixture of starch, insoluble proteins and lipids, and the lower layer, referred to as the primary starch, which was composed of pure starch. The primary starch was carefully separated, freeze-dried and kept at -20 ºC. These samples of pure gluten and starch were used as reference data when analyzing the FF of bread dough. Photographs of the fractionation process of dough are shown in Figure 4-2.

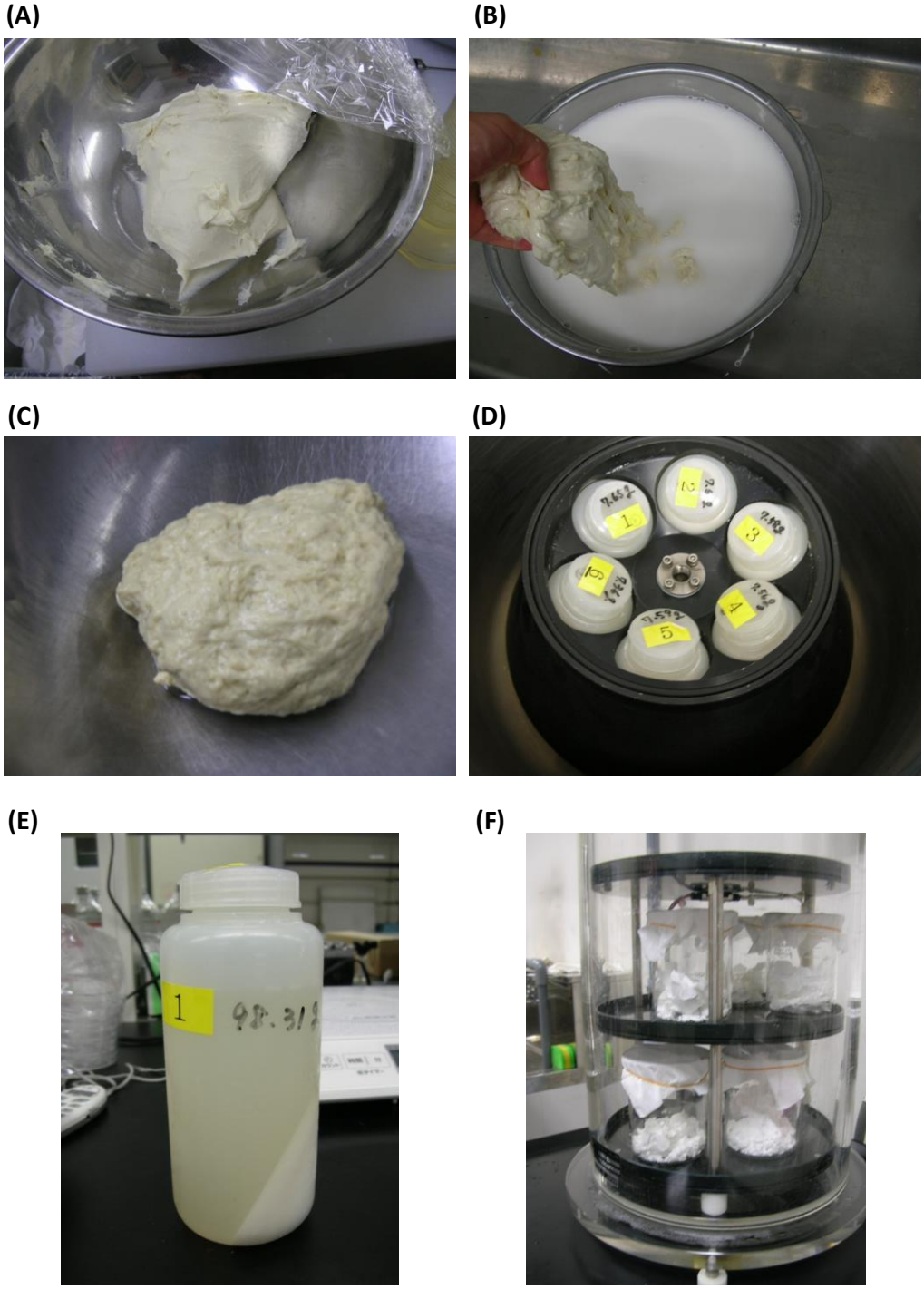

Figure 4-2 Fractionation process.

(A) Optimally mixed dough. (B) The dough being washed in water. The starch is washed away with the water while the gluten remains as an elastic mass. (C) The agglomerated gluten. (D) The plastic bottles set into the rotor. (E) The starch-water mixture after centrifugation, divided into starch and water containing soluble substances. (F) The freeze-dried starch.

Another three batches of dough were prepared in experiment 1 to produce dough in the under-, optimum- and over-mixing stages. The mixing rate and time for each stage are shown in Table 4-1. The mixing times were determined by an experienced baker who watched the actual mixing process. The ingredients and preparation methods followed those for the dough made for the gluten and starch references. The dough was cut into small pieces, frozen and kept at -80 ºC.

Table 4-1 Mixing times for dough at each mixing stage. The mixing speeds for low (L), inter-meditate (IM), mediate (M) and high (H) are 110, 225, 280 and 420 rpm, respectively.

mixing stage	mixing time [min]
under-mixing	L3
optimum-mixing	L3, IM10, M6, H1
over-mixing	L3, IM10, M6, H10

To prepare the gluten and starch references in experiment 2, dough was made by mixing 680 g of tap water into 1000 g of flour and kneading the mixture with a 10 L mixer (SK-10, SK mixer Co., Ltd., Fujimino, Japan) for 1 min at low speed, 3 min at middle speed, and 1 min at high speed. After a 30 min rest in water, the dough was carefully kneaded in water to separate gluten from starch granules and other soluble substances. When the starch granules were washed away, the remaining gluten aggregated into a highly elastic mass which was then cut into pieces approximately 2 cm square and of 1 cm thickness, frozen and kept at -80ºC. The aqueous mixture containing starch and other soluble substances was poured into 500 mL tubes and set into a rotor (R10A3, Hitachi Koki Co., Ltd., Tokyo, Japan) and separated into the liquid and sediment parts by centrifugation. The mixture was centrifuged for 20 min at 7000 rpm with a centrifugal separator (Himac CR21GIII, Hitachi Koki Co., Ltd., Tokyo, Japan) set at 5ºC. The sediment divided into the upper tailing starch and the lower primary starch. The primary starch was carefully separated, freeze-dried with a lyophilizer (Eyela FDU-830, Tokyo Rikakikai Co., Ltd., Tokyo, Japan) and kept at -20ºC.

To make model bread dough for experiment 2, 2040 g of tap water was mixed into 3000 g of flour (Camellia, Nisshin Flour Milling Inc., Tokyo, Japan) and was mixed in a 20 L mixer (HPi-20M, Kanto Kongoki Industrial Co., Ltd., Tokyo, Japan). The dough was mixed for 1 min at low speed (136 rpm) to create dough in the under-mixing

stage, another 1 min at low speed, 4 min at middle speed (248 rpm) and 2 min 30 s at high speed (310 rpm) to create dough in the optimum-mixing stage, and another 7 min at high speed to create dough in the over-mixing stage (Table 4-2). The mixing times were determined by an experienced baker who watched the actual mixing process. All the samples were made from one batch of dough and approximately 100 g of dough was sampled at each stage. The dough sample was cut into small pieces about 2 cm square and of 1 cm thickness and was frozen at -80ºC.

Table 4-2 Mixing times for dough at each mixing stage. The mixing speeds for low (L), mediate (M) and high (H) are 136, 248, and 310 rpm, respectively.

mixing stage	mixing time [min]
under-mixing	L1
optimum-mixing	L2, M4, H2.5
over-mixing	L2, M4, H9.5

The frozen dough and gluten in both experiments were broken into small pieces with a hammer and quickly embedded in a freeze embedding agent (Tissue-Tek O.C.T. compound, Sakura Finetek Japan, Tokyo, Japan) before the sample melted. The sample was frozen at -80 ºC until the O.C.T. compound was completely fixed, transferred to a cryomicrotome (Leica CM1850, Leica Microsystems Japan, Tokyo, Japan) cooled to a temperature of -20 ºC and sliced to make thin sections approximately 5 mm square and of 20 μm thickness. The thin sections were mounted on a glass slide (Matsunami Micro Slide Glass, Matsunami Glass Ind., Ltd., Osaka, Japan) and left to dry completely at room temperature.

The freeze dried starch was mixed with 70% and 80% distilled water for experiments 1 and 2, respectively, to prepare an easily handled paste, and was embedded in O.C.T. compound. The sample was frozen, sliced using a cryomicrotome and dried, following the method for gluten and dough. However, the thin sections of starch were sliced to be of 15 μm thicknesses, which enabled the clear observation of individual starch granules.

4. 4. 2 Measurement of gluten to starch ratio in dough

Three batches of dough were made from 50.00 g of flour (Camellia) and 32.50 g of distilled water. The dough was soaked in distilled water for 2 h to strengthen the connection of gluten. After soaking, the dough was carefully kneaded in water to

separate gluten from starch granules. The retrieved gluten was removed of excess water on the surface and then weighed. The water with the precipitated starch granules were poured into eight centrifuge tubes (50 mL) for each batch of dough and centrifuged for 10 min at 7000 rpm. The water was drained for 30 min and the precipitated starch was weighed. Both gluten and starch were weighed in a wet state.

4. 4. 3 Image acquisition

The samples were set under the FF imaging system and the spatial FF data was acquired. Image acquisition was performed at room temperature. Gluten, starch and dough samples in the three mixing stages were acquired for experiment 1. In experiment 2, three sets of spatial FF data were acquired for dough in each mixing stage, using samples from a different piece of frozen dough each time in order to evaluate the differences in gluten and starch distribution between different parts of the same batch. Two sets of spatial FF data were acquired for both gluten and starch.

The excitation and emission wavelengths used ranged from 260 nm to 320 nm and from 370 nm to 450 nm respectively, at 10 nm intervals. These 7 excitation wavelengths and 9 emission wavelengths were combined to make 63 wavelength conditions.

The exposure time of the camera was set at 1.0, 5.0 or 10 s, depending on the fluorescence intensity of the sample under the specific light condition. The exposure times for each wavelength condition are shown in Table 4-3. The exposure times were fixed throughout all samples.

Table 4-3 Exposure times [s] for each wavelength condition

		Excitation Wavelength (nm)						
		260	270	280	290	300	310	320
		Exposure times [s]						
Emission Wavelength (nm)	370	10.0	10.0	10.0	10.0	10.0	10.0	10.0
	380	1.0	10.0	1.0	1.0	5.0	5.0	5.0
	390	1.0	10.0	1.0	1.0	5.0	5.0	1.0
	400	1.0	10.0	5.0	1.0	5.0	1.0	1.0
	410	5.0	10.0	5.0	5.0	1.0	1.0	1.0
	420	5.0	5.0	5.0	5.0	1.0	1.0	1.0
	430	5.0	5.0	5.0	1.0	1.0	1.0	1.0
	440	5.0	5.0	5.0	1.0	1.0	1.0	1.0
	450	5.0	5.0	1.0	1.0	1.0	1.0	1.0

The set of fluorescence images was taken using 2 × 2 binning. Binning is the combination of multiple (in this case, four) CCD image sensor pixels to improve signal-to-noise-ratio and enhance sensitivity to lower light levels. Figure 4-3 shows an image diagram of 2 × 2 binning. As a result of binning, the size of the images was reduced from 1112 × 1344 pixels to 556 × 672 pixels. The data was stored as a 12-bit image, in which fluorescence intensity was expressed in 4096 levels.

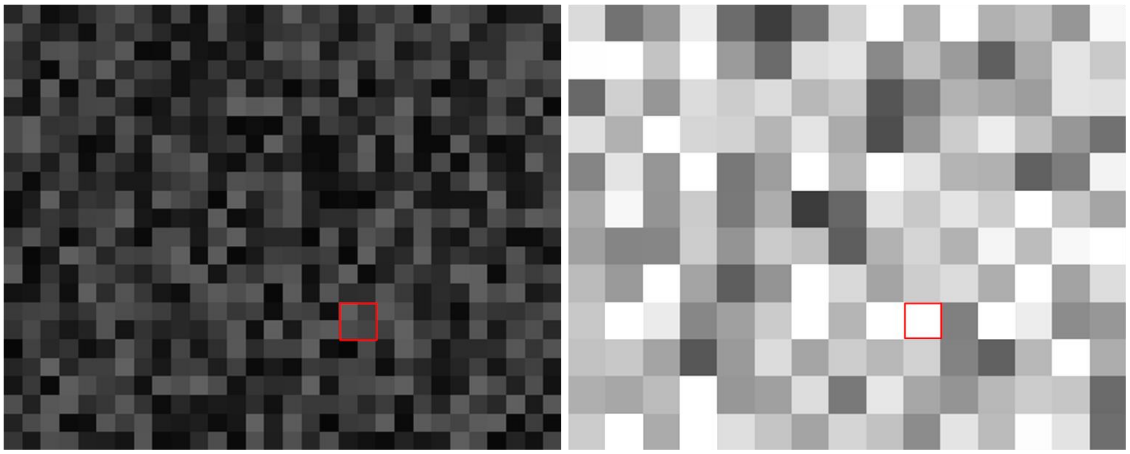

Figure 4-3 Image diagram of 2 x 2 binning
The light intensities of 4 pixels in the original image (left) are summed to make 1 pixel in the binning image (right). The spatial resolution is sacrificed while a brighter image with better S/N ratio is obtained.

The fluorescence images contained dark noise, which is the accumulation of the heat-generated electrons in the sensor. Since the dark noise is highly repeatable as long as the temperature and exposure time do not vary, it is possible to eliminate the noise by subtracting the 'dark image' from the raw data [1, 2]. The dark image was acquired by closing the camera shutter and covering the lens with aluminum foil so that no light enters through the lens. The exposure time was set at 1.0, 5.0 and 10 s to match the exposure time for FF measurement and four images were averaged for each exposure time.

4. 4. 4 Analysis of FF data and image processing

The data processing can be summarized into three steps: position alignment of the FF images, masking the bubble areas, and assignment of a color to each pixel according

to the similarity between the FF of each pixel and that of gluten or starch. The analysis and image processing were carried out using versatile numerical analysis software (MATLAB, The MathWorks, Inc., Massachusetts, USA) and image processing software (ImagePro, Media Cybernetics, Inc., Maryland, USA).

The 63 fluorescence images acquired using the FF imaging system needed to be spatially aligned so that the corresponding pixels in each image all matched a single point in the sample. Fine adjustments were needed, as the measuring device tended to move when the filters were changed, resulting in images where a pixel in one image did not necessarily match the corresponding one in another.

In experiment 1, this process was performed by selecting the same three points on each fluorescence image and using the image registration tools in MATLAB to align the images on the basis of the selected points. To reduce computational load, a region of 256 × 336 pixels was selected for further analysis.

In experiment 2, position alignment was done following the method proposed by Gonzalez, Woodset al. [3]. As in Figure 4-4, the normalized cross-correlation between the base image (the image acquired in wavelengths 260 and 370 nm for excitation and emission) and the input images (all the other images acquired in different wavelength conditions) was calculated while shifting the "template", a part of the input image (41 × 41 pixels), in *x*- and *y*-directions. The point where the normalized cross-correlation showed the maximum value would be the position where the two images “most matched”. The normalized cross-correlation is calculated by equation (1).

$$\gamma(u,v) = \frac{\sum_{x,y}\left[b(x,y)-\overline{b_{u,v}}\right]\left[t(x-u,y-v)-\bar{t}\right]}{\left\{\sum_{x,y}\left[b(x,y)-\overline{b_{u,v}}\right]^2\sum_{x,y}\left[t(x-u,y-v)-\bar{t}\right]^2\right\}^{0.5}} \quad \cdots (1)$$

$\gamma(u, v)$ is the normalized cross-correlation which is a function of the position of the template on the base image. b is the base image, t is the template and $\overline{b_{u,v}}$ is the mean of b in the region under the template.

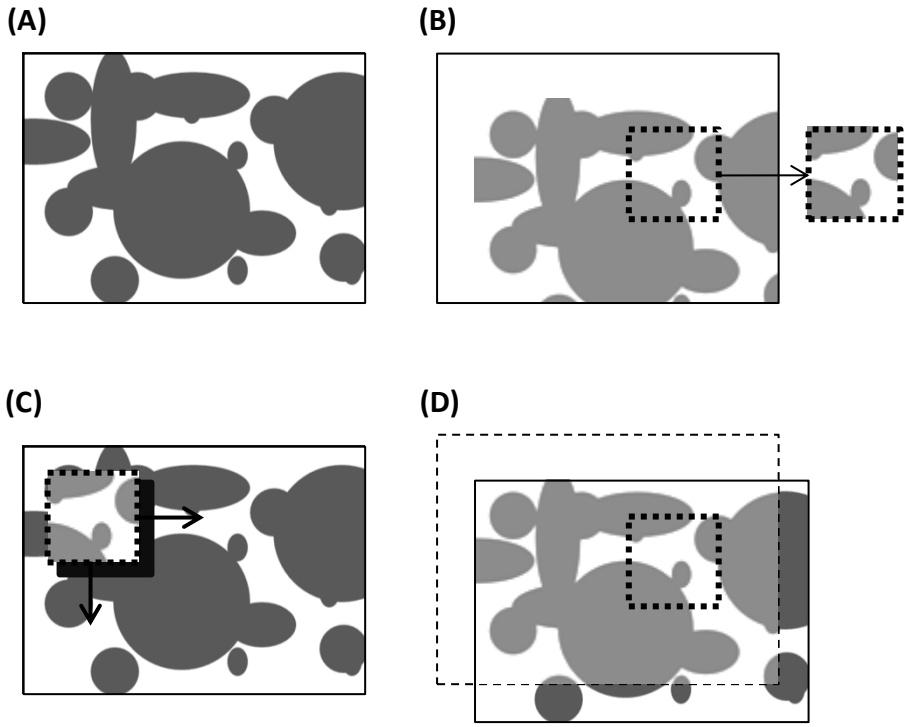

Figure 4-4 Image diagram of position alignment process
(A) base image and (B) input image and template (broken line). (C) The template is superimposed on the base image and shifted in x- and y-directions while calculating the normalized cross correlation value between the base image and the template. (D) The position where the template best matches the base image (broken line) is where the normalized cross-correlation shows the maximum value and the position of the input image (dotted line) is determined accordingly.

After using this method to roughly align each image, an image registration function in MATLAB was used to tune the position so that the image alignment would be accurate to one tenth of a pixel. The fringe parts that were out of view in some of the fluorescence images were deleted, leaving a rectangular area of 478 × 636 pixels for image analysis.

The samples contained small air bubbles, which appeared as holes when the samples were sliced. These areas showed a weak fluorescence response and the data contained noise that was thought to lead to a decrease in the precision of analysis if included in the data. Therefore, a masking process based on linear discrimination analysis was performed prior to FF data analysis to leave out the pixels in the bubble area from the calculations. The same method was used in experiments 1 and 2. Since the bubble areas show weaker fluorescence than the sample areas, the absolute value or the

Euclidean norm of the FF vector was used as the variable for discrimination. The absolute value of the FF vector is defined by equation (2).

$$\begin{aligned} \text{abs} &= |X| \\ &= \sqrt{(x_1)^2 + (x_2)^2 + \cdots + (x_n)^2} \end{aligned} \qquad \ldots (2)$$

Areas that were clearly inside the bubble areas or inside the sample areas were selected from the original fluorescence image to create the training set. The training set is a set of data of known class from which the discriminant function is calculated. Care was taken to select pixels that were clearly inside the bubble areas or inside the sample areas, leaving out the borders to be classified using the discriminant function. Every pixel of the image, including the pixels used to make up the training set, was classified using the discriminant function into the "bubble area" or "sample area". A diagram of this masking process is shown in Figure 4-5.

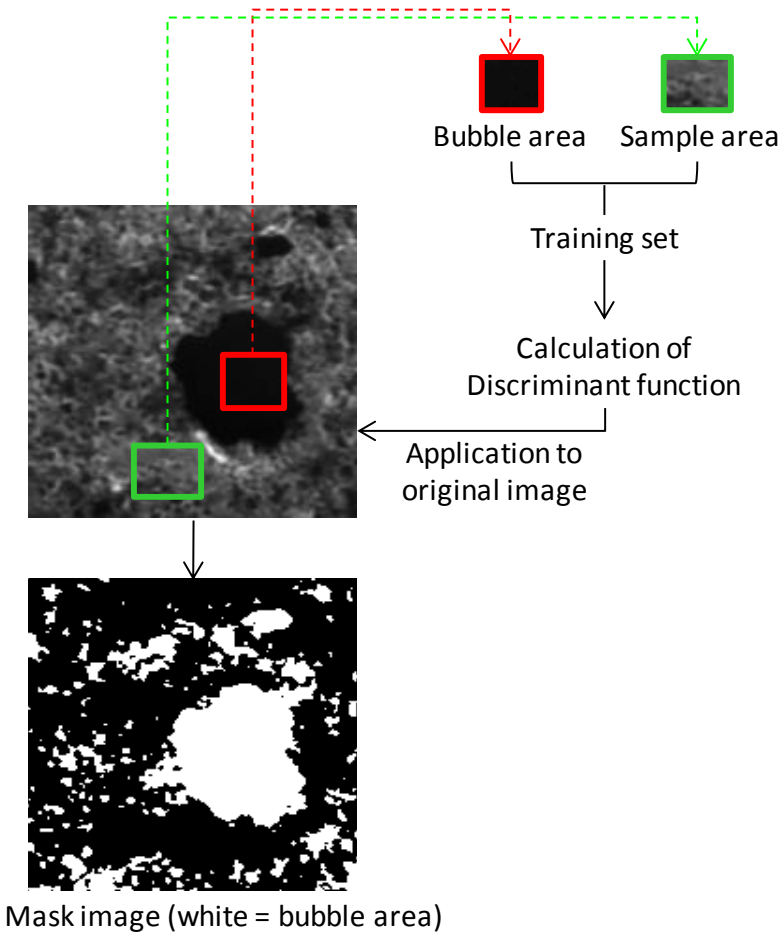

Figure 4-5 Bubble masking process. The red and green squares are the areas which

clearly represent bubbles and dough areas, respectively. These pixels were used to create the training set from which the discriminant function was calculated.

The acquired set of fluorescence images was a four-dimensional data, with two axes assigned to the fluorescence spectrum (excitation and emission wavelength) and the other two assigned to the special plane (the x-and y-position). As shown in Figure 4-6, this data matrix of dimension 7×9×256×336 was "unfolded" by combining the two spectral modes and the two spatial modes so that a matrix of dimension 63 wavelengths×86016 pixels was obtained.

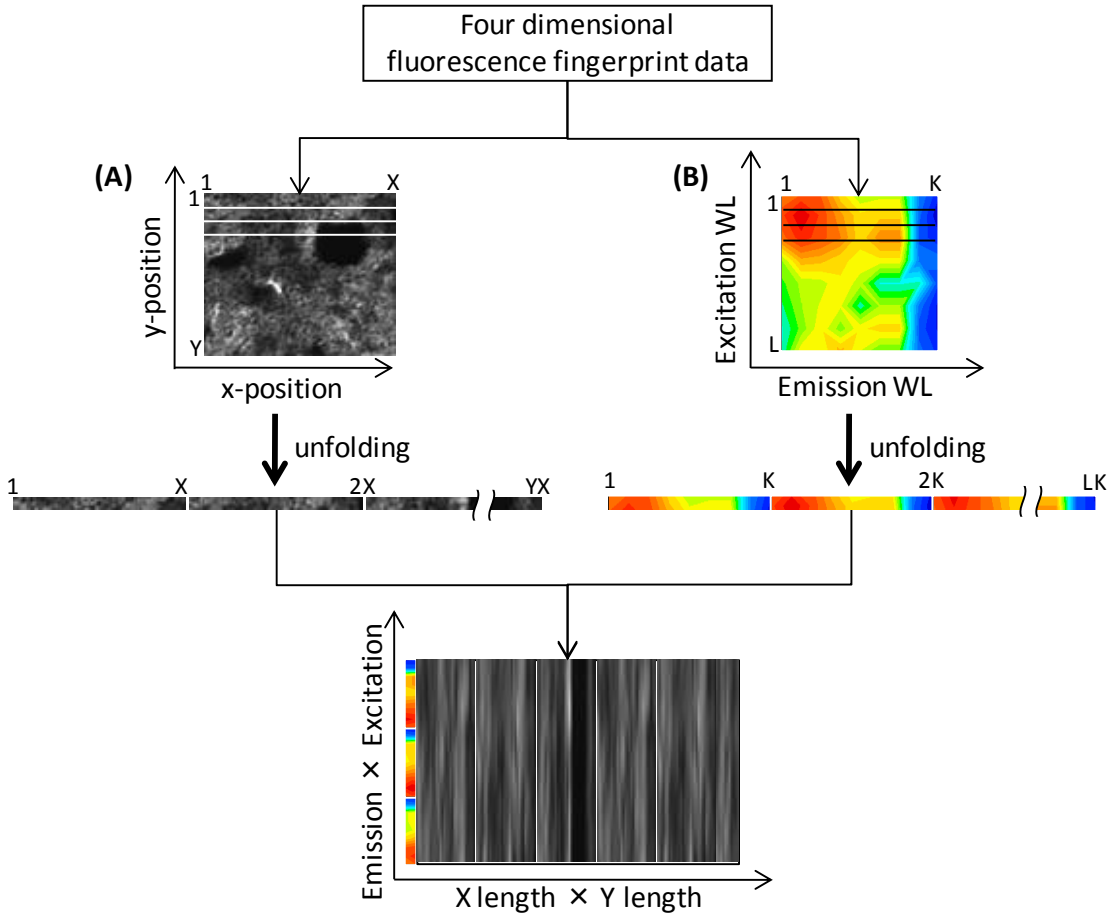

Figure 4-6 Unfolding process of fluorescence fingerprint data. The spatial data (A), initially expressed as a X×Y matrix, is unfolded into a 1×XY vector. Similarly, the spectral data (B) is unfolded into a 1×KL vector when the number of emission and excitation wavelengths is K and L, respectively.

The objective of the data analysis was to extract information on the proportion of gluten or starch at each point of the dough sample, because monitoring the areas showing a high proportion of gluten or starch would result in the visualization of the distributions of these components. The hypothesis was that the degree of similarity between the FF pattern of a particular area and the FF of pure gluten would correlate with the actual proportion of gluten in the area. An FF pattern similar to that of pure gluten would suggest a high proportion of gluten and likewise of starch.

In experiment 1, a simple index explaining the similarity of two multidimensional vectors, i.e., the value of cosine similarity, was introduced to measure the similarity between the FF of each pixel in the dough sample and the FF of pure gluten or starch. The cosine similarity of two vectors is defined by equation (3).

$$\begin{aligned} &\text{similarity} = \cos\theta = \mathrm{X}\cdot\mathrm{Y}/(|\mathrm{X}| * |\mathrm{Y}|) \\ &\mathrm{X}\cdot\mathrm{Y} = x_1 * y_1 + x_2 * y_2 + \cdots + x_n * y_n \\ &\mathrm{X} = [x_1, x_2, \ldots, x_n], \mathrm{Y} = [y_1, y_2, \ldots, y_n] \end{aligned} \qquad \ldots (3)$$

The variables x_1, x_2,…x_n and y_1, y_2,…y_n are the fluorescence intensities of the sample and the target constituent, respectively, under consecutive wavelength conditions ($n = 3$). The target constituent in this case is gluten or starch. The cosine similarity takes values between -1 (exactly opposite) and 1 (exactly the same), with 0 indicating independence. A large value of cosine similarity between the FF vector of a pixel and the FF of pure gluten would indicate the high ratio of gluten in the area corresponding to the pixel and likewise of starch.

The value of cosine similarity was calculated between the FF vector of each pixel in the dough sample and the average FF of gluten and starch. The average FF of gluten and starch, defined by the average fluorescence intensity of all the pixels in each sample excluding pixels in the bubble area were used for the calculations, since the gluten and starch were not completely homogeneous.

After the cosine similarity between the FF of each pixel of the sample images and that of pure gluten or starch was calculated, the cosine values were converted into color indices through a color scale, and a pseudo color image was constructed. The calculated values of cosine similarity to gluten and starch were converted to shades of red and green, respectively, through a color axis. The color axis for the value of cosine similarity to gluten consisted of colors with consecutive values in the red channel of the RGB color coordinate system, with the green and blue values set to 0. The color axis for the cosine similarity to starch had consecutive values in the green channel, with red and

blue values set to 0. The maximum and minimum values of cosine similarity corresponding to the range of the color axes were set so as to optimize the contrast between the pixels of the dough image.

A color was assigned to every pixel in the dough, gluten and starch images according to the calculated value of cosine similarity and the corresponding color axis. The images in shades of red and green representing the values of cosine similarity to gluten and starch, respectively, were composited to obtain a pseudo color image. Finally, the pixels classified to be in the bubble area were masked in black.

In experiment 2, the spectral angular mapper (SAM) algorithm which uses the "angle" value between two vectors as an index of similarity was applied to the FF data. The angle between two vectors is defined by the arccosine value of the cosine similarity, and takes values between 0 (exactly the same) and $-\pi$ (exactly the opposite). The angle value was used in this study instead of the cosine similarity value used in chapter 4, because the angle value was more sensitive than the cosine value in ranges where the sample vector was similar to the reference vector, i.e. when the angle was close to 0 degrees.

The angular values were converted into color indices through a color scale, and a pseudo color image was constructed. The angular value to gluten was converted into shades of red while the angular value to starch was converted into shades of green. In this way, a color was assigned to every pixel in the dough, gluten and starch images according to the calculated angular value and the corresponding color axis. The images showing the angular values to gluten and starch were composited to obtain a pseudo color image. Finally, the pixels classified to be in the bubble area were masked in black.

4. 4. 5 Creating the stained image

To validate the pseudo color image obtained by FF imaging, the exact same area of the same dough sample was stained with fluorescence dyes for gluten and starch immediately after spatial FF data acquisition. This procedure was performed in experiment 1 only. A mixture of rhodamine B and fluorescein isothiocyanate (FITC) (0.1% and 1.0% w/v, respectively) in dimethylformamide was used for the noncovalent labeling of gluten and starch, respectively. The staining process was carried out in a dark room to prevent color degradation, and the staining time was 40 min. The stained dough sample was washed with distilled water and sealed with glycerol (Kishida Chemical Co., Ltd., Osaka, Japan) prior to the observation. The staining methods and conditions conformed to those used in previous studies using these two fluorescence stains to visualize gluten and starch [4, 5, 6, 7, 8, 9].

The stained dough was observed using fluorescence microscopy (BZ-8100, KEYENCE Japan) at excitation/emission wavelengths 470 nm/535 nm for FITC and 540 nm/605 nm for rhodamine B. The images were loaded into analysis software, the contrast was enhanced and the two images were composited to obtain a stained image.

4. 4. 6 Quantification of the distributions of gluten and starch

Quantification calculations were performed in experiment 2 only. In order to evaluate and quantify the distribution of gluten and starch and its differences between each mixing stage, a parameter concerning the evenness of the distribution was extracted. This parameter was calculated with the following algorithm. First, each image was divided into squares whose length and width was k pixels (k = 1, 2,…) and the ratio between the sum of angular value to gluten and starch was calculated for each square. The ratio for the m th square was calculated with equation (4).

$$\mathrm{ratio}_m = \frac{\sum_{i=1}^{k^2} \theta_{\mathrm{m}i_{\mathrm{glu}}}}{\sum_{i=1}^{k^2} \theta_{mi_{\mathrm{str}}}} \qquad \dots (4)$$

θ_{mi_glu} and $\theta_{mi_\mathrm{glu}}$are the angular values between the FF of the i th pixel (i = 1, 2,…, k^2) inside the m th square and the FF of starch and gluten, respectively. Secondly, the standard deviation of ratio_m (m = 1, 2,…) was calculated. As shown in Figure 4-7, in an image where the distribution of gluten and starch is uneven (A), the ratio between gluten and starch varies within each square, i.e., the standard deviation of ratio_m shows a large value. Conversely, if the distribution of gluten and starch is fairly even (B), the standard deviation of ratio_m becomes smaller. As the size of each square becomes larger (k takes a larger value), the standard deviation should become smaller.

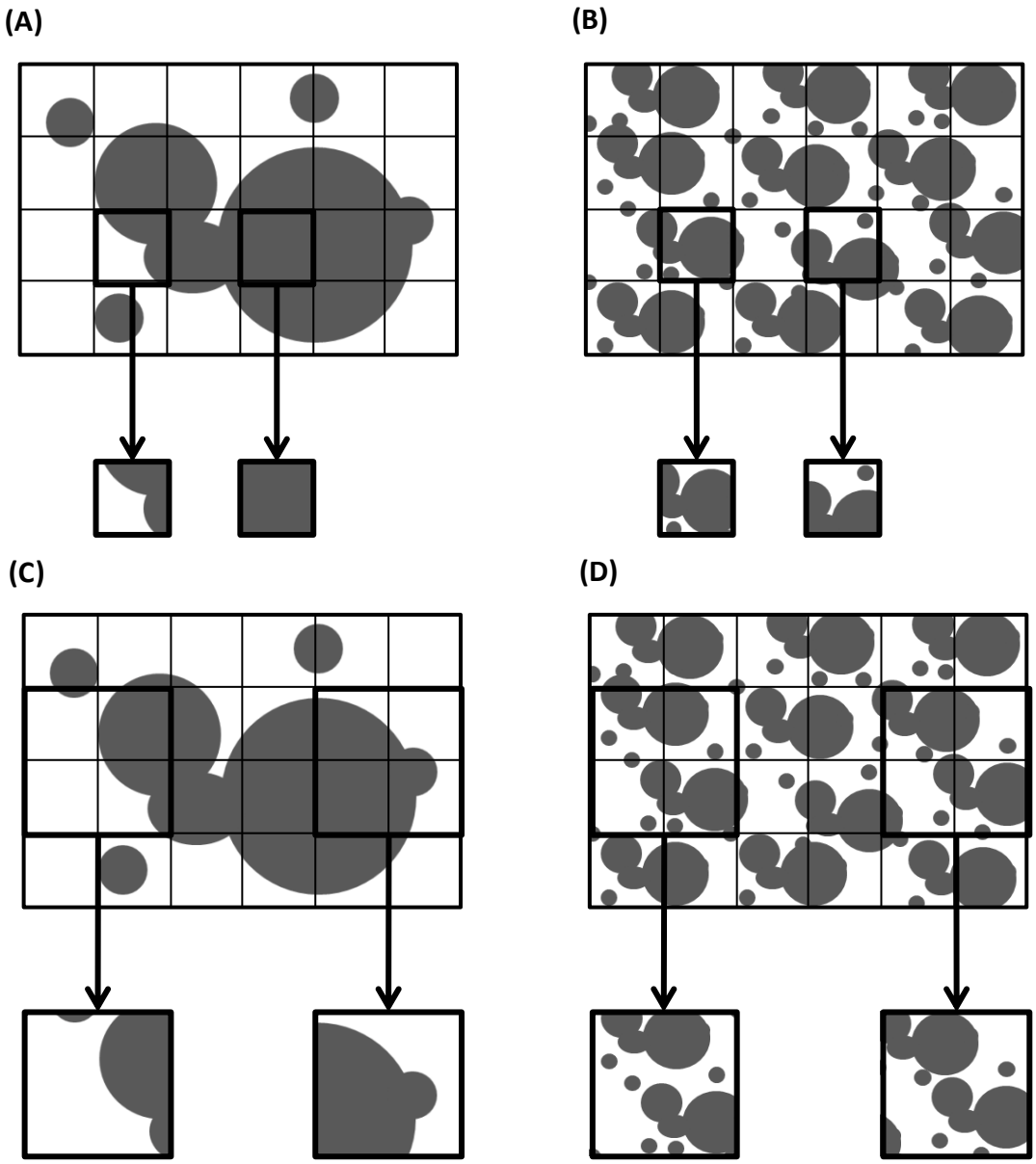

Figure 4-7 Diagram explaining the evenness of gluten and starch distributions

4. 4. 7 Quantification of the distribution of bubbles

The properties of the bubble areas were evaluated by the total bubble area, the distribution of the area of each individual bubble and the eccentricity of the shape of each bubble.

To look into the properties of individual bubbles, a function in MATLAB was used to perform "connected-component labeling", a process of labeling connected components in an image. Two pixels were defined to be "connected" if their edges

touched, meaning they were connected along the horizontal or vertical direction, but not if they were connected along the diagonal direction (Figure 4-8). By examining the number of connected components detected and several parameters of these connected components, the difference between the three mixing stages was shown.

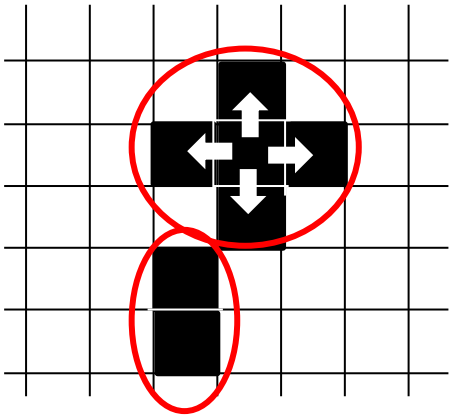

Figure 4-8 Image diagram of a connected-component
The red ellipses are the connected components.

Furthermore, the geometric properties of the bubbles were considered by calculating the ratio of the major axis length to its minor axis length. This value was calculated by defining an ellipse with the same second-moments as the region. Ellipses whose ratio of major axis length to minor axis length range from 10:1 to 10:9 are shown in Figure 4-9.

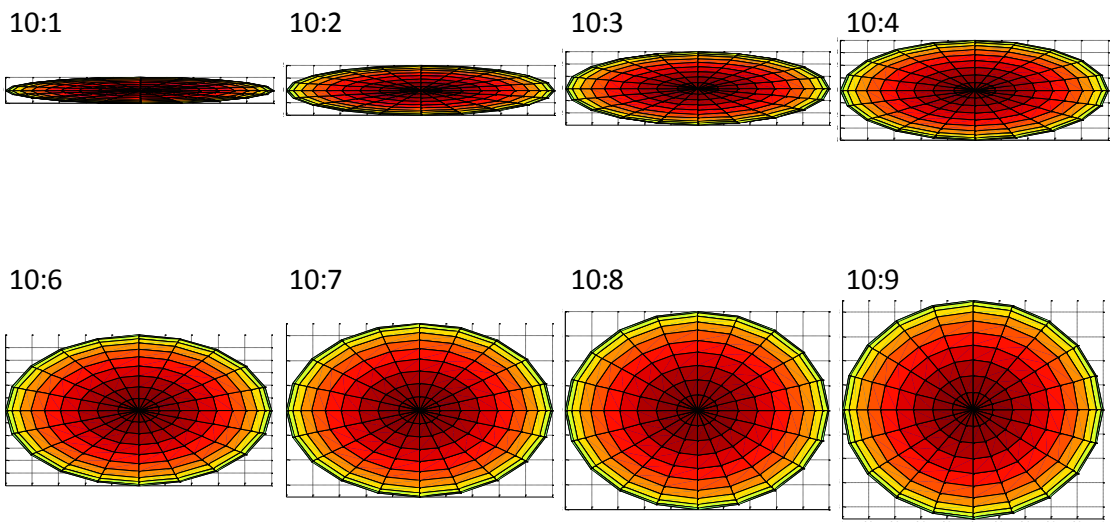

Figure 4-9 Ellipses with different ratios of major axis and minor axis

4. 5 Results and discussion

4. 5. 1 Ratio of gluten to starch in dough

The average ratios of gluten to starch were 20.52% and 79.48%, respectively. The reproducibility between the three batches of dough was good, the standard deviation being 0.35%. These values agree with the literature values [10].

The water contents of the retrieved gluten and starch were 64.8% and 50.7%, respectively. The standard deviations were 0.64% and 1.0% for gluten (three samples) and starch (five samples), respectively. Since gluten and starch absorb different amounts of water [11], the ratio of gluten to starch would be different between wet and dry states. In this study, the visualized dough sample existed in a wet state. Therefore, the retrieved gluten and starch were measured without force-drying the samples.

4. 5. 2 Pseudo color images

Sections 4.5.2 to 4.5.6 show the results for experiment 1. Figure 4-10 shows the pseudo color images of gluten, under-mixed dough and starch, colored according to the cosine similarity. Naturally, the pixels in the gluten sample showed a high similarity to the average FF of gluten and a low similarity to that of starch, and the pixels in the starch sample showed a high similarity to the average FF of starch and a low similarity to that of gluten. Regarding the dough sample, areas that showed high gluten and starch contents were highly complementary.

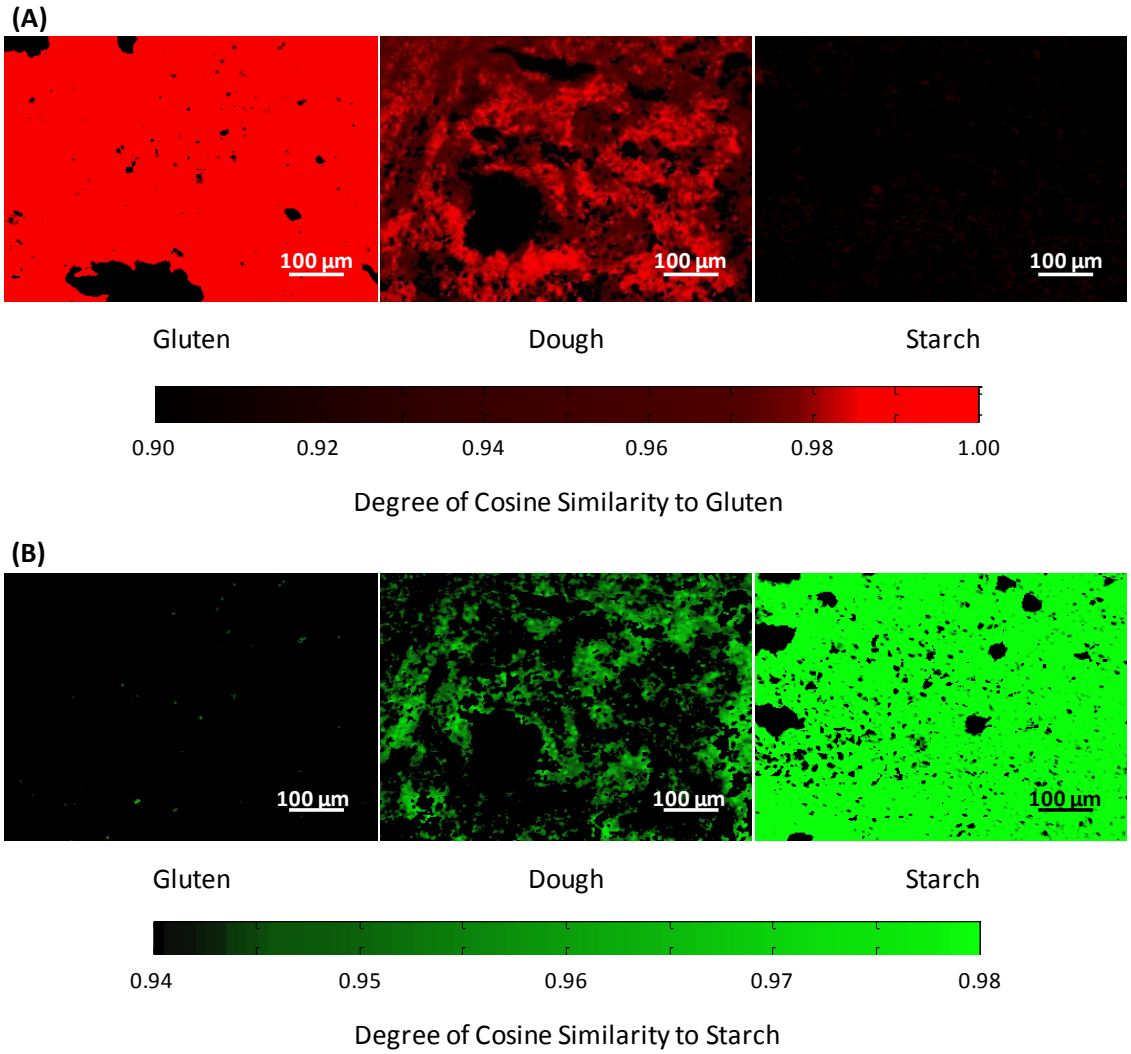

Figure 4-10 Pseudo color images of gluten, dough and starch.
Images of gluten, dough and starch are colored according to the value of cosine similarity between the FF of each pixel and the average FFs of gluten (A) and starch (B). The color axis follows the colors of the fluorescent images taken at wavelengths of 605 [nm] and 535 [nm] for gluten and starch, respectively. The bright red areas in the dough image (A) and the bright green areas in the dough image (B) suggest the existence of gluten and starch, respectively.

4. 5. 3 Comparison with the stained image

Figure 4-11 shows a pseudo color FF image and a stained image of the same dough sample. The pseudo color FF images based on the cosine similarity to those of

gluten (A) and starch (B) showed similar patterns to the fluorescence images stained with a rhodamine B (C) and FITC (D), respectively. The composite image in pseudo color (E) showed clear correspondence with the composite stained image (F), thereby validating the applicability of the FF imaging method.

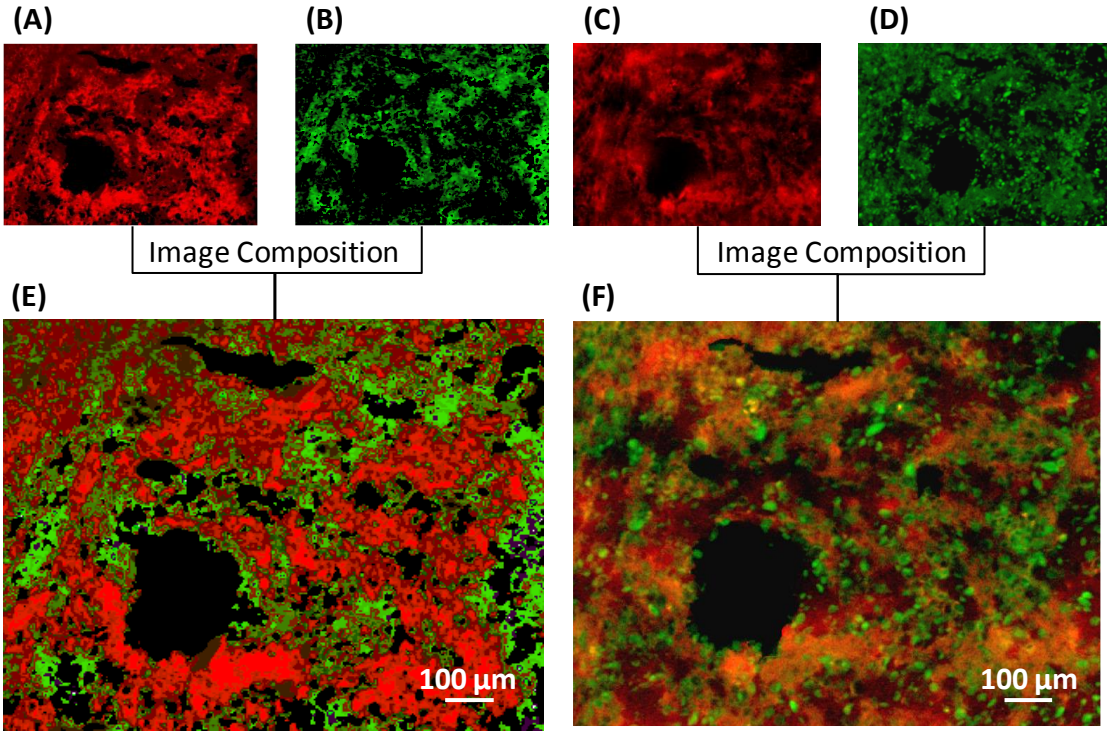

Figure 4-11 Pseudo color image (E) and stained image (F) of dough at under-mixing stage

(A) and (B) are the images colored according to the value of cosine similarity between the FF of each pixel and those of gluten and starch, respectively. (A) and (B) were composited, and the air hole areas were masked to produce (E). (C) and (D) are images taken after staining the sample with a liquid mixture of rhodamine B and FITC, which color gluten and starch, respectively. (C) was taken at 605 [nm] and shows the areas stained with rhodamine B, while (D) was taken at 535 [nm] and show the areas stained with FITC. (C) and (D) were composited to produce (F). Similar patterns can be seen in (E) and (F), validating the applicability of the FF imaging method.

Further studies were carried out to compare the pseudo color image obtained from the spatial FF data and the stained image. For the stained image, rhodamine B and FITC were used to visualize the distributions of gluten and starch, respectively. However, some areas stained with FITC overlapped with the areas stained with rhodamine B. On

the other hand, in the FF pseudo color image, the areas with a high value of cosine similarity to gluten and starch seemed highly complementary.

To confirm this observation, the luminance of pixels in the dough stained with FITC was plotted against the luminance of the same pixels stained with rhodamine B. Similarly, the cosine similarity values to starch were plotted against the similarity values to gluten. (A) and (B) in Figure 4-12 show the difference in the distribution pattern between the stained image and the FF pseudo color image in a scatter plot of 500 randomly selected pixels. The pixels in the stained image are evenly distributed in the coordinate plane, whereas the pixels in the FF pseudo color image show a tendency to be plotted along a down-ward sloping curve. This trend was more clearly observed when the values of fluorescence intensity and cosine similarity were standardized and shown in a new coordination system where the point of origin was set to the mean value (Figure 4-13). The top-right quadrant was numbered as the first quadrant, the top-left as the second, and so on in anti-clockwise order. Pixels falling in the second or fourth quadrant would mean that the fluorescence or cosine similarity values were high for gluten and low for starch or vice-versa. In short, if there were many pixels falling in the second or fourth quadrants, it would mean that the distributions of gluten and starch were complementary. As can be seen from Figure 4-13, the pixels in the stained image are evenly distributed in the coordinate plane, whereas the pixels in the FF pseudo color image are mainly distributed in the second or fourth quadrant. The same analysis was performed using all the pixels in the stained and cosine similarity images. The numbers of pixels falling in the first to fourth quadrant are shown in Figure 4-14. The data show that in the FF pseudo color image, a pixel showing a high value of similarity to gluten tends to show a low value of similarity to starch, and vice versa. However, in the stained image, there are many pixels with high luminance for both FITC and rhodamine B, supporting the observation that the areas stained with FITC overlap with the areas stained with rhodamine B.

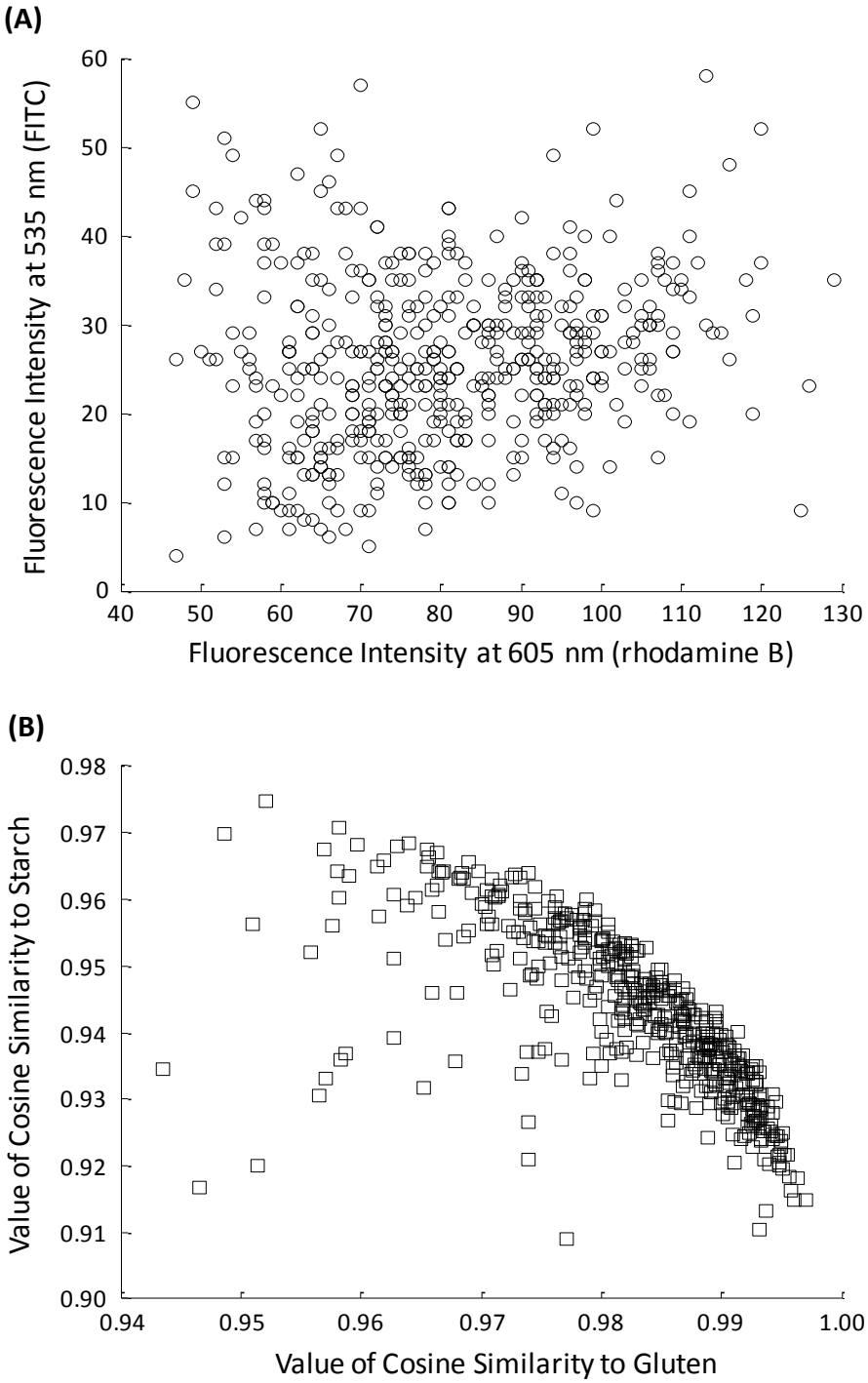

Figure 4-12 Analysis of the degree of complementation between gluten and starch in under-mixed dough

(A) Fluorescence intensities of 500 randomly picked pixels at emission wavelengths of 535 [nm] for FITC and 605 [nm] for rhodamine B plotted against each other. (B) Value of cosine similarity to starch plotted against the value of cosine similarity to gluten for 500 randomly picked pixels.

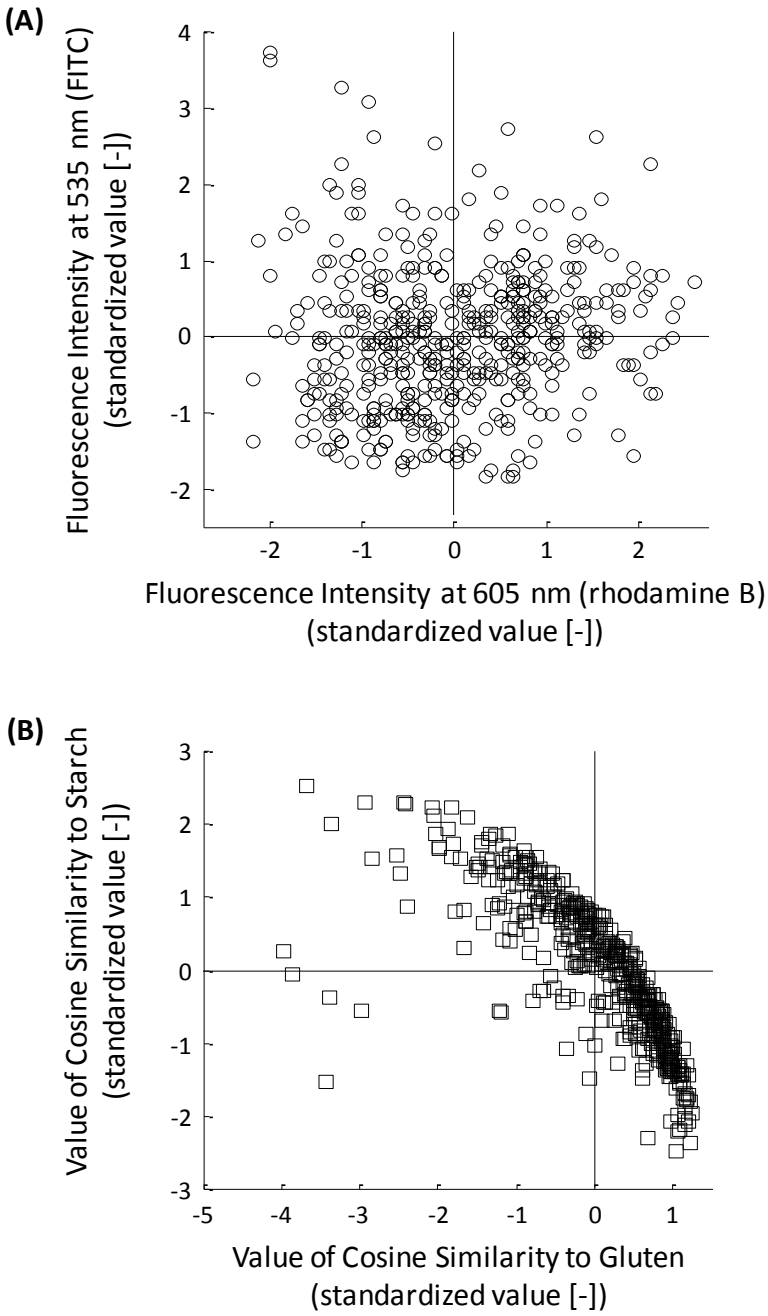

Figure 4-13 Graphs shown in Figure 4-12 with standardized x- and y-axes

The coordinate space was divided into the first to fourth "quadrant" by the mean value.

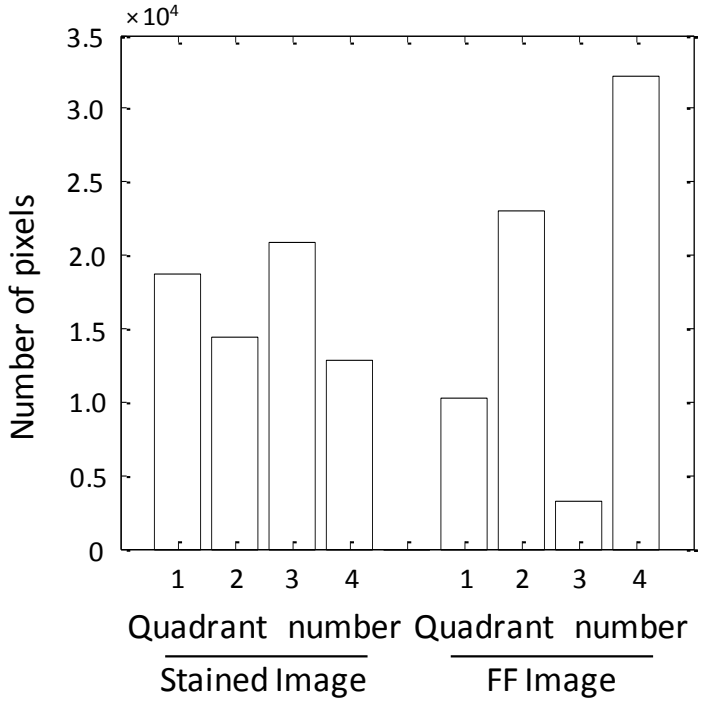

Figure 4-14 Number of pixels falling in each quadrant

The pixels in the stained image are evenly plotted while the pixels in the FF image are grouped in the second and fourth quadrant.

FITC itself has a strong reactive potential with the amino group, and rhodamine B can stain starch in the absence of proteins [9]. It seems that the optimal balance of concentration between rhodamine B and FITC, in which the two stains color gluten and starch selectively is difficult to achieve. It is natural to assume that gluten and starch are distributed separately in the actual dough, so this suggests that the FF pseudo color image more closely represents the actual condition.

4. 5. 4 Pseudo color images of dough in three mixing stages

Figure 4-15 shows the pseudo color FF images of dough in the under-mixing stage (A), optimum-mixing stage (B) and over-mixing stage (C). The agglomerated gluten which could be observed in the under-mixing stage broke up slightly in the optimum-mixing stage. However, the difference was more distinct between the optimum- and over-mixing stages as the agglomerated gluten broke up completely and formed a homogeneous structure with starch. The dough images in each mixing stage were in agreement with the findings of other researchers [7, 12, 13, 14, 15]. The significant change in the structure of gluten between the optimum- and over-mixing stages also corresponded to observations by Amend and Belitz [12].

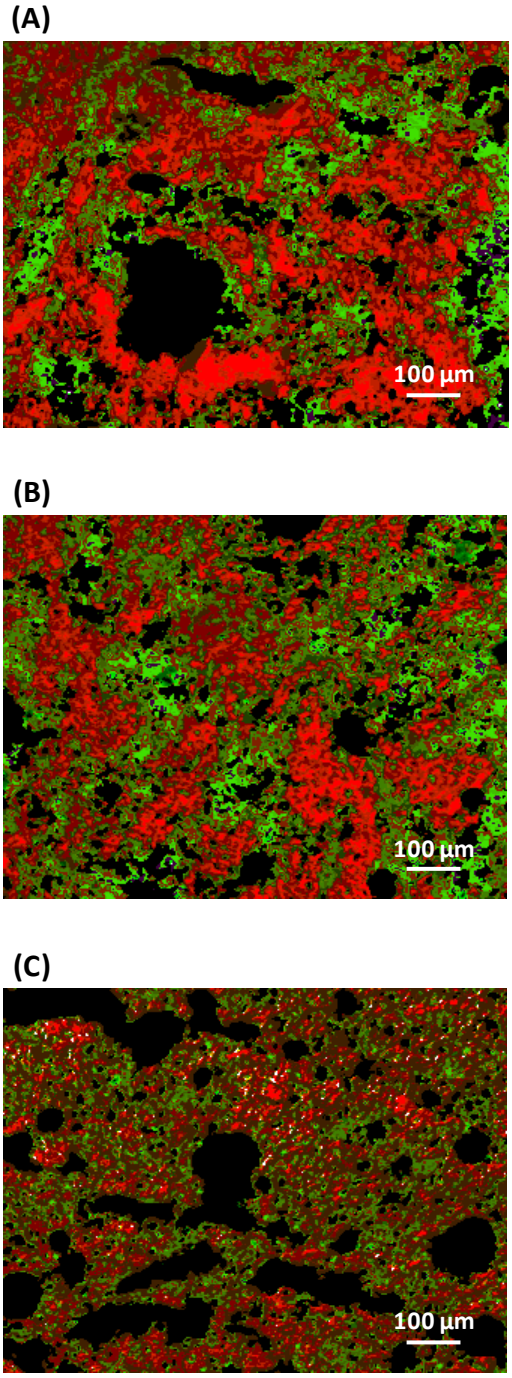

Figure 4-15 Pseudo color images of dough in under-mixing (A), optimum-mixing (B) and over-mixing (C) stages

For each image, two images colored according to the value of cosine similarity between the FF of each pixel and that of gluten or starch were composited. Bright red and green areas are the pixels showing high values of similarity to gluten and starch, respectively, and the black areas are air holes.

As shown in (A) to (F) in Figure 4-16, the values of cosine similarity to gluten and starch changed between the optimum-mixing stage and the over-mixing stage and became much lower in the over-mixing stage. The cosine similarity range assigned to the color axes was altered to optimize the contrast in each image, because using the same range for all three images would result in flattened out images, where fine distributions would be indistinguishable. Therefore, the actual cosine similarity values of the red and green pixels in the over-mixed dough are well under those of the same colored pixels in the optimally mixed dough.

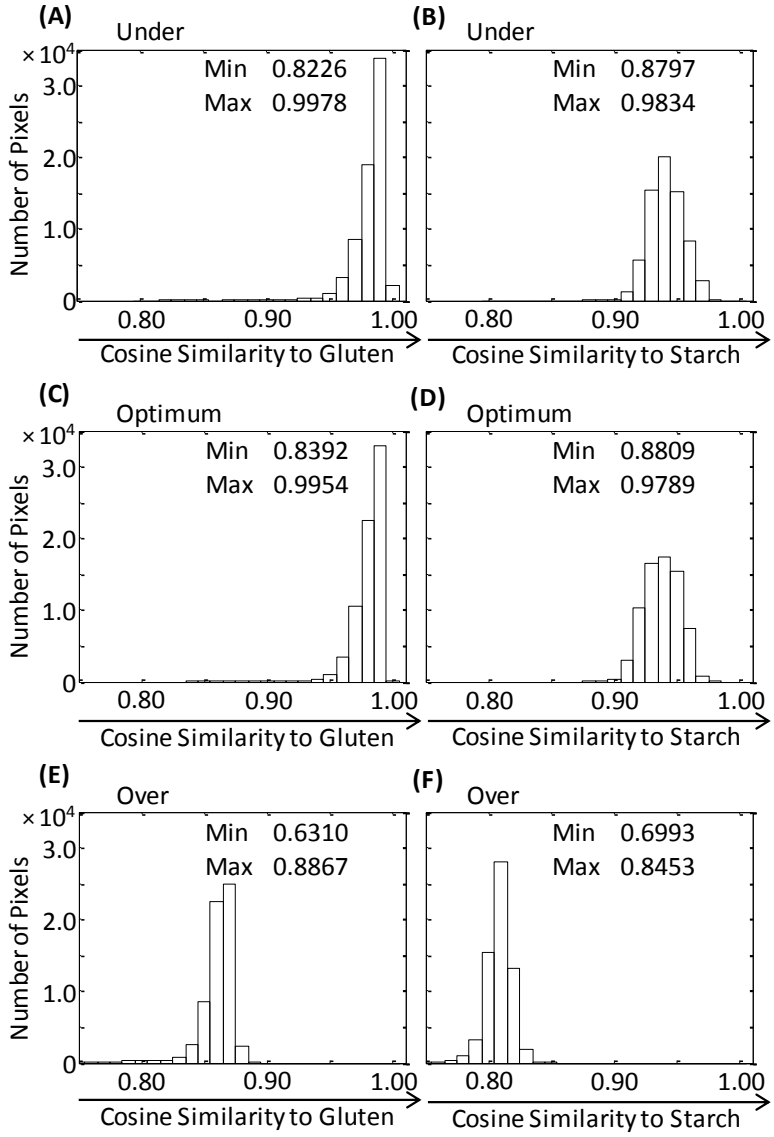

Figure 4-16 Histograms of values of cosine similarity

(A) Cosine similarity between under-mixed dough and gluten. (B) Under-mixed dough and starch. (C) Optimally-mixed dough and gluten. (D) Optimally-mixed dough and

starch. (E) Over-mixed dough and gluten. (F) Over-mixed dough and starch. The distributions are shown with center values ranging from 0.75 to 1.00 at 0.01 intervals.

The adjustment of cosine similarity range assigned to the color axes is convenient to understand the distribution of constituents qualitatively, but introduces subjectivity into the imaging method because there is no strict rule regarding how to match values of cosine similarity to a color. Therefore, another method of assigning colors to each pixel was formulated, and will be explained in the next section.

4. 5. 5 Visualization of distributions of gluten and starch with consideration of gluten to starch ratio

The value of cosine similarity between the FF of a pixel in the dough sample and the FF of gluten (or starch) can be interpreted as the possibility of gluten (or starch) actually existing in the area. This means that the larger the value of cosine similarity, the higher the possibility of existence.

Figure 4-17 shows the cosine similarity image of dough in the under-mixing stage, and the histogram of cosine similarity values. Considering the ratio of gluten to starch obtained from the fractionation experiment (20.52% to 79.48%), 20.52% of pixels with a higher value of cosine similarity to gluten were labeled as “gluten” and the rest, “non-gluten”. Similarly, 79.48% of pixels with a higher value of cosine similarity to starch were labeled as “starch” and the rest, “non-starch”. The “gluten” and “non-gluten” pixels were colored in red and dark red, respectively. The “starch” and “non-starch” pixels were colored in light and dark green, respectively.

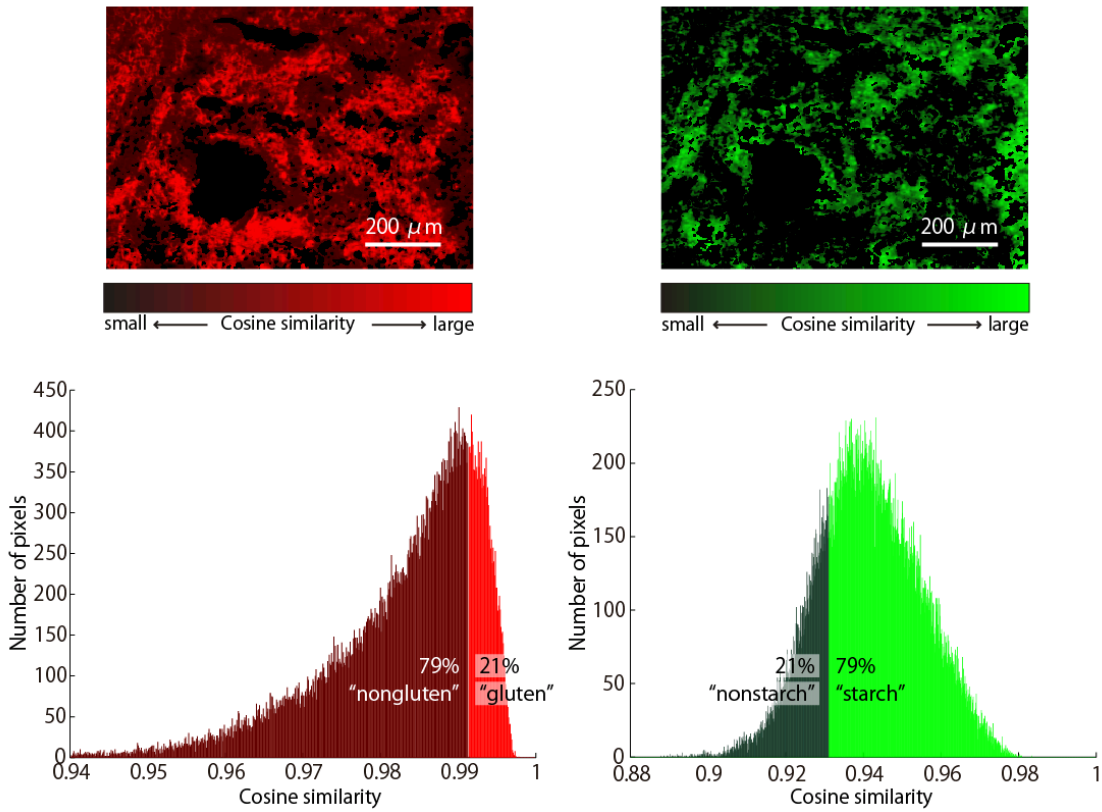

Figure 4-17 Cosine similarity images of dough in the under-mixing stage, and histograms of cosine similarity values. The red and green images show cosine similarity values to gluten and starch, respectively. By considering the gluten to starch ratio of the dough, pixels were divided into "gluten" or "non-gluten", and "starch" and "non-starch".

For each pixel, there are four possible combinations, as can be seen in Figure 4-18: "non-gluten" and "non-starch", "non-gluten" and "starch", "gluten" and "non-starch", and "gluten" and "starch". The colors chosen for each combination are shown in Figure 4-18. These were determined by assigning channels R and G of the RGB color coordinate system to gluten and starch, respectively, and setting "gluten" or "starch" to 255, and "non-gluten" or "non-starch" to 64 (0.25*255). The value of 0 was saved for bubble areas. Channel B was set to 0.

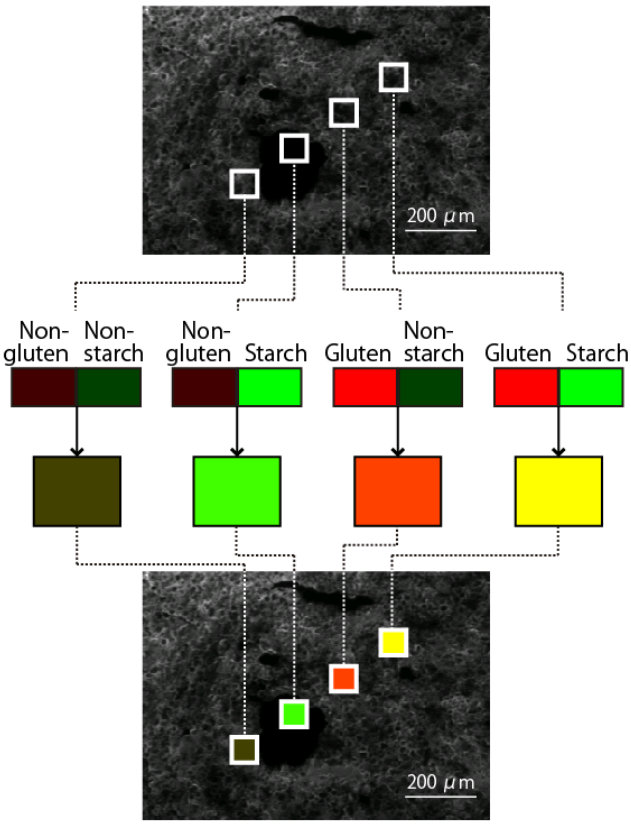

Figure 4-18 Combinations of “gluten” or “non-gluten”, and “starch” or “non-starch”, and the resulting colors. Each pixel was assigned a category based on the cosine similarity to gluten and starch, and colored accordingly.

Figure 4-19 shows images of the dough in the under-, optimum-, and over-mixing stages. The orange areas show a high similarity to gluten and a low similarity to starch, suggesting the existence of gluten. The green areas show an opposite tendency, suggesting that starch exists at that point. The yellow areas show a high similarity to both gluten and starch, probably showing that both constituents exist in nearly equal amounts. The dark green areas that show low similarities to both gluten and starch also suggest a mixture of gluten and starch. These areas may also be other constituents that show a relatively strong but different fluorescence pattern from gluten and starch such as particles of the aleurone layer [16].

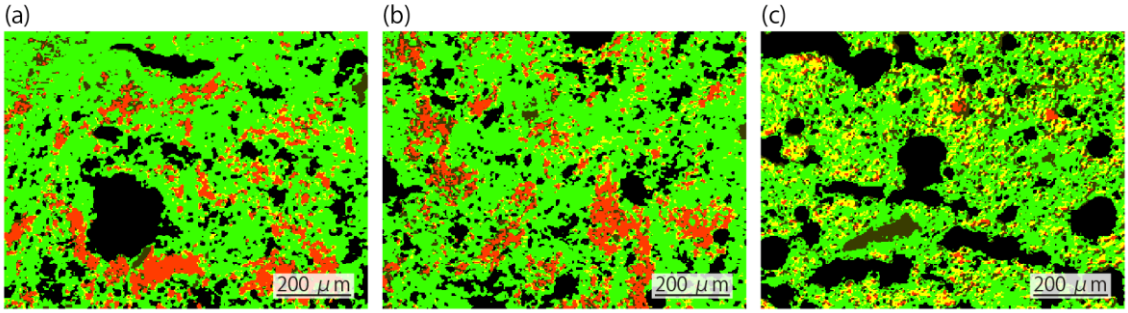

Figure 4-19 Images dough in the (a) under-, (b) optimum-, and (c) over-mixing stages.

Since the resolution of the images is limited, and features that are smaller than a pixel cannot be visualized, thin strands of gluten, which surround starch granules [12] cannot be observed in the images. However, the magnification and resolution of the images can be altered by changing the magnification of the objective lens and binning parameters of the CCD camera, and more detailed images may be acquired in future studies.

4. 5. 6 Quantification of changes in dough through mixing

The gluten particles (orange) that can be seen in the under-mixing and optimum-mixing stages almost disappear in the over-mixing stage. On the contrary, the yellow areas increase significantly. These observations were confirmed by calculating the number of pixels falling in each category for each mixing stage.

Figure 4-20 shows the number of pixels in each category throughout the three mixing stages. There is a significant change in the number of pixels falling in each category from the optimum-mixing stage to the over-mixing stage: the orange and green pixels decrease, while the yellow and dark-green pixels increase in number. Bubble area also increases.

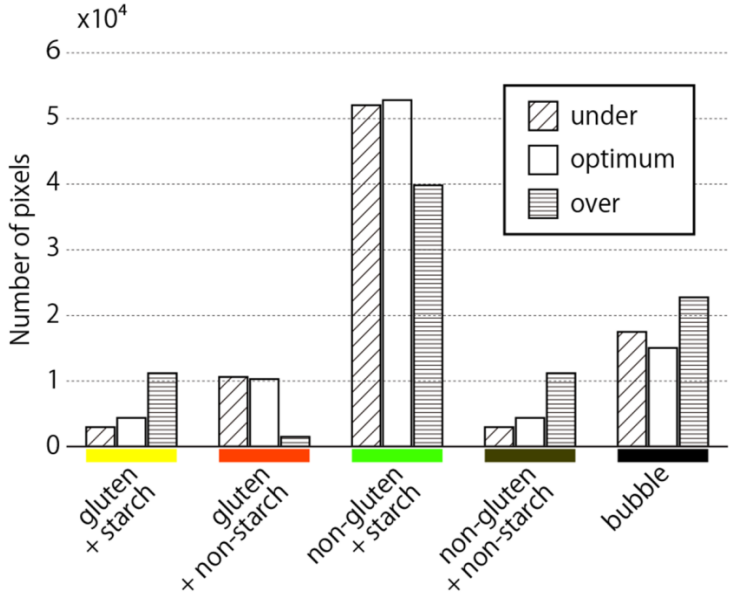

Figure 4-20 Number of pixels in each category throughout the three mixing stages. A significant change in the distribution pattern can be observed between the optimum- and over-mixing stages.

The decrease in the numbers of orange and green pixels and the increase in the numbers of yellow and dark-green pixels suggest that the gluten breaks up into small pieces in the over-mixing stage and mixes with starch granules so that in most of the pixels there is a mixture of gluten and starch. The breaking up of gluten with excessive mixing has been observed by SEM [12].

The threshold values of cosine similarity that divide gluten from non-gluten and starch from non-starch changed markedly from the optimum-mixing stage to the over-mixing stage. The threshold values for gluten are 0.9915 and 0.9894 for the under- and optimum-mixing stages, respectively, but these values decrease to 0.8697 in the over-mixing stage. Similarly, the threshold values for starch are 0.9301 and 0.9261 for the first two mixing stages, respectively, but are 0.8016 in the over-mixing stage. This suggests that, in the over-mixing stage, gluten and starch themselves are altered from the gluten and starch fractionated from the optimally mixed dough.

4. 5. 7 Pseudo color images of dough in experiment 2

Figure 4-21 shows the pseudo color images of dough in the three mixing stages, under, optimum and over, colored according to the angular value between the FF of each pixel and the average FFs of gluten and starch, respectively. The areas in red and green are the areas with a high proportion of gluten and starch, respectively.

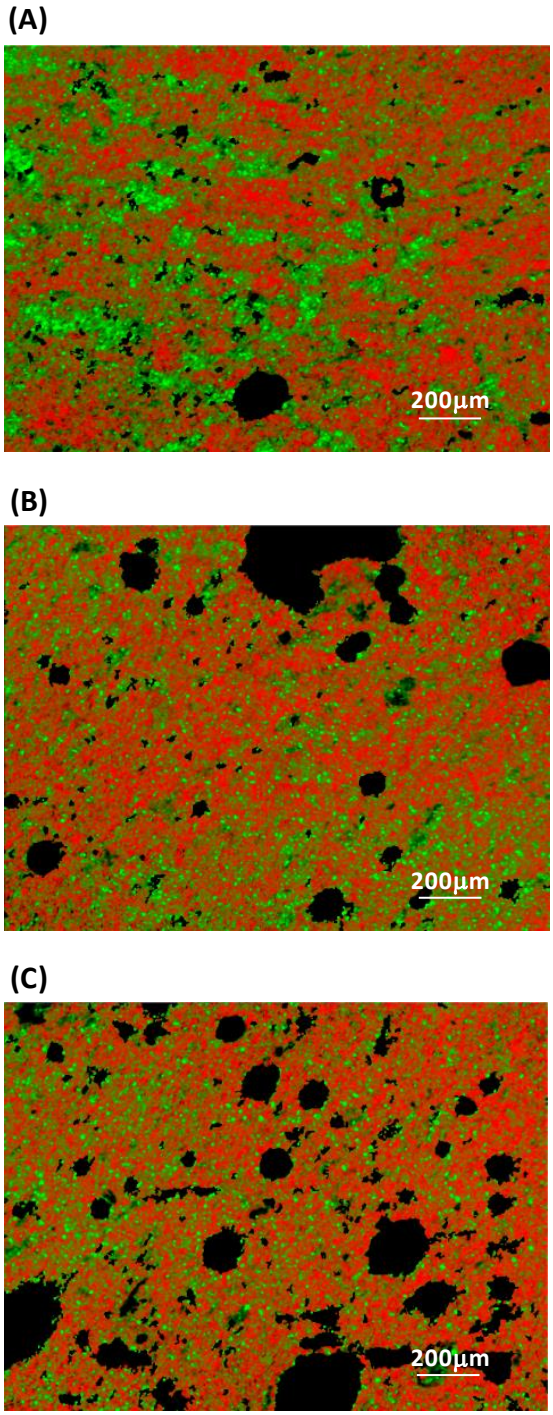

Figure 4-21 Pseudo color images of dough in three mixing stages. (A) Under-mixing stage, (B) Optimum-mixing stage and (C) Over-mixing stage. Red, green and black areas correspond to gluten, starch and bubbles, respectively.

It can be seen that the gluten and starch distribution is heterogeneous in the under-mixing stage, but becomes more homogeneous or more "even" in the optimum- and over-mixing stages. This evenness of gluten and starch does not seem to change much from the optimum-mixing stage to the over-mixing stage.

The over-mixing stage is distinctive in that the area of bubbles (the areas shown in black) is much larger than the other stages. Many large bubbles can be observed, some with a diameter of over 200 μm. The dough in the under-mixing stage contains few of these big, circular bubbles and the black areas which exist mainly on the border between the starch the gluten are small and of an irregular shape.

These observations needed to be confirmed by extracting quantitative parameters from the pseudo color images.

4. 5. 8 Quantitative analysis on the distributions of gluten and starch

Figure 4-22 shows a graph explaining the evenness of gluten and starch in the under-, optimum- and over-mixing stages. As the length of the square becomes longer, the standard deviation of the ratio between gluten and starch existence in the square becomes smaller but the standard deviation value is always higher in the under-mixed dough, i.e., the distribution is more uneven. There is no significant difference between the standard deviation value for the dough in the optimum and over-mixing stages, showing that the evenness of the distribution of gluten and starch does not change after the optimum-mixing stage.

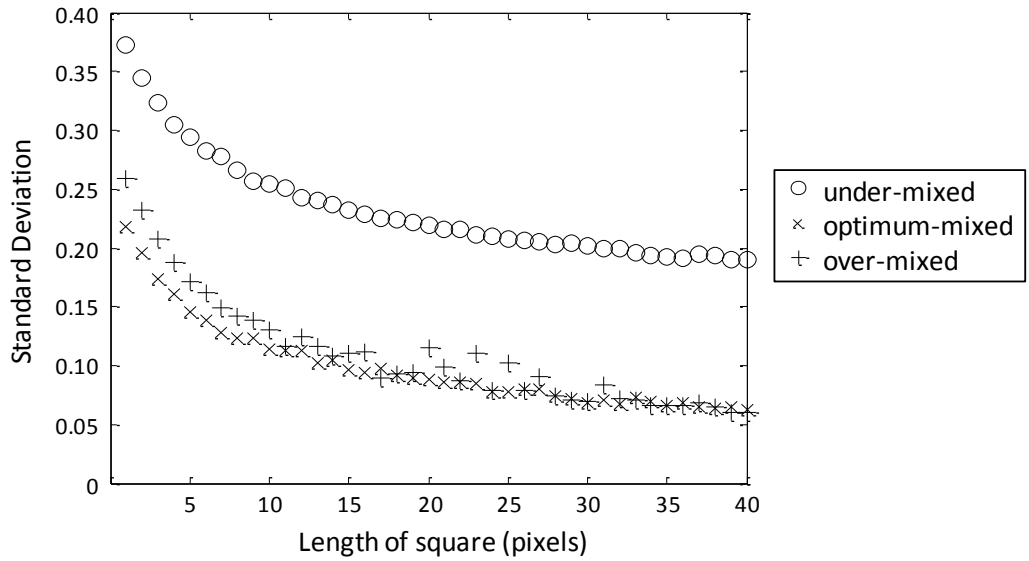

Figure 4-22 Evenness of gluten and starch distributions in the three mixing stages

The standard deviation is calculated from three samples in each mixing stage, which is the reason why the value for the under-mixing stage remains quite high even when the length of the square becomes longer.

4. 5. 9 Quantitative analysis of the size and morphology of bubbles

Total bubble area is the number of pixels classified as “bubble area”. Figure 4-23 shows the ratio of total bubble area to the total image area. The values for each sample shown in the bar graph and the average value for each mixing stage are shown with an asterisk.

A noticeable aspect in the under-mixing stage is that the second sample shows a much higher ratio value than the other two samples. The average bubble ratio value of the other two samples was calculated and shown in the graph with a “+” sign. If this sample were to be excluded, it could be said that the area of bubbles increases significantly from the under-mixing stage to the optimum-mixing stage. This supports previous studies showing that one of the main functions of mixing is the incorporation of air nuclei [17]. On the other hand, this sample may indicate that the condition of the dough in the under-mixing stage varies greatly from place to place and that more mixing is needed to produce dough in which the bubbles are distributed evenly.

The total bubble area in the over-mixed dough was significantly higher than the other two mixing stages, conforming the observation from the pseudo color image. From this data, two possibilities can be derived: 1) that new air is being incorporated into the dough, and 2) that small bubbles below the resolution of the FF images are being integrated to form bigger bubbles, resulting in a seeming increase in bubble area.

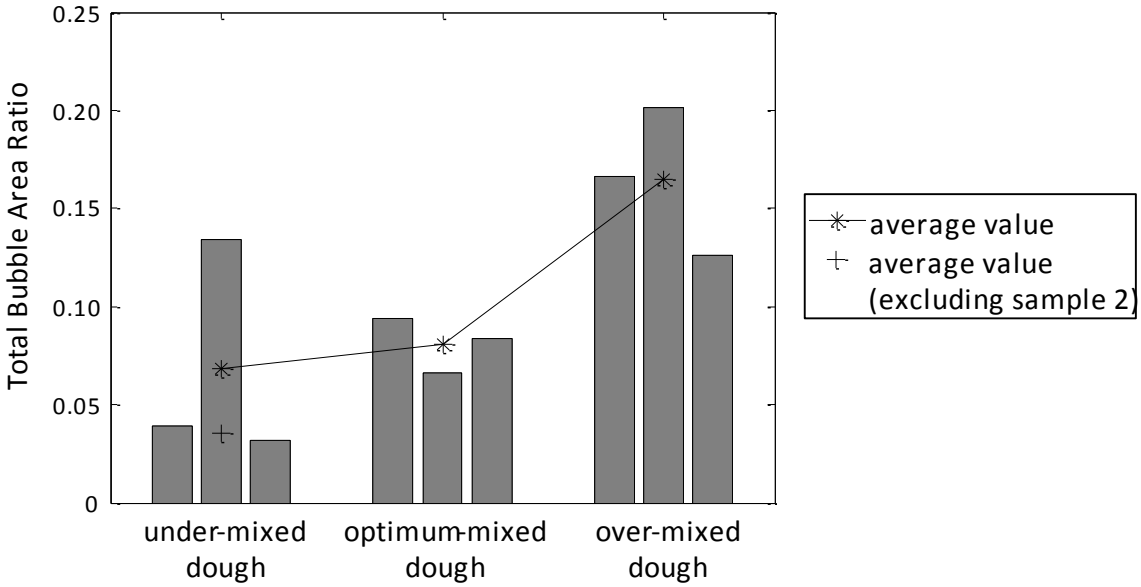

Figure 4-23 Total bubble area ratio of dough in the three mixing stages

Furthermore, in order to verify the results shown in エラー! 参照元が見つかりません。, the specific volume of dough in the three mixing stages was measured. The specific volume $v[\mathrm{cm}^3/\mathrm{g}]$ is calculated by dividing the volume V [cm^3] by the weight m [g]. If more bubbles are incorporated in the dough, the volume would increase while the weight would remain the same, i.e., the specific volume would increase.

The volume of the sample was calculated by measuring the buoyancy of each sample when the sample was completely submerged in water. The dough sample was suspended to a spring scale with a fine thread and the weight measured (m_0 [g]). Next, the dough sample was completely submerged in water and the weight measured (m_1 [g]). The buoyancy of the sample, F_b [N] is calculated from the difference between m_0 and m_1

$$F_b = (m_0 - m_1)\mathbf{g} \qquad \ldots (5)$$

where $\mathbf{g}$ [N· m^2/kg^2] is the gravitational constant. The buoyancy of a sample is equal to the gravitational force on water with the same volume as the sample. The gravitational force, F_g [N] is expressed as

$$F_g[\mathrm{N}] = 1[\mathrm{g/cm^3}] \times V[\mathrm{cm^3}] \times \mathbf{g}[\mathrm{N/g}] \qquad \ldots (6)$$

where V [cm^3] is the volume of the dough sample. From equations (3) and (4), V [cm^3]

can be calculated as

$$V[\mathrm{cm}^3] = (m_0 - m_1) \times 1[\mathrm{g/cm}^3] \quad \ldots (7)$$

Assuming that the dough does not absorb water during measurement, the volume of the sample can be measured in this way.

Figure 4-24 shows the specific volume of dough in the three mixing stages. Four samples were measured for each mixing stage. It can be seen that the specific volume increases significantly as the dough is mixed, verifying the results shown from the FF pseudocolor images. The results also show that new air is actually incorporated into the dough as the dough is mixed, turning down the possibility that the increase in bubble area is only the result of the integration of small air bubbles below the resolution of the FF images.

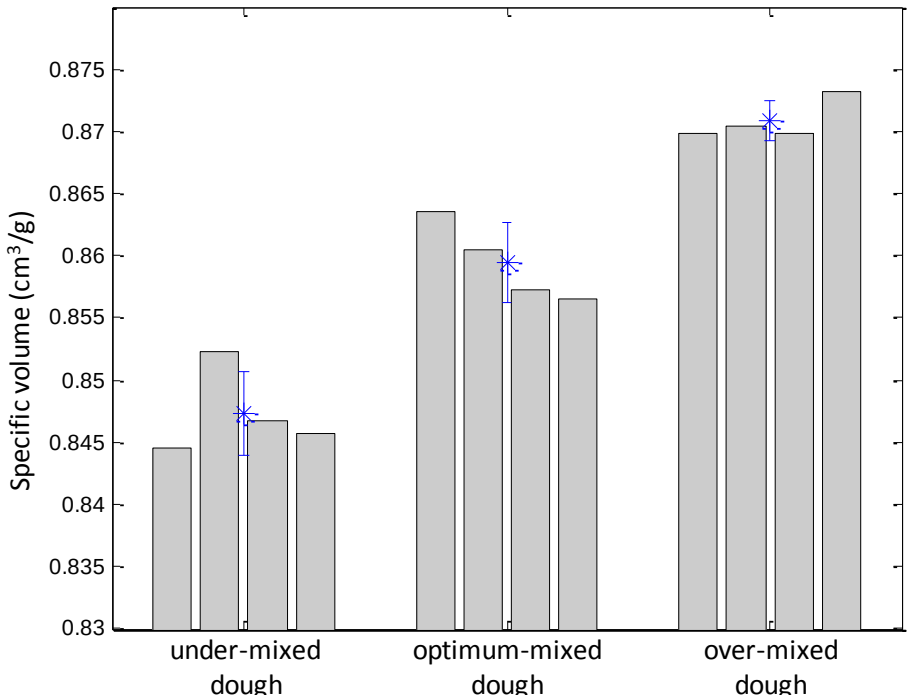

Figure 4-24 Specific volume of dough in the three mixing stages

Furthermore, this data supports the assumption that the bubble area ratio calculated from a two-dimensional image can sufficiently predict the bubble volume ratio in three-dimensional space. In a study on pore volume in concrete, Neithalath et al. [18] compared the pore area ratio calculated from the cross section of a concrete sample with the pore volume ratio of the same sample and found that the two ratios correlated

significantly. Although the samples measured for the image and the specific volume are different parts of the same batch of dough, this result indicates that complicated measurement in three-dimensional space may be substituted with a more straight-forward measurement in two-dimensional space.

Figure 4-25 shows the accumulative bubble area plotted against the area of independent bubbles for the three mixing stages. The accumulative bubble area is calculated by adding up the area of the bubbles falling into each area category. The graph shows that the dough in the under-mixing stage contains many small bubbles which account for a large proportion of the total bubble area. As the mixing proceeds, these small bubbles seem to be integrated to form larger bubbles. When the dough is mixed past the optimum-mixing stage, the number of small bubbles increases once more. The over-mixed dough also contains a large number of big bubbles which add up to the high ratio of bubble area shown in Figure 4-23.

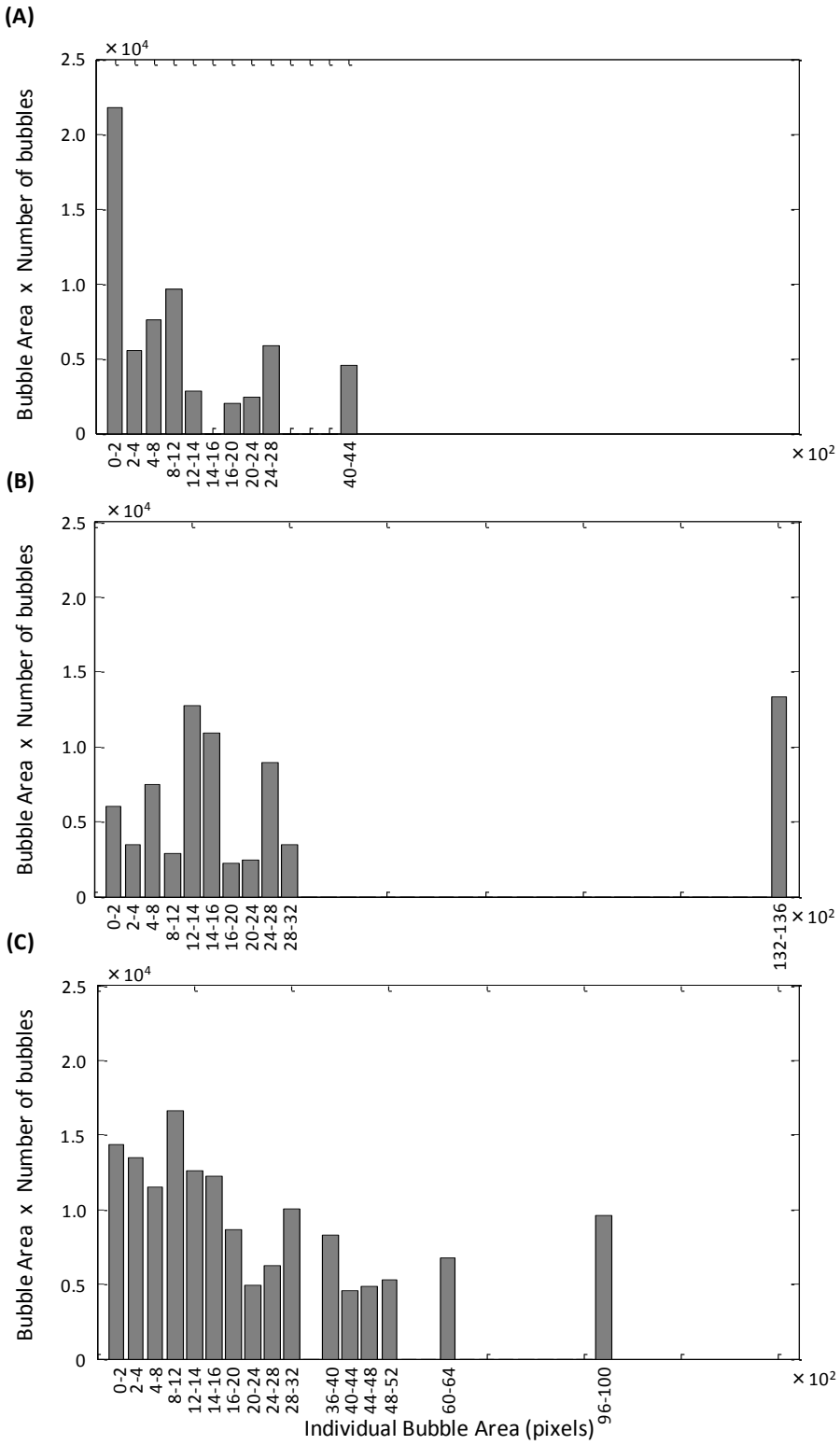

Figure 4-25 Histogram of the bubble area in the three mixing stages

The vertical axis shows the product of individual bubble area and number of bubbles showing the degree of contribution to the total bubble area.

The eccentricity of the bubbles in the dough of the three mixing stages is shown by the ratio of the major axis to the minor axis. Because the total number of bubbles differs among the three mixing stages, the actual number of bubbles within each eccentricity range is divided by the total number and is shown as a percentage. The fraction of bubbles whose ratio of major axis to minor axis is in the range of 10:5 to 10:3 is especially large in the under-mixing stage, followed by the over-mixing stage. Conversely, the proportion of bubbles whose major to minor axis ratio is from 10:10 to 10:7 is highest in the optimum-mixing stage. This shows that the shapes of the bubbles in the optimum-mixing stage are close to a circle, or when viewed three-dimensionally, a sphere while the bubbles in the under- and over-mixing stages are elongated or of irregular shapes.

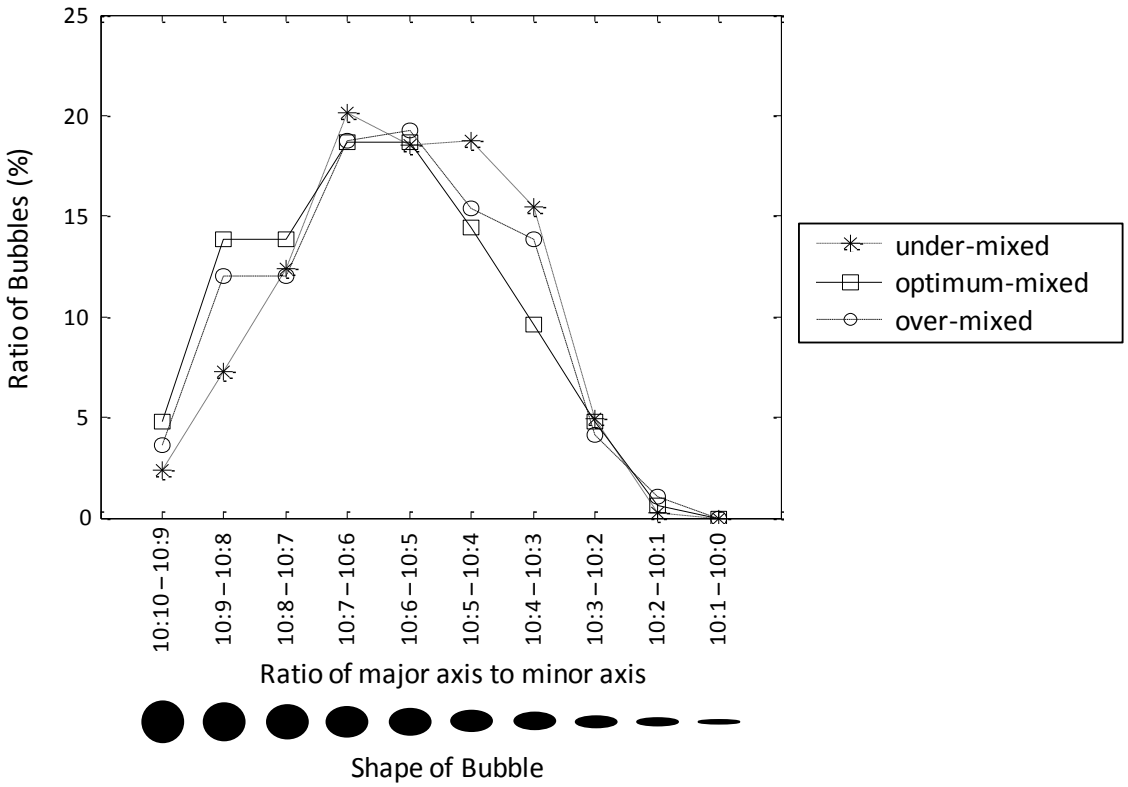

Figure 4-26 Eccentricity of bubbles and their ratio to the total number

4. 5. 10 Discussion

The FF imaging method overcomes several problems with conventional microscopic methods, especially preprocesses such as staining in light microscopy and drying or freezing in electron microscopy. The main problem with these preprocesses is that it always involves the risk of chemical or physical sample alteration. For example,

in this study, thin dough sections were stained after spatial FF data acquisition. In this process, the thin sections were vulnerable to soaking and rinsing with liquids and needed careful handling to keep the samples from separating from the slide glass. The FF imaging method eliminates these risks, allowing the samples to be measured under a condition close to the original state.

Another problem of preprocessing is that the prepared sample is markedly affected by the preparation conditions and the researcher's technique. The staining conditions include parameters such as staining time and stain concentration, which need optimization, and sample handling techniques that should stain the sample evenly or prevent color degradation are not easy to develop. The same could be said about preprocesses required for electron microscopy. The FF imaging method is much easier to perform, with few simple processes that could affect the final result. FF measurement and analysis could easily be automated, and sample preparation can also be simplified, as discussed in the next paragraph. Therefore, the same reliable result could be acquired by anyone performing the experiment.

Two problems which are harder to tackle are (1) the validity of using gluten and starch extracted from the dough sample as references for visualization and (2) validation methods of the visualized result. The question of whether extracted gluten and starch can be used as references for the actual gluten and starch in dough is difficult, since it has been reported that the reconstitution of fractionated flour results in a deterioration of functional properties [19]. The structure of gluten definitely changes through the extracting process, physically, by the kneading of the dough, and chemically, through the contact with water and air. The extracted starch goes through many processes such as freeze drying, absorption of water, freezing, thawing and drying, and there is no proving that these processes change the fluorescence response. However, the only alternatives for the reference samples are commercially available samples of pure starch and gluten, which face the same problems. Furthermore, using the starch and gluten extracted from different flours may have a negative effect on the supervised analysis. Therefore, the only apparent solution is to carry out the extraction procedure so that the sample alteration is limited to a minimum. A study on fractionation methods by Macritchie [10] show that the temperature during the extraction process is an important factor determining the quality of the extracted gluten and starch. Paying attention to these conditions could enhance the accuracy of the visualization method.

Another major problem is proving the validity of the imaging method. In this study, the same sample was stained with fluorescence dyes and the result compared with the FF pseudo color result. However, since the image acquired by the FF imaging

method proved to be closer to the actual condition than the stained method, the stained image cannot be completely relied on as the ultimate reference. Rather, the stained image and the FF pseudo color image seem to support each other. This problem of the reliability of the imaging method will remain as long as the actual constituent distribution of the sample is not known.

With the present technology, visualizing the constituent distributions in dough in order to check its condition during mixing is not realistic. Destructive methods which need sampling can only check the condition of that particular piece of dough, and the time it takes for preprocessing cannot be shortened. FF imaging requires a certain amount of time to measure and analyze the sample, but with a stronger light, limited number of wavelengths and high speed calculation system, the imaging speed could be greatly improved.

There have been many reports on the change in dough structure with mixing, but most studies have limited the descriptions to qualitative explanations of the structure image and a few have gone on to extracting quantitative parameters from the acquired images. A few studies [7, 20] have focused on the area fraction of the protein matrix (PMV), assuming that it correlated with the volume fraction. However, the evaluations of the PMV value are not constant, with some studies concluding that it is not necessarily a measure of dough quality.

Most studies agree that gluten and starch are heterogeneously distributed at the beginning of the mixing stage and that the two constituents become homogenized as the mixing progresses [14]. A few studies claim that the homogenization proceeds even after the dough is optimally mixed [8], a phenomenon that was not observed in our study.

As for the area of bubbles in the dough, Tlapale-Valdivia et al. [21] have also reported the emergence of big holes in the overdeveloped dough, but studies that have actually calculated the total ratio of bubble in the dough are few. These large bubbles may be an important factor that weakens the dough when it is over-mixed, since there have been reports that excessive dough aeration has a negative impact on rheological parameters such as the strain hardening index and failure stress [22].

This study has shown that two different phenomena progress when dough is mixed, the distributions of gluten and starch become more “even” as the dough approaches the optimally mixed condition and excessive air is incorporated as the dough goes beyond it. Therefore, optimally mixed dough could be defined as a condition where the gluten and starch are homogeneously distributed, while there is no excessive air incorporated in the dough.

Extracting quantitative parameters from the FF pseudo color images is very straightforward since the data is already expressed in digital form. The images can be processed directly with analysis software and many parameters can be extracted with the image processing toolbox implemented in the software. Therefore, caution needs to be taken against using parameters which may not explain the actual changes through the mixing process but just fit the few samples analyzed in the study. To be sure that the parameters extracted in this study really represent the changes in the mixing process, another batch of dough may be needed to be analyzed and checked to see if the same tendency can be observed.

By measuring several samples in different mixing stages, a border which defines the optimal mixing state may be obtained. This could lead to a completely automated dough mixing system where the mixing process is controlled with the FF imaging system. The distributions of gluten, starch and bubbles would be monitored, the image acquired, and quantitative parameters extracted continuously until the extracted parameters show a certain value which indicates that the dough has reached an optimum.

4. 6 Conclusions

In this study, the cosine similarities between the FF of each pixel in the dough and the FF of gluten (or starch) were used as a measure of the gluten (or starch) existing in that area. The values of cosine similarity were converted into color with two methods: the first method involved assigning continuous color scales of red and green to the cosine similarity values to gluten and starch, respectively, and the second method assigned one out of four colors to each pixel depending on their cosine similarity values. In the second method, the colors were assigned so that the total ratio of gluten and starch in the image was equal to that of the sample. The pseudo color image created with the first method was compared to the stained image, and similar patterns were confirmed. Images of dough in the three mixing stages, under-, optimum- and over-mixing stage, showed notable changes with both imaging methods.

By quantification methods, this chapter showed that the change in gluten and starch distribution in wheat flour dough that occurs with mixing can be visualized and quantified with FF imaging and morphological analysis. The changes observed were as follows: (1) the distribution of gluten and starch became more even from the under- to the optimum-mixing stage, (2) the total bubble area became larger from the optimum- to the over-mixing stage (this was supported by the increase in specific volume), (3) the

mean area of the bubbles became larger in the over-mixing stage, and (4) the shapes of the bubbles were circular in the optimum-mixing stage but were more elongated in the under- and over-mixing stages. Although more samples need to be analyzed to confirm that these changes generally occur in the mixing process, the methodology of visualization and quantification has been established and is readily applicable to other samples.

References

1. Sugiyama, J., Visualization of sugar content in the flesh of a melon by near-infrared imaging. Journal of Agricultural and Food Chemistry, (1999). **47**(7): p. 2715-2718.

2. Tsuta, M., Sugiyama, J., Sagara, Y., Near-infrared imaging spectroscopy based on sugar absorption band for melons. Journal of Agricultural and Food Chemistry, (2002). **50**(1): p. 48-52.

3. Gonzalez, R.C., Woods, R.E., Eddins, S.L., Digital image processing using matlab. 2nd ed. (2009): Gatesmark Publishing. 827.

4. Renzetti, S., Arendt, E.K., Effect of protease treatment on the baking quality of brown rice bread: From textural and rheological properties to biochemistry and microstructure. Journal of Cereal Science, (2009). **50**(1): p. 22-28.

5. Peressini, D., Peighambardoust, S.H., Hamer, R.J., Sensidoni, A., van der Goot, A.J., Effect of shear rate on microstructure and rheological properties of sheared wheat doughs. Journal of Cereal Science, (2008). **48**(2): p. 426-438.

6. Primo-Martin, C., de Pijpekamp, A.V., van Vliet, T., de Jongh, H.H.J., Plijter, J.J., Hamer, R.J., The role of the gluten network in the crispness of bread crust. Journal of Cereal Science, (2006). **43**(3): p. 342-352.

7. Peighambardoust, S.H., van der Goot, A.J., van Vliet, T., Hamer, R.J., Boom, R.M., Microstructure formation and rheological behaviour of dough under simple shear flow. Journal of Cereal Science, (2006). **43**(2): p. 183-197.

8. Peighambardoust, S.H., Dadpour, M.R., Dokouhaki, M., Application of epifluorescence light microscopy (eflm) to study the microstructure of wheat dough: A comparison with confocal scanning laser microscopy (cslm) technique. Journal of Cereal Science, (2010). **51**(1): p. 21-27.

9. van de Velde, F., Weinbreck, F., Edelman, M.W., van der Linden, E., Tromp, R.H., Visualisation of biopolymer mixtures using confocal scanning laser microscopy (cslm) and covalent labelling techniques. Colloids and Surfaces B-Biointerfaces, (2003). **31**(1-4): p. 159-168.

10. Macritchie, F., Studies of the methodology for fractionation and reconstitution of wheat flours. Journal of Cereal Science, (1985). **3**(3): p. 221-230.

11. Kokawa, M., Sugiyama, J., Tsuta, M., Yoshimura, M., Fujita, K., Shibata, M., Araki, T., Nabetani, H., Development of a quantitative visualization technique for gluten in dough using fluorescence fingerprint imaging. Food and Bioprocess Technology, (2013). **6**(11): p. 3113-3123.

12. Amend, T., Belitz, H.D., The formation of dough and gluten - a study by scanning electron-microscopy. Zeitschrift Fur Lebensmittel-Untersuchung Und-Forschung, (1990). **190**(5): p. 401-409.

13. Moss, R., Gore, P.J., Murray, I.C., The influence of ingredients and processing variables on the quality and microstructure of hokkien, cantonese and instant noodles. Food Microstructure, (1987). **6**(1): p. 63-&.

14. Paredeslopez, O., Bushuk, W., Development and undevelopment of wheat dough by mixing - microscopic structure and its relations to bread-making quality. Cereal Chemistry, (1983). **60**(1): p. 24-27.

15. Amend, T., Belitz, H.D., Moss, R., Resmini, P., Microstructural studies of gluten and a hypothesis on dough formation. Food Structure, (1991). **10**(4): p. 277-288.

16. Irving, D.W., Fulcher, R.G., Bean, M.M., Saunders, R.M., Differentiation of wheat based on fluorescence, hardness, and protein. Cereal Chemistry, (1989). **66**(6): p. 471-477.

17. Mehta, K.L., Scanlon, M.G., Sapirstein, H.D., Page, J.H., Ultrasonic investigation of the effect of vegetable shortening and mixing time on the mechanical properties of bread dough. Journal of Food Science, (2009). **74**(9): p. E455-E461.

18. Neithalath, N., Sumanasooriya, M.S., Deo, O., Characterizing pore volume, sizes, and connectivity in pervious concretes for permeability prediction. Materials Characterization, (2010). **61**(8): p. 802-813.

19. Grassberger, A., Schieberle, P., Koehler, P., Fractionation and reconstitution of wheat flour - effect on dough rheology and baking. European Food Research and Technology, (2003). **216**(3): p. 204-211.

20. Lee, L., Ng, P.K.W., Whallon, J.H., Steffe, J.F., Relationship between rheological properties and microstructural characteristics of nondeveloped, partially developed, and developed doughs. Cereal Chemistry, (2001). **78**(4): p. 447-452.

21. Tlapale-Valdivia, A.D., Chanona-Perez, J., Mora-Escobedo, R., Farrera-Rebollo, R.R., Gutierrez-Lopez, G.F., Calderon-Dominguez, G., Dough and crumb grain changes during mixing and fermentation and their relation with extension properties and bread quality of yeasted sweet dough. International Journal of Food Science and Technology, (2010). **45**(3): p. 530-539.

22. Chin, N.L., Martin, P.J., Campbell, G.M., Dough aeration and rheology: Part 3. Effect of the presence of gas bubbles in bread dough on measured bulk rheology and work input rate. Journal of the Science of Food and Agriculture, (2005). **85**(13): p. 2203-2212.

5 Visualization of gluten, starch, and butter in pie pastry

5. 1 Abstract

In this study, the distributions of gluten, starch and butter in pie pastry were visualized by combining FF imaging with spectral unmixing methods. Two types of pie pastry were made: puff pastry, in which wheat flour dough and butter are alternately layered, and short pastry, in which flour and butter are mixed together with water. Samples of 10 μm thickness were made, and fluorescence images were acquired with excitation and emission wavelengths in the range of 270-320 nm and 350-420 nm, respectively, at 10 nm increments. The FFs of each pixel were unmixed into the FFs and abundances of five constituents, gluten, starch, butter, slide glass, and ferulic acid, using two spectral unmixing methods: non-negative matrix factorization (NMF) and constrained least squares method. NMF was only applicable to puff pastry and was unable to visualize starch and butter in the short pastry which were mixed together. Least squares method was coupled with constraints of non-negativity, full additivity (the sum of the constituents in one pixels is unity) and quantum restraint on the abundances of the slide glass (abundances take values of one or zero). With this method, distributions of the constituents in both puff and short pastry were visualized.

5. 2 Introduction and objective

Chapters 3 and 4 have shown that we have succeeded in visualizing two constituents in model dough and wheat flour dough, gluten and starch. This could be generalized to state that we have visualized proteins and polysaccarides. Proteins and polysaccarides make up the structure of food, along with one other constituent, fat. Therefore, if we could visualize fat, proteins and polysaccarides all together by using the FF, the range of application would be largely widened. This is the reason we chose “fat” as the third constituent to visualize.

The role of fat in bread dough and its structure has been discussed by many. Fat is known to form membranes around the starch granules and protein in dough [1], and Li, Dobraszczyket al. [2] have visualized the fat with the combination of fluorescence stains and confocal scanning lazar microscopy (CSLM). The sizes of fat crystals are reported to be between 2 to 60 μm [3, 4] but other studies have reported that fat globules cannot be observed in the bread dough with scanning electron microscopy (SEM) [5, 6]. From

these previous studies, we speculated that it would be difficult, if not impossible, to visualize the fat incorporated in bread dough.

Therefore, we chose pie pastry as observation targets. Pie pastry is also made from wheat, water and butter, but the fat is incorporated in relatively large sizes to provide the typical crunchy texture. There exist many types of pie pastry, which differ in structure and texture, depending on manufacturing methods. In this work, we focused on two typical types of pie pastry, puff pastry and short pastry. Puff pastry is made by layering wheat flour dough and butter, so that when the butter melts in the baking process, the remaining dough forms thin crisp layers. On the other hand, short pastry is named after its “short” texture, which means that the food forms small crumbles in the mouth when bitten into. This is because the butter is mixed into the wheat flour, inhibiting the development of gluten.

Although these structures can be estimated from the manufacturing method, there are few studies which have actually visualized them. Therefore, the visualization of these structures would clearly show the strong link between food structure and their known textures.

From a larger view point, the development of a method to visualize the three main components of food would have large applications in other areas of science such as biology and medicine.

5. 3 Materials and methods

5. 3. 1 Preparation of pie pastry samples

Two types pie pastry were made: puff pastry and short pastry. Both were made so that the overall ratio of gluten, starch and butter was equal. Table 5-1 shows the composition of ingredients for the two pastry dough.

Table 5-1 Composition of puff pastry and short pastry dough

	puff pastry	short pastry
strong flour	70	70
weak flour	30	30
salt	1	1
shortning	7	–
water	53	40
butter	97	85

For the puff pastry, the first five ingredients were mixed in a dough mixer for 1 min at low speed and 6 min at medium speed. The temperature at the end of mixing was 23 to 24 ℃. The mixture was rolled to a thickness of 3-4 cm and stored at 5 ℃ for 15-20 h. After resting, the dough was wrapped around the butter and rolled to 5 mm thickness with a sheeter. The sheet of dough was folded in three, turned around 90 degrees and folded in four. After a 30 min rest at -7 to -8 ℃, the dough was folded in three, turned around 90 degrees and folded in three again (total 108 layers). After resting again at -7 ℃ to -8 ℃ for 30 min, the dough was rolled to 2.5 mm.

For the short pastry, refrigerated butter was cut into pieces approximately 1 cm^3 in size and mixed with the two types of flour and salt in a mixer (Kenwood, United Kingdom) with a beating attachment until the butter particles were 2 to 3 mm in size. Water was added and the mixture was kneaded lightly into dough.

Both pastry dough were cut into pieces approximately 1 cm^3, embedded in compound (3% CMC embedding medium, iTec Science, Ibaraki, Japan) and frozen immediately in the cooling bath of a cold trap (Eyela UT-2000, Tokyo Rikakikai Co. Ltd, Tokyo, Japan) with hexane as the cooling medium.

When the samples were completely frozen, the samples were sliced to 10 μm using a cryotome (CM-1900, Leica) with a Surgipath DH80HS blade (Leica). The thin slices were mounted on a slide glass (S-8215 and S-9901, Matsunami Glass Ind., Ltd., Osaka, Japan) and kept at -20 ℃ until observation (Figure 5-1).

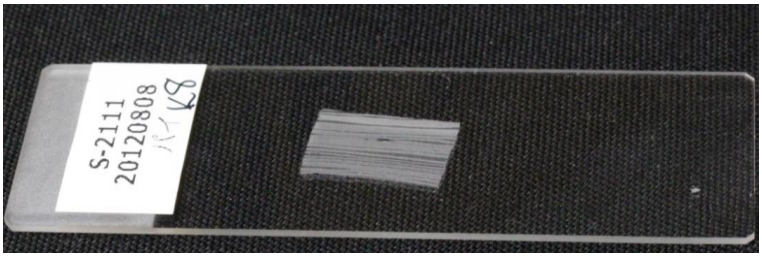

Figure 5-1 Photograph of a thin slice of puff pastry on a slide glass

5. 3. 2 Fractionation of gluten and starch

Gluten and starch were fractionated, based on the method by Macritchie [7]. Fractionation was performed with 50 g strong flour, 50 g weak flour and 65 g of pure water. The flours used were of the same batches as those used for the pie pastry. The flour and water were cooled to 4 ℃ before mixing.

The flour and water were mixed with a pin mixer (National MFG., Nebraska, USA) (Figure 5-2) at 20 ℃ for 60 s. The temperature of the dough at the end of mixing was

18.1°C. The dough was soaked in pure water for 60 min to strength gluten connectivity and then kneaded in the water separate insoluble protein fraction (gluten) with starch granules and other soluble substances. A sum of 2800 mL of water was used in this process. The bowl was cooled while washing off starch granules since it has been reported that gluten yield is higher when the temperature is kept low [7].

(A) (B)

Figure 5-2 (A) Pin mixer and (B) dough at the end of mixing

The water and washed out starch were poured into 500 mL centrifuge tubes and gluten was put into another centrifuge tube with pure water. These tubes were centrifuged for 20 min at 7000 rpm and at 5 °C (centrifuge: Hitachi HIMAC CR21G3) (Figure 5-3A). The agglomerated gluten was kept at 4 °C until sectioning. The precipitated starch was separated into the top yellow layer (tailing starch) and the bottom white layer (primary starch). Both starches were freeze-dried at -80 °C with an Eyela FDU-830 freeze-dryer (Tokyo Rikakikai) (Figure 5-3B).

The obtained gluten was cut into small pieces, embedded in compound, frozen and sliced into 10 mm slices in a similar way to pie dough. Dried starch was dispersed in compound, frozen and sliced in the same way.

The weight and water content of the obtained gluten and two types of starch were measured to calculate the ratio of gluten to starch in the dough. Water content was measured by the drying the samples at 130 °C for 3 h (oven dry method).

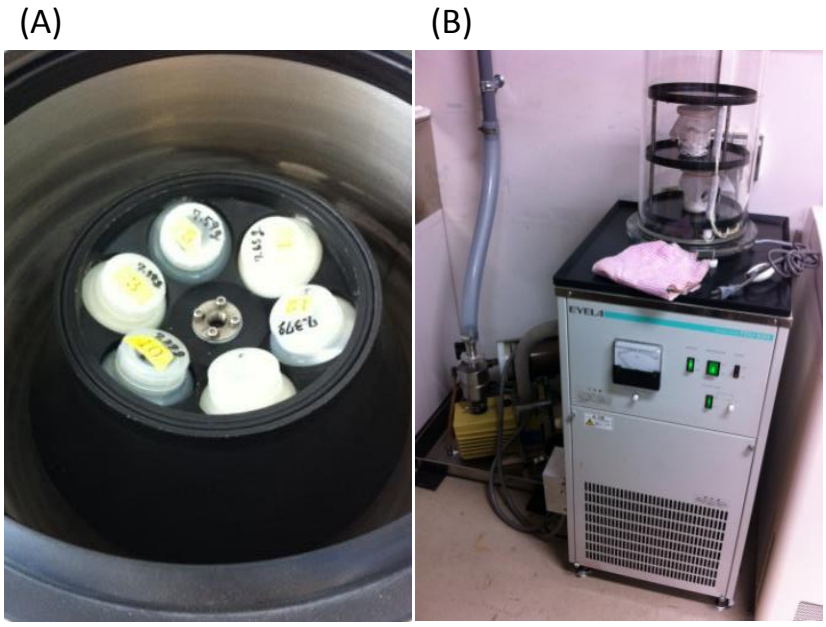

Figure 5-3 (A) Centrifugation of gluten and starch (B) Freeze dryer

Fractionation of starch was also performed, based on the method by Whistler and Wolfrom [8]. Flour (50 g strong flour and 50 g weak flour) were mixed with 75 mL of pure water and aged at room temperature for 2 h. The loose dough was set over a nylon bolting sieve with mesh openings of 75 μm. While pouring water over the dough, the dough was kneaded gently to wash the starch granules through the mesh. The remaining mixture of gluten and starch was discarded, and the starch was passed through the mesh another two times. This starch slurry was poured into four 50 mL plastic tubes and centrifuged at 2300 *g* for 15 min at room temperature (centrifuge: Himac CR 22G, rotor: R10A2). After centrifugation, the upper fraction containing tailing starch was scraped off and the remaining starch was suspended in pure water. This process of centrifugation, scraping off the top layer and suspension was repeated three times to obtain pure starch. Thin samples of starch samples were created as previously explained.

5. 3. 3 Selection of wavelength conditions for imaging

Since there is a limit in the number of band-pass filters that can be used in the FF imaging system (eight wavelengths for both excitation and emission light), wavelength conditions that are effective in discriminating butter, gluten and starch need to be selected. This was done by measuring the three constituents with a spectrophotometer (F7000, Hitachi high technologies) and applying principal component analysis (PCA) to the data.

Six samples of gluten, three samples of butter and five samples of starch were

measured in the spectrophotometer using a solid sample cell. The measured wavelengths were 250 to 700 nm for both excitation and emission wavelengths, with intervals of 10 nm. The slit width was 10 nm for both the excitation and emission wavelengths, scanning speed was 60000 nm/min and photomultiplier voltage was 350 V.

Since the imaging system showed low sensitivity for excitation wavelengths below 270 nm and emission wavelengths below 350 nm, fluorescence data of excitation wavelengths 250- 260 nm and emission wavelengths 250-340 nm were excluded from the analysis. Furthermore, data from the fluorescence spectrophotometer showed secondary fluorescence over emission wavelengths 500 nm and over. These wavelengths were excluded from the data. Principal component analysis was conducted with fluorescence data in the range 270-500 nm and 350-500 nm for excitation and emission wavelengths, respectively.

5. 3. 4 Acquisition of fluorescence images

Fluorescence images of two types of pie pastry, gluten and starch were acquired with the FF imaging system, using the excitation and emission wavelengths selected with PCA. The fluorescence images were acquired in decreasing order of wavelengths, i.e., 330 nm to 270 nm for the excitation wavelengths and 420 nm to 350 nm for the emission wavelengths. This was to minimize the denaturation of the sample due to exposure to UV light.

The light intensity of the excitation, exposure times and z-position for each wavelength condition was determined by the method explained in chapter 2.

5. 3. 5 Alignment of fluorescence images

One deficiency of the FF imaging system was that the fluorescence images tended to move between different wavelengths of emission light. This was because the emission filters were not aligned horizontally to the optical path with great accuracy, and as a result, bent the light path slightly. The emission filters were set in a filter holder with threads, and these threads were used to attach the filter holders to the filter wheel (Figure 5-4). Consequently, the slight tilt of the filter changed with the rotation of the filter holder. This resulted in a set of filters tilted in different directions, thus the fluorescence images moved when the emission filters were changed.

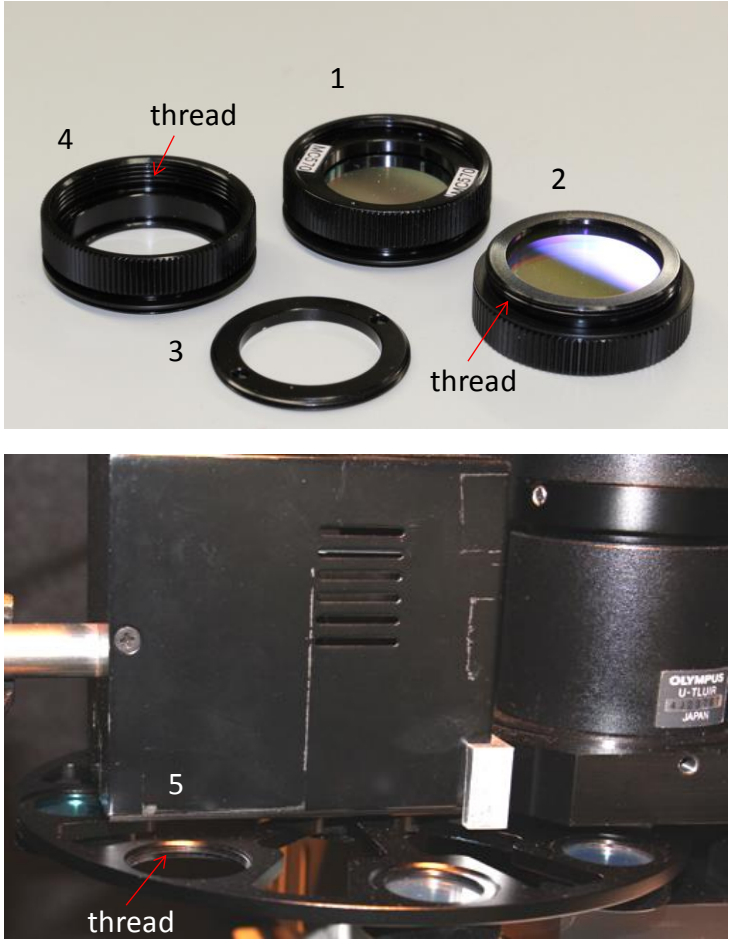

Figure 5-4 Photograph of the filter holder and wheel. The band-pass filter is set inside the holder (4), and fixed from above by a fastener (3), as shown in picture 1. The fastener (3) is fixed by turning it through a thread. The filter composition (1) is turned upside down (2) and is set in the filter wheel (5) with the threads. Since the band-pass filter is held in place by threads, it is tilted slightly relative to the horizontal direction.

Since eliminating the slight tilt of the filters would require more accurately made hardware, the misalignment of the fluorescence images was corrected digitally after image acquisition. Image registration was performed by calculating the correlation of two images as a function of the relative displacement of the input image to the base image [9]. However, this resulted in inaccurate registration for some images because different constituents fluoresce under different wavelength conditions (Figure 5-5). Therefore, fluorescence images of a microscope scale (NOB1, MeCan Imaging, Inc., Japan) was acquired in advance, under all the emission wavelengths used. The scale shows similar images under different emission wavelengths, therefore, alignment of the scale images was easily performed. Since misalignment occurred only between different emission

wavelengths, and fluorescence images with the same emission wavelengths were basically aligned to each other, images with the same emission wavelengths could be roughly aligned using the same displacement for the microscopic scale.

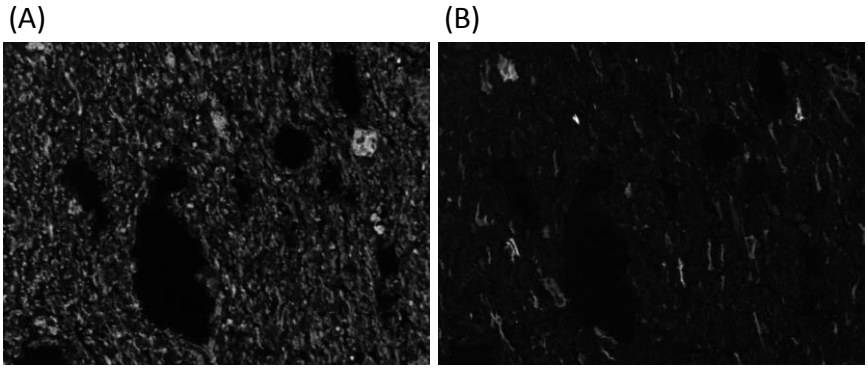

Figure 5-5 Fluorescence images of the same short pastry in wavelengths Ex270/Em350 and Ex330/Em420 for (A) and (B), respectively.

After a rough alignment, the images were adjusted with an accuracy of a tenth of a pixel, using the image registration tools in MATLAB.

5. 3. 6 Extraction of reference FF data

In order to visualize the gluten, starch and butter in pie pastry, reference FFs of these three constituents were extracted from the fluorescence images of fractionated gluten and starch, and puff pastry. The fluorescence image of fractionated gluten showed many air holes. Therefore, these air hole areas were left out and the FFs of the remaining area were averaged to acquire the reference FF of gluten (Figure 5-6).

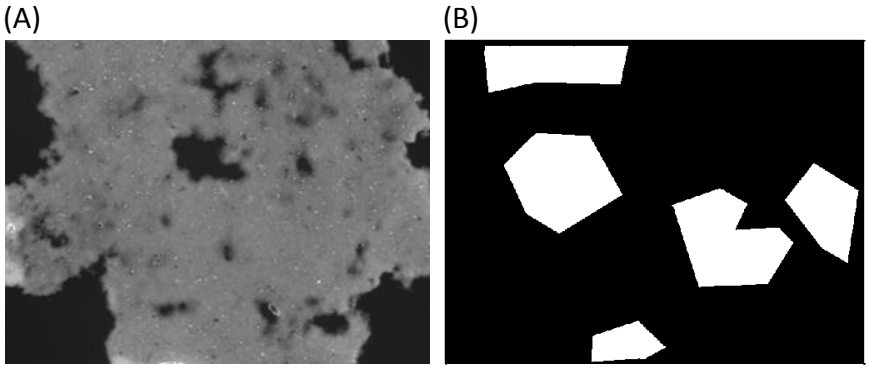

Figure 5-6 (A) Fluorescence image of fractionated gluten and (B) the areas used for obtaining the reference gluten FF.

The starch granules in the thin samples were dispersed in compound. Since

compound showed no fluorescence, starch granules were detectable against the background (Figure 5-7). Therefore, a few circular areas corresponding to the starch granules were manually selected, and the FFs of the selected pixels were averaged to acquire the reference FF of starch.

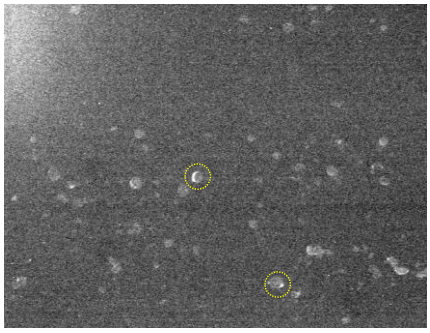

Figure 5-7 Fluorescence image of starch granules dispersed in compound. Areas surrounded by dotted lines are examples of clearly observable starch granules.

Butter areas were manually selected from the puff pastry images, which showed alternating layers of dough and butter (Figure 5-8). All the FFs of the selected areas were averaged to acquire the reference FF of butter.

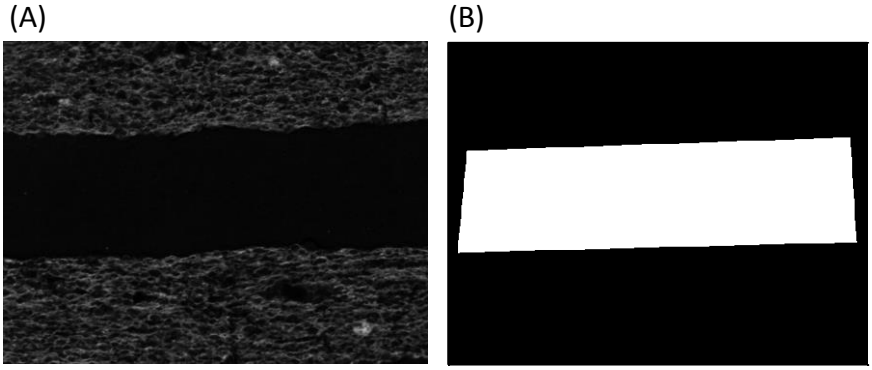

Figure 5-8 (A) Fluorescence image of puff pastry and (B) the areas used for obtaining the reference butter FF.

5. 3. 7 Visualization of gluten, starch, and butter by similarity angle

The similarity angles of FFs of each pixel in the puff pastry image and the reference FFs of gluten, starch and butter were calculated as explained in chapters 5 [9, 10] and similarity images were created. Similarities to gluten, starch and butter were shown in red, green and blue, respectively.

5. 3. 8 Visualization of gluten, starch, and butter by PCA

PCA was applied to all the FFs in the pie pastry image. PC scores for PC 1, 2 and 3 were converted into color by the same method used for cosine similarity [10] (Figure 5-9). The correlation coefficients of PC 1, 2 and 3 were used to interpret the meaning of the PCs.

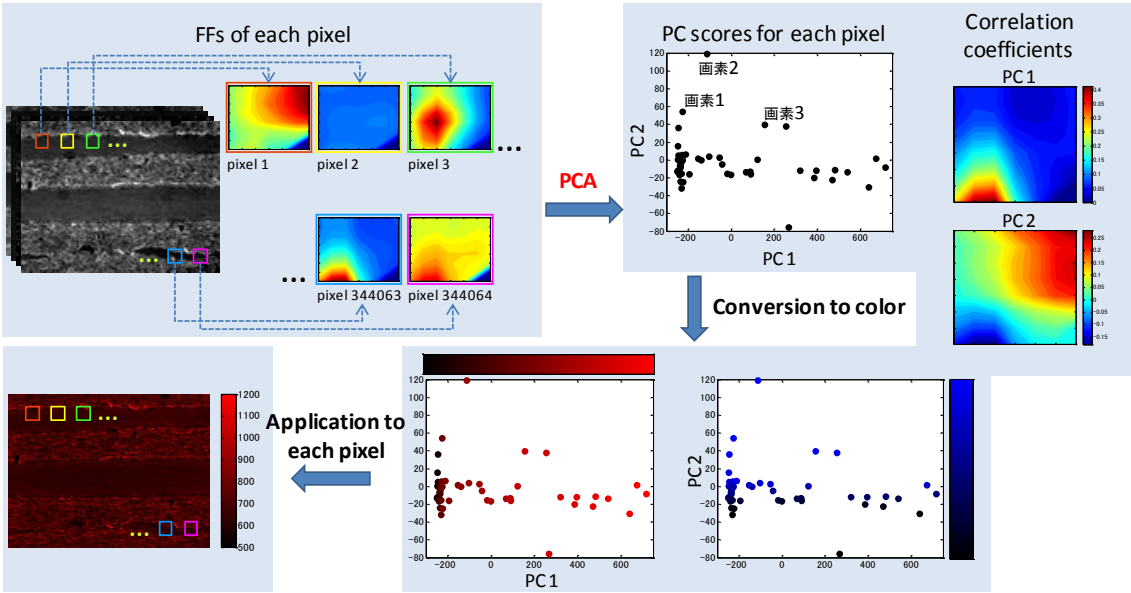

Figure 5-9 Flowchart of imaging by PCA. The FFs of each pixel in the pie pastry image are analyzed by PCA and each pixel is colored based on the PC scores. The correlation coefficients take the form of FFs and can be used to interpret each PC.

5. 3. 9 Visualization of gluten, starch, butter and aleurone fragments by spectral unmixing

Spectral unmixing is a collective term for methods to decompose observed spectra into a collection of constituent spectra, or endmembers, and a set of corresponding fractions, or abundances, that indicate the proportion of each endmember present in the pixel [11]. In this research, the endmembers would be the spectra of gluten, starch and butter. By unmixing the FFs of each pixel in the pie pastry images, the content of the three constituents at each pixel can be calculated, and a distribution map for each constituent can be obtained.

Many spectral unmixing techniques based on the linear mixing model have been developed in recent decades [12, 13, 14], and two methods were used in this study, constrained least squares method and non-negative matrix factorization [15, 16, 17, 18].

Constrained least squares method

This method requires the endmembers to be known and assumes that the spectra of all the pixels in the sample can be expressed as a mixture of these endmembers. If appropriate endmembers can be acquired, least squares inversion is performed with dual physical constraints, full additivity (the sum of constituent abundances in one pixel equals 1) and non-negativity (all abundances are equal to or larger than 0). This corresponds to solving the following problem:

$$\begin{aligned} &\underset{\boldsymbol{\alpha}}{\operatorname{argmin}} \frac{1}{2} \|\mathbf{y} - \mathbf{D}\boldsymbol{\alpha}\|_2^2 \\ &\text{subject to } \boldsymbol{\alpha} \geq 0, \sum_{i=1}^{m} \alpha_i \leq 1 \end{aligned} \qquad \text{... (1)}$$

when $\mathbf{y} \in \mathbb{R}^{\mathrm{L}}$ is the observed spectra, and $\mathbf{D} \in \mathbb{R}^{\mathrm{L}\times\mathrm{M}}$ and $\boldsymbol{\alpha} \in \mathbb{R}^{\mathrm{L}}$ are the endmember and abundance matrices, respectively. The lower index of the norm indicates that this is an Euclidean norm. This can be formulated as

$$\begin{aligned} &\underset{\boldsymbol{\alpha}}{\operatorname{argmin}} \left(\frac{1}{2}\right) \boldsymbol{\alpha}^{\mathrm{T}}\mathbf{D}^{\mathrm{T}}\mathbf{D}\boldsymbol{\alpha} - \mathbf{y}^{\mathrm{T}}\mathbf{D}\boldsymbol{\alpha} \\ &\text{subject to } \mathbf{G}\boldsymbol{\alpha} \leq \mathbf{h} \end{aligned} \qquad \text{... (2)}$$

where $\mathrm{G} = \begin{bmatrix} -\mathbf{I} \\ \mathbf{1}^{\mathrm{T}} \end{bmatrix}$ $(\mathbf{I} \in \mathbb{R}^{\mathrm{M}\times\mathrm{M}}, \mathbf{1} \in \mathbb{R}^{\mathrm{M}})$ and $\mathrm{h} = [\mathbf{0}^{\mathrm{T}} \quad 1]^{\mathrm{T}} (\mathbf{0} \in \mathbb{R}^{\mathrm{M}})$. This is solved by optimization methods for quadratic programming, such as active-set [19] and interior-point [20] methods.

Since abundances can be calculated unambiguously from the endmembers, choosing them is the most important step. In this research, we experimented with different endmembers for gluten, starch and butter, and compared the results.

- Gluten 1: the average FF from the fractionated gluten sample was used.
- Gluten 2: the endmember spectrum was extracted by Vertex Component Analysis (VCA) [21]. VCA extracts candidates for endmembers by projecting the data onto subspaces and choosing the vertices of the data group. The subspaces are determined by dimensionality reduction algorithms such as PCA, singular value decomposition (SVD) and maximum-noise fraction (MNF).

- Starch 1: the average FF from the fractionated starch was used.
- Starch 2: a small area corresponding to a starch granule in the pie pastry image was selected manually, and the FFs of the pixels in this area were averaged.

- Butter: the average FF from the butter layer area in the puff pastry was used.

Non-negative matrix factorization (NMF)

NMF assumes that the endmembers are unknown and that there are no pure pixels (pixels that contain only one constituent and whose spectrum could therefore be used as an endmember) in the sample image. NMF uses endmember spectra determined by methods such as VCA as initial values. The initial endmember values and the corresponding abundances are updated by alternate optimization, while satisfying the non-negativity and full additivity constraints.

The endmember data used for the constrained least squares method were used as the initializing values for NMF. Alternate optimization of the endmember and abundance matrices was performed, and the abundance map was obtained [22].

5. 4 Results and discussions

5. 4. 1 Selection of slide glass type

As a pre-experiment, slide glasses were measured for their intrinsic fluorescence. Three types of slide glasses, S-2111 (non-coat), S-8215 (APS-coat), and S-9902 (MAS-GP-coat) were measured, both with the imaging system and spectrophotometer (F7000). Figure 5-10 shows the fluorescence images of pie pastry on the three slide glasses and the FFs (measured by the spectrophotometer) of the slide glasses, background and gluten samples. The color scale is shown in log-scale, so that a difference in one indicates a 10 times difference in fluorescence intensity. S-8215 and S-9902 are slide glasses that are coated for enhanced adhesiveness. Compared to the non-coated slide glass, the fluorescence emitted from the glass seems to be suppressed. Although the fluorescence from the non-coated slide glass is weaker than gluten in order of approximately three, it is still strong enough to influence the fluorescent image. Slide glasses, S-8215 and S-9901 were used for further imaging experiments.

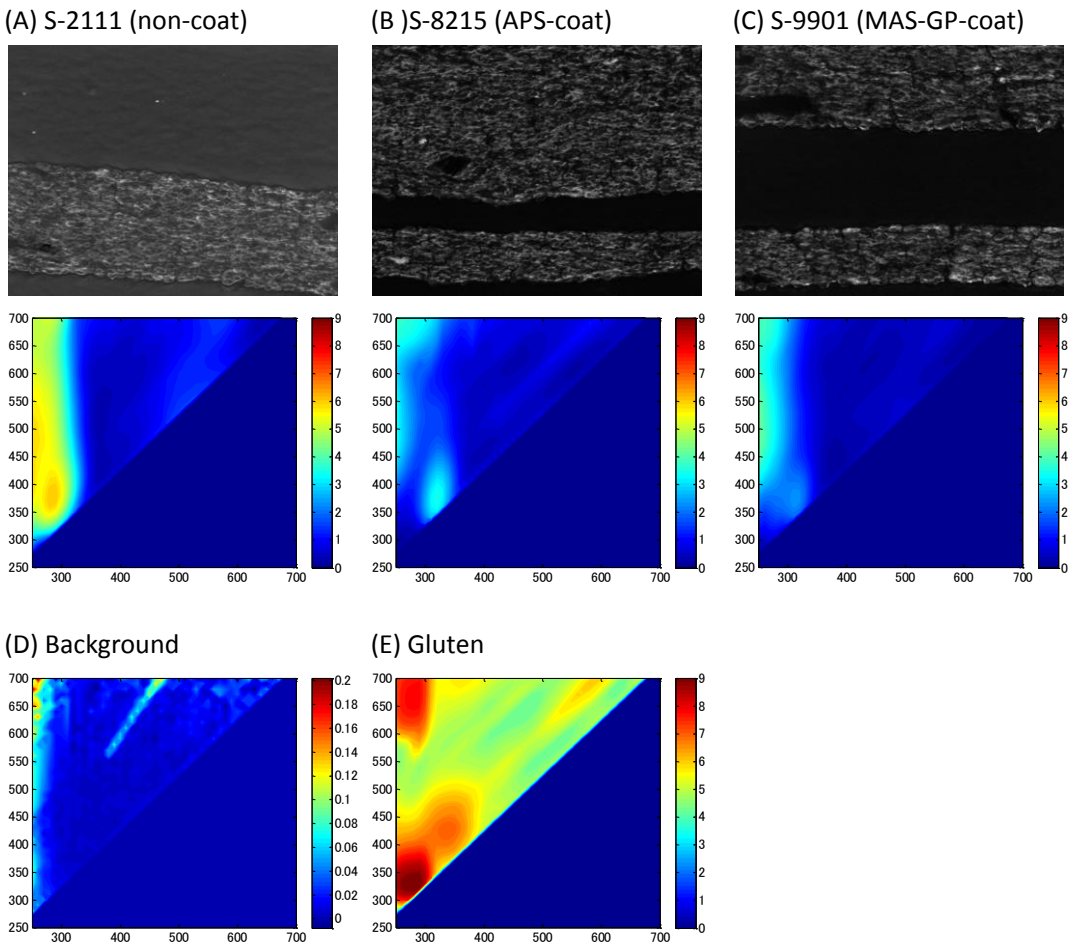

Figure 5-10 (A), (B) and (C) show the fluorescence images at Ex280 and Em350nm of pie pastry on slide glasses S-2111, S-8215 and S-9901, respectively (top row), and FFs of the slide glass measured in reflectance mode of the spectrophotometer. (D) and (E) show FFs of the background and gluten, respectively. The color scale is shown in log scale. Note that the scale for the Background is from 0 to 0.2.

5. 4. 2 Fractionation results

The first fractionation experiment based on the method by Macritchie [7] yielded 23.27 g of gluten, 48.01 g of primary starch and 20.31 g of tailing starch. The water content of these samples were 65.00% (n=4), 1.74% (n=2), and 1.71% (n = 2), respectively. The water content of the original flours were also measured, resulting in 12.45% and 12.44% for the weak and strong flours, respectively. Therefore the yield of fractionated substances was 85.85% and the ratio of gluten to starch was 10.68% to 89.32%. The yield loss is assumed to be small pieces of gluten and starch granules that

were washed away with the water, and water soluble proteins and sugars.

Figure 5-11 shows light microscopic images and FFs of starch obtained by the method of Macritchie [7] (A) and Whistler and Wolfrom [8] (B). The white arrows in (A) indicate small lumps of gluten that were mixed with the starch granules. Starch obtained by the second method few of these lumps.

The fluorescence from gluten (Ex280, Em330) and ferulic acid (Ex350, Em400) [23] was observed strongly in starch (A), but much weaker in starch (B). This indicated that starch (B) was more deprived of proteins and cell wall structures than starch (A). Therefore, starch (A) was used for further studies.

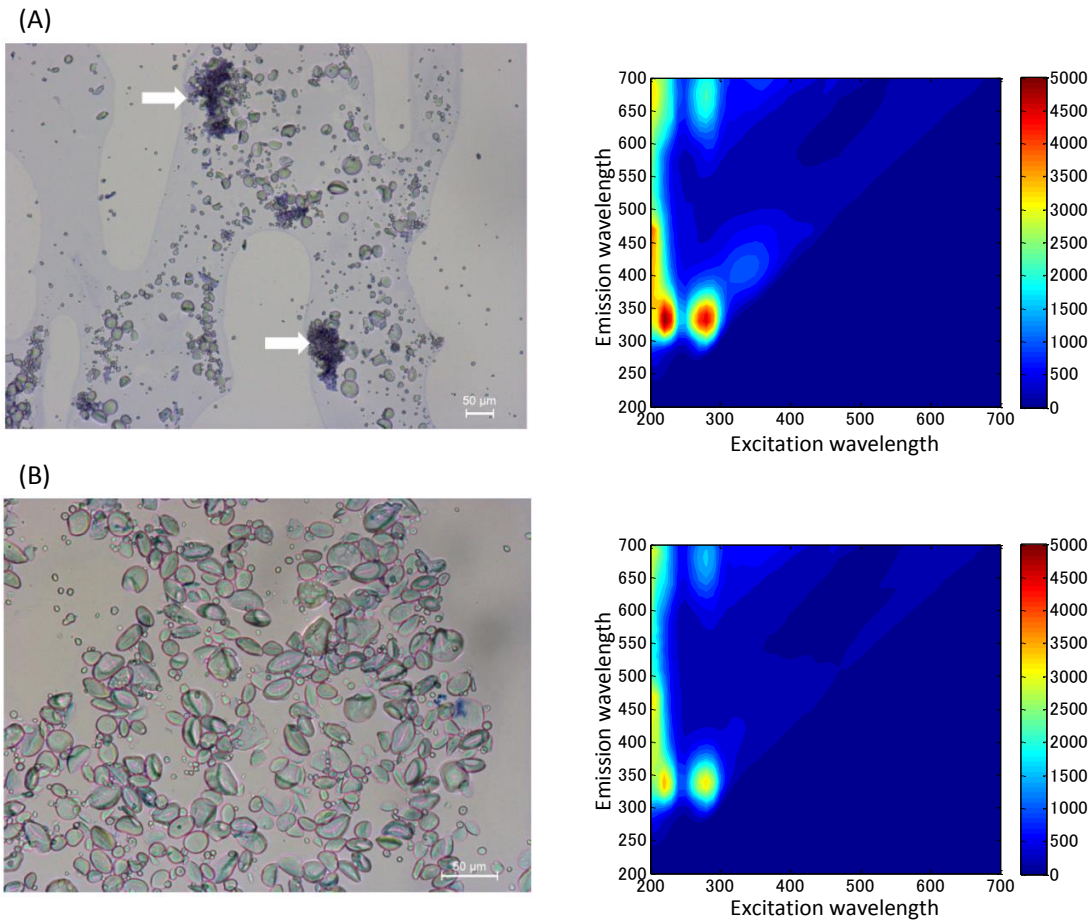

Figure 5-11 Light microscopic images (right) and FFs (left) of starch obtained by the first (A) and second (B) method.

5. 4. 3 Wavelengths for imaging

Figure 5-12 shows the results of the PCA of butter, gluten and starch samples. The

score plot (A) shows that both principal component (PC) one and two are effective in separating the fluorescence of the three components. Coefficients are the weights that map the original fluorescence data to each score. A large absolute value indicates a large contribution of the variable to the scores, meaning that it is effective in separating the three constituents. Therefore, wavelength conditions were selected in order of their PC one and two coefficients until the number of excitation or emission wavelengths reached the maximum of eight. As a result the excitation and emission wavelengths shown in Table 5-2 were selected to use for imaging.

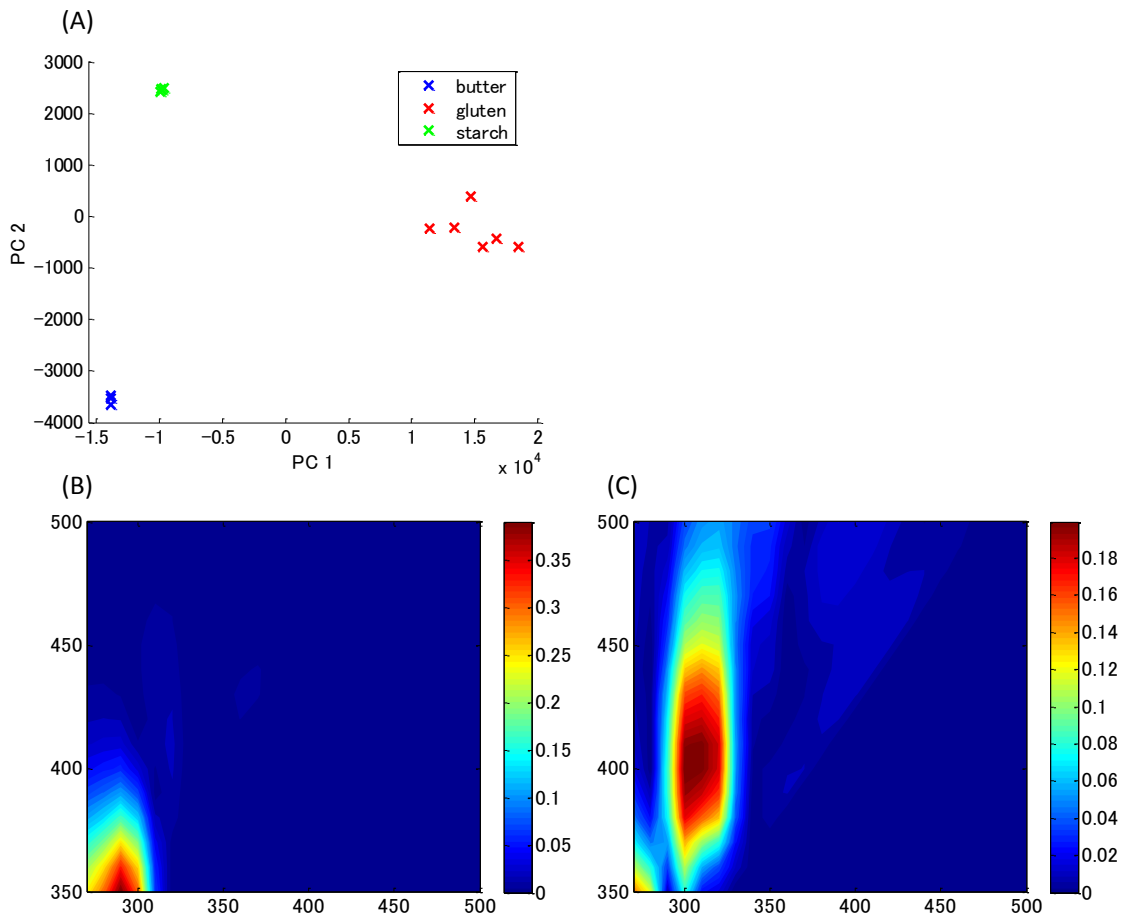

Figure 5-12 Results for the PCA of butter, gluten and starch samples. (A) Scatter plot for PC scores one and two. (B) and (C) Absolute values of PC one and two coefficients, respectively.

Table 5-2 Excitation and emission wavelengths selected for imaging

No.	Excitation [nm]	Emission [nm]
1	270	350
2	280	360
3	290	370
4	300	380
5	310	390
6	320	400
7	330	410
8		420

5. 4. 4 FFs of reference data

Figure shows the reference data of gluten, starch and butter. Gluten shows the typical fluorescence pattern of aromatic amino acids, mainly tryptophan, which has a peak at typically Ex 280 and Em 350 nm. Figure 5-14 shows the fluorescence image at Ex 280 and Em 350 nm. The thin thread-like features are the well-developed gluten strands.

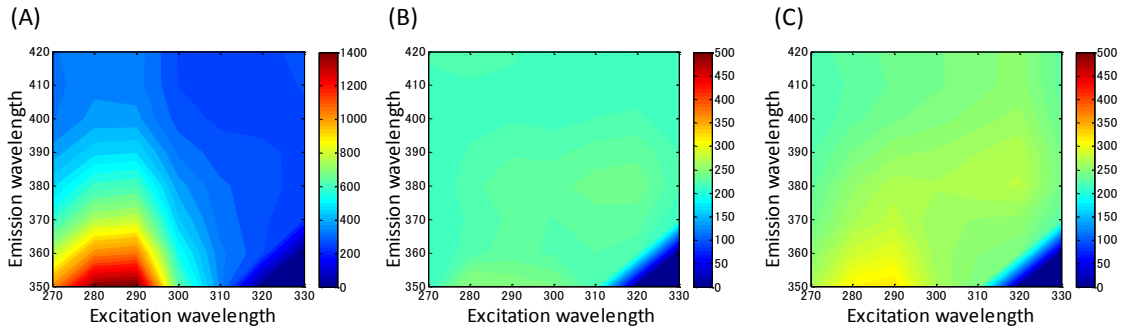

Figure 5-13 Reference FFs of gluten (A), starch (B) and butter (C). Note that the color scales for starch and butter are different from that of gluten

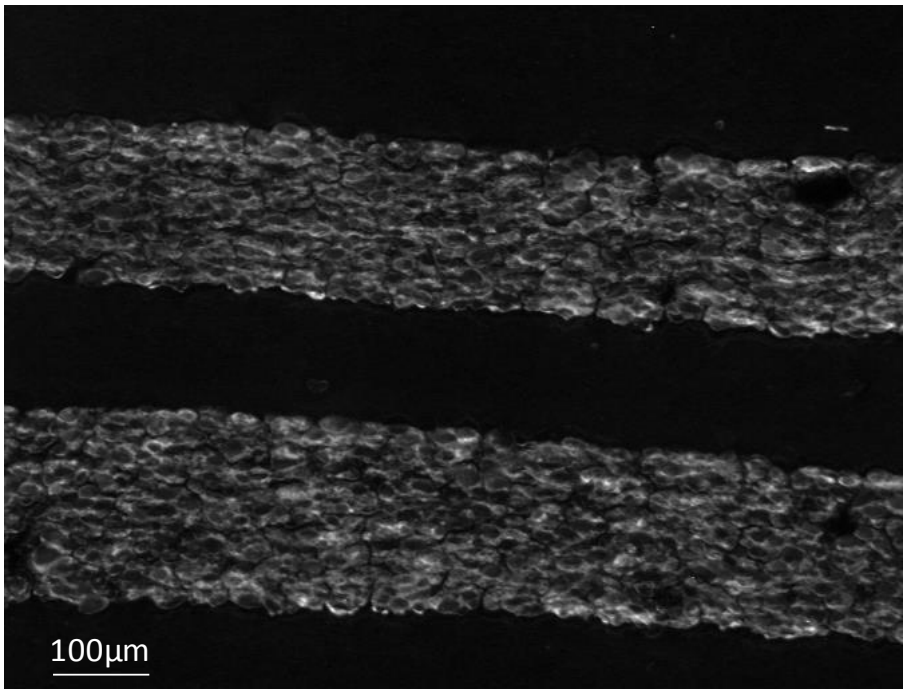

Figure 5-14 Fluorescence image of puff pastry at Ex 280, Em 350 nm. White thread-like structures are gluten strands.

Starch and butter show very low fluorescence intensity, and do not have a characteristic pattern. Butter is known to contain fluorophors such as carotenoids, and the fluorescence from these constituents can be measured with a fluorescence spectrophotometer if the sample is thick enough (approximately 2 mm thickness). However, the fluorescence becomes very weak when the sample is thinly sliced and is hardly detectable with the FF imaging system.

Amylose and amylopectin in starch are not fluorescent, since all their molecular bonds are σ bonds. However, starch granules are detectable (as shown in Figure 5-7) against the background of compound. There are two possible reasons for this detectability, the first is that starch granules are known to have a thin protein membrane on their surface [24] and this shows weak fluorescence. The second possibility is that we are observing reflected or diffused light (excitation wavelength equal to emission wavelength) which has passed through the band-pass filters. As explained in chapter 2, actual filters do not completely shut out light outside the band-pass wavelengths. As a result, a small portion of the light transmitted through the excitation band-pass filter may directly pass thorough the emission band-pass filter after being reflected by the starch granule.

5. 4. 5 Visualization of distribution by similarity angle

Figure shows the similarity angle image to gluten, starch and butter. The distribution image of gluten shows decent results, the pixels in the butter layer are dark and there are bright areas in the dough layer. However, the distribution image of butter and starch are almost identical. The pixels in the butter layer show a large similarity to starch.

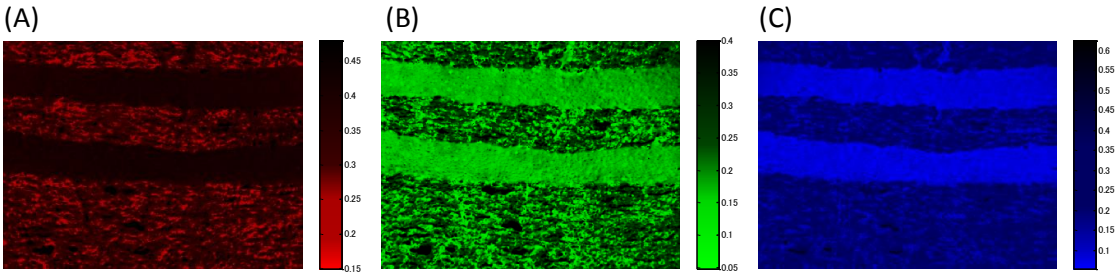

Figure 5-15 Similarity angle images to gluten (A), starch (B) and butter (C). A similarity angle takes a maximum of 0.

This is thought to be because there is a large difference in fluorescence between the fractionated starch which is used as the reference and the starch granules in the pie pastry. The fractionated starch which is used as the reference has almost no fluorescence, since it is almost completely derived of protein fragments. On the other hand, starch in the pie dough is covered with soluble proteins and thin layers of gluten and shows moderately strong fluorescence.

To explore the difference in fluorescence, several areas that corresponded to starch and butter in the pie pastry image were selected manually, and their cosine similarities to reference starch and butter were plotted (Figure 5-16). Since the reference butter FF is extracted from the pie pastry image itself, the butter pixels show a very high similarity value to reference butter. On the contrary, the starch pixels show low similarity to reference starch, and the butter pixels show similarity values in the same range.

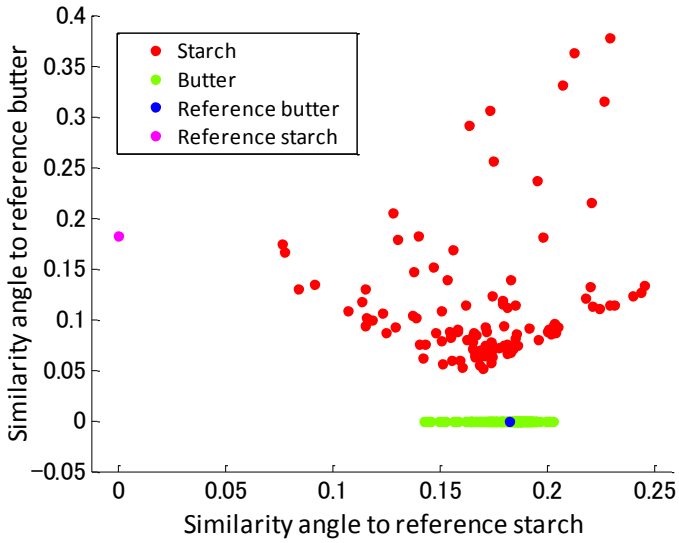

Figure 5-16 Plot of similarity angles of starch and butter to reference butter and reference starch. Pixels in the butter area have similarity angles near 0 degrees to reference butter. However, pixels in the starch area (in the puff pastry image) have similarity angles around 0.2 degrees to reference starch. Pixels in the butter area have similar angular values to reference starch.

This showed that the results of similarity angles relied mainly on the choice of reference data, and that similarity angles would not be an appropriate method to visualize constituents such as starch and butter which show only weak fluorescence and do not have a characteristic FF pattern.

5. 4. 6 Visualization of distribution by PCA

The largest difference between similarity angles and PCA is that the latter only uses the data from the puff pastry image. Therefore, the results are unaffected by the selection of reference data. However, the reference data can be used to interpret the results of PCA.

Figure 5-17 shows the distribution images created from the scores of PC 1, 2, and 3, and the corresponding coefficients.

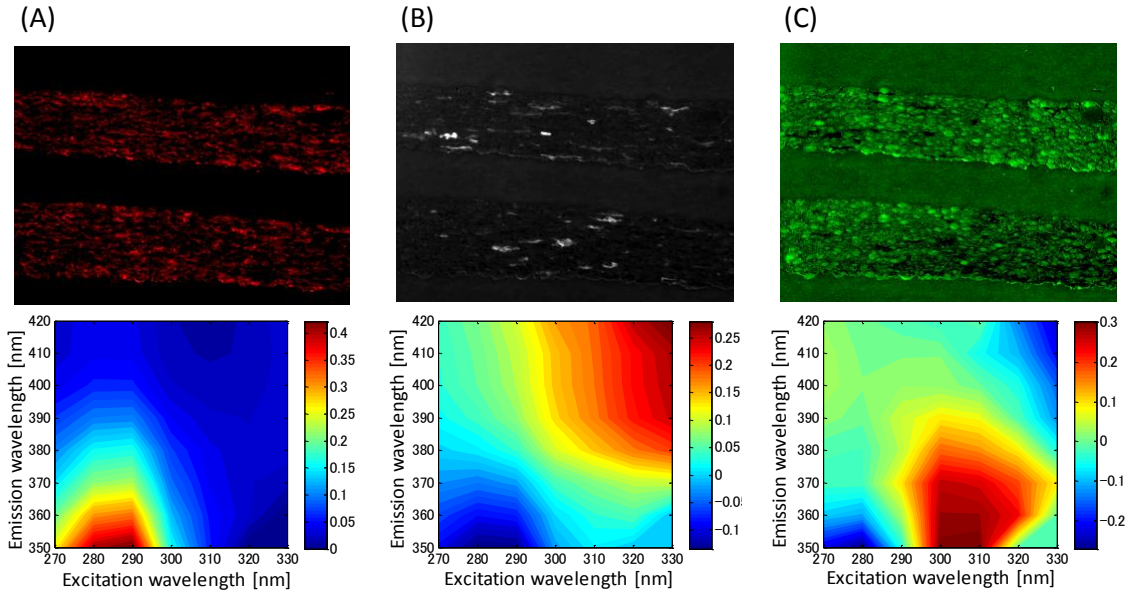

Figure 5-17 Distribution images of PC 1, 2 and 3 and the corresponding coefficients. The coefficient of PC 1 and 2 can be related to the FFs of gluten and ferulic acid, respectively. The distribution image of PC 3 show granular features, and is assumed to show starch granules.

The coefficient of PC 1 shows a similar pattern to the reference FF of gluten, and the strip-like features of the distribution image are very like that of gluten. Therefore, we concluded that PC 1 showed the distribution of gluten.

The coefficient of PC 2 shows high values in the longer wavelength conditions, and the distribution image shows strip like features. The fluorescence is presumed to be ferulic (4-hydroxy-3-cinnamic) acid [23] which is known to be contained in the aleurone cell walls, and fluoresces at Ex 350nm and Em 430nm. Although the fluorescence peak wavelengths are not included in our measurement, the high coefficient values in the longer wavelengths are assumed to show the tail of the fluorescent peak. Therefore, we concluded that PC 2 shows the distribution of ferulic acid.

The coefficients for PC 3 show a peak at Ex 300-310 and Em 350. However, there is no particular constituent that fluoresce in this region. On the other hand, granule-like features can be observed from the distribution image. Although interpretation of this PC is difficult, we judged from the distribution image that it had some element that distinguished starch from butter [25].

5. 4. 7 Visualization of distribution by spectral unmixing methods

NMF of puff pastry image

NMF was performed with two sets of initial endmember spectra as shown in Table 5-3. The number of endmembers used in the analysis is an important factor that determines the accuracy of the analysis. Although the three constituents of interest were gluten, starch and butter, it was necessary to add the fluorescence pattern of ferulic acid and the slide glass, in order to obtain decent results. The slide glass area corresponded to areas where there were air holes in the sample. When the samples were sliced, small holes were observed in the thin slice, where the slide glass could be seen though. Since the slide glasses were not completely fluorescence free and showed weak fluorescence, their FFs were included as one endmember.

Table 5-3 Initial endmember spectra for NMF

Constituent	set 1	set 2
gluten	fractionated gluten sample	fractionated gluten sample
starch	fractionated starch sample	starch granule from puff pastry image
butter	butter layer from puff pasty image	butter layer from puff pasty image
ferulic acid	extracted by VCA from puff pastry image	extracted by VCA from puff pastry image
slide glass	extracted from puff pastry image	extracted from puff pastry image

With endmember set 1, the reference FF of starch was obtained from the fractionated starch sample. Reference gluten was also obtained from the fractionated gluten sample. All the other references were extracted from the puff pastry image, manually for the butter and slide glass and automatically for the ferulic acid.

Figure 5-18 shows the distribution image for the four constituents, gluten, starch, butter and ferulic acid. Gluten and ferulic acid are visualized relatively well, probably due to their distinct FF patterns. The distribution image of starch shows granule-like features similar to starch, but also shows abundances in the pie layer, which is unlikely. The abundance values, ranging from 0 to 1, were very low for the starch image, with most of the pixels showing abundances lower than 0.5. The distribution image of butter shows thin, line-like abundances in the dough image, which is also unlikely.

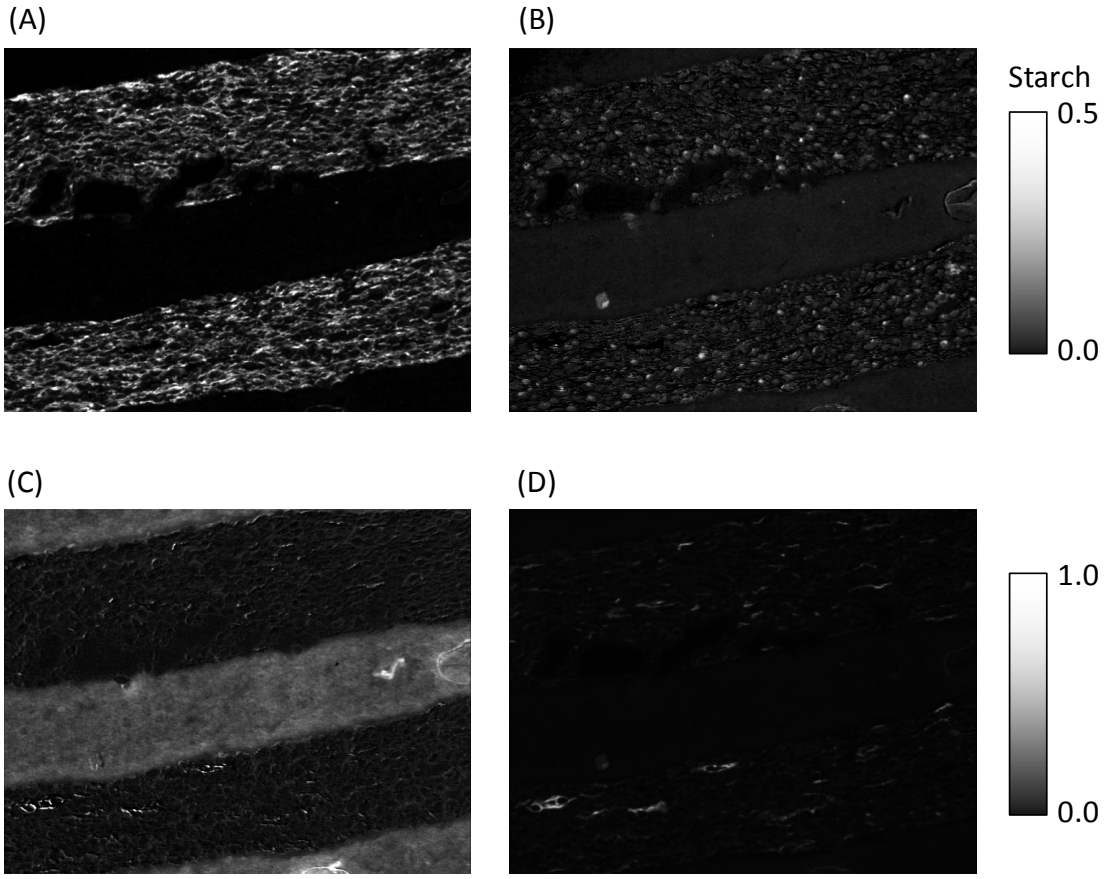

Figure 5-18 Abundance images of gluten (A), starch (B), butter (C) and ferulic acid (D). The grayscale for starch shows abundances ranging from 0.0 to 0.5 and those for the others shows abundances ranging from 0.0 to 1.0.

These problems were thought to be due to the dissimilarity between the reference FF of starch, extracted from the fractionated starch, and the starch in the puff pastry. Starch granules in the puff pastry show weak but clear fluorescence of tryptophan, suggesting that they are covered in some kind of protein fraction in the wheat. Since most of the protein is washed off in the fractionated starch, their FFs are different from the starch observed in the puff pastry.

Therefore, with endmember set 2, two small areas in the puff pastry image corresponding to starch granules were selected manually to create the reference FF of starch. The selected areas were clearly distinguishable as starch granules due to low intensity in the fluorescence image and circular morphology (Figure 5-19)

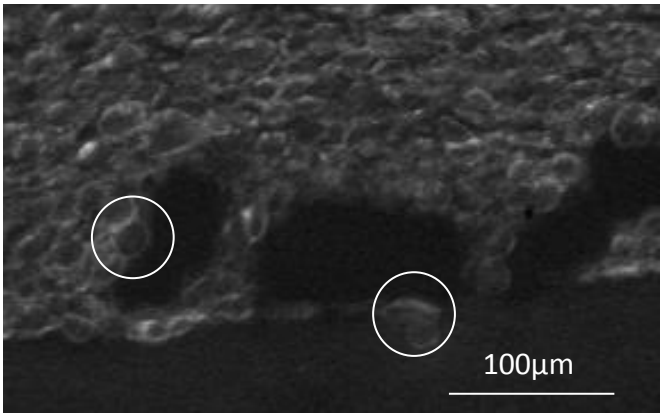

Figure 5-19 Two starch granules from where the endmember FFs were selected

By using this FF as one of the initial endmembers, a larger area was distinguished as starch granules the abundance became higher. Most of the line-like features in the butter image were eliminated (Figure 5-20).

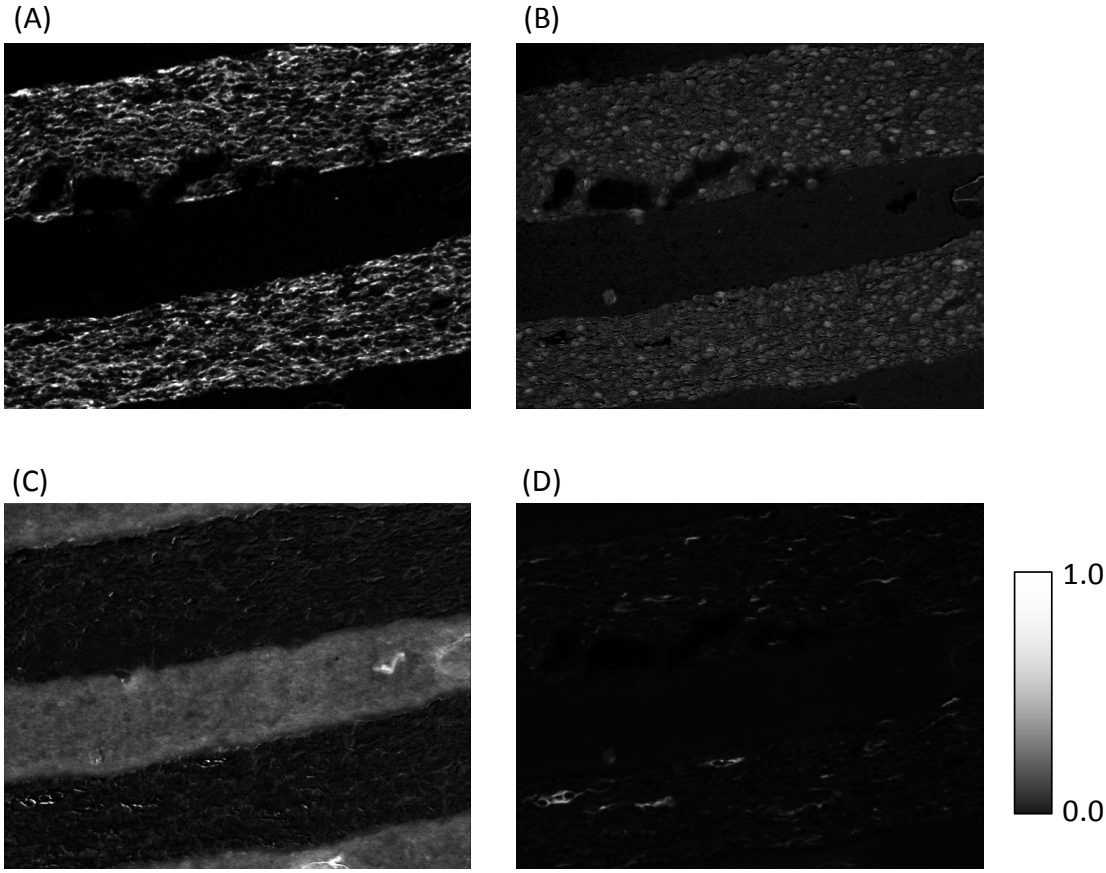

Figure 5-20 Abundance images of gluten (A), starch (B), butter (C) and ferulic acid (D) calculated with the starch FF extracted from the puff pastry image as an initial

endmember. The grayscale shows abundances ranging from 0.0 to 1.0.

Figure 5-21 shows the RGB image of the abundance image of gluten, starch and butter shown in R, G and B channels, respectively, and the stained image of the same sample. In the stained sample, fat and protein are colored orange and blue, respectively. The network of well-developed gluten and the starch granules trapped inside the network can be seen clearly.

(A) (B)

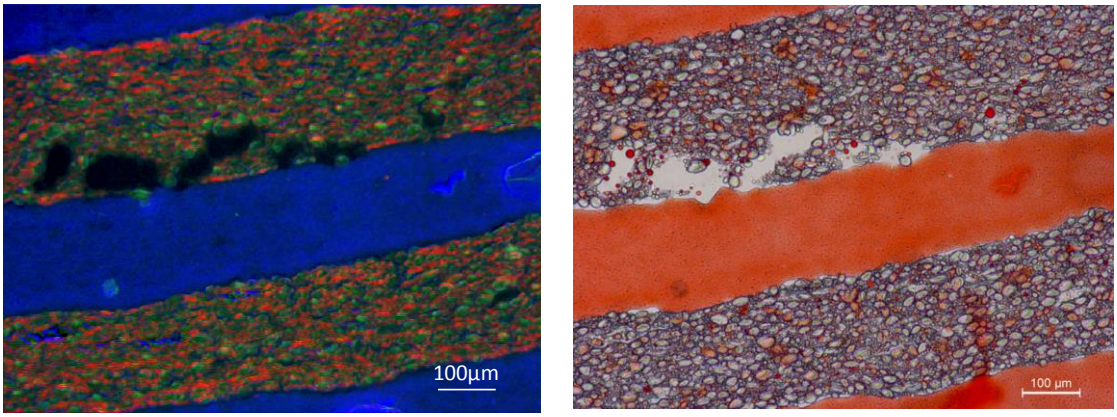

Figure 5-21 (A) RGB image of gluten (red), starch (green) and butter (blue) and (B) stained image of the same sample. The band of butter, air bubbles in the pastry, and matrix of gluten can be observed clearly.

Extracting the reference FF of starch manually from the puff pastry itself may seem subjective, since it relies on the analyzer to perceive the features of the starch granule. However, as can be seen from the figure, the starch granule used for the reference was very clearly observable, compared to most other granules. Only a few pixels were selected from this starch granule to create the reference FF, which in turn enabled the visualization of all the other starch granules.

Methods of extracting endmember spectra have been discussed in many papers [26, 27]. Manual and automatic endmember extraction both have their strength and weaknesses. In the case of starch FF extraction, automatic methods would not work well, since the fluorescence intensity of starch is very weak and the FF does not have a typical pattern. However, there may have been more objective methods for manual extraction, which would be more suitable in the future.

Visualization by the constrained least squares method

Although NMF performed very well for the puff pastry, it could not distinguish the constituents in short pastry, where the butter is mixed into the wheat dough instead of existing in layers. The similarity of the FFs of starch and butter (both show weak fluorescence and no characteristic peak) meant that alternative calculations in NMF resulted in FFs that were different from the original FFs.

Therefore, the reference FFs were kept constant, and the abundance images were calculated by constrained least squares method. Figure shows the abundance images of gluten, starch, butter, ferulic acid, and slide glass in short pastry.

Since the image obtained from this method were quite different from realistic assumptions, the method was improved in two ways: the endmember FF of gluten was extracted from the short pastry image by VCA, in the same method as that for ferulic acid, and a constraint was applied on the abundances of “slide” to be either 0 (the slide is covered with the short pastry) or 1 (there is no sample on the slide).

The endmember FF that was extracted from the fractionated gluten showed the same characteristics as the gluten in the short pastry image. However, the fluorescence intensity was much higher in the fractionated gluten, since the density of aromatic amino acids such as tryptophan was much higher. Using this reference FF as an endmember resulted in an abundance image where the distribution of gluten was roughly correct but the absolute quantities were far from realistic values. Since there is a constraint on the sum of abundance fractions in one pixel, quantities of one constituent affects the quantities of others, and therefore, all the other abundance matrices were distorted. We tried to solve this problem by extracting the endmember FF from the puff pastry image itself.

The quantum restraint on the abundances of slide were introduced in the calculation by altering the cost function in equation (1) to

$$\frac{1}{2}\|\mathbf{y}-\mathbf{D}\boldsymbol{\alpha}\|_2^2+\frac{1}{2}\lambda\left(\alpha_{\mathrm{slide}}-\mathrm{U}\left(\alpha_{\mathrm{slide}}-\frac{1}{2}\right)\right)^2 \qquad \text{... (3)}$$

where $U(x)$ is a step function that is expressed as

$$U(x)=\begin{cases}0, & x<0\\ 1, & x\geq 0\end{cases} \qquad \text{... (4)}$$

The second term is added only to the slide data. This optimization becomes the following minimization:

$$\underset{\boldsymbol{\alpha}}{\operatorname{argmin}} \begin{cases} \left(\frac{1}{2}\right)\boldsymbol{\alpha}^{\mathrm{T}}(\mathbf{D}^{\mathrm{T}}\mathbf{D}+\lambda\mathbf{C})\boldsymbol{\alpha}-\mathbf{y}^{\mathrm{T}}\mathbf{D}\boldsymbol{\alpha}+\left(\frac{1}{2}\right)\mathbf{y}^{\mathrm{T}}\mathbf{y} & \alpha_{\mathrm{i}} \leq 1/2 \\ \left(\frac{1}{2}\right)\boldsymbol{\alpha}^{\mathrm{T}}(\mathbf{D}^{\mathrm{T}}\mathbf{D}+\lambda\mathbf{C})\boldsymbol{\alpha}-(\mathbf{y}^{\mathrm{T}}\mathbf{D}+\lambda\mathbf{b}^{\mathrm{T}})\boldsymbol{\alpha}+\left(\frac{1}{2}\right)(\mathbf{y}^{\mathrm{T}}\mathbf{y}+\lambda) & \alpha_{\mathrm{i}} > 1/2 \end{cases} \quad \text{... (5)}$$

$$\text{subject to } \mathbf{G}\boldsymbol{\alpha} \leq \mathbf{h}$$

where $\mathbf{b} \in \mathbb{R}^{\mathrm{M}}$ has unit for b_{slide} and zero values for other components and $\mathbf{C} = \mathbf{b}\mathbf{b}^{\mathrm{T}}$. Both these functions are quadratic programming problems. In order to overcome the case statement, problem (1) (without quantum regularization) was optimized first, followed by either of the problems in (5) depending on the α_i value first obtained by optimization of (1).

Figure 5-22 shows the abundance images of ferulic acid, butter, starch, gluten and "slide" in short pastry. Abundances for "slide" are shown in black (abundance = 0.0) and white (abundance = 1.0), and abundances for the other constituents are shown in continuous values between 0.0 and 1.0. Figure 5-23 shows the abundance images of the same constituents in puff pastry. The image shows a band of butter sandwiched between two layers of wheat dough.

The two sets of images show distinct differences between the structures of short pastry and puff pastry. Apart from the obvious difference in the distribution of butter (mixed into the wheat dough or existing in layers), there is a large difference in the morphology of gluten. The gluten in the short pastry is observed in small and large clumps, whereas those in the puff pastry have formed a net-like structure, spread in the direction of dough extension (parallel to the layers of dough and butter). The net-like structure of gluten in the puff pastry is presumed to be due to the mixing of dough (6 minutes at medium speed) in the absence of fat. On the other hand, the flour for the short pastry is mixed directly to fat, which is known to inhibit the formation of gluten [28]. The small clumps of gluten in the short pastry are presumably aggregations of the protein fraction existing in the flour particles.

The size distribution of the "slide" areas are also very different. Short pastry shows many large voids compared to the small airspaces seen in the puff pastry. Puff pastry is rolled many times during its manufacture, and this would eliminate large voids. Consequently, short pastry is mixed only roughly, which leaves or even incorporates air in the dough.

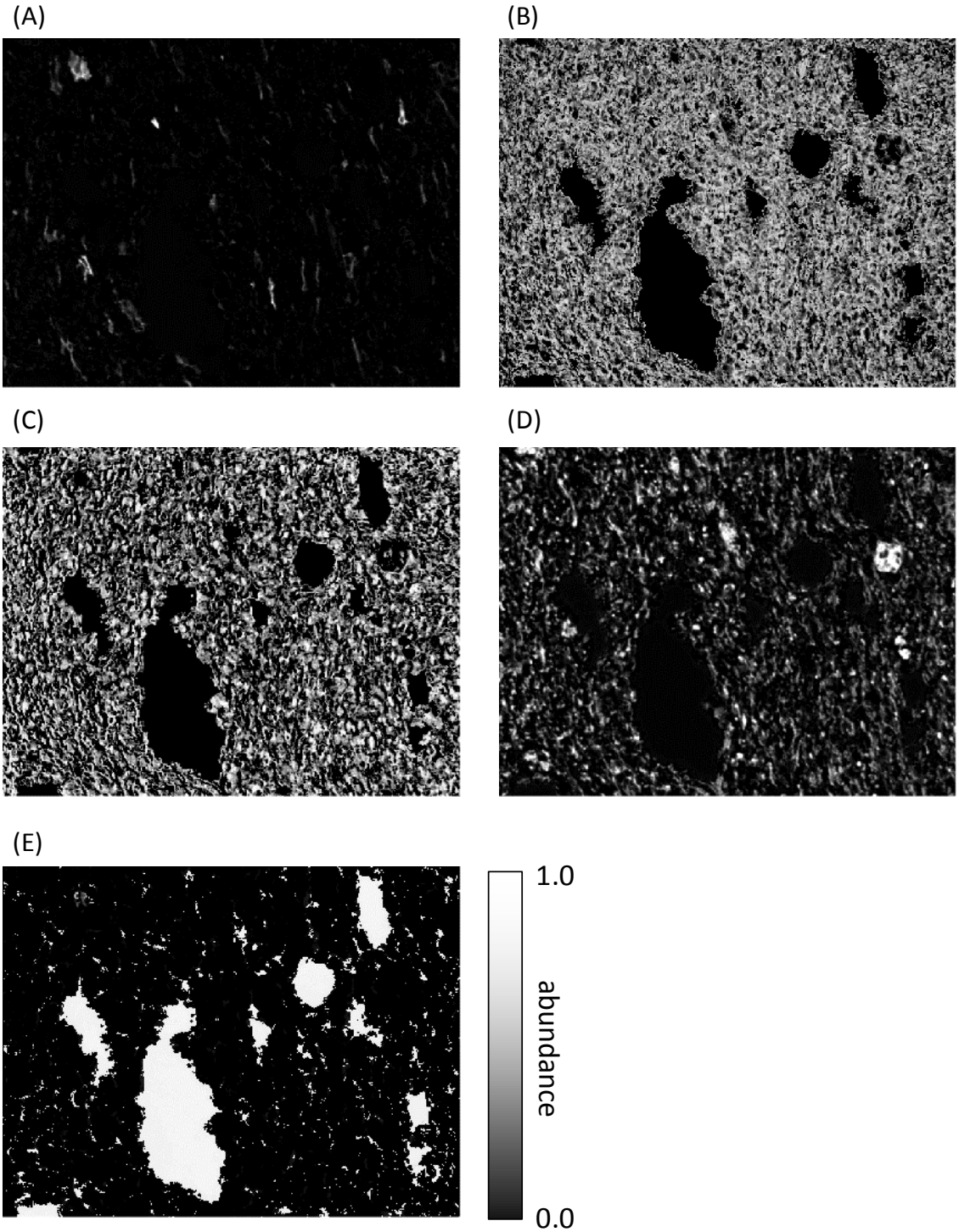

Figure 5-22 Abundance images of ferulic acid (A), butter (B), starch (C), gluten (D), and slide (E) in short pastry. The grayscale corresponds to an abundance of 1.0 (white) to 0.0 (black).

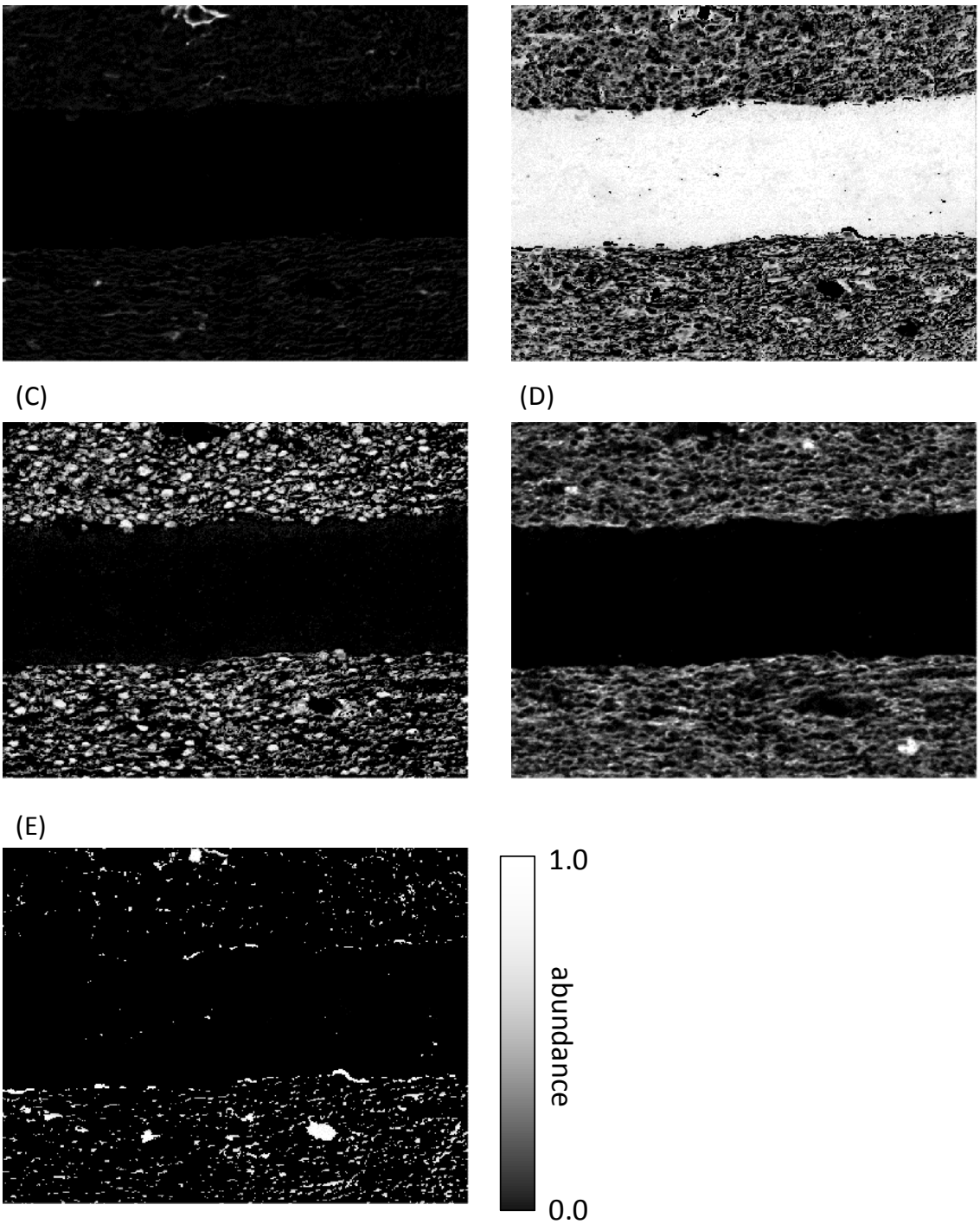

Figure 5-23 Abundance images of ferulic acid (A), butter (B), starch (C), gluten (D), and slide (E) in puff pastry.

In order to validate the analysis results, the short pastry was stained in the same way as the puff pastry. Figure 5-24 shows the composite image of butter, starch and gluten abundances shown in RGB and the corresponding stained image.

(A) (B)

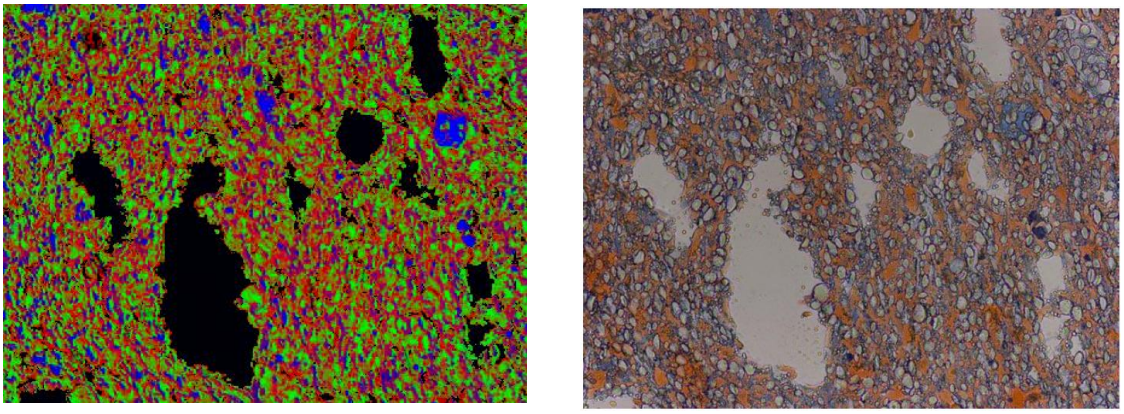

Figure 5-24 (A) Composite image of the abundance images of butter (red), starch (green) and gluten (blue), and (B) stained image of the same sample. Protein is stained blue and fat is stained orange.

Although the stained color of protein in the stained image is a little faint, large aggregates of gluten can be observed in both images. The positions of starch granules and fat in the analyzed image are largely correspondent with those of the stained image. Although the FFs of butter and starch were difficult to distinguish by visual judgment, it was possible to obtain their abundances accurately.

Compared to the stained image, the FF image seems to show a large quantity of butter. Therefore, the total quantity of gluten, starch and butter calculated from the abundance image was compared to the value calculated from the ratio of ingredients used for the pastry.

In the short pastry, 97 g of butter was mixed to 153 g of wheat flour dough. Around 20% of the wheat flour dough is gluten, and the rest, starch [29]. This means that the weight ratio of gluten, starch and flour is 12%:50%:38%. Since fluorescence intensity would be proportional to the volume of these constituents, the specific gravity of 1.1, 1.5 and 0.91 for gluten, starch and butter, respectively, was used to convert the ratio to volume ratio. This gave 12.7%:28.8%:48.5% for gluten, starch, and butter ratio.

On the other hand, the ratio calculated from the abundance matrix was 16.6%:37.6%:45.8% for gluten, starch and butter, respectively. This is very close to the ratio calculated from the ingredients of pie pasty, and seems to support the accuracy of the imaging method.

5. 5 Conclusions

In this study, FF imaging was used to visualize three constituents, gluten, starch and butter. In chapters 3 to 5, discriminations were made between gluten, which shows strong fluorescence, and starch, which shows little fluorescence. The third constituent, butter, made measuring and analysis very difficult because both starch and butter showed low fluorescence intensities.

This was overcome by applying spectral unmixing methods that decompose the FFs of each pixel into the product sum of FFs of pure constituents and their abundances. It was indicated that the results were better when the initial FFs of each pure constituent were derived from the pie sample rather than fractionated samples. With certain constraints such as non-negativity, unit summation (sum of abundances for one pixel equals one), and quantum restraints (abundances take values of 0 or 1), it was possible to discriminate between butter and starch, even when these two constituents were mixed together in a short pastry dough.

The results of this study are very significant because it indicates that a broad range of constituents have a possibility of being visualized with FF imaging, even constituents that show low levels of fluorescence. Imaging with autofluorescence is seemingly restricted compared to NIR or IR imaging because only samples that are fluorescent can be visualized. However, this study showed that many constituents that are categorized to be measured by vibrational information (measured by NIR and IR) such as starch and fat can actually be measured by fluorescence.

The results also indicate a possibility of simplifying the experimental scheme because there would be no need to acquire and measure “reference” samples such as fractionated starch and gluten every time a new experiment is performed. By accumulating FF data of pure constituents and creating a database, it would be possible to compare FFs of pure constituents and the “reference” FFs extracted from the sample, it would be possible to verify that the right constituents are being visualized (Figure 5-25).

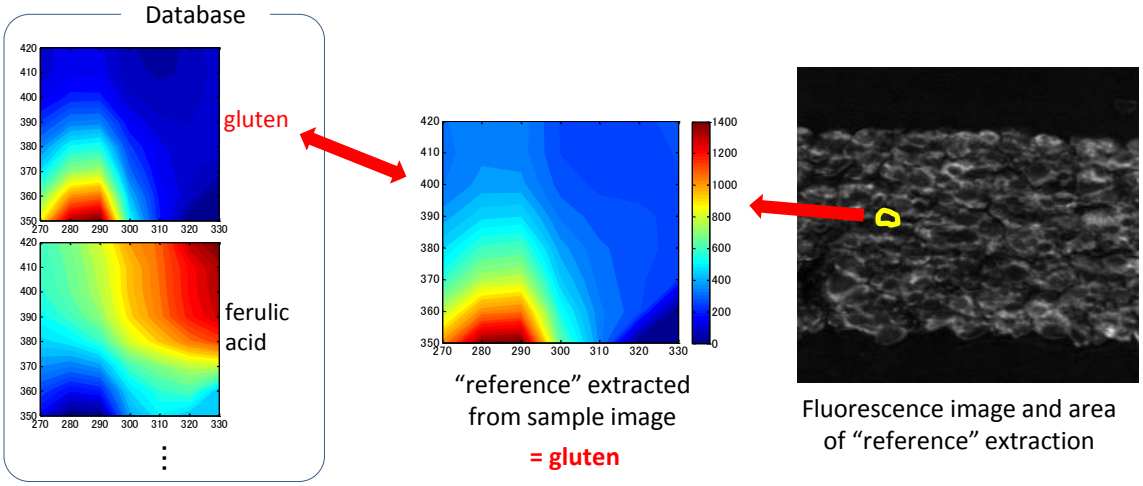

Figure 5-25 Scheme of FF data base. The "reference" used to analyze the image is extracted from the sample image itself, and the FF patterns are compared to the data base to confirm the actual constituent.

Finally, this study showed that FF imaging could be improved greatly by introducing analysis methods used mainly in the field of electronics and informatics. Since agro-engineering and food engineering has been based mainly on applications, there is much to learn from other areas of research.

References

1. Pareyt, B., Finnie, S.M., Putseys, J.A., Delcour, J.A., Lipids in bread making: Sources, interactions, and impact on bread quality. Journal of Cereal Science, (2011). **54**(3): p. 266-279.

2. Li, W., Dobraszczyk, B.J., Wilde, P.J., Surface properties and locations of gluten proteins and lipids revealed using confocal scanning laser microscopy in bread dough. Journal of Cereal Science, (2004). **39**(3): p. 403-411.

3. Cauvain, S.P., Young, L.S., Baked products: Science, technology and practice. (2006), Oxford: Blackwell Publishing Ltd. 228.

4. Ghotra, B.S., Dyal, S.D., Narine, S.S., Lipid shortenings: A review. Food Research International, (2002). **35**(10): p. 1015-1048.

5. Watanabe, A., Larsson, H., Eliasson, A.C., Effect of physical state of nonpolar lipids on rheology and microstructure of gluten-starch and wheat flour doughs. Cereal Chemistry, (2002). **79**(2): p. 203-209.

6. Sowmya, M., Jeyarani, T., Jyotsna, R., Indrani, D., Effect of replacement of fat with sesame oil and additives on rheological, microstructural, quality characteristics and fatty acid profile of cakes. Food Hydrocolloids, (2009). **23**(7): p. 1827-1836.

7. Macritchie, F., Studies of the methodology for fractionation and reconstitution of wheat flours. Journal of Cereal Science, (1985). **3**(3): p. 221-230.

8. Whistler, R.L., Wolfrom, M.L., eds. Methods in carbohydrate chemistry. Starch, ed. Whistler, R.L. Vol. 4. (1964), Academic Press: New York.

9. Kokawa, M., Fujita, K., Sugiyama, J., Tsuta, M., Shibata, M., Araki, T., Nabetani, H., Quantification of the distributions of gluten, starch and air bubbles in dough at different mixing stages by fluorescence fingerprint imaging. Journal of Cereal Science, (2012). **55**(1): p. 15-21.

10. Kokawa, M., Fujita, K., Sugiyama, J., Tsuta, M., Shibata, M., Araki, T., Nabetani, H., Visualization of gluten and starch distributions in dough by fluorescence fingerprint imaging. Bioscience Biotechnology and Biochemistry, (2011). **75**(11): p.

2112-2118.

11. Keshava, N., Mustard, J.F., Spectral unmixing. Signal Processing Magazine, IEEE, (2002). **19**(1): p. 44-57.

12. Keshava, N., A survey of spectral unmixing algorithms. Lincoln Laboratory Journal, (2003). **14**(1): p. 55-78.

13. Boardman, J.W. Geometric mixture analysis of imaging spectrometry data. in *Geoscience and Remote Sensing Symposium, 1994. IGARSS '94. Surface and Atmospheric Remote Sensing: Technologies, Data Analysis and Interpretation., International*. (1994).

14. Nascimento, J.M.P., Bioucas Dias, J.M., Does independent component analysis play a role in unmixing hyperspectral data? Geoscience and Remote Sensing, IEEE Transactions on, (2005). **43**(1): p. 175-187.

15. Pauca, V.P., Piper, J., Plemmons, R.J., Nonnegative matrix factorization for spectral data analysis. Linear Algebra and its Applications, (2006). **416**(1): p. 29-47.

16. Liu, S., Zhang, D.X., Liu, L., Wang, M., Du, G.C., Chen, J., Enhanced water absorption of wheat gluten by hydrothermal treatment followed by microbial transglutaminase reaction. Journal of the Science of Food and Agriculture, (2010). **90**(4): p. 658-663.

17. Miao, L.D., Qi, H.R., Endmember extraction from highly mixed data using minimum volume constrained nonnegative matrix factorization. Ieee Transactions on Geoscience and Remote Sensing, (2007). **45**(3): p. 765-777.

18. Jia, S., Qian, Y.T., Constrained nonnegative matrix factorization for hyperspectral unmixing. Ieee Transactions on Geoscience and Remote Sensing, (2009). **47**(1): p. 161-173.

19. Gill, P.E., Murray, W., Saunders, M.A., Wright, M.H., Procedures for optimization problems with a mixture of bounds and general linear constraints. ACM Trans. Math. Softw., (1984). **10**(3): p. 282-298.

20. Gondzio, J., Presolve analysis of linear programs prior to applying an interior point method. INFORMS Journal on Computing, (1997). **9**(1): p. 73-91.

21. Nascimento, J.M.P., Bioucas Dias, J.M., Vertex component analysis: A fast algorithm to unmix hyperspectral data. Geoscience and Remote Sensing, IEEE Transactions on, (2005). **43**(4): p. 898-910.

22. Yokoya, N., Yairi, T., Iwasaki, A., Coupled nonnegative matrix factorization unmixing for hyperspectral and multispectral data fusion. Geoscience and Remote Sensing, IEEE Transactions on, (2012). **50**(2): p. 528-537.

23. Irving, D.W., Fulcher, R.G., Bean, M.M., Saunders, R.M., Differentiation of wheat based on fluorescence, hardness, and protein. Cereal Chemistry, (1989). **66**(6): p. 471-477.

24. Yoshino, Y., Hayashi, M., Seguchi, M., Presence and amounts of starch granule surface proteins in various starches. Cereal Chemistry, (2005). **82**(6): p. 739-742.

25. 粉川美踏，杉山純一，蔦瑞樹，藤田かおり，吉村正俊，柴田真理朗，荒木徹也，鍋谷浩志，光の指紋によるパイ生地中のグルテン・澱粉・バターの分布可視化, in *日本食品科学工学会平成２５年度関東支部大会*(2013.3.7) 東京，東京農業大学. p. 34.

26. Plaza, A., Martinez, P., Perez, R., Plaza, J., A quantitative and comparative analysis of endmember extraction algorithms from hyperspectral data. Geoscience and Remote Sensing, IEEE Transactions on, (2004). **42**(3): p. 650-663.

27. Bateson, A., Curtiss, B., A method for manual endmember selection and spectral unmixing. Remote Sensing of Environment, (1996). **55**(3): p. 229-243.

28. Figoni, P., How baking works exploring the fundamentals of baking science. 2 ed. (2008), New Jersey: John Wiley & Sons, Inc. 399.

29. Kokawa, M., Sugiyama, J., Tsuta, M., Yoshimura, M., Fujita, K., Shibata, M., Araki, T., Nabetani, H., Fluorescence fingerprint imaging of gluten and starch in wheat flour dough with consideration of total constituent ratio. Food Science and Technology Research, (2013).

6. Conclusions and future perspectives

6. 1 The development of FF imaging through this thesis

As is discussed in chapters 3 to 6, the FF imaging method has been developed through this thesis in two main aspects, imaging acquisition method and analysis method. The development in the image acquisition method has been mainly explained in chapter 2, and this section will summarize the development in the analysis method.

Table 6-1 summarizes the analysis methods used in this thesis.

Table 6-1 Summary of the analysis methods used in chapter 3 to 6

	Analysis method	Data required to construct model	Advantages and Disadvantages
Chapter 3	PLS	FFs of samples with different constituent ratios	○ accurate prediction possible × difficult to acquire data required for model construction
Chapter 4	cosine similarity	FFs of reference	○ straightforward and intuitive × qualitative
Chapter 5	similarity angle		× only relative values can be acquired
Chapter 6	NMF, constrained least squares	FFs of reference (optional)	○ analysis can be performed with data of sample only ○ abundances can be obtained as absolute values × only applicable to linear models

The ideal analysis method would not need any initial information such as the FFs of references, and would calculate the amount of each constituent accurately and quantitatively. PLS regression used in chapter 3 accurately connects the FFs of each pixel to the ratio of gluten to starch, but samples with a large range of gluten to starch ratio are needed to construct an accurate PLS model, and this is difficult with real samples.

Cosine similarity and the similarity angle used in chapters 4 and 5 are much easier to apply than PLS, and has been used in areas of remote sensing by the name of spectral angle mapping (SAM). The accuracy of this method relies on the selection of “reference” data. Cosine similarity works well in situations where the constituents to be visualized have completely different FFs such as gluten and starch. However, it cannot discriminate between constituents whose FFs are similar, as shown in chapter 6. In addition, the values of similarity are not directly connected to the actual quantities of the constituents, and results are largely qualitative.

Spectral unmixing methods such as NMF and constrained least squares used in chapter 6 stand between the former two methods, enabling quantitative analysis without having to prepare multiple samples. With constrained least squares, it was possible to discriminate between starch and butter, which both showed weak fluorescence. Furthermore, the reference FFs of each constituent were shown to be extracted from the sample itself, meaning that other samples such as fractionated starch and gluten were unnecessary. Concerning applicability and accuracy, these spectral unmixing methods are best suited as the analysis method for FF imaging.

6. 2 Advantages and drawbacks of FF imaging

This thesis has shown the theories and applications of fluorescence fingerprint (FF) imaging, an imaging method which can be categorized as a type of hyperspectral imaging. However, FF imaging has distinct advantages which should be highlighted in this chapter:

1. The achievable spatial resolution is higher than most hyperspectral imaging methods. This is illustrated by figure 1-21 in chapter 1. Compared to near-infrared (NIR), fluorescence shows high sensitivity, and therefore, the thickness of sample can be reduced greatly (10 μm for fluorescence compared to over 100 μm for NIR). This enables the acquisition of clear images at high resolution. Furthermore, scattered light, which lowers the spatial resolution in imaging methods measuring the absorption of light, is cut out in fluorescence images. Therefore it is possible to visualize granular structures such as starch at the same high spatial resolution as other non-granular structures.

2. Sample preparation does not have to be as precise as other hyperspectral imaging methods, when comparing samples visualized in the same magnification. Methods such as infrared (IR) imaging with an attenuated total reflection (ATR) accessory can achieve high spatial resolution, but the samples need to be completely flat. This requires preprocessing steps such as sample immobilization. Chapter 3 showed that FF imaging requires the sample to be made into thin slices if microscopic features are to be visualized. However, if the desired thickness is realized, small irregularities on the surface (such as those due to granular structures) affect the image relatively weakly.

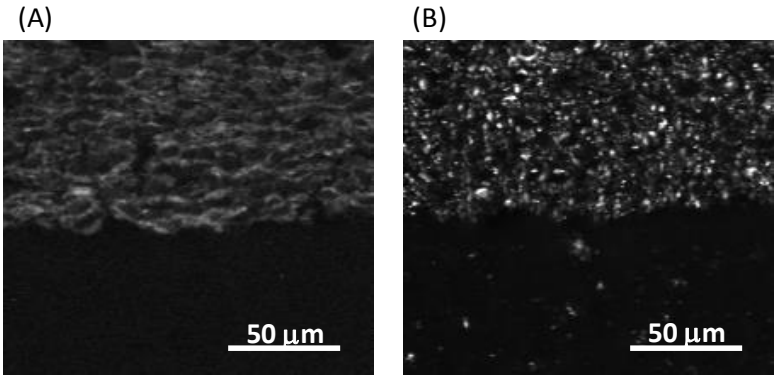

Figure 6-1 Fluorescence (A) and reflectance (B) images of the same puff pastry.

This is shown in Figure 6-1 where the same sample is observed in fluorescence mode (emission wavelength ≠ excitation wavelength) and reflectance mode (emission wavelength = excitation wavelength). The fluorescence image shows thin strands of gluten surrounding the black starch granules in the top half, and a dark area in the bottom half where there is a layer of butter. The image shows a flat sample where light intensities are proportional to the amount of fluorescent molecules. In the reflectance image, small specks of light can be seen, which do not correspond to the starch granules. This is because the surface of the starch granule facing the excitation light gets illuminated strongly, compared to the other areas, and this light is directly reflected into the camera. When observing with fluorescence, the light is initially absorbed and then, emitted. This indirect emission seems to lower the effect of surface irregularities.

3. Constituents that are known to be “non-fluorescent” (such as starch) can be observed due to traces of fluorescent constituents that exist together (such as protein membranes on the surface of starch granules). This is a significant characteristic of fluorescence “fingerprint” imaging, not fluorescence imaging with a single wavelength. It is especially true when FF imaging is applied to complex samples such as foods. “Starch” and “fat” in the chemical sense are not fluorescent since these molecules are made up of single bonds. However, in food systems, these constituents exist as complex assemblies, sometimes containing fluorophors such as aromatic amino acids and vitamins. FF measurement is basically a “non-targeted” method, where the wavelengths used for measurement are not linked to a specific target. Therefore, it is possible to capture “non-fluorescent” constituents by other constituents that fluoresce in

other wavelengths.

4. Measuring equipment is less expensive than most imaging methods. Since the FFs in this study are measured in the near-UV to VIS region, light sources, cameras and band-pass filters are much less expensive than other wavelength regions. Furthermore, FF imaging uses simple optical systems, compared to laser induced imaging methods etc. which makes it very affordable (see also figure 1-21).

Above are the advantages of FF imaging, compared to other imaging methods. On the other hand, there are also some disadvantages, which are listed below. The first two disadvantages are fundamental but the third can be overcome by improvement of the imaging system.

1. The sample needs to be made into thin slices for micro-scale features to be observed, which means that the imaging method is not completely non-destructive. This is due to the characteristics of near-UV to VIS light, which penetrates into the sample to a certain deepness which is larger than the scale of the features that we are aiming to visualize, such as starch granules. This phenomenon is shown in chapter 3, where we tried to visualize the distribution of gluten and starch with a sample that was not sliced.
   This does not apply to macroscopic samples, such as pork and beef slices, where the sample is measured directly with a macroscopic FF imaging system. In this case, the penetration of light into the sample is negligible.
   Observation of microstructures in bulk samples may be possible if a focusing device such as those used in confocal scanning laser microscopes (CSLM) are used. The coupling of CSLM and FF imaging may be an exciting technology in the future.

2. Only constituents that are fluorescent can be visualized. This seems to contradict with the third advantage of FF imaging, but both views are true. In this study we aimed at visualizing the basic constituents that make the structure of food, proteins, starch, and fat. Two of these constituents, starch and fat, are non-fluorescent, and although it was possible to visualize these constituents with the help of spectral unmixing techniques, many trials and errors were needed to get a decent result. This is a major disadvantage compared to imaging methods such as NIR, IR, and Raman imaging, which basically measure the vibrational energy of molecules and can therefore measure covalent bonds between C, H, and O.

3. Data acquisition time is long, in the order of minutes. Although this could be a major drawback when using FF imaging for practical purposes, image acquisition time can be reduced largely by improvement of the controlling system (which is presently programmed by LabVIEW) and the sensitivity of the camera, especially in near UV regions.
   Data acquisition times can be reduced by selecting or designing optimum band-pass filters, so that constituents of interest can be distinguished using a minimum number of filters.

If the third drawback could be improved to achieve measurement times in the order of a few seconds, the high spatial resolution, low demand towards sample preparation and high sensitivity towards certain constituents (fluorophors) should make FF imaging a very attractive imaging method.

6. 3 Future perspectives

FF imaging has proved to be an attractive method to observe samples in micro-scale. However, in food science, the time and money applicable for everyday measurement is scarce, meaning that methods such as FF imaging would only be used for fundamental research purposes. Although fundamental research is important in food science, and there are many foods whose structure and constituent distribution is yet to be studied, it would be greatly beneficial if FF imaging could be used in other fields, such as biology and medicine, where observation of the sample (ex. cells) is a routine procedure. In these fields, incorporating some kind of stain into the sample before observation is a common practice, and it should be a great impact if the same samples could be observed non-destructively.

For practical use, FF imaging needs to be developed in two ways: in terms of the image acquisition system, and data analysis methods.

The current imaging system is a prototype and has been constructed by collecting the parts from multiple manufacturers. One problem that we faced when selecting the parts was that few devices had satisfactory performance in the near UV (250-400 nm). The near UV region is very important in FF imaging because many fluorophors including aromatic amino acids fluoresce in this wavelength band. However, the development of devices with satisfactory performance in these wavelengths has not been so active due to the lack of demand. As a result, most devices used in the current imaging system have low sensitivity or transmission coefficients in the near UV region. To ensure equal measuring conditions for all the images, the conditions for all the other wavelengths are

currently adjusted to be equal to the weakest and least sensitive wavelength, which is a large waste. We are working with several manufacturers who could develop light sources, cameras and optical devices which show high performance in the near UV region. With high performance in these regions, the exposure times would become shorter (enabling shortening of total measurement time) and the images clearer.

There is also a large scope for improvement of analysis methods. In chapter 6, we incorporated some given information into the analysis model, i.e., that the abundance values of “slide glass” only took values of 1 or 0. This information improved the analysis greatly. Similarly, the incorporation of theoretical knowledge into the model may improve or stabilize it. For example, we are currently using analysis methods such as PLS and least squares regression that are based the assumption of linearity between fluorescence intensity and constituent abundance. However, fluorescence is known to show non-linear characteristics such as concentration quenching, and this is shown in chapter 3, where gluten ratios over 80% could not be modeled accurately with PLS. In this case, non-linear models may be considered.

Appendix

I. Absorbance

The energy of light

In order for light to be absorbed by a molecule, the photon of the light needs to have the proper energy to reach a discrete excited state of the molecule. The energy of light absorbed (mole basis) is given by the Planck frequency relation:

$$E = Nh\nu = \frac{Nhc}{\lambda} \qquad \dots (1)$$

E is the energy associated with frequency ν and wavelength λ, c is the velocity of light, and N is Avogadro's number. Absorption only occurs if E equals the difference in energy between the ground electronic state and an excited state of the absorber.

In this study, we are focusing on light in the near UV to VIS region, i.e. approximately 200-700 nm. According to the Planck frequency relation, this corresponds to an energy value of 170-598 kJ/mol ($N = 6.022 \times 10^{23}$, $h = 6.626 \times 10^{-34}$, $c = 2.998 \times 10^{8}$). However, the energy differences between electronic states of most molecules are larger than this value. For example, the smallest energy difference in ethylene ($CH_2 = CH_2$) is between the π and π^* orbitals, and equals 725 kJ/mol [1] which corresponds to a wavelength of 165 nm (Figure I-1). In ethylene, there exists an orbital with lower energy than the π orbital, the σ orbital, and an orbital with higher energy than the π^* orbital, the σ^* orbital. Therefore, electronic transitions between these orbitals would require more energy than 725 kJ/mol.

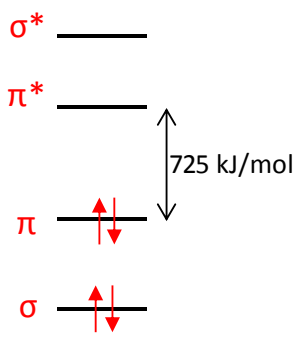

Figure I-1 Energy levels of ethylene

In this section, molecular orbitals and their energies, and the mechanisms that work to lower the energy difference between electronic states are explained. This may help to generalize the division between molecules that absorb light in the near UV to VIS and those who do not.

Atomic orbitals

In atoms and molecules, electrons are found only in certain regions of space, and this space is referred to as its orbital [1]. Atomic and molecular orbitals are described by the wave equations (Schrodinger equations), and the solutions to the wave equations are called wave functions (written as Ψ). Schrodinger equations have the form:

$$\hat{H}\Psi = E\Psi \qquad \dots (2)$$

where $\hat{H}$ is the Hamiltonian operator concerning the kinetic and potential energy of a particle and E is the energy value [2]. The wave function Ψ has characteristics which are similar to waves and can take both positive and negative values. Since $|\Psi|^2$ is known to show the probability distribution of the particle in question, solving the Schrodinger equations allows us to understand the orbitals of molecules, or where the probability to find the electrons is at its highest. However, an exact solution can only be obtained for atoms that have one electron, the hydrogen atom [3]. For atoms and molecules with more electrons, the wave functions are obtained by approximations which are based on several hypotheses.

The simplest atomic orbital is that of a single nucleus, which is spherically symmetric in space and is called the *s* orbital. Hydrogen and helium have a 1*s* orbital. The third electron in lithium cannot occupy the 1*s* orbital due to the Pauli principle which states that only two electrons can occupy one orbital. Therefore, lithium has another orbital, the 2*s* orbital. The third and fourth electrons in beryllium also occupy the 2*s* orbital. The boron atom has another type of orbital, the *p* orbital. There are three types of *p* orbitals, conventionally called p_x, p_y and p_z orbitals. These orbitals are shaped like a dumbbells with one lobe taking a positive wave function, and the other taking a negative wave function. The fifth electron in boron occupies one of the *p* orbitals. The following atoms, carbon, nitrogen, oxygen, etc. follow the same rules and occupy the *p* orbitals. Figure I-2 shows the shapes of the atomic orbitals.

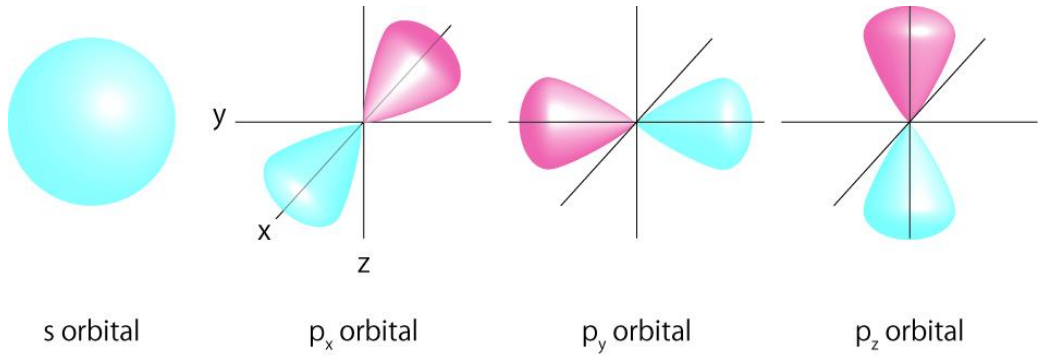

Figure I-2 Atomic orbitals. The blue and red lobes defer positive and negative orbitals.

Molecular orbitals

When atoms are combined to form molecules, these atomic orbitals are also combined to make molecular orbitals. There are mainly three types of orbitals, σ, π and *n*. The σ orbitals are symmetrical to the axis and are the most stable. The π orbitals are orbitals that are non-symmetrical to the axis. Nonbonding electrons in atoms such as nitrogen and oxygen occur in *n* orbitals. Due to the characteristics of the wave functions, the number of orbitals combined always equals the number of orbitals which are newly made. Therefore, when two atomic orbitals are combined and make the σ orbital, another orbital, the σ^* orbital is made. The same goes for π and π^* orbitals. Orbitals with an asterisk (*) have higher energies than the ones that do not.

The σ orbitals are the most stable orbitals, meaning that they are lowest in energy. Conversely, σ^* orbitals are very high in energy. Therefore the energy gap between the σ and σ^* orbitals is very large. Compared to the σ orbitals, π orbitals are less stable and have higher energies, meaning that the energy gap between π and π^* orbitals are smaller than the σ and σ^* orbitals. The relatively small energy gap means that in some molecules the excitation of an electron from the π orbital to the π^* orbital can be obtained by the absorption of light in the near UV to VIS wavelengths. Therefore the π orbital is the key to light absorption and fluorescence.

As an example, in chlorophylls and carotenoids, the energy of the π^* orbital is 160-300 kJ/mol higher than the π orbital, so the absorption of visible light can lead to the excitation of π electrons. Transitions from σ to σ^* orbitals require much more energy since the σ orbital is very stable. Transitions from *n* to σ^* orbitals are possible but are less probable to happen, which means that the molar absorptivity (absorbance of a substance at a concentration of 1 mol/l) is very low [4, 5].

In order to know how π orbitals are made, we need to know the shapes and

characteristics of molecular orbitals. Molecular orbitals are also explained by the Schrodinger functions, but again it is impossible to solve the Schrodinger equations for molecules having many nuclei and electrons, and approximations are needed. There are two main methods of approximating molecular orbitals, the Valance Bond Method (VB method) and the Molecular Orbital Method (MO method). The VB method focuses on how the atomic orbitals of the dissociated atoms combine to give individual chemical bonds when a molecule is formed [6]. On the other hand, the MO method assumes orbitals that cover the whole molecule. The MO method is more precise but the VB method is easier to understand. Therefore, we first focus on the VB method.

Valance bond theory and hybridized orbitals

Simple bonds between *s* and *p* atomic orbitals are shown in Figure I-3. Bonds between *s* and *s* orbitals and p_y and p_y orbitals are symmetrical to the axis and become σ orbitals. Bonds between p_x and p_x orbitals are asymmetrical to the axis and are therefore π orbitals. In the nitrogen molecule (N_2), there is one σ orbital between the two p_y orbitals and two π orbitals between the two p_x and p_z orbitals.

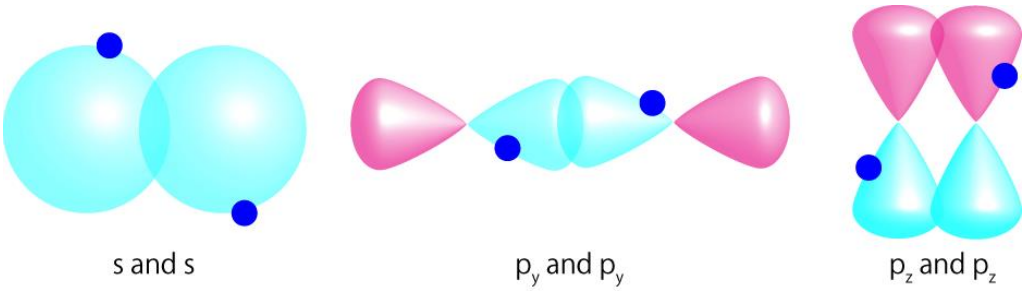

Figure I-3 Bonds between *s*, p_y and p_z orbitals

When three or more atoms are bonded together, it becomes more difficult to predict the shapes of the molecular orbits. Here we introduce the idea of hybridization.

Hybridization is the combining of atomic orbitals to make new orbitals that can explain the characteristics of existing molecules. For example, methane is known to be a tetrahedron molecule with the center carbon connected to four hydrogen atoms. Carbon has two electrons in the 2*s* orbital and two electrons in the 2*p* orbitals. If the carbon-hydrogen bonds are made between these orbitals and the 1*s* orbital of hydrogen, methane would not take the shape of a tetrahedron.

To understand the characteristics of methane, we combine the 2*s*, $2p_x$, $2p_y$, and $2p_z$ orbitals as shown in equation (3) to make a sp^3 hybridized orbital.

$$t_1 = \frac{1}{2}(s + p_x + p_y + p_z)$$
$$t_2 = \frac{1}{2}(s - p_x + p_y + p_z)$$
$$t_3 = \frac{1}{2}(s - p_x - p_y + p_z) \qquad \ldots (3)$$
$$t_4 = \frac{1}{2}(s - p_x - p_y - p_z)$$

Since all these orbitals are equivalent, the new hybridized orbitals locate themselves equally in space, i.e., the hybridized orbitals form a tetrahedron shape (Figure I-4). The molecular orbitals between these hybridized orbitals and the *s* orbital of hydrogen is symmetrical to the axis and are therefore σ orbitals. Ammonia (NH_4) and water (H_2O) also form a sp^3 hybridized orbital. In water, one of the sp^3 orbitals is occupied with two electrons from the oxygen atom.

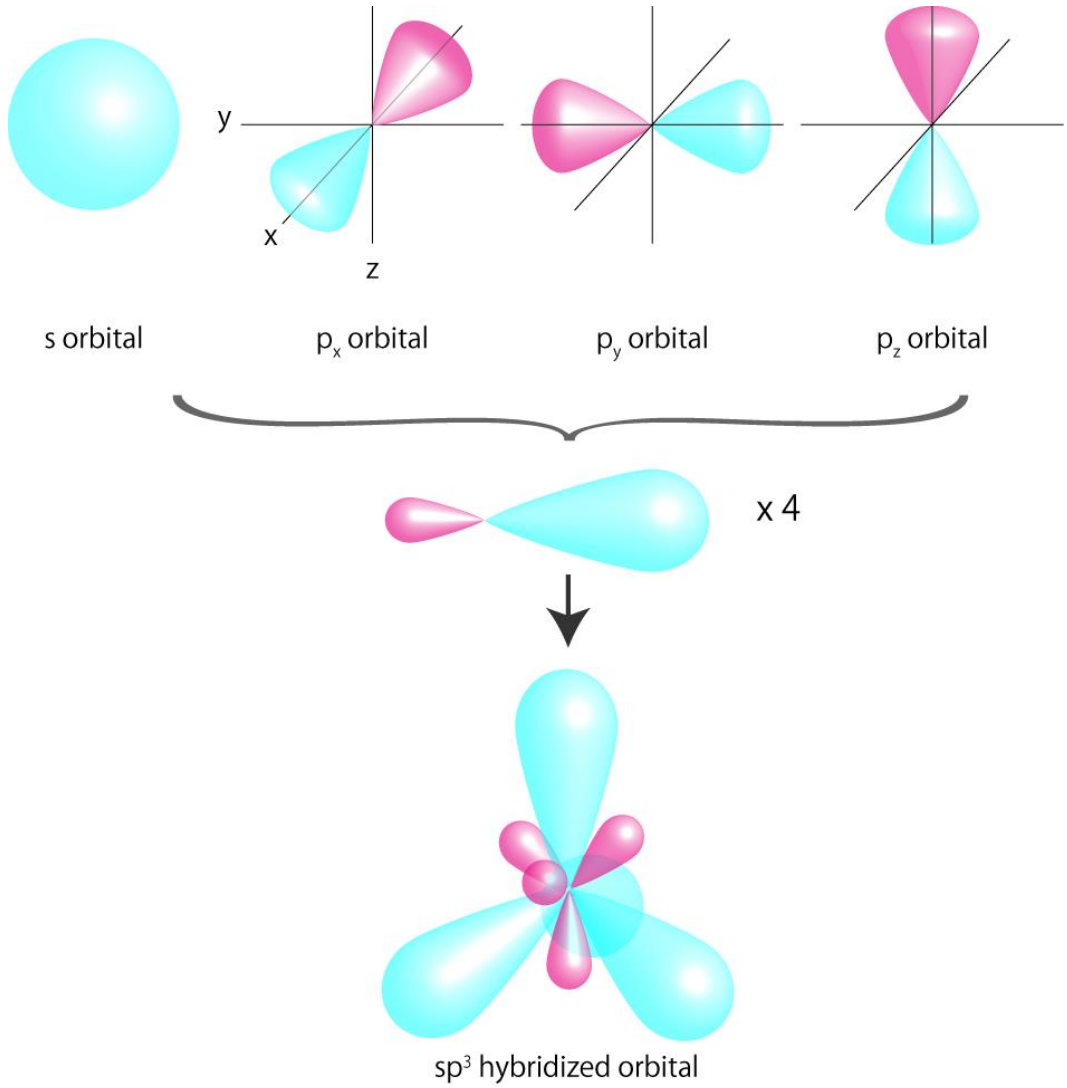

Figure I-4 *sp^3* hybridized orbitals are made by combing 4 orbitals

Ethylene ($CH_2 = CH_2$) is known have a planar configuration. This is explained by the *sp^2* hybridized orbital, which is a combination of the 2*s*, 2p_x and 2p_y orbitals. The three orbitals are combined as shown in equation (4) to form 3 new orbitals.

$$
\begin{aligned}
T_1 &= \left(\frac{1}{3}\right)^{\frac{1}{2}} s + \left(\frac{2}{3}\right)^{\frac{1}{2}} p_x \\
T_2 &= \left(\frac{1}{3}\right)^{\frac{1}{2}} s - \left(\frac{1}{6}\right)^{\frac{1}{2}} p_x + \left(\frac{1}{2}\right)^{\frac{1}{2}} p_y \\
T_3 &= \left(\frac{1}{3}\right)^{\frac{1}{2}} s - \left(\frac{1}{6}\right)^{\frac{1}{2}} p_x - \left(\frac{1}{2}\right)^{\frac{1}{2}} p_y
\end{aligned}
\qquad \ldots (4)
$$

When these three equivalent orbitals space themselves as far away from each other as possible, they form an equilateral triangle (Figure I-5). This is the reason for the triangular planer formation.

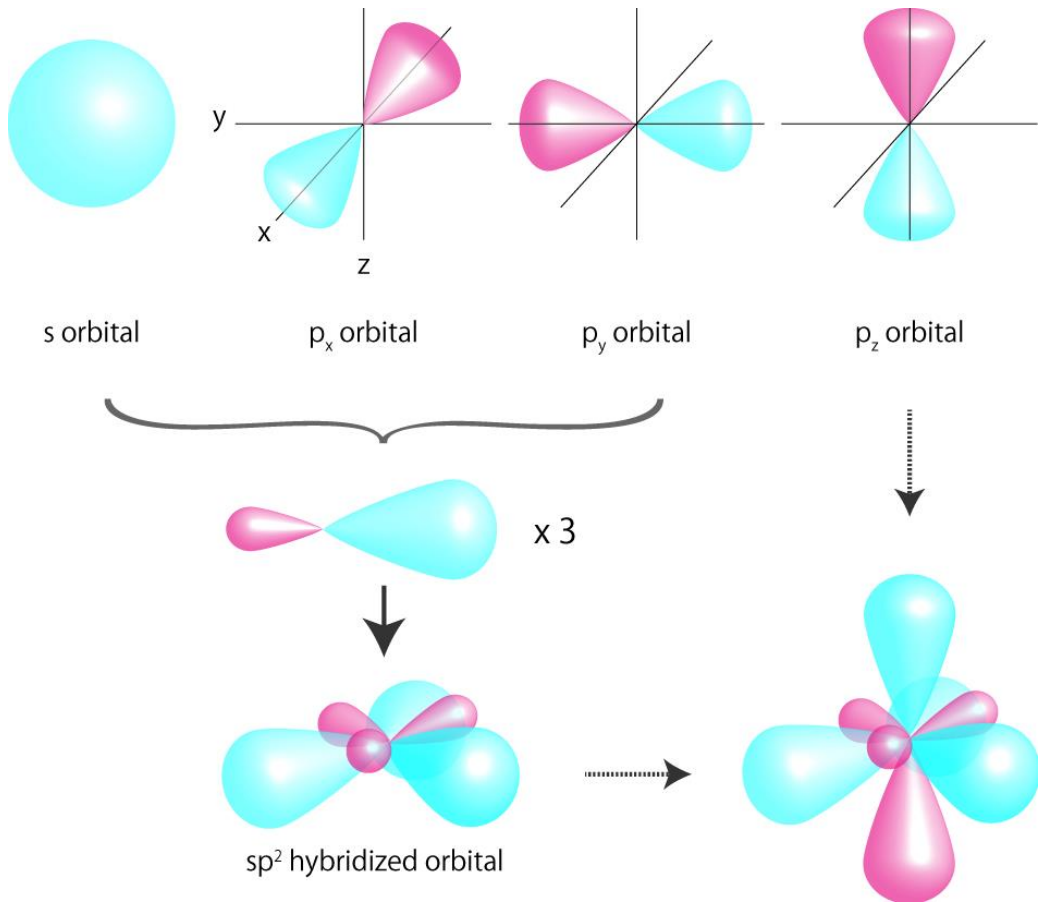

Figure I-5 *sp^2* hybridized orbitals are made from 3 orbitals

The important thing here is that the $2p_z$ orbital is not included in the hybridized orbital and sticks out of the x-y plane. When two carbon atoms are bonded to each other as in ethylene, one bond is made between sp^2 orbitals. This is an σ orbital. However, another bond forms between the two $2p_z$ orbitals. This orbital is asymmetrical to the axis and is therefore a π orbital (Figure I-6). The σ and π orbitals are shown together as a double bond. We can see from here that double bonds have an π orbital.

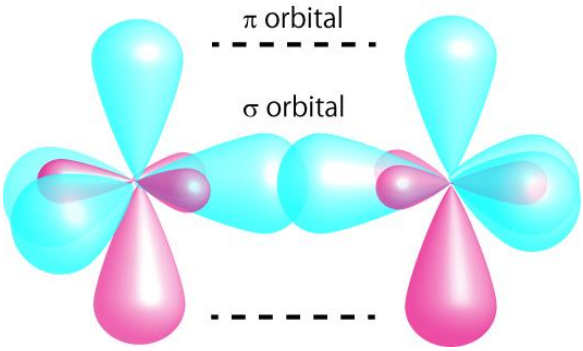

Figure I-6 π orbitals are formed in *sp2* orbitals

Acetylene ($CH \equiv CH$) takes a linear formation. This is explained by the *sp* hybridized orbital. This orbital is a combination of the 2*s* and 2p_y orbitals.

$$D_1 = \left(\frac{1}{2}\right)^{\frac{1}{2}} (s + p_x)$$
$$D_2 = \left(\frac{1}{2}\right)^{\frac{1}{2}} (s - p_x) \qquad \ldots (5)$$

These two orbitals space themselves 180° apart. The two leftover orbitals, 2p_x and 2p_z form π orbitals with the neighboring carbon atom (Figure I-7).

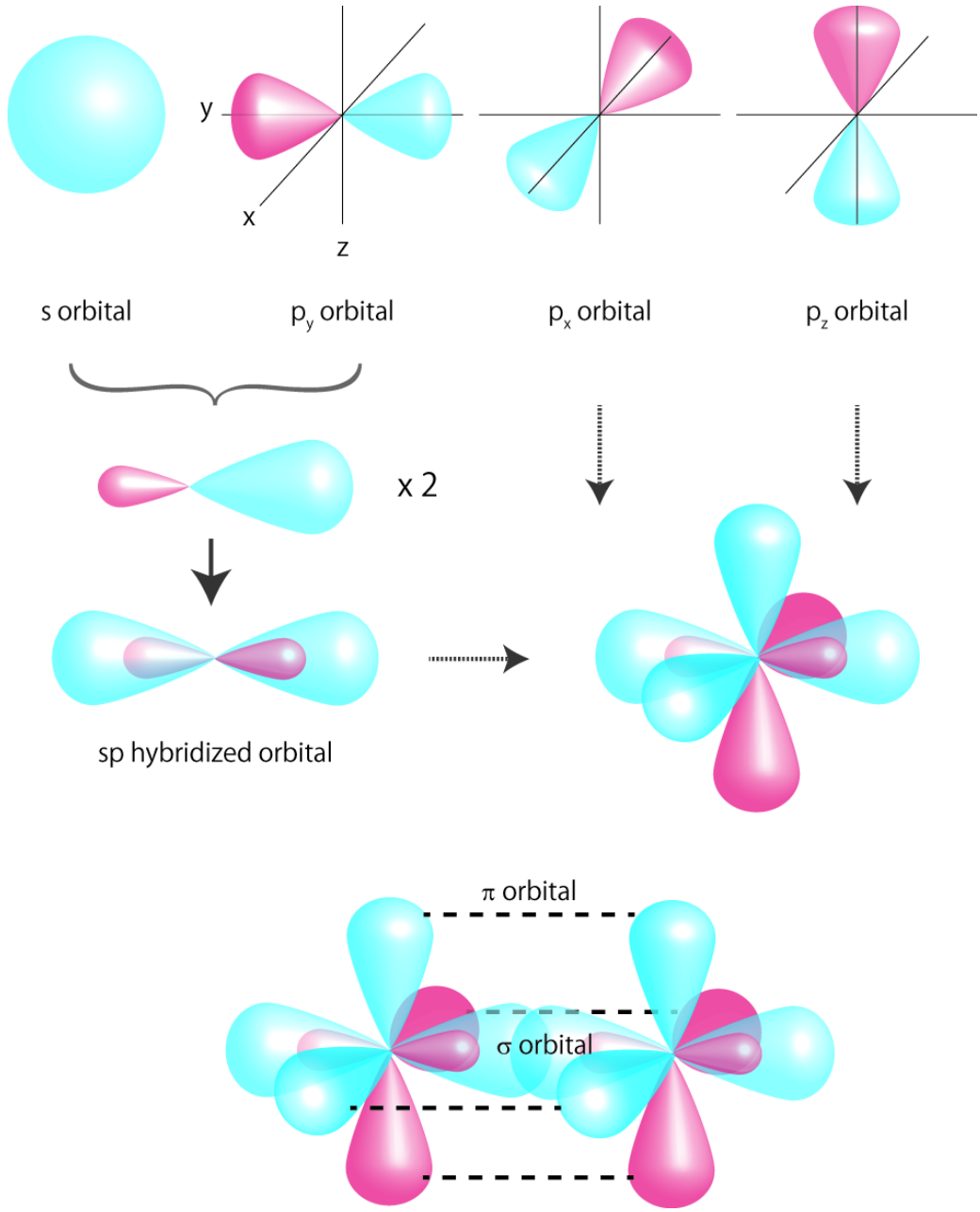

Figure I-7 *sp* orbitals and the two π orbitals

Molecular orbital theory

The molecular orbital theory assumes that the molecular orbital formed between several atoms spread across the whole molecule [7]. The molecular orbitals are approximated by adding or subtracting the original atomic orbitals. Adding the atomic orbitals creates a molecular orbitals that spreads across the two atoms, i.e., a bonding orbital. Subtracting the atomic orbitals creates an anti-bonding orbital. Figure I-8 shows

the bonding and anti-bonding molecules created between *s* orbitals.

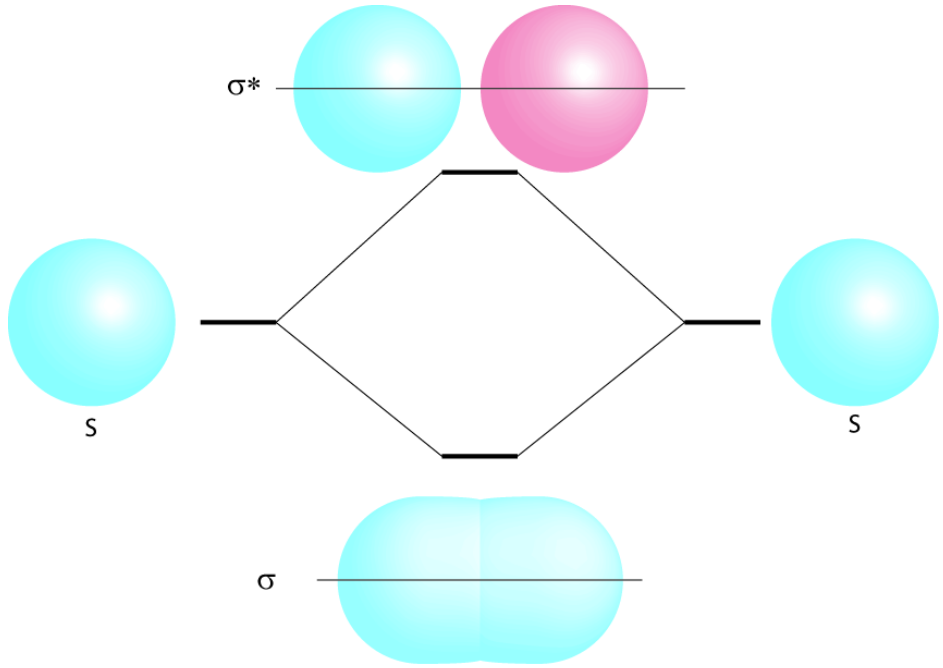

Figure I-8 σ and σ^* orbitals are made from s orbitals

Figure I-9 shows the bonding and anti-bonding molecules created between p_y orbitals.

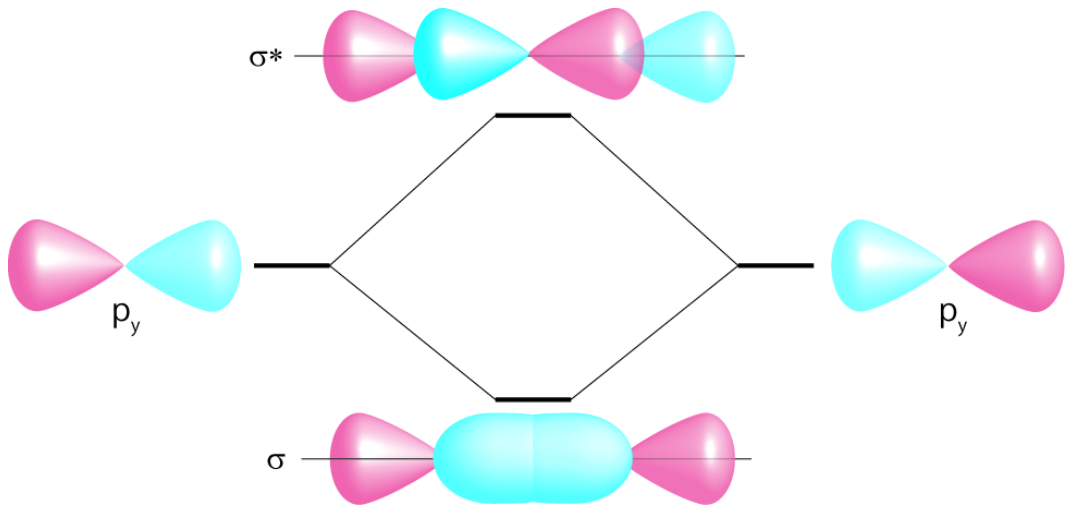

Figure I-9 σ and σ^* orbitals are made from p_y orbitals

Figure I-10 shows the bonding and anti-bonding molecules created between *s* orbitals.

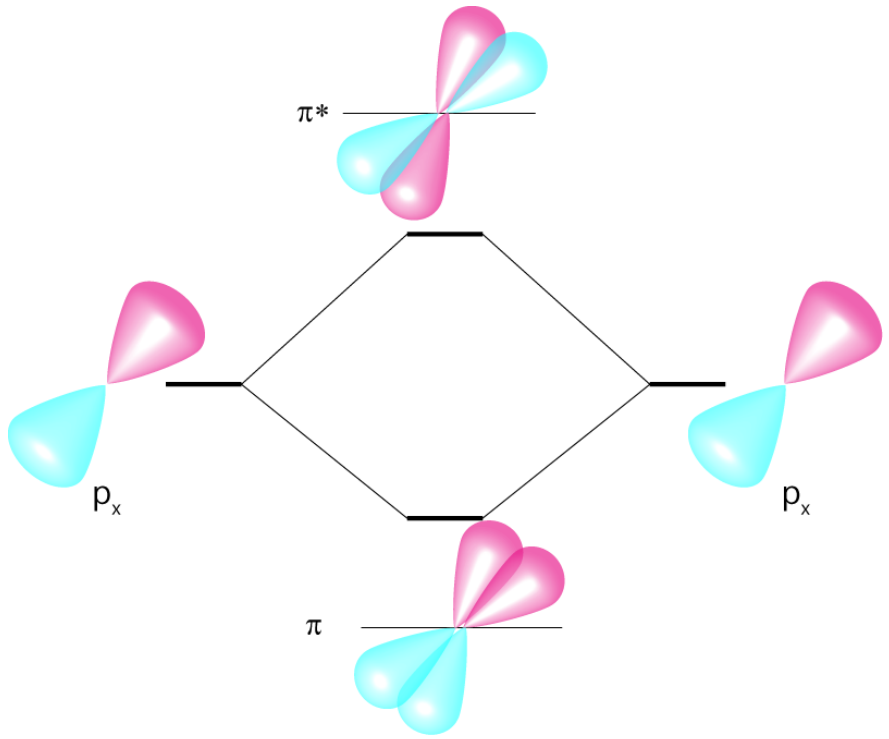

Figure I-10 π and π^* orbitals made from p_x orbitals

Bonding orbitals have lower energy than the original atomic orbitals and therefore are more stable. Conversely, anti-bonding orbitals have higher energy than the original orbitals and are unstable. Anti-bonding orbitals are marked with a "*" (σ^* and π^*).

Electrons that originally occupied the atomic orbitals fall into the molecular orbitals, occupying the orbitals that are lowest in energy first. Only two electrons can occupy one orbital, due to the Pauli principle. The electron-occupied orbital with the highest energy is called HOMO (highest occupied molecular orbital) and the electron-unoccupied orbital with the lowest energy is called LUMO (lowest unoccupied molecular orbital). These two orbitals are very important because the smallest energy gap between orbitals is between the HOMO and the LUMO, and excited electrons are most likely to move between these two orbitals.

By combining the hybridization orbital method and the MO theory, it is possible to consider energy levels of molecular orbitals in complex molecules. Figure I-11 shows the energy levels of molecular orbitals in ethylene molecule. As can be seen from the molecular energy levels the HOMO and LUMO are the π and π^* orbitals, respectively.

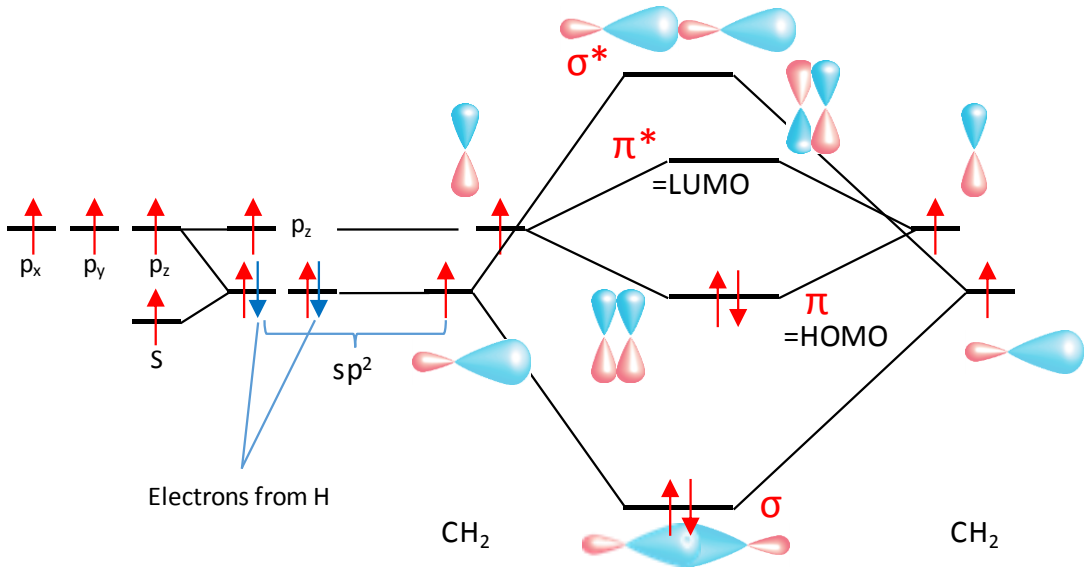

Figure I-11 Energy levels of molecular orbitals of ethylene

The π and π^* orbitals also exist in bonds between other atoms. Table I-1 shows some functions groups and examples of molecules containing the function group. These function groups that absorb light are called chromophores [1, 5, 8]. The existence of chromophores alters the absorption wavelength and intensity of the molecule [9].

Table I-1 Chromophores and absorbing wavelengths

Chromophore	Molecule	Wavelength [nm]
C=C	Ethylene	165
C≡C	Acethylene	180
C=O	Acetone	180
N=O	Nitromethane	200
COOH	Acetic acid	204
CONH2	Acetamide	208

Conjugation of double bonds

We have seen that double and triple bonds are one condition for absorbance to occur. However, one double bond is still insufficient for absorbance of light in the near UV to VIS to occur. For example, the energy gap between the π and π^* orbitals in ethylene equals 725 kJ/mol [1] which corresponds to a wavelength of 165 nm. In order to absorb light in the range of 200-700 nm, the energy gap between HOMO and LUMO needs to be smaller.

This happens when double bonds are conjugated, i.e., multiple double bonds are connected by single bonds. While ethylene absorbs at 165 nm, 1, 3-butadiene ($CH_2 = CH - CH = CH_2$) absorbs at 217 nm. While this has been proved experimentally, understanding the logic behind this phenomenon requires solving the Schrodinger equations [10].

We use the example of 1, 3-butadiene ($CH_2 = CH - CH = CH_2$). We focus on the π orbital in the molecule and represent the wave function of the π orbital with ψ. The energy of ψ is expressed as

$$E = \frac{\int \psi H \psi d\tau}{\int \psi^2 d\tau} \qquad \dots (6)$$

The wave function ψ can be approximated as the sum of the p_z atomic orbitals of the four carbons: $\varphi_1, \varphi_2, \varphi_3, \varphi_4$ as

$$\psi = c_1\varphi_1 + c_2\varphi_2 + c_3\varphi_3 + c_4\varphi_4 \qquad \dots (7)$$

By substituting equation (7) in (6) and setting the partial differential for c_1 to c_4 to zero

$$\frac{\partial \mathrm{E}}{\partial \mathrm{c}_1} = \frac{\partial E}{\partial c_2} = \frac{\partial E}{\partial c_3} = \frac{\partial E}{\partial c_4} = 0 \qquad \dots (8)$$

This is the equivalent of calculating the following determinant:

$$\begin{bmatrix} H_{11} - ES_{11} & \cdots & H_{14} - ES_{14} \\ \vdots & \ddots & \vdots \\ H_{41} - ES_{41} & \cdots & H_{44} - ES_{44} \end{bmatrix} = 0 \qquad \dots (9)$$

Each term is defined as follows:

$$\begin{aligned} S_{mm} &= \int \varphi_m^2 d\tau = 1 \\ S_{mn} &= \int \varphi_m \varphi_n d\tau = 0 \\ H_{mm} &= \int \varphi_m H_m \varphi_m d\tau = \alpha \\ H_{mn} &= \int \varphi_m H_{\varphi_m d\tau} \\ &= \beta \ \text{(2 orbitals are side by side)} \\ &\quad 0 \ \text{(2 orbitals are far away)} \end{aligned} \qquad \dots (10)$$

Therefore, the determinant becomes

$$\begin{vmatrix} \alpha - E & \beta & 0 & 0 \\ \beta & \alpha - E & \beta & 0 \\ 0 & \beta & \alpha - E & \beta \\ 0 & 0 & \beta & \alpha - E \end{vmatrix} = 0 \qquad \dots (11)$$

If we define $X = \frac{\alpha - E}{\beta}$, the determinant becomes,

$$\begin{vmatrix} X & 1 & 0 & 0 \\ 1 & X & 1 & 0 \\ 0 & 1 & X & 1 \\ 0 & 0 & 1 & X \end{vmatrix} = 0 \qquad \dots (12)$$

It is possible to calculate X from this determinant,

$$\begin{vmatrix} X & 1 & 0 & 0 \\ 1 & X & 1 & 0 \\ 0 & 1 & X & 1 \\ 0 & 0 & 1 & X \end{vmatrix} = \mathrm{X} \begin{vmatrix} X & 1 & 0 \\ 0 & X & 1 \\ 0 & 1 & X \end{vmatrix} - \begin{vmatrix} X & 1 \\ 1 & X \end{vmatrix} \qquad \dots (13)$$

If we define the $\mathrm{n} \times \mathrm{n}$ determinant shown above as D_n, D_n can be calculated from D_{n-1} and D_{n-2} as

$$D_n = XD_{n-1} - D_{n-2} \qquad \dots (14)$$

Actually, this is one of the characteristics of trigonometric functions [11]:

$$\sin m\omega = 2 \cdot \cos \omega \cdot \sin(m-1)\omega - \sin(m-2)\,\omega \qquad \dots (15)$$

If we set $\mathrm{D_n}$ as $\sin m\omega$ and X as $2\cos\omega$,

$$\begin{aligned} &D_n = 0 \rightarrow \sin m\omega = 0 \\ &\omega = \frac{i}{m}\pi \ \ (i = 1, 2, \dots m-1) \end{aligned} \qquad \dots (16)$$

When $\mathrm{n} = 2$,

$$D_2 = \begin{vmatrix} X & 1 \\ 1 & X \end{vmatrix} = X^2 - 1$$
$$D_2 = 0 \rightarrow X = \pm 1 \qquad \ldots (17)$$

Since we set X as $2\cos\omega$,

$$\cos\omega = \pm\frac{1}{2} \rightarrow \omega = \frac{1}{3}\pi, \frac{2}{3}\pi \qquad \ldots (18)$$

Therefore,

$$m = n + 1 \rightarrow X = 2\cos\frac{i\pi}{n+1} \ (i = 1, 2, \ldots n) \qquad \ldots (19)$$

Since we defined $X = \frac{\alpha - E}{\beta}$, $E = \alpha - X\beta$. Therefore, the energy levels of a conjugated molecule with n carbon atoms can be represented graphically as in Figure I-12. In a conjugated molecule with *n* carbon atoms, there are *n* electrons occupying the π orbital. Since two electrons occupy one orbital, the HOMO and LUMO are the two orbitals just below and above α. The larger the number of carbon atoms, the smaller the energy gap between HOMO and LUMO. Therefore, the more conjugated a molecule is, the smaller energy it needs for electron transition to occur. Table I-2 shows the absorbance wavelengths of conjugated polyenes [12].

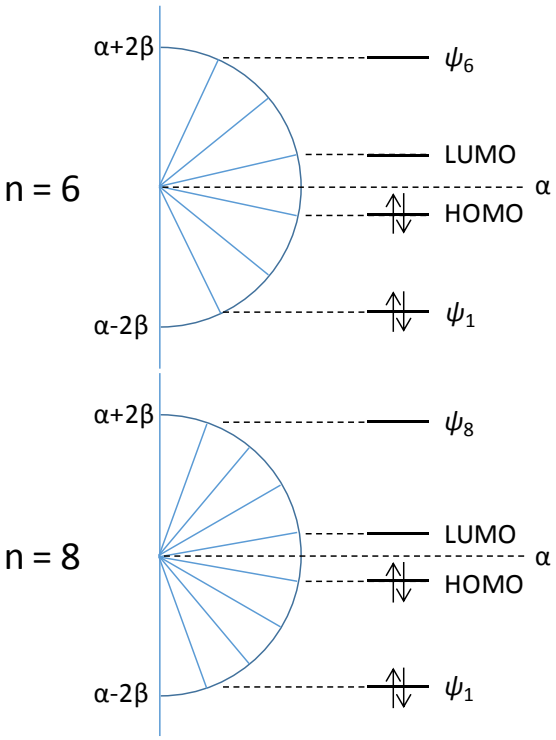

Figure I-12 Energy levels of a conjugated molecule with 6 and 8 molecules

Table I-2 Absorbance wavelengths of conjugated polyenes

n	molecule	structure	wavelength [nm]
1	ethylene	CH2=CH2	165
2	butadiene	CH2=CH−CH=CH2	217
3	hexatriene	CH2=CH−CH=CH−CH=CH2	268
4	octatetraene	CH2=CH−CH=CH−CH=CH−CH=CH2	304
5	decapentaene	CH2=CH−CH=CH−CH=CH−CH=CH−CH=CH2	334
6	dodecahexaene	CH2=CH−CH=CH−CH=CH−CH=CH−CH=CH−CH=CH2	364
7	tetradecaheptaene	CH2=CH−CH=CH−CH=CH−CH=CH−CH=CH−CH=CH−CH=CH2	390
8	hexadecaoctaene	CH2=CH−CH=CH−CH=CH−CH=CH−CH=CH−CH=CH−CH=CH−CH=CH2	410
10	eicosadecaene	CH2=CH−CH=CH−CH=CH−CH=CH−CH=CH−CH=CH−CH=CH−CH=CH−CH=CH−CH=CH2	450

Aromatic molecules

Conjugated systems also show π to π^* transition when they are cyclized (turned into rings), but some of these molecules show characteristics that cannot be explained by the conjugated systems alone. One of these molecules is benzene (C_6H_6).

Benzene has three single bonds and three double bonds. However, the actual bond lengths between the carbon atoms are all the same. This is explained by the delocalization of electrons in the ring. As shown in Figure I-13, the $2p_z$ orbitals of all the carbon atoms are equivalent, and therefore, π orbitals can be made between every combination of carbon atoms.

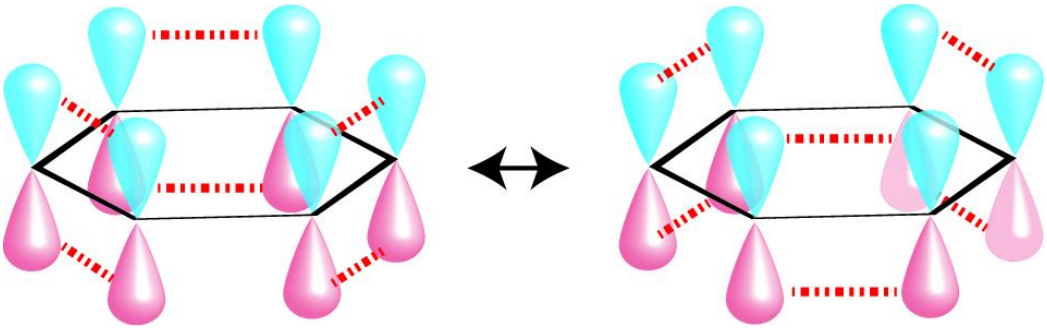

Figure I-13 Delocalized electrons form orbitals between all combinations of π orbitals

The delocalization of electrons makes the benzene molecule a very stable one. This is why benzene absorbs at a shorter wavelength (255 nm) than hexatriene, a linear conjugated hydrocarbon with the same number of carbon atoms and double bonds. Cyclized conjugated molecules that show the typical characteristics of benzene are called aromatic compounds.

Molecules formed from fused benzenes such as naphthalene (two benzenes combined) and anthracene (three benzenes combined) show absorbance at longer wavelengths than benzene [13]. Furthermore, the combination of functional groups such as –OH and $–NO_2$ to benzene also shifts the absorbance to longer wavelengths.

Aromatic amino acids such as phenylalanine, tyrosine, histidine, and tryptophan also show near UV to VIS absorbance. Table I-3 shows some typical aromatic compounds and their absorbing wavelengths [14].

Table I-3 Typical aromatic compounds and absorbing wavelengths

molecule	structure	wavelength [nm]
benzene	C_6H_6	255
naphthalene	(two benzenes fuzed) $C_{10}H_8$	286
anthracene	(three benzenes fuzed)$C_{14}H_{10}$	375
phenole	benzene + OH	290

As we have seen, the condition for absorption to occur in the near UV to VIS is that the molecule contains conjugated double bonds, or aromatic structures.

II. Fluorescence

Deexcitation, rate constants and lifetimes

We have looked at one condition for fluorescence to occur, the absorption of light. Now we look at the other condition, the absorbed light needs to be released again as fluorescence.

The absorption of light causes the molecule to transfer to an "excited" state. This is a very unstable state, so the energy is released again and the molecule goes back to its most stable state. This release of energy is called deexcitation. There are many deexcitation processes, and for a molecule to show fluorescence, the release of energy as light needs to dominate over the other deexcitation processes. Below are the main deexcitation processes:

1. Fluorescence (includes phosphorescence)
2. Radiationless transition (molecule loses energy as heat)
3. Excitation energy is transformed to another molecule
4. Excited electron leaves the molecule that absorbed the photon

The rate of each process is explained with a constant number, k. Generally, in a chemical reaction

$$nA + mB \rightarrow C + D \qquad \dots (20)$$

k is expressed as

$$\frac{dC}{dt} = k(t)A^n B^m \qquad \dots (21)$$

where t is the time elapsed from the moment the illumination ceases [15]. The larger the value of k, the faster the reaction. In the case of deexcitation, if we denote $S_{(\pi,\pi*)}$ as the excited state and k_1, k_2,… as the rate constants for each deexcitation process,

$$\begin{aligned} -\frac{dS_{(\pi,\pi*)}}{dt} &= (k_1 + k_2 + \cdots)S_{(\pi,\pi*)} \\ S_{(\pi,\pi*)}(t) &= S_{(\pi,\pi*)}(0)e^{-(k_1+k_2+\cdots)t} \end{aligned} \qquad \dots (22)$$

Here we introduce the lifetime, τ, which is the time required for the number of

molecules in a given state to decrease to 1/e = 37% of the initial state (deexcitation is known to occur exponentially). Then

$$\text{when } t = \tau,$$
$$\frac{S_{(\pi,\pi*)}(t)}{S_{(\pi,\pi*)}(0)} = \frac{1}{e} \qquad \dots (23)$$

From equation (22),

$$\mathrm{e}^{-(k_1+k_2+\cdots)\tau} = e^{-1}$$
$$(k_1 + k_2 + \cdots)\tau = 1 \qquad \dots (24)$$
$$\tau = \frac{1}{(k_1 + k_2 + \cdots)}$$

This shows that if one particular process has a large rate constant (the reaction proceeds quickly), the overall lifetime of the excited state becomes short.

Furthermore, we can calculate the quantum yield, ϕ_i, which is the number of molecules using i th deexcitation reaction divided by the total number of excited molecules. Φ_i is expressed as

$$\Phi_i = \frac{k_i}{\sum_j k_j} = \frac{\tau}{\tau_i} \qquad \dots (25)$$

This means that for fluorescence to be observed strongly (quantum yield is large), the range constant k for fluorescence needs to be relatively large compared to the other reactions.

Electronic, vibrational and rotational energy

In the section of absorbance, we mainly discussed the electronic energy state of molecules, which is determined by the molecular orbitals occupied by the electrons. However there are other energy levels which need to be concerned in order to understand the spectrum of fluorescence emission. While the levels of electronic energy correspond to light in the UV to VIS wavelengths, vibrational energy levels are much smaller and correspond to infrared (IR) wavelengths. Rotational energy levels are even smaller and correspond to microwave wavelengths. The existence of these different levels of energy

is the reason absorbance spectra become broad.

Molecule vibration can be approximated as the motion of a spring. The bond between two atoms acts as the spring, and the oscillation of atoms depends on the energy level. There are many ways in which atoms can vibrate, such as stretching, bending, rocking, wagging and twisting. The number of vibrational modes depends on the molecule [2]. Figure II-1 shows the energy of vibrational levels and conformation of the corresponding molecules.

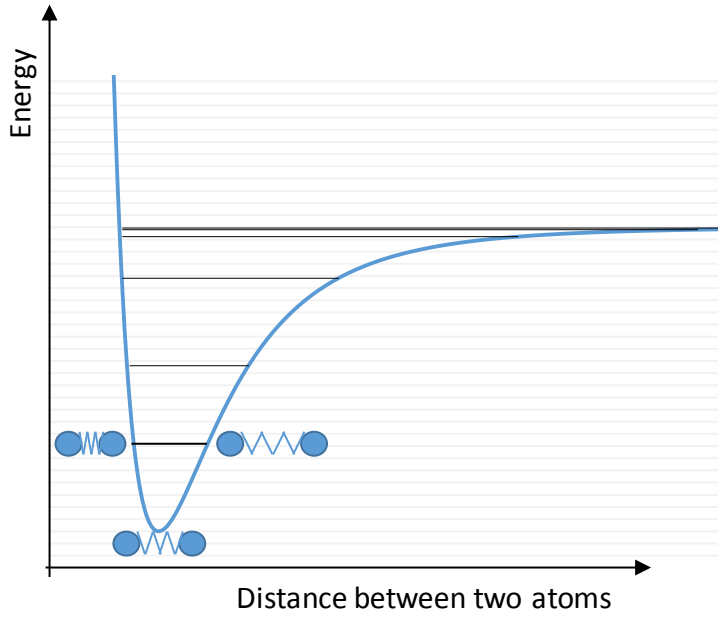

Figure II-1 Energy of vibrational levels

Furthermore, molecules show rotational movements. Rotational energy is explained by the moment of inertia of the molecule, which is defined as the mass of each atom multiplied by the square of its distance from the rotational axis.

An important point regarding vibrational and rotational energies is that the energy absorbed is quickly dissipated as heat. This is explained by the oscillation frequency of nuclei, which is about 10^{13} Hz, meaning that one wave of oscillation takes about 10^{-13} s. This is the order of time in which excess vibrational energy can be dissipated as heat by interactions with other nuclei. Therefore, transitions within the same electronic state are usually complete in the order of 10^{-12} s. This occurs much faster than the emission of light such as fluorescence. Therefore, when a molecule absorbs light to be excited to an energy level that is higher in electronic, vibrational, and rotational energies, the excess vibrational and rotational energies are dissipated quickly before fluorescence and other deexcitation processes occur.

Vibrational and rotational levels of ground and excited state differ in energy of approximately 15 kJ/mol and 1 kJ/mol, respectively. In the green to yellow wavelengths, this is equal to 40 nm and 3 nm difference, respectively. Since these energies are quickly dissipated as heat before fluorescence can be emitted, the energy of fluorescence light is lower than the light originally absorbed. This results in a wavelength shift between the excitation and emission light. This difference is expressed as the Stokes shift which is defined as follows:

$$\text{Stokes shift } [\text{cm}^{-1}] = 10^7 \left(\frac{1}{\lambda_{ex}} - \frac{1}{\lambda_{em}}\right) \qquad \ldots (26)$$

where λ_{ex} [nm] and λ_{em} [nm] are the wavelengths of the excitation and emission peaks, respectively.

Competing deexcitation pathways

There are many pathways in which deexcitation can occur. First we look at the process of fluorescence. With fluorescence, the excited molecule drops back to the ground state by releasing light. We set the rate constant as k_1:

$$S_{(\pi,\pi*)} \xrightarrow{k_1} S_{(\pi,\pi)} + h\nu \qquad \ldots (27)$$

The fluorescence lifetime is typically 10^{-8} s [16].

Next we consider radiationless transitions, where the electronic energy is dissipated as heat (rate constant $= k_2$).

$$S_{(\pi,\pi*)} \xrightarrow{k_2} S_{(\pi,\pi)} + \text{heat} \qquad \ldots (28)$$

This dissipated energy is often passed on to other parts of the same molecule and causes the excitation of vibrational modes for other atoms. Radiationless transitions can occur within an electronic state as we have seen for vibrational and rotational energies, and also between electronic states.

Energy transfer between molecules can happen (rate constant $= k_3$):

$$S_{(\pi,\pi*)} + S_{2(\pi,\pi)} \xrightarrow{k_3} S_{(\pi,\pi)} + S_{2(\pi,\pi*)} \quad \ldots (29)$$

as well as photochemical reactions (rate constant $= k_4$):

$$S_{(\pi,\pi*)} \xrightarrow{k_4} D_{(\pi)} + e^* \quad \ldots (30)$$

Using the rate constants k_1 to k_4, the quantum yield of fluorescence is expressed as:

$$\Phi = \frac{k_1}{k_1 + k_2 + k_3 + k_4} \quad \ldots (31)$$

This shows that the quantum yield of fluorescence depends largely on the rate constants of other processes. For example, at high temperature, radiationless transitions are more likely to happen, i.e., the rate constant k_2 is large. This results in a smaller Φ which means weaker fluorescence.

In another case, a substance that is easily excited may be mixed with the measured sample, in which case, energy transfer between molecules may be activated and k_3 may become larger. This also results in a smaller Φ. The introduced substance would be referred to as a “quencher”.

As we have seen, the condition for fluorescence emission to occur is that the rate constants for other deexcitation processes to be relatively smaller than the rate constant of fluorescence. Causes for large rate constants for other deexcitation processes are high temperature, existence of other substances, etc.

III. Applications of fluorescence

Time-resolved spectroscopy

Since many competing deexcitation paths exist, the lifetime of the same fluorophors can differ depending on the environment, ex. the amount of interactions with substrates and other macromolecules. If two fluorophors show the same fluorescence spectra and intensities, they cannot be differentiated by steady-state data. However, if their lifetimes are different, they can be resolved by time-resolved fluorescence.

There are two ways of measuring time-resolved fluorescence: time-domain and frequency-domain methods. With the time-domain method, the sample is excited with a pulse of light whose endurance is much shorter than the decay time τ, and the time-dependent intensity of the fluorescence is measured. The frequency-domain method uses excitation light whose intensity is varied at a high frequency, typically near 100 MHz. This causes the emission to respond at the same frequency but be delayed due to fluorescence lifetime. This delay is measured as a phase shift (ϕ) which can be used to calculate the decay time.

One application of time-resolved fluorescence is to use fluorescent probes with a long decay time and to measure the emission within a time-gate after excitation (Figure III-1). With this method, unwanted auto-fluorescence of the sample (such as those from amino-acids) that have a relatively short decay time can be eliminated [17].

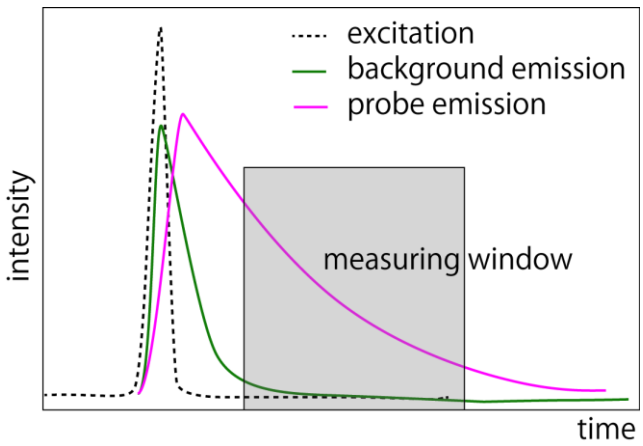

Figure III-1 Time-gate measurement [17]

Time-resolved fluorescence has also been used for imaging, where the image contrast is based on the lifetime of each pixel. This method is called fluorescence lifetime imaging microscopy (FLIM) and is used in cell biology [18]. In this study, images are

acquired in multiple wavelengths as well as multiple lifetimes. The trend to develop techniques used for one-point measurement to imaging seems to be universal.

Fluorescence anisotropy

Anisotropy shows the extent of polarity of the emitted light when the sample is excited with polarized light [19]. With the measurement of fluorescence anisotropy, we excite the sample with polarized excitation light and measure how much the emission light has been "depolarized".

Molecules have transition moments that lie along specific directions in the molecule. When molecules are excited by polarized light, only the molecules with their transition moments oriented along the excitation light can be excited. During the fluorescent lifetime, rotational diffusion changes the orientation of these molecules causing emission light to be depolarized. Since the rate of rotational diffusion depends upon the viscous drag by the solvent, measuring fluorescence anisotropy gives us an idea of the viscosity or "mobility" of the sample. For example, fluorescence anisotropy measurements have been used to quantify protein denaturation, since denatured protein has more mobility than their counterparts.

Resonance energy transfer (RET)

RET occurs when two fluorescence molecules are close enough for the emission light of one molecule (donor) is transferred to the other molecule (acceptor) by long-range dipole-dipole interactions, causing the acceptor to be excited [19]. The acceptor then emits fluorescence that has a much longer wavelength than the original light.

RET is most commonly used to measure the distances between two sites on a macromolecule. If two sites of a molecule is covalently labeled with a fluorophor (intrinsic or extrinsic), measuring the efficiency of RET would show how close these two sites are. Molecules showing RET can also be used as probes for measuring solvent properties such as pH. If the protein probe can be designed to fold and unfold according to its environment such as pH, measuring the efficiency of RET would show the configuration of the protein and as a result, the properties of the solvent.

Forster distance is the distance at which RET occurs at 50% efficiency, and is typically 20 to 60 Å. The rate of energy transfer $k_T(r)$ is

$$k_T(r) = \frac{1}{\tau_D}\left(\frac{R_0}{r}\right)^6 \qquad \ldots (32)$$

where R_0 is the Forster distance, r is the distance between the donor and acceptor and τ_D is the decay time of the donor. When $= R_0$, the rate of transfer is equal to the decay rate, $\frac{1}{\tau_D}$, meaning that energy transfer efficiency is 50%.

Multi-photon excitation microscopy

Although many molecules are excited by light in the near UV, exposing the sample to strong UV light may have a negative effect on the sample. This can be overcome by multi-photon excitation (MPE). MPE occurs when two or more electrons interact simultaneously with a fluorophor, and the fluorophor absorbs energy equal to the sum of the multiple electrons. Therefore the wavelength of the excitation light used is much longer than that used for one photon excitation.

For multiple photons to be absorbed simultaneously, illumination intensities must be high. The intensity of MPE is in the order of second power of the excitation light (I^2). In this respect, MPE is referred to as non-linear fluorescence. This non-linearity is favorable in imaging since it enables the excitation of a specific point. When an excitation light is focused on a point in space, the planes in front or behind the focal point are also illuminated. However, the probability of MPE to happen (or the intensity of MPE) is lowered in order of second power, so essentially, only the molecules at the focal plane are excited (Figure III-2).

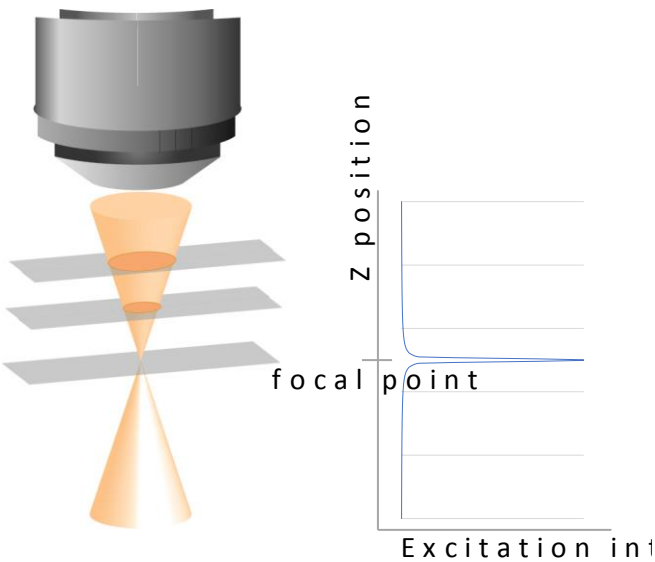

Figure III-2 Pinpoint excitation by MPE [20]

MPE is almost always coupled with extrinsic fluorophors which are inducted in the sample in advance. Using MPE to observe intrinsic fluorophors would be an interesting study.

References

1. Maitland, J., Steven, F., Organic chemistry. 4th ed. (2010).

2. Peter, A., Julio, d.P., Atkins' physical chemistry. 8th ed. (2006).

3. 井上均. 化学結合の話. http://hr-inoue.net/zscience/topics/chemicalbond/chemicalbond.html. Last accessed: 2014.1.23

4. 電子状態（wikipedia）. http://ja.wikipedia.org/wiki/%E9%9B%BB%E5%AD%90%E7%8A%B6%E6%85%8B. Last accessed: 2014.1.23

5. Reusch, W. Visible and ultraviolet spectroscopy. http://www2.chemistry.msu.edu/faculty/reusch/VirtTxtJml/Spectrpy/UV-Vis/spectrum.htm http://www2.chemistry.msu.edu/faculty/reusch/VirtTxtJml/Spectrpy/UV-Vis/uvspec.htm#uv3. Last accessed: 2014.1.23

6. Valence bond theory (wikipedia). http://en.wikipedia.org/wiki/Valence_bond_theory. Last accessed: 2014.1.23

7. 棚瀬知明. 基礎化学４　化学結合と分子の形２. http://www.chem.nara-wu.ac.jp/~tanase/ClassesInfo/kisokagaku4-1.pdf. Last accessed: 2014.1.23

8. Tony, O., Fundamentals of uv-visible spectroscopy.

9. Khan, M. Ultraviolet/visible absorption spectroscopy. http://www2.mpip-mainz.mpg.de/documents/aksp/Seminare/Basisseminars/UV-VIS.pdf. Last accessed: 2014.1.23

10. 御崎洋二. 有機化学特論ｉ　平成 19 年度　分子軌道. http://www.misaki-lab.jp/pdf/lecture/tokuron_H19/2nd-MO.pdf. Last accessed: 2014.1.23

11. 三角関数の公式の一覧（wikipedia）. http://ja.wikipedia.org/wiki/%E4%B8%89%E8%A7%92%E9%96%A2%E6%95%B0%E3%81%AE%E5%85%AC%E5%BC%8F%E3%81%AE%E4%B8%80%E8%A6%A7. Last accessed: 2014.1.23

12. 遠藤泰樹. 基礎現代科学　第３章　光と分子. http://bunshi.c.u-tokyo.ac.jp/~endolab/Jpn/lab/kisogendai/no6_web.pdf. Last accessed: 2014.1.23

13. 島津製作所. Uv talk letter vol.2(2008) 紫外可視吸収と有機化合物の構造との関係. http://www.an.shimadzu.co.jp/uv/support/lib/uvtalk/uvtalk2/apl.htm. Last accessed: 2014.1.23

14. 山本勝博. 紫外スペクトル法による天然水中の有機成分の測定. http://www.osaka-c.ed.jp/kak/rika1/osaka-ch/chem11-4.htm. Last accessed: 2014.1.23

15. Reaction rate constant (wikipedia). http://en.wikipedia.org/wiki/Reaction_rate_constant. Last accessed: 2014.1.23

16. Nobel, P.S., Physicochemical and environmental plant physiology. 4th ed. (2009): Academic Press. 582.

17. Rich, R.M., Stankowska, D.L., Maliwal, B.P., Sorensen, T.J., Laursen, B.W., Krishnamoorthy, R.R., Gryczynski, Z., Borejdo, J., Gryczynski, I., Fudala, R., Elimination of autofluorescence background from fluorescence tissue images by use of time-gated detection and the azadioxatriangulenium (adota) fluorophore. Analytical and Bioanalytical Chemistry, (2013). **405**(6): p. 2065-2075.

18. Chorvat, D., Chorvatova, A., Multi-wavelength fluorescence lifetime spectroscopy: A new approach to the study of endogenous fluorescence in living cells and tissues. Laser Physics Letters, (2009). **6**(3): p. 175-193.

19. Lakowicz, J.R., Principles of fluorescence spectroscopy. 3rd Edition ed. (2006), NewYork: Springer Science+Business Media, LLC.

20. Diaspro, A., Bianchini, P., Vicidomini, G., Faretta, M., Ramoino, P., Usai, C., Multi-photon excitation microscopy. Biomedical Engineering Online, (2006). **6**: p. 5-36.

Acknowledgements

この博士論文には、修士課程から博士課程にかけての 5 年間の研究をまとめました。この間、数えきれないほど多くの方々にお世話になりました。改めて振り返ってみると、自分がいかに恵まれた立場にあったかを強く感じます。関わった方のなかでもほんの一部になりますが、ここで御礼を申し上げたいと思います。

鍋谷浩志 教授　（東京大学大学院農学生命科学研究科 連携教授、独立行政法人 農業・産業技術総合研究機構 食品総合研究所 食品工学研究領域 領域長）
指導教官として、学部から修士課程、博士課程まで本当にお世話になりました。食品総合研究所では、いつもいろいろな部屋を回ってそこの方と直接話されているのを見て、直接話をしてコミュニケーションをとることの大切さを教えられました。仕事への真面目さと飲み会でのフランクさ、どちらも見習いたいと思っています。

杉山純一 博士　（独立行政法人 農業・産業技術総合研究機構 食品総合研究所 計測情報工学ユニット ユニット長）
すべての研究の直接指導者として、大変お世話になりました。計測情報工学ユニットの中で、そしてこのテーマで研究させていただけたことは本当に幸運だったと思っています。杉山様の研究に対する熱意や柔軟な考え方、そしてある種の「勘」にはいつも驚かされています。学生だからという遠慮は全くなく、いつも自由に発言させていただいていましたが、そのような雰囲気を作ってくださった杉山様に感謝しています。

蔦瑞樹 博士　（独立行政法人 農業・産業技術総合研究機構 食品総合研究所 計測情報工学ユニット 主任研究員）
研究の指導者として、そして先輩として、尊敬してやまない存在です。何か迷ったときは必ず相談させていただいていましたし、いただいたアドバイスはほとんど全部実現させてきたと思っています。10 年かかっても今の蔦様にはかなう気はしませんが、少しずつ頑張っていきたいと思っています。

藤田かおり 博士　（独立行政法人 農業・産業技術総合研究機構 食品総合研究所 計測情報工学ユニット 研究員）
研究全般について、いつも細かいところまで見ていただき、たくさんのアドバイスをいただきました。外部の人との積極的な関わり、実験のときの細やかな気づかい、研究に対する粘り強さ、どれも自分には足りないところで、藤田様を見ていて本当にすごいな、と毎回思っています。女性であることは、デメリットよりもメリットの方が大きいかもしれないと思わせてくれた存在です。本当にありがとうございます。

吉村正俊 博士　（独立行政法人 農業・産業技術総合研究機構 食品総合研究所 計測情報工学ユニット、日本学術振興会 特別研究員）
この研究の途中から、同じ蛍光指紋イメージングに取り組まれた吉村様からは、逆に蛍光やイメージングの基礎的部分を教えられました。今の研究は、過去の様々な研究の上に成り立っている、ということを身をもって教わり、それが本論の第一章を書く原動力にもなりました。ありがとうございました。

柴田真理朗 博士　（独立行政法人 農業・産業技術総合研究機構 食品総合研究所 計測情報工学ユニット、日本学術振興会 特別研究員）
研究室の最も近い先輩として、多くのことを教えていただきました。時々、自分の研究にも鋭い指摘をいただき、ハッとさせられることがありました。淡々と実験に取り組み、論文をどんどん出していく姿勢をとても尊敬します。

荒木徹也 博士　（東京大学大学院農学生命科学研究科 農学国際専攻 准教授）
私は主に食品総合研究所で研究を進めながらも、大学で研究内容を別の視点から見ていただくという、大変恵まれた境遇にありました。その筆頭として荒木先生からは少し離れた立場からアドバイスをいただくことができ、本当に有難いことだと思っています。研究の進め方や留学などについても、親身になって相談にのってくださり、ありがとうございました。

溝口勝 教授　（東京大学大学院農学生命科学研究科 農学国際専攻）
同じ体育会系だからか感覚が似ているところが多く、いつもお話していて楽しかったです。国際学会中に語っていらっしゃった大学院での研究や教育についてのお話や、東日本大震災以降の研究の有り方についてのお話はとても印象的で、少なからず影響を受けました。少し分野が異なるものの、同じ国際情報研究室の中に二つの研究室が入っていてよかったと思っています。

斎藤幸恵 博士　（東京大学大学院農学生命科学研究科 農学国際専攻 准教授）
斎藤先生には、修士論文に続き、博士論文でも副査になっていただき、細やかなアドバイスをいただきました。普段はあまり一緒に研究をしていない方から、新たな視点でご指摘をいただくことはとても刺激的で、博士論文をまとめて良かったと感じた瞬間でもありました。ありがとうございました。

相良泰行 教授　（東京大学 名誉教授、一般社団法人食感性コミュニケーションズ）
食品総合研究所でも大学でもない、もう一か所の相談先が相良先生でした。「実用研究ではいつもその学問の基礎を参照し、基礎研究ではいつも実用的な出口を考える」という方針は

いろいろな場面で思い出されます。同行させていただいた北海道帯広市の視察では、国産小麦の生産・加工・消費という正に現場を見ることができ、大きな影響を受けました。今後ともご指導いただければと思います。

前田竜郎 博士　（日清フーズ株式会社）
本研究は観察対象として小麦製品を扱っていますが、この分野の多くの知識は前田様から教わりました。御社の研究所にて、パン生地の作り方と小麦粉の分画方法を教えていただいたところからこの研究は始まっています。何よりも、小麦粉という一つの作物の特異性や面白さを教えていただいたことは大きいと思っています。ありがとうございました。

芦田祐子 様　（不二製油株式会社）
芦田様には第 6 章のパイ生地のイメージング実験において、試料作製から染色・観察まで行っていただき、大変お世話になりました。まだ研究段階である蛍光指紋イメージングでは、失敗や装置などの問題もあり、長い期間結果が出ないこともありましたが、本当に親身になってアドバイスをくださり、感謝しきれません。すばらしい切片や染色画像は自分一人の力ではどう頑張っても得られないもので、いろいろな方と一緒に研究することの意義が実感できた研究でした。

横矢直人 博士　（東京大学大学院工学系研究科 先端学際工学専攻 助教）
部活時代からの良き友達であると同時に、ハイパースペクトルの解析でははるかに進んでいるリモートセンシング分野の先生でもあり、第 6 章のパイ生地のイメージング実験では蛍光指紋データを解析してくださりました。どんどん研究成果を出す同期の存在はいつも刺激的で、前に進む原動力となっています。

Ms. Tsai Karin、中村結花子 様、Mr. Dheni Mita Mala、平野由香里 様、松山信悟 様、今村義則 様
食品総合研究所にて今まで一緒に研究をしてきた学生は、皆研究に熱心で、面倒な実験も厭わずに行う人たちで、そのような姿は私にとっても大きな支えになりました。やはり自分と同年代の人たちがいる研究室は楽しく、ほとんどストレスもなく研究を進められたのは皆さまのおかげだと思っています。

等々力節子 博士、亀谷宏美 博士、桂洋子 様、齊藤希己江 様、森下みずほ 様、吉田元美 様、鈴木洋子 様
食品総合研究所の同じ研究室で働く方々には、いろいろなところで助けていただきました。どうしても考えがまとまらないとき、一つの課題が終わって次に取り組む元気が出ないとき、全然関係ない話題で笑い気分を新しくしていました。研究では直接関わっていないから

こそ、弱気な気持ちや愚痴を漏らしやすく、うまくガス抜きができていたと思います。ありがとうございました。

家族

改めて、博士課程への進学を認めてくれ、支えてくれた両親と妹達に感謝します。この研究の元には「食品の『おいしさ』はどのように計測できるのか」という大きなテーマがあります。この、「食」への興味は、人一倍食べることに熱意をかける家族の中で育ったからこそ、生まれたものだと思っています。博士課程を修了した後も平坦な道ではないと思いますが、自分の興味を大切に精一杯研究したいと思います。